Direct photon measurement with virtual photon method in d+Au collisions at $\sqrt{s_{NN}} = 200$ GeV

Yorito Yamaguchi

Center for Nuclear Study,
Graduate School of Science,
University of Tokyo

A Dissertation Submitted in Partial Fullfillment of
the Requirements for the Degree of Doctor of Science

Abstract

Quark Gluon Plasma (QGP) is a de-confined state of quarks and gluons, and the phase transition from normal nuclear matter to the QGP can occur under the condition of the energy density of above 1 GeV/fm^3 and the temperature of above $150 \sim 200$ MeV predicted by theoretical calculations based on Quantum chromodynamics (QCD).

High-energy heavy ion collisions are a powerful tool to realize the QGP in the laboratory. Direct photons are a unique probe to directly investigate properties of the matter created by heavy ion collisions since they leave the medium without a strong interaction once they are generated. Although direct photons could be generated in every stage of the heavy ion collisions, their transverse momenta are characterized by their origins. In particular, thermal photons from the QGP are considered to be a primary contributor in the low p_T region of $1 \sim 3$ GeV/c.

The PHENIX experiment at Relativistic Heavy Ion Collider at the Brookhaven National Laboratory demonstrated that the direct photon yield can be determined via di-electron measurements even in the low p_T region of $1 \sim 3$ GeV/c and a significant excess yield over the expectation from the p+p data is observed in Au+Au collisions at $\sqrt{s_{NN}} = 200$ GeV. The observed excess yield is a positive indication of the existence of thermal photons from the QGP.

However, nuclear effects, which are involved in Au+Au collisions but not in p+p collisions, can affect the direct photon yield in such low p_T region. The contribution of nuclear effects in the direct photon yield should be evaluated with d+Au collisions. The measurement of direct photons via di-electrons in d+Au collisions has been made and the direct photon yield has been successfully determined in p_T of $1 \sim 6$ GeV/c.

The obtained d+Au result is consistent with the binary-scaled p+p result, and this fact implies that the contribution of nuclear effects is very small in direct photon production. Comparing the Au+Au result with the scaled d+Au result, an excess yield in Au+Au collisions is clearly seen in $p_T < 2.0$ GeV/c as well as the comparison between the p+p and Au+Au results. Thus, it is concluded that the observed excess yield in Au+Au collisions is due to non-initial effects. Assuming the origin of the excess yield is thermal radiation from the created matter, the initial temperature is higher than $220 \pm 15^{stat} \pm 18^{syst}$ MeV.

Contents

1 Introduction **1**
1.1 Quantum ChromoDynamics . . . 1
1.2 Quark Gluon Plasma . . . 1
1.3 Direct Photon Production . . . 2
1.4 Objective of This Study . . . 6
1.5 Organization of This Thesis . . . 7
1.6 Major Contributions . . . 7

2 Physics Background **9**
2.1 Relativistic Heavy Ion Collisions . . . 9
2.1.1 Collision Geometry . . . 9
2.1.2 Space-Time Evolution of Matter . . . 12
2.1.3 Initial Energy Density . . . 14
2.2 Previous Experimental Results . . . 15
2.2.1 WA80 . . . 15
2.2.2 WA98 . . . 15
2.2.3 PHENIX . . . 19
2.3 Virtual Photon Method . . . 22
2.3.1 p+p and Au+Au Results . . . 26
2.4 Nuclear Effects . . . 31
2.4.1 Measured Nuclear Effects for Hadrons . . . 33
2.4.2 Theoretical Expectation for Nuclear Effects on Direct Photon Production . . . 37

3 Experimental Setup **39**
3.1 RHIC Accelerator Complex . . . 39
3.2 PHENIX Experiment . . . 41
3.2.1 Global Coordinate System . . . 42
3.2.2 Detector Overview . . . 42
3.3 PHENIX Global Detectors . . . 44
3.3.1 Beam-Beam Counter . . . 44
3.3.2 Zero-Degree Calorimeter . . . 45

3.4 PHENIX Magnet . . . 47
3.5 PHENIX Central Arms . . . 48
3.5.1 Drift Chamber . . . 50
3.5.2 Pad Chamber . . . 52
3.5.3 Ring Imaging Cherenkov Detector . . . 54
3.5.4 Electromagnetic Calorimeter . . . 56
3.6 Trigger . . . 58
3.6.1 BBC Local Level-1 Trigger . . . 58
3.6.2 EMCal-RICH Local Level-1 Trigger . . . 59
3.7 Data Acquisition System . . . 60

4 Experiment **63**
4.1 RHIC Run Overview . . . 63
4.2 d+Au Collisions at $\sqrt{s_{NN}} = 200$ GeV in 2008 . . . 64

5 Data Analysis **67**
5.1 Invariant Yield . . . 67
5.2 Event Classification . . . 68
5.2.1 Determination of Minimum Bias Trigger Efficiency . . . 68
5.2.2 Centrality Determination . . . 68
5.2.3 BBC Trigger Bias . . . 70
5.3 Track Reconstruction and Momentum Determination . . . 70
5.3.1 Track Reconstruction Technique . . . 71
5.3.2 Momentum Determination . . . 72
5.3.3 Analysis Variable . . . 73
5.4 RICH Calibration . . . 74
5.4.1 Charge Calibration . . . 74
5.4.2 Mirror Alignment Calibration . . . 75
5.5 Electron Identification . . . 79
5.5.1 Electron Identification with RICH . . . 79
5.5.2 Electron Identification with EMCal . . . 81
5.5.3 Cuts for Electron Identification . . . 82
5.5.4 Check of Detector Response . . . 83
5.6 Acceptance Evaluation . . . 85
5.7 Run Selection . . . 88
5.8 Invariant Mass Spectrum . . . 90
5.8.1 Pair Cuts . . . 92
5.8.2 External Photon Conversion . . . 93
5.8.3 Background Pairs . . . 97
5.8.4 Background Evaluation . . . 98
5.9 Efficiency Correction . . . 101
5.9.1 Electron Efficiency . . . 101

5.9.2 Acceptance and Pair Cuts Efficiency 103
5.9.3 ERT Trigger Efficiency 105
5.10 Hadronic Cocktail Calculation 111
5.11 Determination of Direct Virtual Photon Fraction 114
5.12 Inclusive Photon Spectrum 120
5.13 Systematic Error Evaluation 121
5.13.1 Systematic Errors on r_{γ^*} 121
5.13.2 Systematic Errors on Inclusive Photon Yield 128

6 Results **131**
6.1 Direct Virtual Photon Fraction 131
6.2 Direct Photon Yield 133

7 Discussion **135**
7.1 Nuclear Effects 135
7.1.1 Comparison with p+p Result 135
7.1.2 Nuclear Modification Factor R_{dA} 137
7.1.3 Parameterization of d+Au Data 138
7.2 Thermal Photons 138
7.2.1 Comparison with Au+Au Result 138
7.2.2 Upper Limit of Nuclear Effects 144

8 Conclusion **147**

Acknowledgments **149**

A e^+e^- Mass Spectra **151**
A.1 Determination of r_{γ^*} 151
A.2 $R(m_{ee}) = (\text{data} - \text{cocktail})/f_{dir}(m_{ee})$ 156

List of Figures

1.1 The entropy density ($s = (\epsilon + p)/T$) as a function of T by the lattice QCD calculation. 2
1.2 A schematic phase diagram of QCD matter. 3
1.3 Theoretical calculation of the direct photon spectrum in central Au+Au collisions at $\sqrt{s_{NN}} = 200$ GeV showing contributions of direct photons from different phases. 4
1.4 Diagrams for direct photon production in the leading order. 5
1.5 Fractions of contributions of the direct (Compton and annihilation) and fragmentation processes in the hard photon yield as a function of p_T. 5

2.1 An illustration of the colliding nuclei before and after a collision in the participant-spectator picture. 10
2.2 A cartoon of central and peripheral collisions of nuclei with radii R. . 11
2.3 A space-time picture of evolution of the matter created in a heavy ion collision at RHIC. 13
2.4 The upper limits of the direct photon production for most central collisions in $200A$ GeV ^{32}S+Au in the WA80 experiment. 16
2.5 The yield ratios of inclusive photons to photons from hadron decays for peripheral and central collisions in $158A$ GeV Pb+Pb reactions. . 17
2.6 The direct photon invariant yield in the central collisions of $158A$ GeV Pb+Pb reactions. 18
2.7 The direct photon invariant cross section in 200 GeV p+p collisions at the PHENIX experiment. 20
2.8 The direct photon invariant yields for 8 centrality selections in 200 GeV Au+Au collisions at the PHENIX experiment. 21
2.9 The nuclear modification factor for direct photons with $p_T > 6$ GeV/c as a function of the number of the participating nucleons. 22
2.10 The lowest order diagrams for gluon Compton scattering with a real photon and an e^+e^- pair via a virtual photon. 23
2.11 The diagrams for two photon decay and Dalitz decay of π^0. 24
2.12 The direct virtual photon fractions in p+p and Au+Au collisions obtained by the virtual photon method. 26

2.13 The direct photon invariant yield in p+p and Au+Au collisions with the virtual photon method together with the measured results by the EMCals and the NLO pQCD calculations. 28
2.14 The comparison of several hydrodynamical models with the data for central Au+Au collisions. 29
2.15 The initial temperature T_{init} and the thermalization time τ_0 in the hydrodynamical models which can reproduce the central Au+Au data. 30
2.16 The ratio of structure functions in heavy nuclei and the deuteron together with calculations the NLO NPDF parameterization. 32
2.17 The expected ratios of parton distribution functions for valence quarks, sea quarks and gluons in a nuclei of Ca to those in a proton with different NPDF parameterizations. 32
2.18 The nuclear modification factor R_{dA} for pions, kaons and protons as a function of p_T for minimum bias d+Au collisions measured by the PHENIX detector. 34
2.19 The R_{dA} for pions, kaons and protons in four different centrality selections. 35
2.20 The R_{dA} for π^0 and η in different centrality selections and minimum bias data. 36
2.21 The expectation of the nuclear effects on the direct photon production in d+Au and d+Cu collisions with $\sqrt{s_{NN}} = 200, 62.4$ GeV. 38

3.1 The accelerator complex including RHIC at BNL. 40
3.2 Definition of the global coordinate system used in the PHENIX experiment. 42
3.3 Layout of the PHENIX detector configuration in the Year-2008 Run. 43
3.4 The acceptance coverages of the central and muon arms with respect to η-ϕ plane. 45
3.5 Pictures of the BBC. 46
3.6 Layout of the ZDC location. 47
3.7 The layout of the PHENIX magnets with a cutaway to show the interior structures. 48
3.8 The field lines of the central magnet and muon magnets shown on a vertical cutaway drawing of the PHENIX magnets. 49
3.9 A frame of the drift chamber. 50
3.10 The layout of wire positions in one sector. 51
3.11 A schematic view of the PCs (PC1, PC2, PC3). 52
3.12 The pad and pixel geometry of the PC. 53
3.13 A cutaway view of RICH. 54
3.14 A schematic view of RICH cut along the beam axis. 55

3.15 Interior view of a lead scintillator calorimeter module showing a stack of scintillator and lead plates, wavelength shifting fiber readout and leaky fiber inserted in the central hole. 57
3.16 Exploded view of a lead glass calorimeter supermodule. 58
3.17 The principal scheme of the ERTLL1_E trigger. 59
3.18 The schematic flow diagram of the data acquisition system. 60

4.1 The integrated luminosity of d+Au collisions in Run8 recorded at the PHENIX experiment as a function of date. 64

5.1 The BBC South charge distribution in the real data showing the charge region corresponding to each centrality class. 69
5.2 Schematic views of a trajectory of a charged particle in the x-y and z-r planes at the track reconstruction in the DC. 70
5.3 The Hough transformation of the DC hits in the x-y plane to the feature space of α and ϕ. 71
5.4 The number of photo-electron distribution after the gain calibration. . 75
5.5 Example of the track association to the RICH phototube plane. . . . 76
5.6 The accumulated RICH ring image after the alignment calibration. . 77
5.7 The obtained ring radius distribution after the alignment calibration. 78
5.8 A schematic view of the definition of variables used for determination of the RICH variables 80
5.9 The single electron p_T distributions from the experiment and from the simulation for check of the detector response. 84
5.10 The real and simulated distributions for the eID variables. 84
5.11 The simulated dcphi distribution compared to the real one. 86
5.12 The simulated zed distribution compared to the real one. 86
5.13 The simulated pemcphi distribution compared to the real one. 87
5.14 The simulated pemcz distribution compared to the real one. 87
5.15 The number of electrons per event with the $0.5 < p_T < 5.0$ GeV/c cut in MB data. 89
5.16 The number of triggered electrons per MB equivalent event in the ERT data for all good runs. 89
5.17 The Δzed distribution for like-sign pairs. 92
5.18 The $\Delta\phi_{cross}$ and Δz_{cross} distributions for like-sign pairs. 93
5.19 Production of a conversion electron pair. 94
5.20 The invariant e^+e^- mass spectra before/after external conversion pairs are removed. 95
5.21 The ϕ_V distributions in different mass regions for $1.0 < p_T^{ee} < 2.0$ GeV/c compared to non-conversion pair contribution. 96
5.22 The like-sign pair distributions in the real data showing the background components with the normalization factors determined by the 3-component fit. 99

5.23 The $\Delta\phi_{ee}$ distributions of like-sign pairs in the real data together with the sum of the background components with the normalization factors. 100
5.24 The e^+e^- pair distribution in the real data together with the all background pair contributions and the correlated e^+e^- pairs after the background subtraction. 101
5.25 The electron efficiencies for single electrons and positrons calculated using the PISA simulation. 102
5.26 The electron efficiency as a function of m_{ee} for e^+e^- pairs in $1.0 \leq p_T^{ee} < 1.1$ GeV/c. 103
5.27 Mean values of the electron efficiency for e^+e^- pairs in $0.00 < m_{ee} < 0.05$ GeV/c^2 and $0.10 < m_{ee} < 0.30$ GeV/c^2 as a function of p_T^{ee}. . . . 104
5.28 The loss efficiency due to dead areas and pair cuts as a function of m_{ee} for e^+e^- pairs in $2.0 \leq p_T^{ee} < 2.1$ GeV/c. 105
5.29 Mean values of the loss efficiency due to dead areas and pair cuts for e^+e^- pairs in $0.00 < m_{ee} < 0.05$ GeV/c^2 and $0.10 < m_{ee} < 0.30$ GeV/c^2 as a function of p_T^{ee}. 106
5.30 The p_T distributions and the EMC2x2 trigger efficiency for the EMC2x2 supermodule in the run group G1 (the energy threshold is 600 MeV). 108
5.31 The p_T distributions and the RICH trigger efficiency for the RICH supermodule in the run group G1. 108
5.32 The ERT trigger efficiency for e^+e^- pairs as a function of m_{ee} in $2.5 \leq p_T^{ee} < 2.6$ GeV/c. 109
5.33 Mean values of the ERT trigger efficiency for e^+e^- pairs in $0.00 < m_{ee} < 0.05$ GeV/c^2 and $0.10 < m_{ee} < 0.30$ GeV/c^2 as a function of p_T^{ee}. 110
5.34 The compilation of meson production cross sections in d+Au collisions at $\sqrt{s_{NN}} = 200$ GeV together with m_T scaled modified Hagedorn functions determined by a fit to the pion data. 112
5.35 The measured yield over the m_T scaling function for η. 113
5.36 The number of e^+e^- pairs in the p_T^{ee}-m_{ee} space from the MB data and the ERT data. 115
5.37 The e^+e^- pair mass spectrum in $1.5 < p_T^{ee} < 2.0$ GeV/c together with the fit result and the fit result and the cocktail components. 117
5.38 The R as a function of m_{ee} for $1.5 < p_T^{ee} < 2.0$ GeV/c. 119
5.39 The inclusive real photon spectrum in d+Au collisions determined from the e^+e^- pair yields in the data and the photon cocktail calculation for known hadron decays. 122

6.1 The direct virtual photon fractions as a function of p_T in p+p, d+Au and Au+Au collisions. 132
6.2 The direct photon spectrum in d+Au collisions compared to the NLO pQCD calculations with different theoretical scales. 134

7.1 The invariant yield of the direct photons in d+Au collisions compared to the binary-scaled p+p result. 136
7.2 The R_{dA} for the direct photons compared to the R_{dA} for π^0. 137
7.3 The direct photon spectrum in d+Au collisions fitted with the modified power-law function for parameterization of the d+Au data. 139
7.4 The direct photon spectrum in minimum bias Au+Au collisions compared to the scaled d+Au result. 140
7.5 The ratio of the MB Au+Au data to the scaled d+Au data. 141
7.6 The fit result to the MB Au+Au data with Eq. 7.1. 142
7.7 The fit result to the d+Au data with Eq. 7.2 for determination of effective nuclear effects. 145
7.8 The Au+Au result compared to the N_{coll}-scaled p+p fit result plus the expected upper limit of nuclear effects calculated with consideration for systematic uncertainties of the d+Au fit result. 146

A.1 The e^+e^- pair mass spectrum in $1.0 < p_T^{ee} < 1.5$ GeV/c at determination of direct r_{γ^*}. 151
A.2 The e^+e^- pair mass spectrum in $2.0 < p_T^{ee} < 2.5$ GeV/c at determination of direct r_{γ^*}. 152
A.3 The e^+e^- pair mass spectrum in $2.5 < p_T^{ee} < 3.0$ GeV/c at determination of direct r_{γ^*}. 152
A.4 The e^+e^- pair mass spectrum in $3.0 < p_T^{ee} < 3.5$ GeV/c at determination of direct r_{γ^*}. 153
A.5 The e^+e^- pair mass spectrum in $3.5 < p_T^{ee} < 4.0$ GeV/c at determination of direct r_{γ^*}. 153
A.6 The e^+e^- pair mass spectrum in $4.0 < p_T^{ee} < 4.5$ GeV/c at determination of direct r_{γ^*}. 154
A.7 The e^+e^- pair mass spectrum in $4.5 < p_T^{ee} < 5.0$ GeV/c at determination of direct r_{γ^*}. 154
A.8 The e^+e^- pair mass spectrum in $5.0 < p_T^{ee} < 5.5$ GeV/c at determination of direct r_{γ^*}. 155
A.9 The e^+e^- pair mass spectrum in $5.5 < p_T^{ee} < 6.0$ GeV/c at determination of direct r_{γ^*}. 155
A.10 The R as a function of m_{ee} for $1.0 < p_T^{ee} < 1.5$ GeV/c. 156
A.11 The R as a function of m_{ee} for $2.0 < p_T^{ee} < 2.5$ GeV/c. 157
A.12 The R as a function of m_{ee} for $2.5 < p_T^{ee} < 3.0$ GeV/c. 157
A.13 The R as a function of m_{ee} for $3.0 < p_T^{ee} < 3.5$ GeV/c. 158
A.14 The R as a function of m_{ee} for $3.5 < p_T^{ee} < 4.0$ GeV/c. 158
A.15 The R as a function of m_{ee} for $4.0 < p_T^{ee} < 4.5$ GeV/c. 159
A.16 The R as a function of m_{ee} for $4.5 < p_T^{ee} < 5.0$ GeV/c. 159
A.17 The R as a function of m_{ee} for $5.0 < p_T^{ee} < 5.5$ GeV/c. 160
A.18 The R as a function of m_{ee} for $5.5 < p_T^{ee} < 6.0$ GeV/c. 160

List of Tables

2.1 Summary of past and current accelerators for heavy ion collisions. . . 10
2.2 Summary of the fits. The first and second errors are statistical and systematic, respectively. 27

3.1 Summary of the major design parameters of RHIC. 41
3.2 Summary of the information of the PHENIX subsystem detector. . . 44
3.3 Performance of pad chambers in Year-2002 and a cosmic ray test. . . 53

4.1 The recorded data summary at the PHENIX experiment before Run8. 63
4.2 The configurations in the Run8 d+Au 200 GeV period. 65

5.1 The mean number of binary collisions in d+Au collisions and the trigger bias factor for each centrality class. 69
5.2 The bit definition of quality. 73
5.3 Summary of the global and track variables used in this thesis. 74
5.4 Summary of the variables for electron identification. 79
5.5 Difference on counts between the real and simulation (simulation/real) for each DC side. 85
5.6 Difference on counts between the real and simulation (simulation/real) for each EMCal sector. 86
5.7 Summary of run groups. 88
5.8 The normalization factors of the meson yields to the pion yield with uncertainties. 113
5.9 Summary of the fit results with Eq. 5.52 in the range $0.10 < m_{ee} < 0.30$ GeV/c^2. 118
5.10 The differences of the resulting direct virtual photon fractions with $\pm 1\sigma$ variation of the normalization factors from the nominal value. . 123
5.11 The difference on the direct virtual photon fraction due to the variations of the efficiency correction function with different fit range. . . . 124
5.12 The differences of the direct virtual photon fraction with the nominal and $\pm 1\sigma$ varied particle compositions. 125

5.13 The difference on the direct virtual photon fraction with the nominal and upper/lower limit of the modified Hagedorn parameterization of the pion data as an input p_T distribution for mesons in the cocktail calculation. 126
5.14 The differences on the direct virtual photon fraction due to different mass regions for the cocktail normalization. 127
5.15 The differences on the resulting direct virtual photon fractions with the different mass ranges for fitting. 127
5.16 Summary of the systematic errors on the direct γ^* fraction. 128

6.1 Summary of the mean value, the statistical error, the systematic error and mean p_T of each data point in d+Au collisions. 131
6.2 Summary of the mean values, the statistical errors, the systematic errors on the direct photon yield determined by the virtual photon method in d+Au collisions. 133

7.1 Summary of the coefficients of the d+Au fit results and χ^2/NDF at fitting. 138
7.2 Summary of the fits to the Au+Au data with the d+Au fit result as a baseline. 143
7.3 dN/dy ($p_T > 1$ GeV/c) and the inverse slope T obtained by fitting to the Au+Au data (MB) with p+p and d+Au fit results as a baseline. The first and second errors are statistical and systematic ones, respectively. 143
7.4 Summary of α, β and χ^2/NDF at fitting. 144

Chapter 1

Introduction

1.1 Quantum ChromoDynamics

Quantum ChromoDynamics (QCD) is the non-Abelian SU(3) gauge theory to describe the strong interaction. Gluons are the massless gauge bosons of QCD and they are allowed to make self-interactions.

One of the most important features of QCD is 'asymptotic freedom' [1, 2]. The strong coupling constant, α_s, can be expressed as a function of a momentum transfer, Q^2:

$$\alpha_s(Q^2) \simeq \frac{12\pi}{(33-2N_f)\ln(Q^2/\lambda_{QCD}^2)}, \tag{1.1}$$

where N_f is the number of quark flavors and λ_{QCD} is the typical QCD scale ($\lambda_{QCD} \sim$ 0.2 GeV). With larger Q^2, α_s gets smaller and interactions at high-Q^2 can be treated perturbatively.

However when Q^2 is on the order of λ_{QCD}, interactions get strong and non-perturbative, and it consequently leads to a confinement of quarks and formation of color neutral hadrons.

1.2 Quark Gluon Plasma

Under extreme conditions of high temperature and/or density environments, α_s can also decrease. Thus the color confinement may be broken at high temperature and/or density, and then a phase transition from the confined nuclear matter to the deconfined partonic state can happen. The deconfined state is called as 'Quark Gluon Plasma' (QGP) [3].

Calculations based on lattice QCD, which is a numerical approach based on the first principle to describe interactions in the non-perturbative regime of QCD [4, 5], predict that the phase transition to the QGP occurs at the transition temperature

$T_c \simeq 170$ MeV and/or the transition energy density $\epsilon_c \simeq 1$ GeV/fm^3 [6, 7, 8]. Figure 1.1 shows the entropy density ($s = (\epsilon + p)/T$) as a function of T by the lattice QCD calculation [9]. The entropy density increases dramatically around the transition temperature $T_c \sim 170$ MeV, which can be interpreted to happen due to an increase of the degrees of freedom of quarks and gluons.

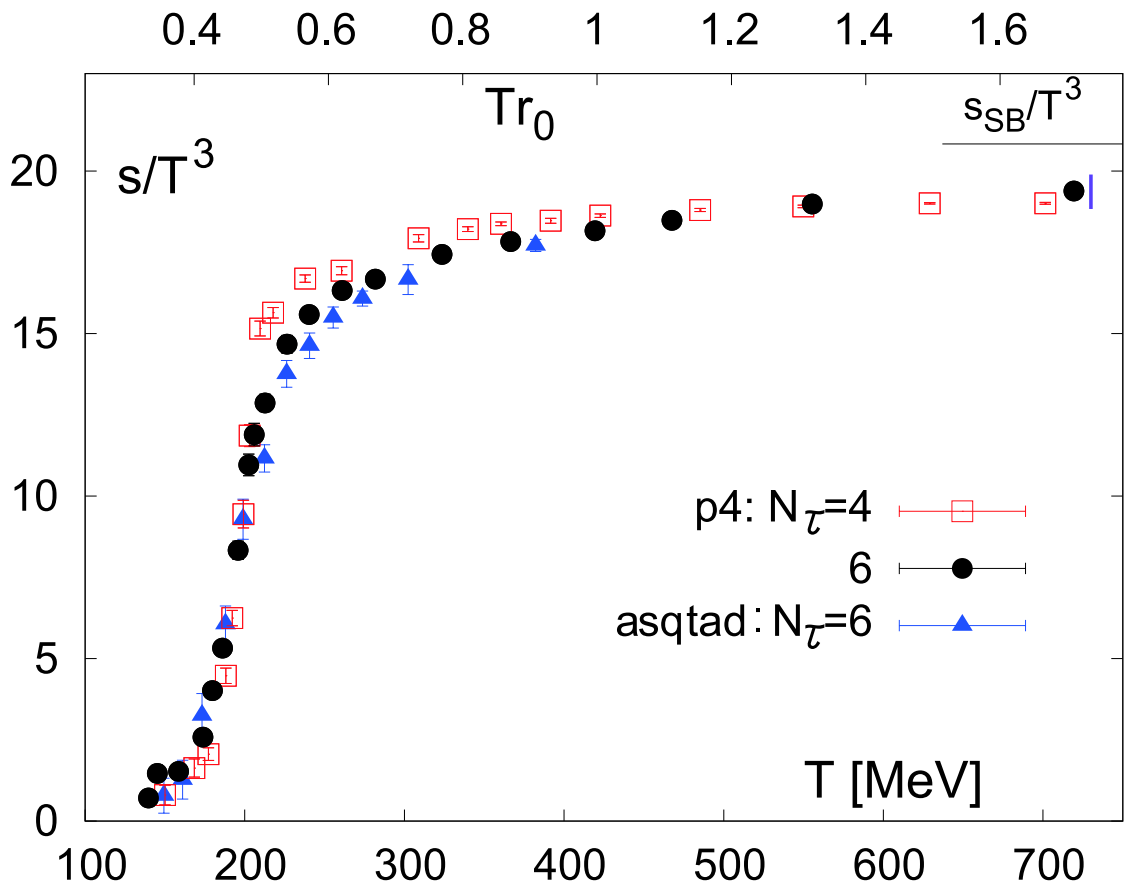

Figure 1.1: The entropy density ($s = (\epsilon + p)/T$) as a function of T by the lattice QCD calculation [9].

A schematic phase diagram of QCD matter is shown in Fig. 1.2. The horizontal axis indicates the baryon density normalized to the density of a normal nucleus ($\sim$0.15 GeV/fm^3) and the vertical axis indicates the temperature. It is thought that a QGP existed in the early universe, a few micro seconds after the Big Bang.

1.3 Direct Photon Production

Direct photons, which do not originate from hadron decays, are a unique probe to directly investigate properties of the matter created by heavy ion collisions, since they

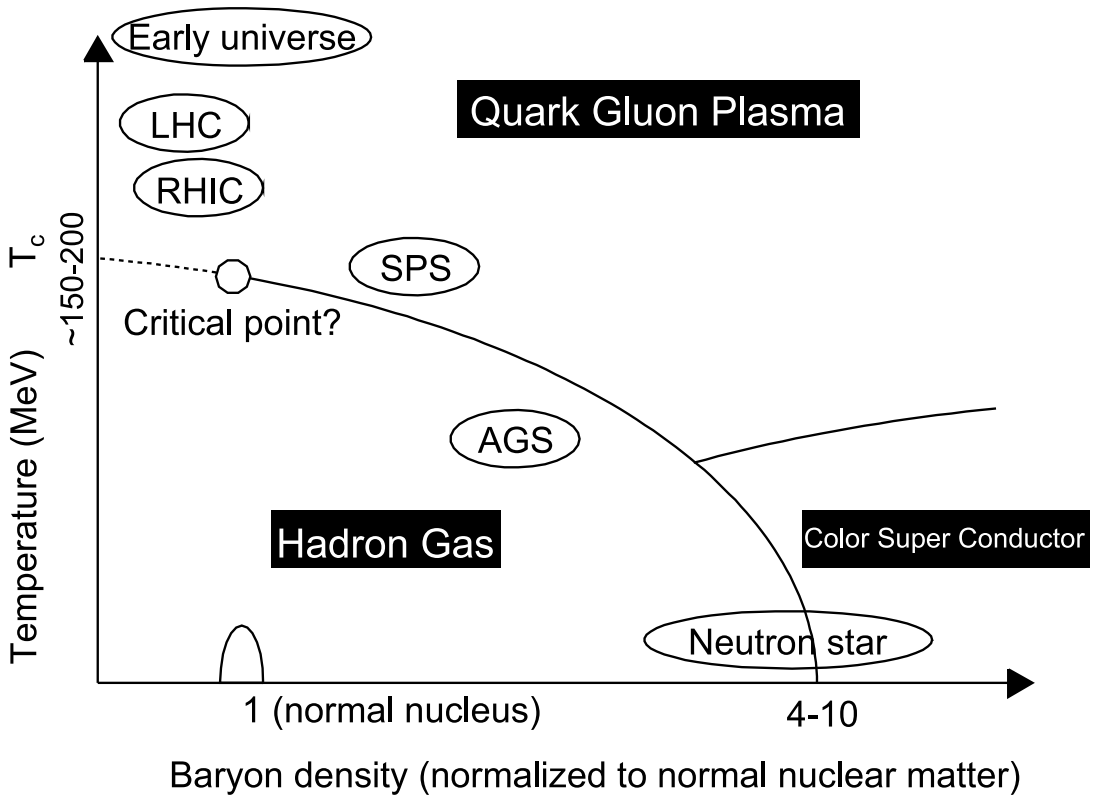

Figure 1.2: A schematic phase diagram of QCD matter. The horizontal axis indicates the baryon density normalized to the density of a normal nucleus, and the vertical axis indicates the temperature.

leave the medium without a strong interaction once they are produced.

High-energy heavy-ion collisions are employed to realize a QGP in the laboratory as explained later (Section 2.1). Direct photons could be generated in every stage of the heavy ion collision and are classified into three groups depending on their origins as follows:

1. Hard photons from initial hard scatterings
2. Thermal photons from QGP
3. Thermal photons from the hadron gas

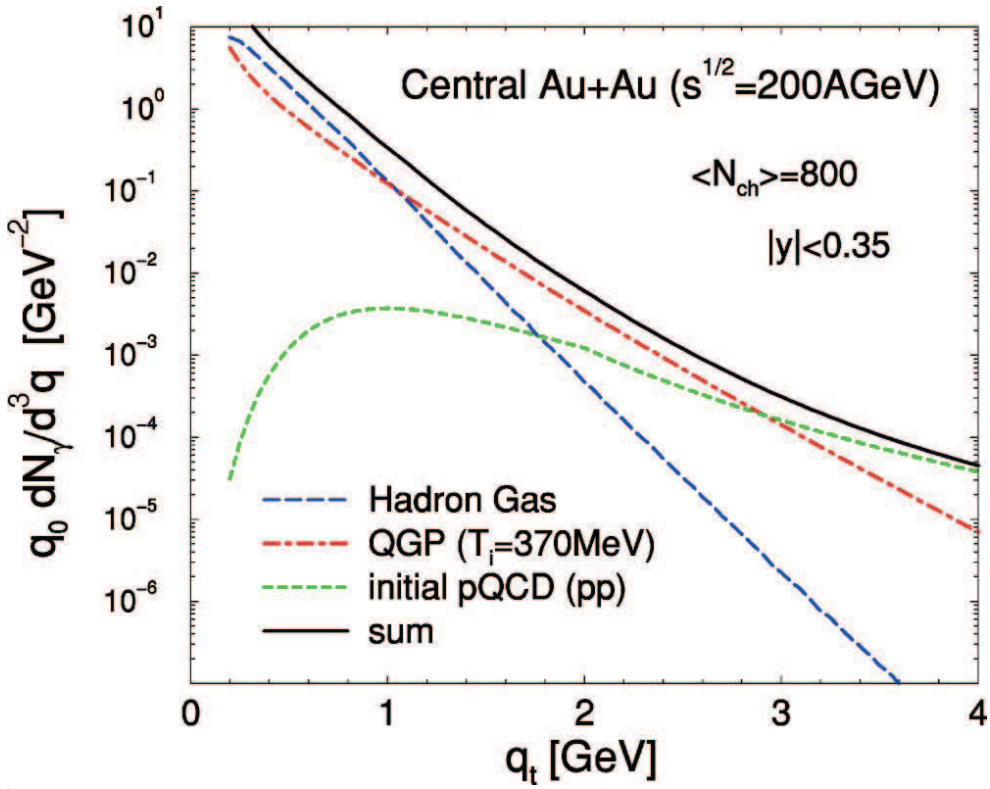

Figure 1.3: Theoretical calculation of the direct photon spectrum in central Au+Au collisions at $\sqrt{s_{NN}} = 200$ GeV showing contributions of direct photons from different phases [10].

Although the experimentally measured direct photon yield is the sum of above photons, there exist suitable momentum windows where a particular photon source is dominant, as shown in Fig. 1.3 [10].

Initial Hard Scatterings

Initial hard scatterings of incoming partons are one of the main sources for direct photon production, occurring at the earliest stage of the collisions. Figure 1.4 shows

diagrams for direct photon production in the leading order (LO). The left and right diagrams are gluon-Compton scattering and quark-antiquark annihilation processes, respectively. In addition to the above processes, fragmentation processes such as

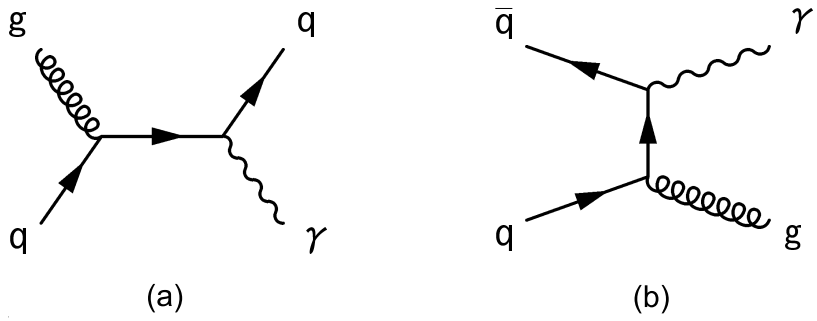

Figure 1.4: Diagrams for direct photon production in the leading order in both initial hard scatterings and the QGP. (a) Gluon-Compton scattering, (b) Quark-antiquark annihilation.

Bremsstrahlung of partons and jet fragmentations are also important, especially in the low p_T region for the next-to-leading order (NLO) calculation [11, 12], while the fragmentation processes occur with a smaller rate than the gluon-Compton scattering and quark-antiquark annihilation processes by a factor of α_s. The contribution of fragmentation photons are expected to be large in $p_T < 3$ GeV/c as shown in Fig. 1.5 [13]. Bremsstrahlung photons are emitted electromagnetically from partons

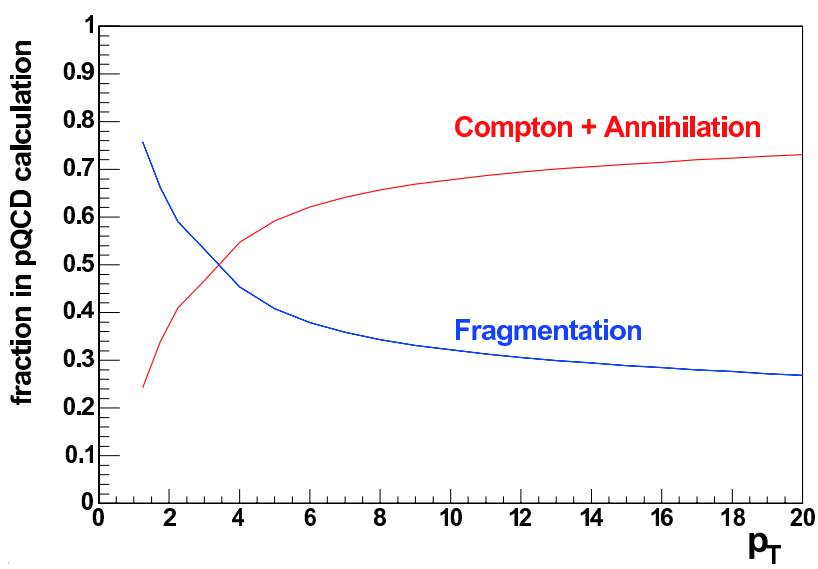

Figure 1.5: Fractions of contributions of the direct (Compton and annihilation) and fragmentation processes in the hard photon yield as a function of p_T [13].

hard-scattered at initial collisions with large momentum transfer. Partons in a jet

can fragment into photons among other particles and are accompanied by hadrons generated in the same jet with the fragmentation process as well.

The cross section of the process preceding the fragmentation, *e.g.* $q + g \rightarrow q + g$ and $q + q \rightarrow q + q$, is calculable. However, the information of the parton fragmentation function is needed for the theoretical calculation of the fragmentation photon contribution, and it brings additional uncertainties which make the theoretical evaluation difficult. Thus, the hard photon contribution in the low p_T region needs to be evaluated experimentally with p+p collisions.

Thermal Radiation in QGP

Thermal photons are not only the direct signature of the QGP formation but also carry the thermodynamical information of QGP directly. Production processes of thermal photons in QGP are supposed to be mainly gluon-Compton scatterings and quark-antiquark annihilations. The suitable momentum window for measuring thermal photons is expected to be $1 < p_T < 3 \sim 5$ GeV/c from theoretical calculations as shown in Fig. 1.3.

Thermal Radiation in Hadron Gas

Thermal photons are also emitted in the hadron gas phase, which is the subsequent phase of QGP. In the hadron gas, the main constituents of the matter are mesons such as π, η and ρ. For example, the following hadronic processes may occur in the hadron gas:

- $\pi^{\pm}\rho \rightarrow \pi^{\pm}\gamma$
- $\pi^{+}\pi^{-} \rightarrow \rho\gamma$
- $\rho \rightarrow \pi^{+}\pi^{-}\gamma$
- $\omega \rightarrow \pi^{0}\gamma$

Thermal photons from the hadron gas phase are considered to be dominant in the low p_T region, $p_T < 1$ GeV/c.

1.4 Objective of This Study

The objective of this thesis is the study of nuclear effects on direct photon production using d+Au collisions at $\sqrt{s_{NN}} = 200$ GeV.

The observation of thermal photons from QGP, which are expected to be dominant in $1 < p_T < 3$ GeV/c, is long-awaited. But we faced an experimental challenge to measure direct photons in such low p_T region due to finite resolutions of detectors.

Recently, the PHENIX experiment has successfully demonstrated that the direct photon yield can be determined via di-electron measurements even in such low p_T region for p+p and Au+Au collisions. A significant excess over the expectation from the p+p data is observed in Au+Au collisions for $p_T < 2.5$ GeV/c [14].

However, nuclear effects, which are initial effects in A+A collisions and are absent in the p+p data, can modify the direct photon yield in such low p_T regions. Thus, nuclear effects need to be investigated in order to extract the contribution of the QGP medium effects from the observed excess yield in Au+Au collisions. Since these effects cannot be estimated by theoretical calculations due to large uncertainties, it is crucial to experimentally determine the degree of modification by nuclear effects using p+A collisions.

1.5 Organization of This Thesis

Production of direct photons in d+Au collisions at $\sqrt{s_{NN}} = 200$ GeV in the RHIC Year-2008 Run has been studied via di-electron measurements at the PHENIX experiment.

The organization of this thesis is as follows. Chapter 2 introduces the theoretical and experimental background for the direct photon production in high energy heavy ion collisions. In Chapter 3, the RHIC accelerator complex and the PHENIX experiment are briefly explained. The conditions of beams and triggers during the d+Au run in 2008 are summarized in Chapter 4. Details on the analysis of the direct photon measurement with the virtual photon method is described in Chapter 5. In Chapter 6, the result of the direct photon measurement is shown. Interpretation of the obtained result is discussed comparing the result with the p+p and Au+Au results in Chapter 7. Finally the conclusion of this thesis is given in Chapter 8.

1.6 Major Contributions

The major contributions of the author as a PHENIX collaborator are as follows:

1. Operation of the ring imaging Cherenkov detector (RICH)

2. Operation of the RICH Level-1 trigger boards which is a part of the EMCal-RICH trigger (ERT) system

3. Calibration of the RICH mirror alignment

4. Participation in the Paper Preparation Group (PPG) of the paper "Enhanced Production of Direct Photons in Au+Au Collisions at $\sqrt{s_{NN}} = 200$ GeV and Implications for the Initial Temperature" [14] on behalf of the PHENIX collaboration

5. Analysis of the direct photons with the virtual photon method for determination of the direct photon yield in d+Au collisions

6. Organization of the PPG as a chairperson for publication of the paper on the measurement of direct photons in d+Au collisions on behalf of the PHENIX collaboration

Chapter 2

Physics Background

In the first half of this chapter, ingredients of relativistic heavy ion collisions, which are a unique tool to study the deconfined QGP phase, are described. Then, the existing results on the direct photon production in heavy ion collisions are briefly introduced as references related to the motivation of this thesis.

2.1 Relativistic Heavy Ion Collisions

Relativistic heavy ion collisions are a powerful tool to realize a high temperature and high density state which is required to form a QGP in the laboratory. In heavy ion collisions, a lot of nucleon-nucleon collisions are involved. Kinetic energies carried by the colliding nuclei are dissipated by collisions, and then huge energies are released into a small collision volume.

Historically, fixed target experiments with high-energy heavy-ion collisions were performed at the Bevalac in the Lawrence Berkeley National Laboratory (LBL) using $\sim 2A$ GeV beams in the middle of 1970's. The Alternating Gradient Synchrotron (AGS) at the Brookhaven National Laboratory (BNL) with $\sim 14A$ GeV beams and the Super Proton Synchrotron (SPS) in the European Organization for Nuclear Research (CERN) with $\sim 160A$ GeV beams started to be operated in 1986.

The Relativistic Heavy Ion Collider (RHIC) at BNL is the first colliding-type accelerator in which a gold nucleus (^{197}Au) can be accelerated up to $100A$ GeV, and it started its operation in 2000. Furthermore, the first Pb+Pb collision with $2.76A$ TeV occurred at the Large Hadron Collider (LHC) in CERN in November, 2010. The accelerator, its collision energy at center of mass frame and colliding nuclear species are summarized in Table 2.1.

2.1.1 Collision Geometry

The geometrical aspects of high energy heavy ion collisions play an important role in collision dynamics. Determination of the number of inelastic nucleon-nucleon colli-

Table 2.1: Summary of past and current accelerators for heavy ion collisions.

Accelerator	collision energy	colliding nucleus
AGS (BNL, 1986∼)	$\sim 5A$ GeV	p+A, O+A, Si+A, Au+Au
SPS (CERN,1986∼)	$17.3, 19.4A$ GeV	p+A, S+U, Pb+Pb, In+In
RHIC (BNL, 2000∼)	$39, 62.4, 200A$ GeV	p+p, d+Au, Cu+Cu, Au+Au
LHC (CERN,2009∼)	$2.76, 5.5A$ TeV	p+p, p+Pb, Pb+Pb

sions and the number of participating nuclei in the collisions are based on the collision geometry.

Participant-Spectator Picture

The participant-spectator picture is a simple geometrical picture characterizing the collision with an impact parameter, b. As shown in Fig. 2.1, the incoming nuclei

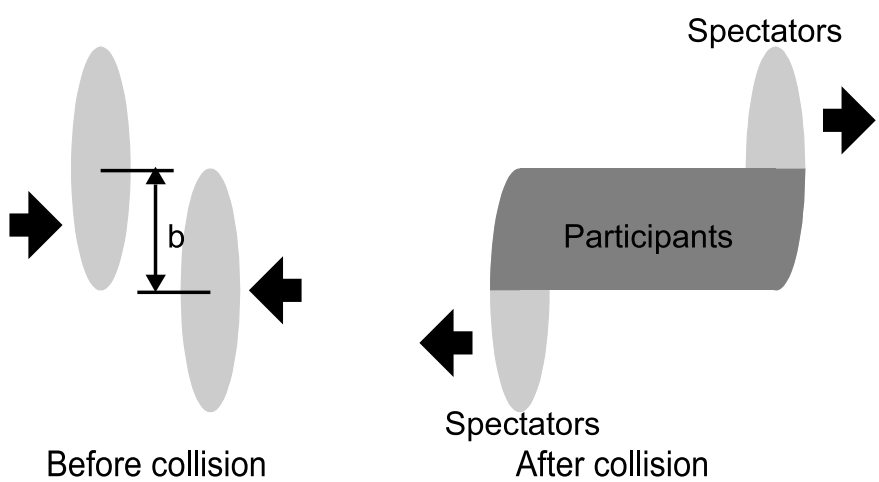

Figure 2.1: An illustration of the colliding nuclei before (left) and after (right) a collision in the participant-spectator picture.

look like a thin pancake because of the Lorentz contraction. Only the overlapping region of the nuclei, called participants, participates in the collision, while the other region of the nuclei, called spectators, are passing by while keeping its longitudinal momenta. Figure 2.2 illustrates central and peripheral collisions of nuclei with radii R. Information about the impact parameter b is obtained by measuring the sizes of the spectators and/or the participants for each collision.

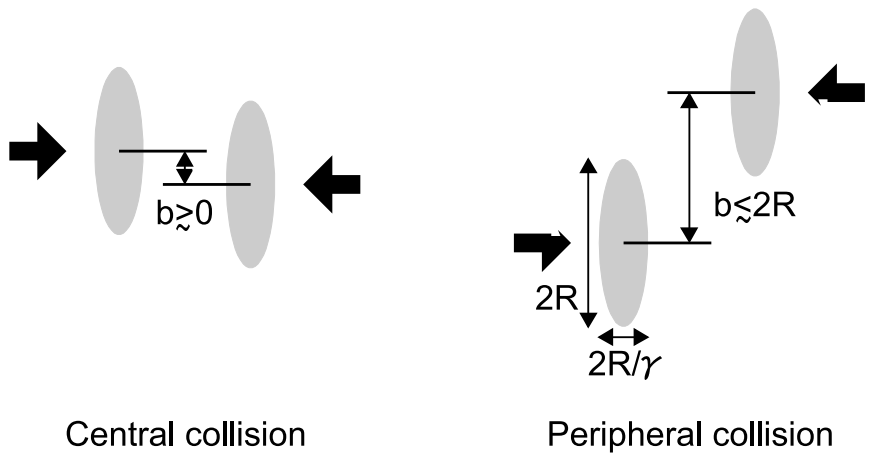

Figure 2.2: A cartoon of central (left) and peripheral (right) collisions of nuclei with radii R.

Glauber Model

The Glauber model provides the practical frame work of the participant-spectator model, based upon the eikonal approximation of the collision processes [15, 16]. The inputs to the model are the nuclear density distribution of the colliding nuclei and the nucleon-nucleon interaction cross section σ_{NN}. This model gives the total inelastic cross section of collisions between nuclei A and B from the nucleon-nucleon inelastic cross section σ_{NN}. The number of binary nucleon-nucleon collisions (N_{coll}) and the number of the participants (N_{part}) in a collision are evaluated from their relations to the impact parameter b in the Glauber model. The model is useful to study scaling properties of the particle production in heavy ion collisions. The coherent interaction with a small momentum transfer Q^2, which is called a soft process, is scaled by N_{part}. On the other hand, N_{coll} scaling is applicable for the interaction with a large Q^2. Such interactions can be considered as the incoherent sum of binary nucleon-nucleon collisions and are called hard processes.

The nucleons in each colliding nucleus are assumed to be distributed according to the Wood-Saxon distribution,

$$\rho(r) = \frac{\rho_0}{1 + \exp\left(\frac{r-R}{d}\right)} \tag{2.1}$$

where ρ_0 stands for the normal nuclear density, R is the radius and d is the diffuseness parameter.

The probability of an occurrence of a nucleon-nucleon collision between the nuclei A and B along the z-axis at an impact parameter $\mathbf{b}$ is expressed in the integral

formula,

$$T_{AB}(\mathbf{b})\,\sigma_{NN} = \int d\mathbf{b}_A dz_A \rho_A(\mathbf{b}_A, z_A)\, d\mathbf{b}_B dz_B \rho_B(\mathbf{b}_B, z_B)\, t(\mathbf{b} - \mathbf{b}_A - \mathbf{b}_B)\,\sigma_{NN}, \tag{2.2}$$

where $t(\mathbf{b})$ is the probability for having a nucleon-nucleon collision within a transverse element $d\mathbf{b}$ when A and B collide with an impact parameter $\mathbf{b}$. The number of nucleon-nucleon collisions in each $A+B$ collision can be up to $A \times B$. The probability of having n nucleon-nucleon collisions can be written using a binomial relation,

$$p(n, \mathbf{b}) =_{AB} C_n \left[T_{AB}(\mathbf{b})\,\sigma_{NN}\right]^n \left[1 - T_{AB}(\mathbf{b})\,\sigma_{NN}\right]^{AB-n}. \tag{2.3}$$

The total probability of having at least one nucleon-nucleon collision in the collision of nuclei A and B at an impact parameter $\mathbf{b}$ is;

$$\frac{d\sigma_{AB}}{d\mathbf{b}} = \sum_{n=1}^{AB} p(n, \mathbf{b}) = 1 - p(0, \mathbf{b}) = 1 - \left[1 - T_{AB}(\mathbf{b})\,\sigma_{NN}\right]^{AB}. \tag{2.4}$$

Therefore, the total inelastic cross section σ_{AB} is described as follows:

$$\sigma_{AB} = \int d\mathbf{b} \left(1 - \left[1 - T_{AB}(\mathbf{b})\,\sigma_{NN}\right]^{AB}\right). \tag{2.5}$$

The average number of inelastic nucleon-nucleon collisions N_{coll} at the impact parameter $\mathbf{b}$ is expressed as:

$$N_{coll}(\mathbf{b}) = \langle n(\mathbf{b}) \rangle = \sum_{n=1}^{AB} np(n, \mathbf{b}) = ABT_{AB}(\mathbf{b})\,\sigma_{NN}. \tag{2.6}$$

2.1.2 Space-Time Evolution of Matter

The matter created by high-energy heavy-ion collisions evolves through various phases based on the space-time evolution scenario proposed by J.D. Bjorken [17]. Figure 2.3 shows a space-time picture of evolution of the matter created in a heavy ion collision at RHIC with the longitudinal coordinate z and the time coordinate t. It is assumed that the space-time evolution depends on only the proper time $\tau = \sqrt{t^2 - z^2}$ in the high energy limit. The space-time evolution of the matter can be separated into mainly the following four different phases shown as dotted lines in Fig. 2.3:

1. Pre-equilibrium ($\tau = 0 \sim \tau_0$)
   A collision between two incoming nuclei occurs and then a huge amount of energy is released in a tiny volume. Free partons, mainly gluons, are produced, and the dynamics may be described by a cascade of colliding partons. The subsequent multiple parton scattering leads the matter to local equilibrium.

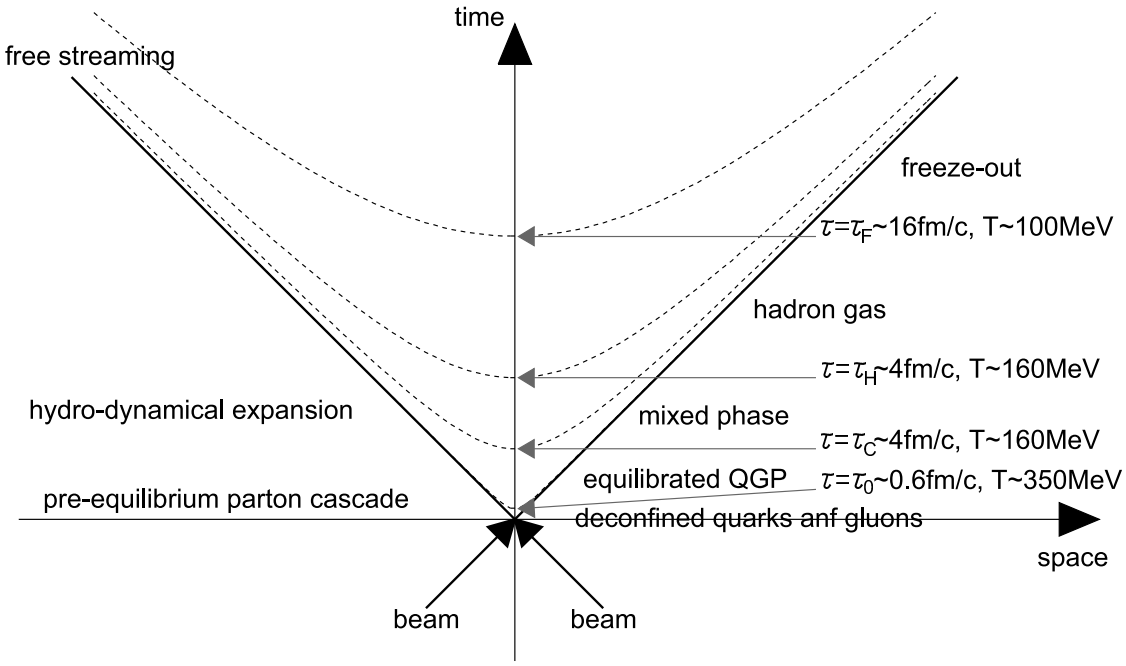

Figure 2.3: A space-time picture of evolution of the matter created in a heavy ion collision at RHIC. The proper times τ and temperatures T for different phases are expected from a hydrodynamical model [18]. The mixed phase would exist only if the transition is first order.

2. Deconfined partonic phase (QGP) in thermal equilibrium ($\tau = \tau_0 \sim \tau_C$)
   If the deposited energy is large compared to the transition energy density, the QGP phase can be formed at $\tau = \tau_0$. The QGP is likely to evolve like a fluid, expand and cool down according to hydrodynamics.

3. Mixed phase between QGP and hadrons ($\tau = \tau_C \sim \tau_H$)
   The mixed phase between QGP and hadrons would exist only if the transition is first order. When the system reaches the transition temperature T_C from the QGP to a phase of ordinary hadronic matter, hadronization starts, and the mixed phase consisting of the quarks, gluons and hadrons is made.

4. Hadron gas ($\tau = \tau_H \sim \tau_F$)
   The system finishes hadronization and produced hadrons keep interacting with each other until the temperature drops down to the kinematic freeze-out temperature T_F. After $\tau = \tau_F$ hadrons cease to interact and move away.

We never know in which phase each particle detected experimentally is generated. Thus, it is crucial to extensively understand the space-time evolution of the matter created in high-energy heavy-ion collisions via various measurements which can focus on a particular phase.

2.1.3 Initial Energy Density

The achieved energy density in a collision system at the formation time, τ_0, can be estimated from experimental observables, a particle multiplicity and a transverse energy according to the Bjorken's scenario [17]. Once a high energy heavy ion collision occurs, many inelastic nucleon-nucleon collisions occur in a very short time when the two colliding pancake-like nuclei pass through each other. Then a large amount of energy is deposited in a small volume. The particle density for an overlap region in a longitudinal thickness Δz and a transverse area S at $z = 0$ and $t = \tau_0$ can be expressed as:

$$\frac{\Delta N}{S\Delta z} = \frac{1}{S}\frac{dN}{dy}\frac{dy}{dz}\bigg|_{y=0}, \tag{2.7}$$

$$= \frac{1}{S}\frac{dN}{dy}\frac{1}{\tau_0 \cosh y}\bigg|_{y=0}, \tag{2.8}$$

where N is the number of particles and y is a rapidity of a particle. It should be noted that thermalization is achieved at $t = \tau_0$. The energy of a particle with a rapidity y is $m_T \cosh y$ where $m_T = \sqrt{m^2 + p_T^2}$ is a transverse mass of a particle. Thus, the

energy density, ϵ_0, is written as:

$$\epsilon_0 = (m_T \cosh y) \frac{\Delta N}{S \Delta z}, \tag{2.9}$$

$$= \frac{m_T}{S\tau_0} \left. \frac{dN}{dy} \right|_{y=0}, \tag{2.10}$$

$$= \frac{1}{S\tau_0} \left. \frac{dE_T}{dy} \right|_{y=0}, \tag{2.11}$$

where E_T is a transverse energy in a collision.

Assuming $\tau_0 = 1$ fm/c in central Au+Au collisions at RHIC ($\sqrt{s_{NN}} = 200$ GeV), the estimated energy density reaches to ~ 5.4 GeV/fm^3, which exceeds the transition energy density of $\epsilon_c \sim 1$ GeV/fm^3 for the phase transition.

2.2 Previous Experimental Results

To date, a number of experiments, which aim to reveal the existence of QGP and to investigate its properties, have been carried out. In the following, the experiments which have aimed to measure direct photons produced in ultra-relativistic nucleus-nucleus collisions are introduced briefly in order to illustrate the status of the quest for evidence of thermal photons from QGP.

2.2.1 WA80

The first attempt to measure thermal photons from the QGP was made by the WA80 experiment at the CERN SPS. WA80 is a fixed target experiment using 200A GeV ^{16}O and ^{32}S beams and has provided an interesting result on direct photon production in S+Au collisions. Figure 2.4 shows the upper limits of the direct photon production for most central collisions in 200A GeV ^{32}S+Au reactions [19]. The direct photon yield was obtained using the statistical subtraction method, *i.e.* the direct photon yield is estimated by subtracting the contributions of hadron decays (mainly π^0, η) from the inclusive photon yield. The arrows show upper limits at the 90% confidence level on the direct photon yield from the measurement. The solid and dotted curves show the direct photon yields expected from theoretical calculations with QGP formation and pure hadron gas scenarios from Ref. [20], and the dashed curve shows the one expected from another theoretical calculation with a pure hadron gas scenario [21]. Although the WA80 result just gives upper limits, it can rule out a simple thermal hadron gas description of the ^{32}S+Au collision.

2.2.2 WA98

The WA98 experiment is also a fixed target experiment at the SPS and has achieved further improvement from the WA80 result using lead glass electromagnetic calorime-

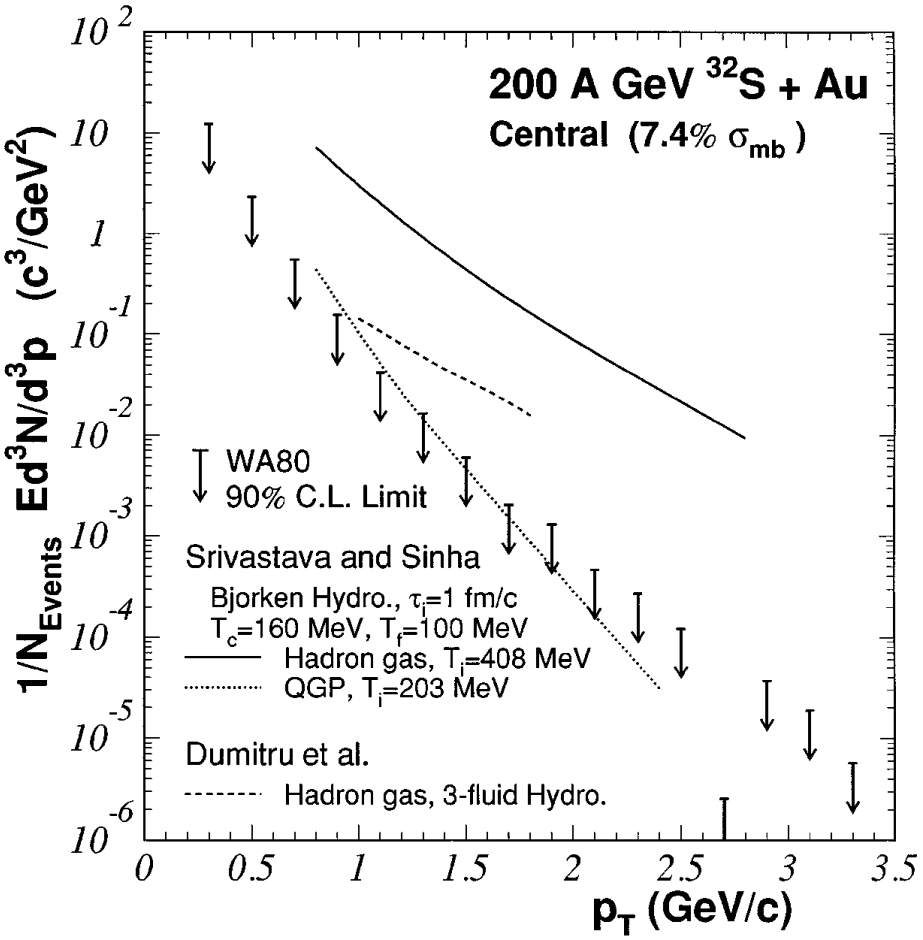

Figure 2.4: The upper limits of the direct photon production for most central collisions in 200A GeV ^{32}S+Au reactions in the WA80 experiment. The arrows show upper limits at the 90% confidence level on the direct photon yield.

ters with very good energy resolution, which are now installed in the PHENIX experiment. The WA98 collaboration has successfully measured direct photons in 158A GeV ^{208}Pb+^{208}Pb collisions by an analysis based on a statistical subtraction of hadron decay photons [22]. Figure 2.5 shows the yield ratios of inclusive photons to photons from hadron decays for peripheral and central collisions in 158A GeV Pb+Pb reactions. The p_T dependent systematic errors on the ratios are indicated by the shaded

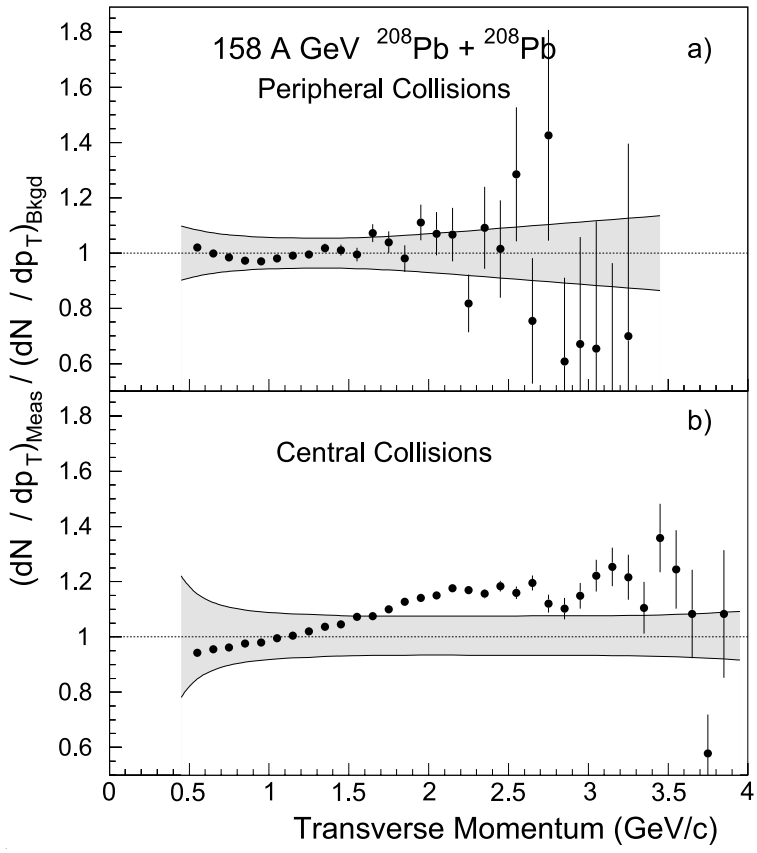

Figure 2.5: The yield ratios of inclusive photons to photons from hadron decays for peripheral (upper) and central (lower) collisions in 158A GeV Pb+Pb reactions. The p_T dependent systematic errors on the ratios are indicated by the shaded bands.

bands, and the errors on the data points are only statistical errors. While no excess exists in the peripheral collisions, excess is observed in $p_T > 1.5$ GeV/c in the central collisions.

Figure 2.6 shows the direct photon invariant yield in the central collisions of 158A GeV Pb+Pb reactions [23]. The error bars indicate the combined statistical and systematic errors, and downward arrows indicate upper limits at the 90% confidence level. The predictions [10] compared to the data is based on the fireball model with a formation time of $\tau_0 = 1$ fm/c and an initial temperature of $T_{init} \simeq 210$ MeV. The two lowest p_T data points are obtained via photon HBT (Hanbury Brown and Twiss

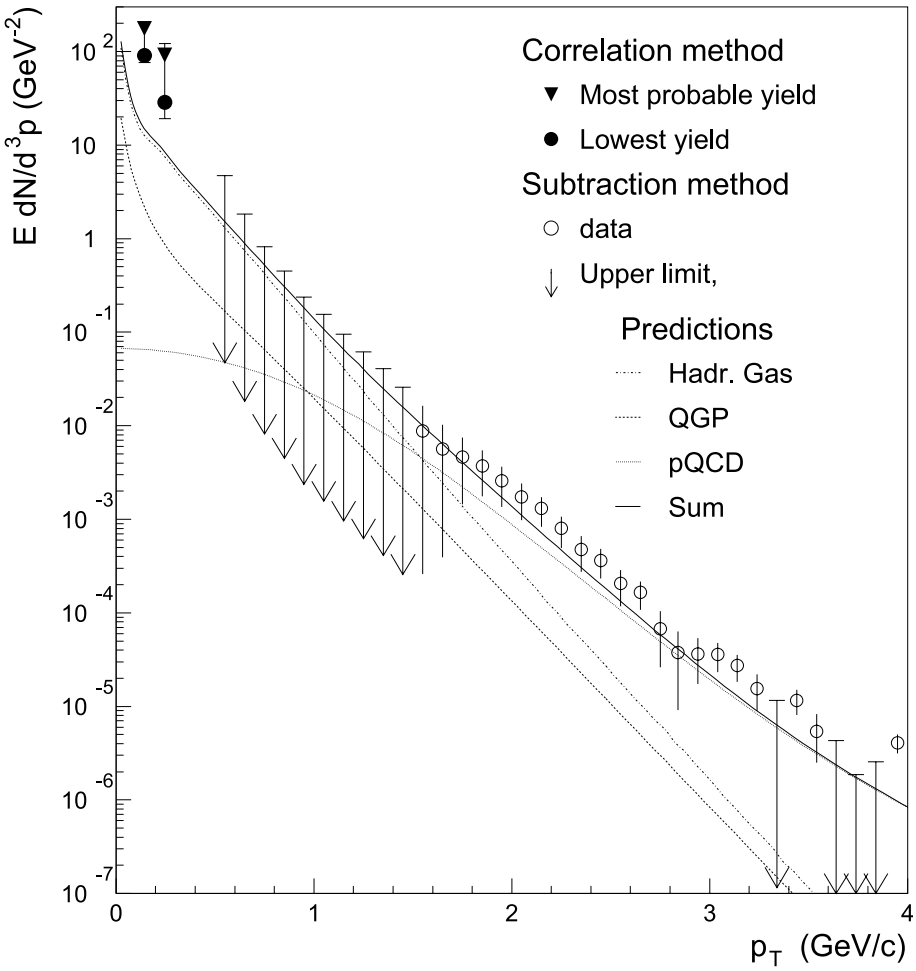

Figure 2.6: The direct photon invariant yield in the central collisions of $158A$ GeV Pb+Pb reactions. The error bars indicate the combined statistical and systematic errors, and downward arrows indicate upper limits at the 90% confidence level.

Effect [24, 25]) interferometry and they are not accounted for by the theoretical calculations which only assume the hadron gas.

2.2.3 PHENIX

The attempts for measuring the thermal photons from QGP in the WA80 and WA98 experiments have provided strong motivation to the direct photon measurements at RHIC. The PHENIX experiment, which has a good capability of measuring leptons and photons, has measured direct photons in p+p and Au+Au collisions at $\sqrt{s_{NN}} =$ 200 GeV with EMCals including the ones used in the WA98 experiment. Figure 2.7 shows the direct photon invariant cross section in p+p collisions at $\sqrt{s} = 200$ GeV [26]. The next-to-leading-order (NLO) pQCD calculations [11, 12] are shown as lines together with the data. The three curves correspond to three different choices of the momentum scale $\mu = 0.5p_T, p_T, 2.0p_T$. There are actually three different scales involved: the renormalization scale μ_{reno}, the factorization scale μ_{fac}, and the fragmentation scale μ_{frag}. All three scales are set to a common value $\mu = \mu_{reno} = \mu_{fac} = \mu_{frag}$ in the calculation. The NLO pQCD calculations are in excellent agreement with the data.

Figures 2.8 and 2.9 show the direct photon invariant yields for 8 centrality selections in Au+Au collisions at $\sqrt{s_{NN}} = 200$ GeV and the nuclear modification factor R_{AA} for direct photons with $p_T > 6$ GeV/c as a function of the number of participating nucleons N_{part} [27]. The direct photon yields in $p_T > 4.0$ GeV/c for different centrality selections are consistent with the binary-collision scaled NLO pQCD calculations which are also consistent with the p+p result shown in Fig. 2.7. The nuclear modification factor R_{AA} is defined as:

$$R_{AA} = \frac{dN_{A+A}/dy}{T_{AA} \times dN_{p+p}/dy}, \tag{2.12}$$

$$T_{AA} = \frac{\langle N_{coll} \rangle}{\sigma_{p+p}}, \tag{2.13}$$

where $\langle N_{coll} \rangle, \sigma_{p+p}$ are the number of binary collisions for A+A collisions and the cross section of inelastic p+p collisions. In Fig. 2.9, the closed and open symbols show the results for direct photons and π^0. The observation that R_{AA} for high p_T direct photons are equal to unity indicates not only that they can penetrate the medium created by Au+Au collisions but also that nuclear effects are small at producing direct photons by hard inelastic scatterings of the incoming partons. On the other hand, the observed π^0 suppression is considered to be evidence of a final state effect due to energy loss of the partons in the created matter even though the production process of high p_T π^0 is expected to be mainly hard scatterings of the incoming partons as same as the high p_T direct photons. It is noted that strong suppression of high p_T hadrons [28, 29] helps to measure direct photons for Au+Au collisions.

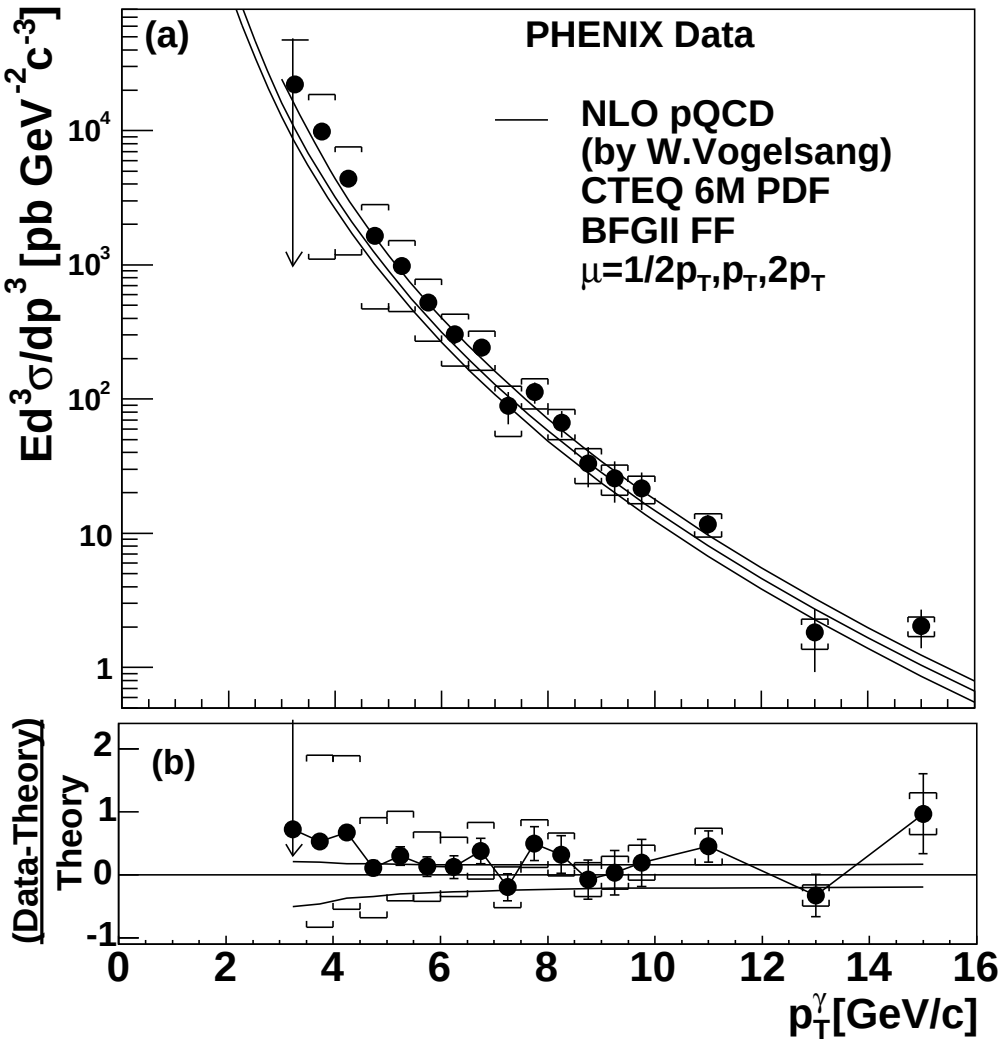

Figure 2.7: The direct photon invariant cross section as a function of p_T in 200 GeV p+p collisions at the PHENIX experiment.

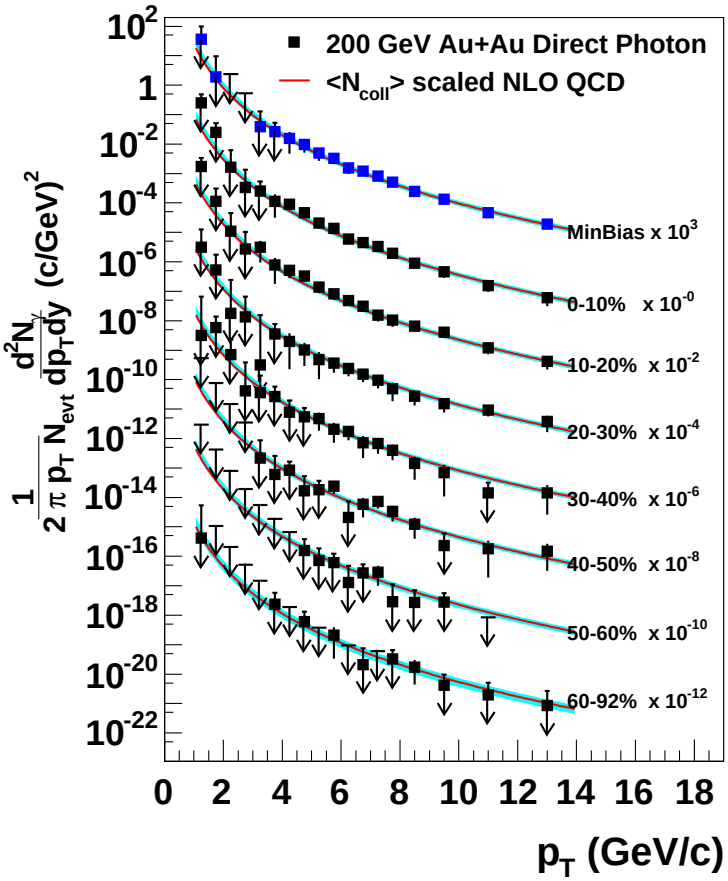

Figure 2.8: The direct photon invariant yields as a function of p_T for 8 centrality selections in 200 GeV Au+Au collisions at the PHENIX experiment.

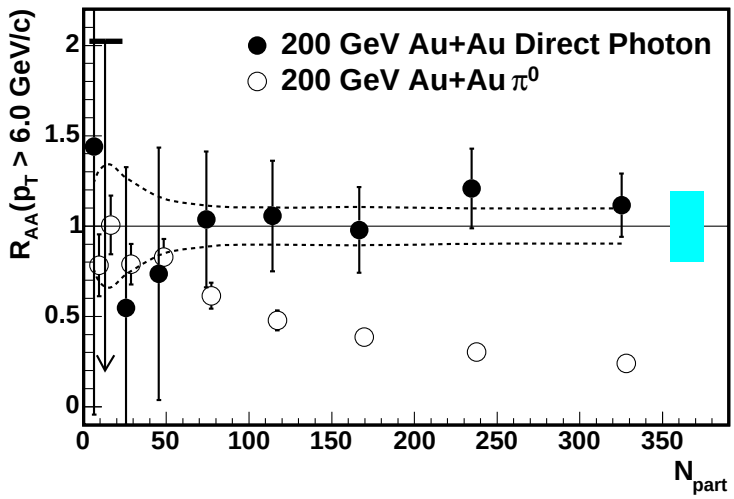

Figure 2.9: The nuclear modification factor R_{AA} for direct photons with $p_T > 6$ GeV/c as a function of the number of the participating nucleons N_{part}. The R_{AA} for π^0 with $p_T > 6$ GeV/c is also shown together.

But the direct photons in $p_T < 4.0$ GeV/c, which are expected to be mainly thermal photons from the QGP, cannot be measured with reasonably small systematic errors, since a finite energy resolution of the EMCal precludes separation of the direct photon signal from a large background from hadron decays, particularly π^0.

2.3 Virtual Photon Method

An alternative method has been developed in the PHENIX experiment to break through the difficulty on the measurement of the low p_T direct photons. An excellent capability of the PHENIX detector to precisely measure electrons makes it possible to measure e^+e^- pairs from direct virtual photon decays. This method to measure e^+e^- pairs from direct virtual photon decays is called the 'virtual photon method',

Internal Photon Conversion

In any process of producing a real photon, the processes to produce a virtual photon which converts to a low mass e^+e^- pair are associated as a higher order diagram in general. The relation between photon production and the associated e^+e^- pair production can be expressed as [30, 31]:

$$\frac{d^2n_{ee}}{dm_{ee}} = \frac{2\alpha}{3\pi}\frac{1}{m_{ee}}\sqrt{1-\frac{4m_e^2}{m_{ee}^2}}\left(1+\frac{2m_e^2}{m_{ee}^2}\right)S(m_{ee})dn_\gamma, \tag{2.14}$$

where α is the fine structure constant and m_e, m_{ee} are the masses of the electron and the e^+e^- pair, and S is a process dependent factor. The process dependent factor $S(m_{ee})$ is a key factor for the virtual photon method since its m_{ee} dependences for direct virtual photon decays and Dalitz decays of hadrons are quite different. Furthermore, it should be noted that the factor $\sqrt{1-\frac{4m_e^2}{m_{ee}^2}}\left(1+\frac{2m_e^2}{m_{ee}^2}\right)$ goes to unity if m_{ee} is large enough compared to m_e and Eq. 2.14 can be simplified as:

$$\frac{d^2n_{ee}}{dm_{ee}} = \frac{2\alpha}{3\pi}\frac{1}{m_{ee}}S(m_{ee})dn_\gamma. \tag{2.15}$$

S for Gluon Compton Scattering

Gluon Compton scattering is considered as an example of a simple photon production process. The lowest order diagrams are shown in Fig. 2.10. The exact expression for

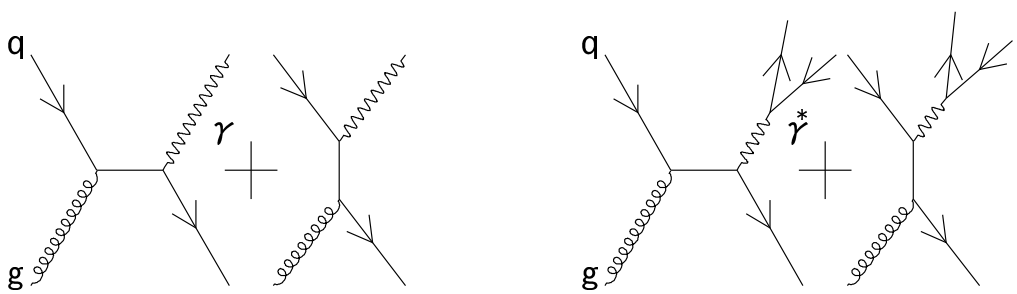

Figure 2.10: The lowest order diagrams for gluon Compton scattering with a real photon (left) and an e^+e^- pair via a virtual photon (right).

the relation between the photon and e^+e^- production processes of the gluon Compton scattering is as follows [32]:

$$\frac{d^2n_{ee}}{dm_{ee}dt} = \frac{2\alpha}{3\pi}\frac{1}{m_{ee}}\sqrt{1-\frac{4m_e^2}{m_{ee}^2}}\left(1+\frac{2m_e^2}{m_{ee}^2}\right)\left(1+\frac{2u}{t^2+s^2}m_{ee}^2\right)\frac{dn_\gamma}{dt}. \tag{2.16}$$

Here the Mandelstam variables s, t, u are defined as:

$$s = (p_q + p_g)^2, \tag{2.17}$$
$$t = (p_q - p_\gamma)^2, \tag{2.18}$$
$$u = (p_q - p_q')^2, \tag{2.19}$$

with the four-momenta of the incoming quark p_q, the incoming gluon p_g, the outgoing real or virtual photon p_γ and the outgoing quark p_q'. Comparing Eq. 2.16 with Eq. 2.14, the S factor can be identified as:

$$S(m_{ee}^2) = \left(1+\frac{2u}{t^2+s^2}m_{ee}^2\right). \tag{2.20}$$

If the scattering angle is 90° at the center of mass system, $t = u = -2p_T^2$ and $s = 4p_T^2$. Thus,

$$S(m_{ee}^2) = \left(1 + \frac{-4p_T^2}{(-2p_T^2)^2 + (4p_T^2)^2} m_{ee}^2\right) \tag{2.21}$$

$$= \left(1 - \frac{m_{ee}^2}{5p_T^2}\right). \tag{2.22}$$

The S factor for the gluon Compton scattering goes to 1 as $m_{ee} \to 0$ or $m_{ee} \ll p_T$.

S for Dalitz Decay and Form Factor

Figure 2.11 shows the diagrams for two photon decay and Dalitz decay of π^0. The

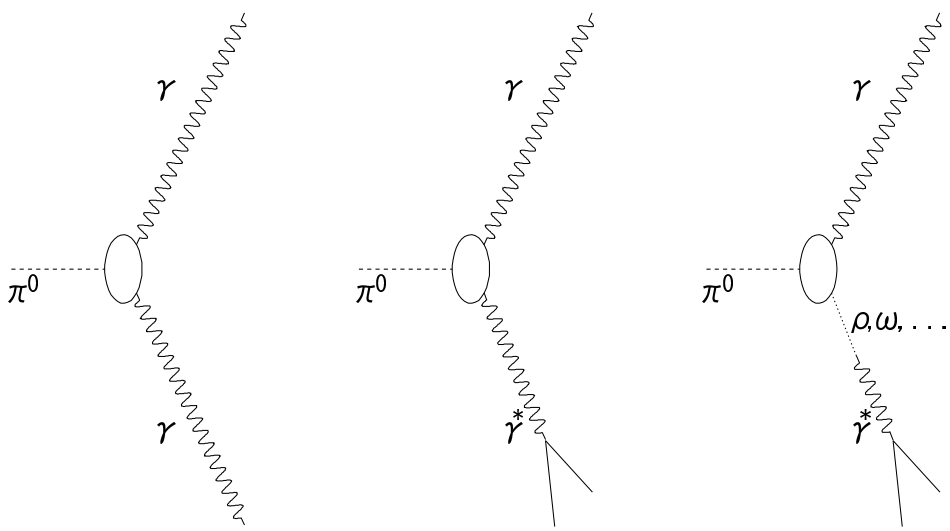

Figure 2.11: The diagrams for two photon decay (left) and Dalitz decay (middle and right) of π^0.

decay rate of the Dalitz decay of pseudo-scalar mesons such as π^0, η, η' is given as [33, 34]:

$$\frac{1}{n_\gamma}\frac{dn_{ee}}{dm_{ee}} = \frac{2\alpha}{3\pi}\frac{1}{m_{ee}}\sqrt{1 - \frac{4m_e^2}{m_{ee}^2}}\left(1 + \frac{2m_e^2}{m_{ee}^2}\right)\left|F(m_{ee}^2)\right|^2\left(1 - \frac{m_{ee}^2}{m_h^2}\right)^3, \tag{2.23}$$

where $F(Q^2 = m_{ee}^2)$ is the electromagnetic form factor and m_h is the mass of the hadron. A similar formula is also known for the Dalitz decays of the vector mesons

e.g. $\omega \to \pi^0 e^+ e^-$. From comparison with Eq. 2.14, the S factor for the Dalitz decay of pseudo-scalar mesons is

$$S(m_{ee}^2) = \left|F(m_{ee}^2)\right|^2 \left(1 - \frac{m_{ee}^2}{m_h^2}\right)^3 . \tag{2.24}$$

It is clearly found that the Dalitz decay rate is suppressed by a factor $\left(1 - \frac{m_{ee}^2}{m_h^2}\right)^3$ due to the finite mass of the parent meson m_h. If the meson is a point-like particle, the form factor $F(Q^2)$ is 1 and this situation corresponds to the diagram shown in the middle of Fig. 2.11. But in the real case, the meson is not a point-like particle and the form factor is required to describe the meson's structure. In the vector dominance model (VDM), the meson is coupled to a virtual photon via a vector meson as illustrated in the right of Fig. 2.11. Among the vector mesons, the contribution from ρ mesons dominates [34]. Thus, the form factor is given by $F(Q^2) = 1/(1 - Q^2/m_\rho^2)$. Here m_ρ is mass of ρ (0.775 GeV/c^2) and normalization of the form factor is determined by the fact that the form factor should be exactly 1 at $Q^2 = 0$.

The form factor of mesons has been studied experimentally, and it is customary to parametrize the form factor by the dipole form with a pole mass Λ, $F(Q^2) = 1/(1 - Q^2/\Lambda^2)$. The Lepton-G collaboration has measured the form factor of η using $\eta \to \gamma\mu^+\mu^-$ decays in $\pi^- p \to \eta n$ reactions and has obtained the pole mass $\Lambda = 0.725$ GeV/c^2 from the measured form factor [35], which is consistent with the VDM expectation. Subsequently, the CELLO collaboration has carried out more precise measurements of the form factors of π^0, η and η' [36] and the measured pole masses are $\Lambda_{\pi^0} = 0.748 \pm 0.30, \Lambda_\eta = 0.839 \pm 0.63$ and $\Lambda_{\eta'} = 0.794 \pm 0.44$, respectively. They are also consistent with the VMD expectation, and the validity of the VMD is successfully demonstrated.

Advantage of Virtual Photon Method

While the measurement of real direct photons suffers from a large background of hadron decays, utilizing the difference in the e^+e^- mass dependence of the S factor for direct virtual photons and Dalitz decays of hadrons allows one to measure direct photons even in the low p_T region. By selecting a mass region above the π^0 mass ($m_{ee} > 135$ MeV/c^2) for determination of the direct virtual photon contribution in the e^+e^- mass spectrum, the signal to background ratio (S/B) for direct photons is dramatically improved. Actually, more than 80% of all hadron decay e^+e^- pairs come from π^0 Dalitz decays. If the direct photon contribution is about 10% in the inclusive e^+e^- yield, the ratio of the direct photon signal to the hadron decay contribution increases by a factor of 5 for $m_{ee} > m_{\pi^0}$ compared to $m_{ee} \geq 0$.

2.3.1 p+p and Au+Au Results

The PHENIX experiment has successfully measured low p_T direct photons in p+p and Au+Au collisions at $\sqrt{s_{NN}} = 200$ GeV using the virtual photon method [14, 31]. Figure 2.12 shows the direct virtual photon fractions in p+p and Au+Au collisions obtained by the virtual photon method. The left and right panels of Fig. 2.12 are

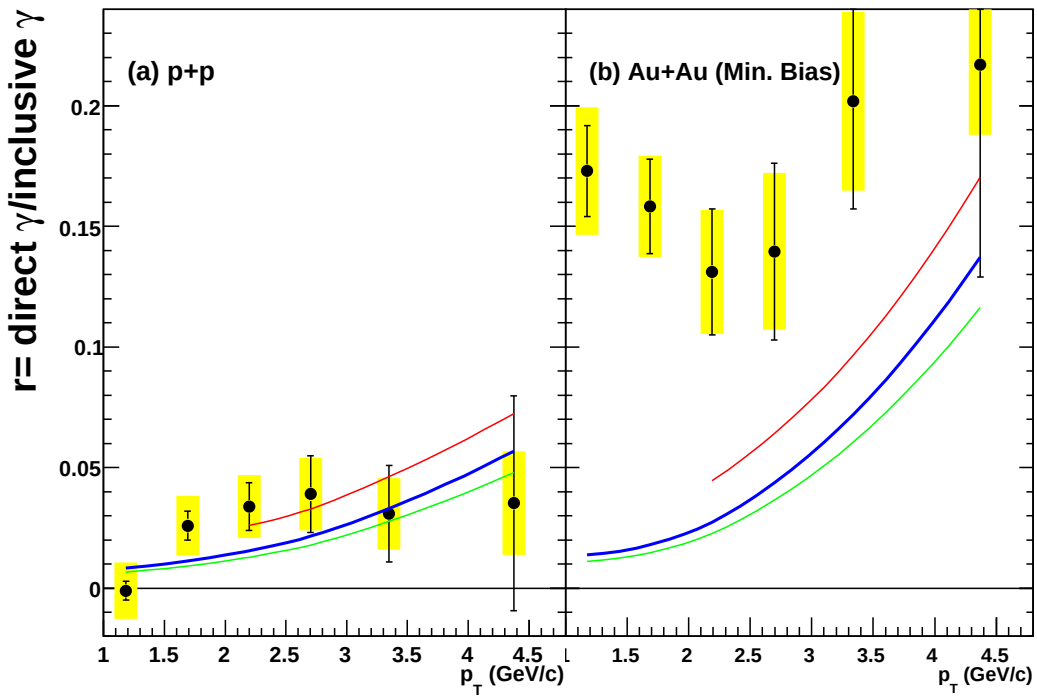

Figure 2.12: The direct virtual photon fractions in p+p (left) and Au+Au (right) collisions obtained by the virtual photon method. The yellow bands indicate systematic errors. The colored curves indicate direct photon fractions expected form the NLO pQCD calculation with different theoretical scales: $\mu = 0.5p_T$(red), p_T(blue), $2p_T$(green) [11].

p+p and Au+Au results, respectively. The yellow bands indicate systematic errors on the direct virtual photon fractions. The colored curves indicate direct photon fractions expected from the NLO pQCD calculation with different theoretical scales: $\mu = 0.5p_T$(red), p_T(blue), $2p_T$(green) [11]. For p+p collisions, the curves show the ratio calculated as

$$r_{\gamma^*}(p_T) = \frac{d\sigma_\gamma^{NLO}(p_T)}{dp_T} \Big/ \frac{d\sigma_\gamma^{incl}(p_T)}{dp_T}, \tag{2.25}$$

where $\sigma_\gamma^{NLO,incl}(p_T)$ represent the direct photon cross section from the NLO pQCD calculation and the measured inclusive photon cross section. The curves for Au+Au

are also calculated as

$$r_{\gamma^*}(p_T) = T_{AA} \cdot \frac{d\sigma_\gamma^{NLO}(p_T)}{dp_T} \Big/ \frac{dN_\gamma^{incl}(p_T)}{dp_T}, \tag{2.26}$$

where N_γ^{incl} is the measured inclusive photon yield for Au+Au collisions. $\sigma_\gamma^{incl}(p_T)$, N_γ^{incl} are measured in the same way as explained later in Section 5.12. While the direct photon fraction is consistent with the expectation from the NLO pQCD calculation in p+p collisions, the data points for $p_T < 3.5$ GeV/c are larger than the expectation in Au+Au collisions.

The obtained direct photon fraction is converted to the direct photon yield using the relation

$$\frac{dN_{dir}(p_T)}{dp_T} = r_{\gamma^*}(p_T) \times \frac{dN_{incl}(p_T)}{dp_T}. \tag{2.27}$$

Figure 2.13 shows the direct photon invariant yield in p+p and Au+Au collisions with the virtual photon method (closed symbols) together with the measured results using the EMCals (open symbols) and the NLO pQCD calculations. Both results with different analysis methods are consistent in $p_T > 4$ GeV/c. The NLO pQCD calculation for p+p collisions is consistent with the data within the theoretical uncertainties for $p_T > 2$ GeV/c. The p+p data can be described better by a modified power-law function, $A_{pp}(1 + p_T^2/b)^{-n}$ (shown as a dotted line), than the NLO pQCD calculations.

An enhanced yield over the N_{coll}-scaled curve fitted to the yield for p+p collisions is clearly seen in Au+Au for $p_T < 2.5$ GeV/c. The Au+Au data are fitted with an exponential plus the N_{coll}-scaled p+p fit function ($Ae^{-p_T/T} + T_{AA} \times A_{pp}(1 + p_T^2/b)^{-n}$), where only A and the inverse slope T in the exponential term are free parameters. The results of the fits are summarized in Table 2.2, where A is converted to dN/dy for $p_T > 1$ GeV/c. The resulted inverse slope for central collisions is $T = 221 \pm 19^{stat} \pm 19^{syst}$ MeV.

Table 2.2: Summary of the fits. The first and second errors are statistical and systematic, respectively.

Centrality	dN/dy ($p_T > 1$ GeV/c)	T [MeV]
0-20%	$1.50 \pm 0.23 \pm 0.35$	$221 \pm 19 \pm 19$
20-40%	$0.65 \pm 0.08 \pm 0.15$	$217 \pm 18 \pm 16$
Min. Bias	$0.49 \pm 0.05 \pm 0.11$	$233 \pm 14 \pm 19$

Several hydrodynamical models can reproduce the central Au+Au data within a factor of 2 as shown in Fig. 2.14 [31]. The initial temperature T_{init} and the thermalization time τ_0 in these hydrodynamical models are shown in Fig. 2.15. The initial temperatures in all models are higher than the transition temperature needed for realization of QGP, if the enhanced direct photon yield in Au+Au are of thermal origin.

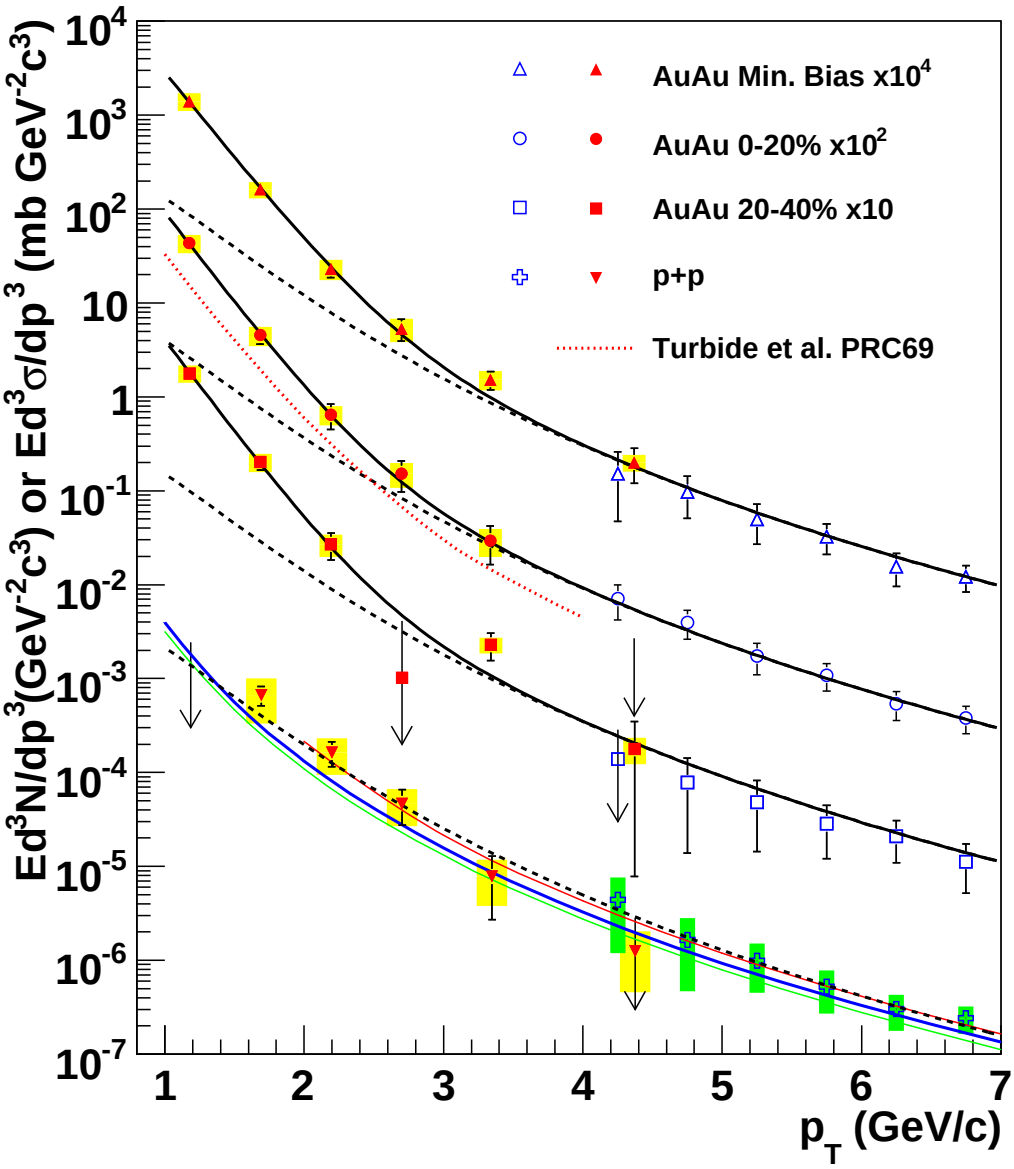

Figure 2.13: The direct photon invariant yield in p+p and Au+Au collisions with the virtual photon method together with the measured results by the EMCals and the NLO pQCD calculations. The fit result to the p+p data points is shown as a dotted line and the binary-scaled p+p fit results are also shown with Au+Au results.

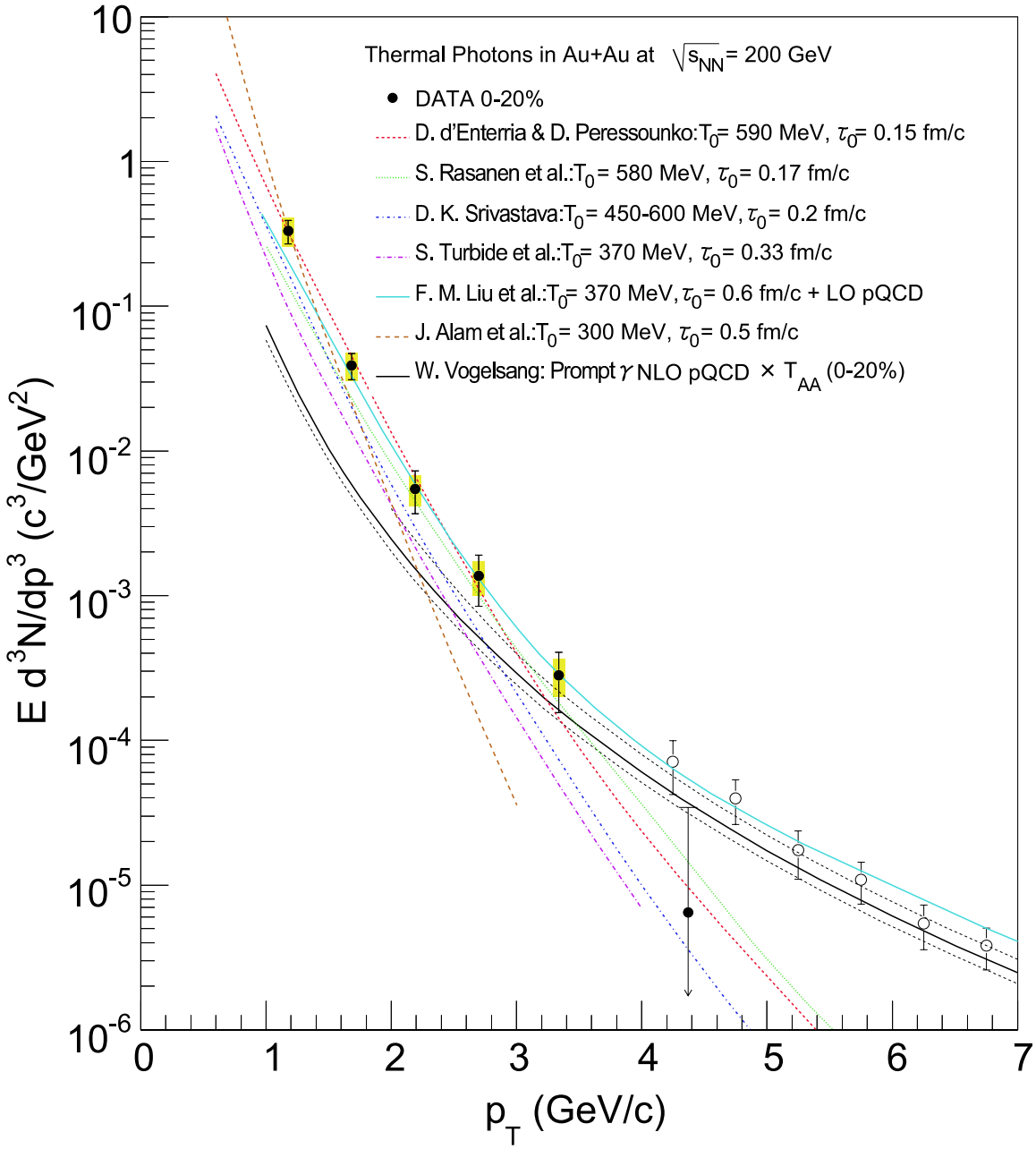

Figure 2.14: The comparison of several hydrodynamical models with the data for central Au+Au collisions [10, 37, 38, 39, 40, 41].

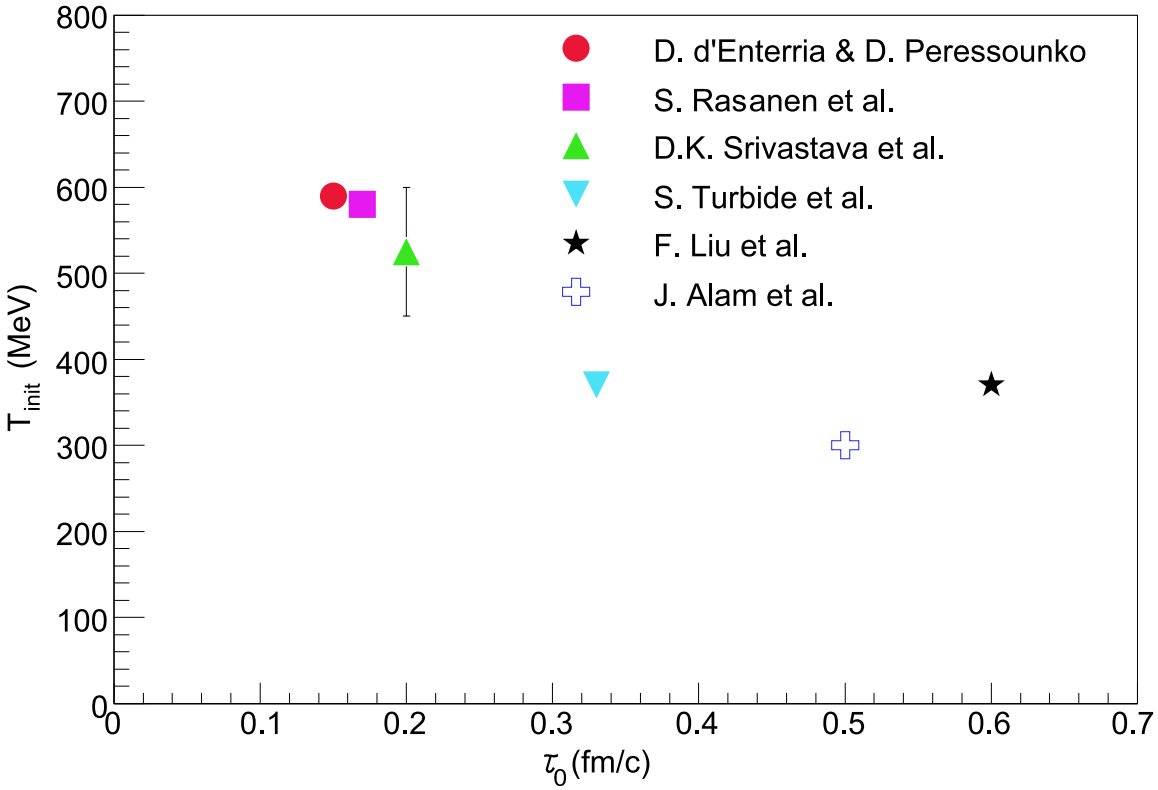

Figure 2.15: The initial temperature T_{init} and the thermalization time τ_0 in the hydrodynamical models which can reproduce the central Au+Au data. The initial temperatures in all models are higher than the transition temperature predicted by a lattice QCD calculation.

2.4 Nuclear Effects

Initial state effects in A+A reactions need to be carefully investigated in order to extract the contribution of the QGP medium effects from the observed excess yield of direct photons in Au+Au collisions. The following effects could increase or decrease the direct photon yield, especially in the low p_T region [42, 43]:

- Isospin effect
- Nuclear shadowing
- Cronin effect

These effects are explained presently in subsequent subsections. The p+A reactions are a useful tool to study the above effects since a hot and dense nuclear medium is not likely to be formed in p+A collisions, while the cold nuclear effects listed above can be investigated.

Isospin Effect

The direct photon production cross sections for p+p, p+n and n+n collisions are different because the cross sections depend on the electrical charges of the quarks. The different quark compositions of a proton and a neutron have an influence on the direct photon production in A+A reactions.

Nuclear Shadowing

The European Muon Collaboration (EMC) measured the nucleon structure functions of ^{56}Fe and the deuteron using μ+Fe ($\mu + d$) deep inelastic scatterings and discovered that the parton distribution function in a nucleon of a nucleus significantly differs from one in a free nucleon [44]. Figure 2.16 shows the ratio of structure functions in heavy nuclei and the deuteron together with calculations from the NLO nuclear parton distribution function (NPDF) parameterization [45]. Shadowing ($F_2^A/F_2^D < 1$ in $x < 0.07$) and anti-shadowing ($F_2^A/F_2^D > 1$ in $0.07 < x < 0.3$) and the EMC effect ($F_2^A/F_2^D < 1$ in $x > 0.3$) are clearly seen.

Attempts to reproduce the observed ratios of structure functions F_2^A/F_2^D have been made by various parameterizations of NPDF. Figure 2.17 shows the expected ratios of parton distribution functions for valence quarks (left panel), sea quarks (middle panel) and gluons (right panel) in a Ca nucleus to those in a proton with different NPDF parameterizations, which can reproduce the observed F_2^A/F_2^D. The solid, dashed and dotted lines indicate the expectations by NDS [45], EKS [46] and HKM [47] parameterizations. While PDFs for valence quarks in these parameterizations look consistent, PDFs for sea quarks and gluons have quite different shapes in different parameterizations. Thus the effect on the direct photon production due to

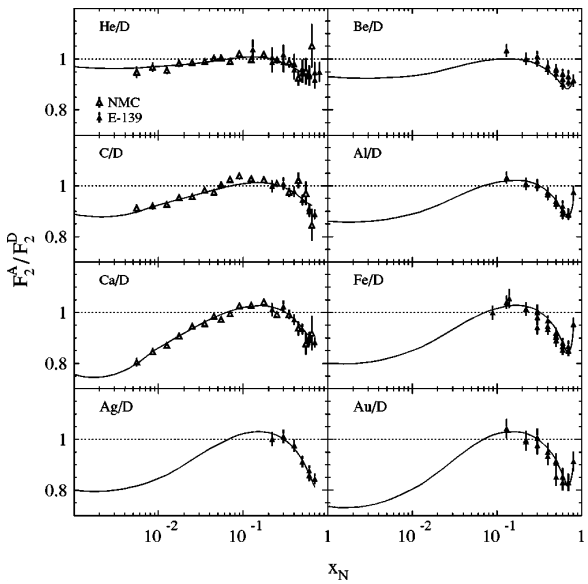

Figure 2.16: The ratio of structure functions in heavy nuclei and the deuteron, F_2^A/F_2^D together with calculations the NLO NPDF parameterization shown as lines.

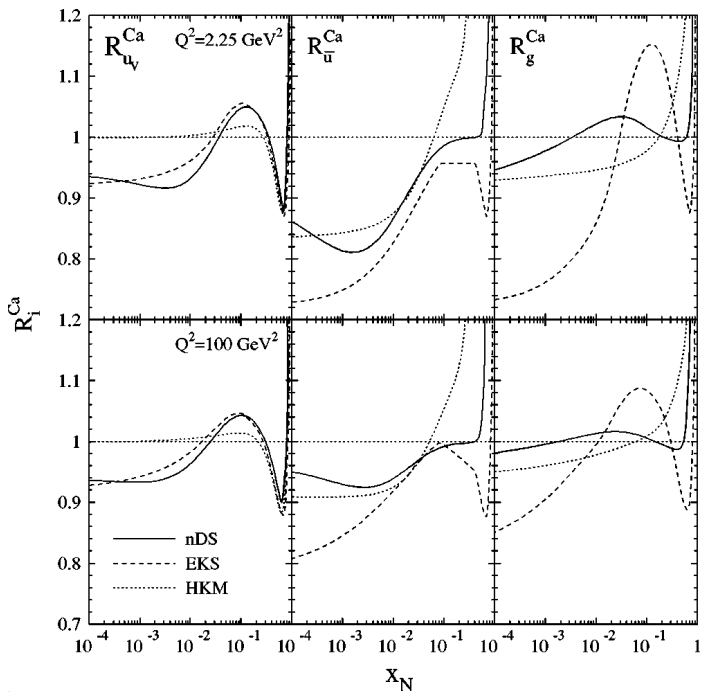

Figure 2.17: The expected ratios of parton distribution functions for valence quarks (left), sea quarks (middle) and gluons (right) in a nuclei of Ca to those in a proton with different NPDF parameterizations, which can reproduce the observed F_2^A/F_2^D.

PDFs for sea quarks and gluons in a heavy nucleus is not calculable, and it should be determined experimentally.

Cronin Effect

It was observed in 1974 that the production cross sections for hadrons in p+A collisions do not obey the binary collision scaling of those in p+p collisions [48], and the A dependence of cross section for particle i in p+A collisions is parameterized as:

$$E\frac{d^3\sigma_i^{p+A}}{dp^3}(p_T) = E\frac{d^3\sigma_i^{p+p}}{dp^3}(p_T) \cdot A^{\alpha(p_T)}. \tag{2.28}$$

Here $\sigma_i^{p+A,p+p}$ are the cross sections for particle i in p+p and p+A collisions. α is greater than 1 above some p_T value, typically 1–1.5 GeV/c, denoting significant enhancement of particle production in p+A collisions. This effect is named the 'Cronin' effect in honor of the person of this finding, J.W. Cronin. The Cronin effect is interpreted as a result that averaged transverse momentum, k_T, of incoming partons increases due to multiple soft scatterings with momentum transfer when propagating through the target nucleus [49].

2.4.1 Measured Nuclear Effects for Hadrons

The nuclear effects on the productions of some hadrons have been studied at the PHENIX experiment comparing their yields in d+Au collisions with those in p+p collisions. The nuclear modification factor for d+Au collisions R_{dA} is introduced to be able to compare the nuclear effects on the different hadron productions and it is calculated as:

$$R_{dA} = \frac{dN_{d+A}/dy}{T_{dA} \times dN_{p+p}/dy}, \tag{2.29}$$

$$T_{dA} = \frac{\langle N_{coll} \rangle}{\sigma_{p+p}}. \tag{2.30}$$

Figure 2.18 shows the R_{dA} for pions, kaons and protons as a function of p_T for minimum bias d+Au collisions measured by the PHENIX detector [50]. The boxes on the proton data points represent the $\sim 10\%$ systematic errors, where the systematic errors on the pion and kaon data are similar to the one in the proton data but not shown in the picture for clarity. The box around $R_{dA} = 1.0$ also indicates the p_T-uncorrelated systematic error including the uncertainties on the p+p absolute cross section and on the calculation of N_{coll}. There is a very small or no enhancement for both pions and kaons in $p_T > 1.0$ GeV/c, however the proton R_{dA} shows a considerably large enhancement. In $p_T \leq 1.0$ GeV/c, the R_{dA} falls below 1.0 regardless of the particle species. It is considered that this depletion results from soft particle

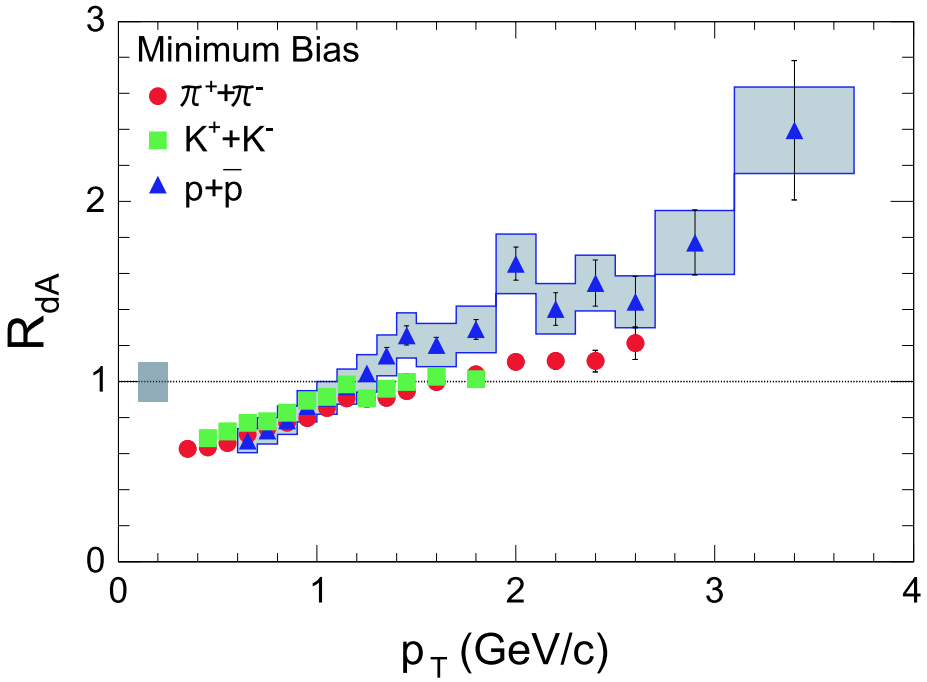

Figure 2.18: The nuclear modification factor R_{dA} for pions, kaons and protons as a function of p_T for minimum bias d+Au collisions measured by the PHENIX detector [50]. The boxes on the proton data points represent the $\sim 10\%$ systematic errors, where the systematic errors on the pion and kaon data are similar to the one in the proton data but not shown in the picture for clarity. The box around $R_{dA} = 1.0$ also indicates the p_T-uncorrelated systematic error including the uncertainties on the p+p absolute cross section and on the calculation of N_{coll}.

productions, which is scaled by the number of participating nucleons and not by the number of binary collisions.

Figure 2.19 also shows the R_{dA} for pions, kaons and protons in four different centrality selections [50]. The boxes around $R_{dA} = 1.0$ and on the proton data points

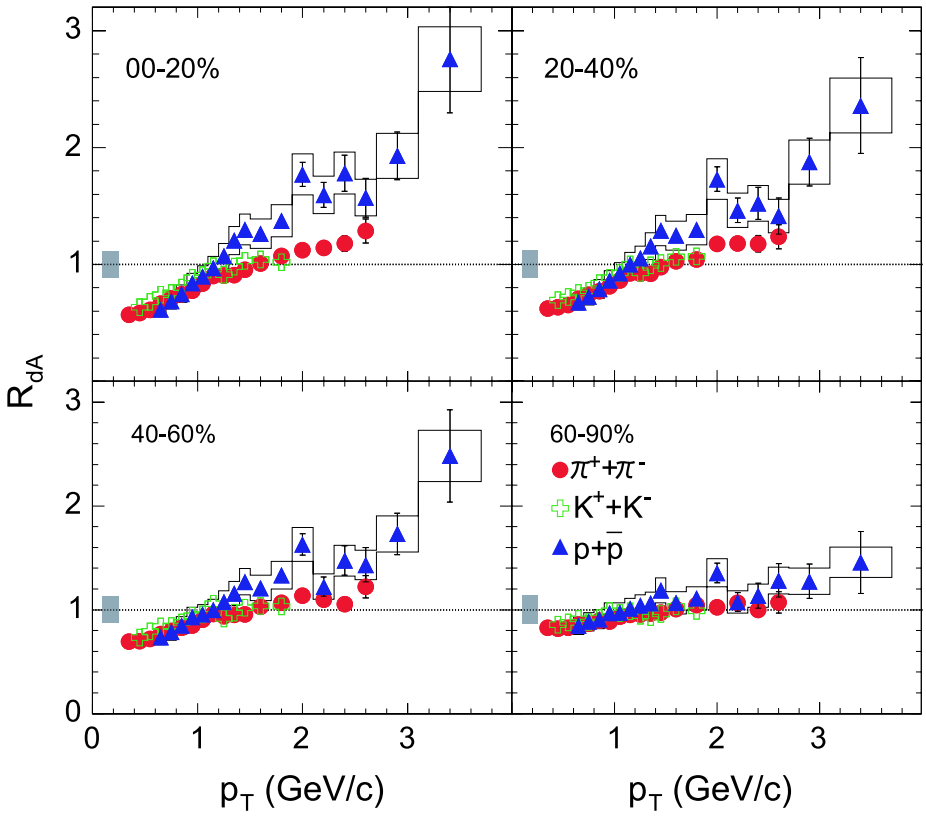

Figure 2.19: The R_{dA} for pions, kaons and protons in four different centrality selections [50]. The boxes around $R_{dA} = 1.0$ and on the proton data points have the same meanings as shown in Fig. 2.18, and the systematic errors on the pion and kaon data is also similar to the proton one but not shown for clarity.

have the same meanings as shown in Fig. 2.18, and the systematic errors on the pion and kaon data is also similar to the proton one but not shown for clarity. The results in central d+Au collisions show increasing enhancement for both pions and protons in the high p_T region while peripheral collisions do not show any modification on the hadron productions.

The R_{dA} for π^0 and η also has been measured. Figure 2.20 shows the R_{dA} for π^0 and η in different centrality selections and minimum bias data [51]. The boxes on the data points represent the p_T-correlated systematic errors and the shaded bands around $R_{dA} = 1.0$ indicate the p_T-uncorrelated systematic error including the uncertainties on the p+p absolute cross section and on the calculation of N_{coll}. The bands located at the left side of the data points indicate the normalization uncertainty due to the

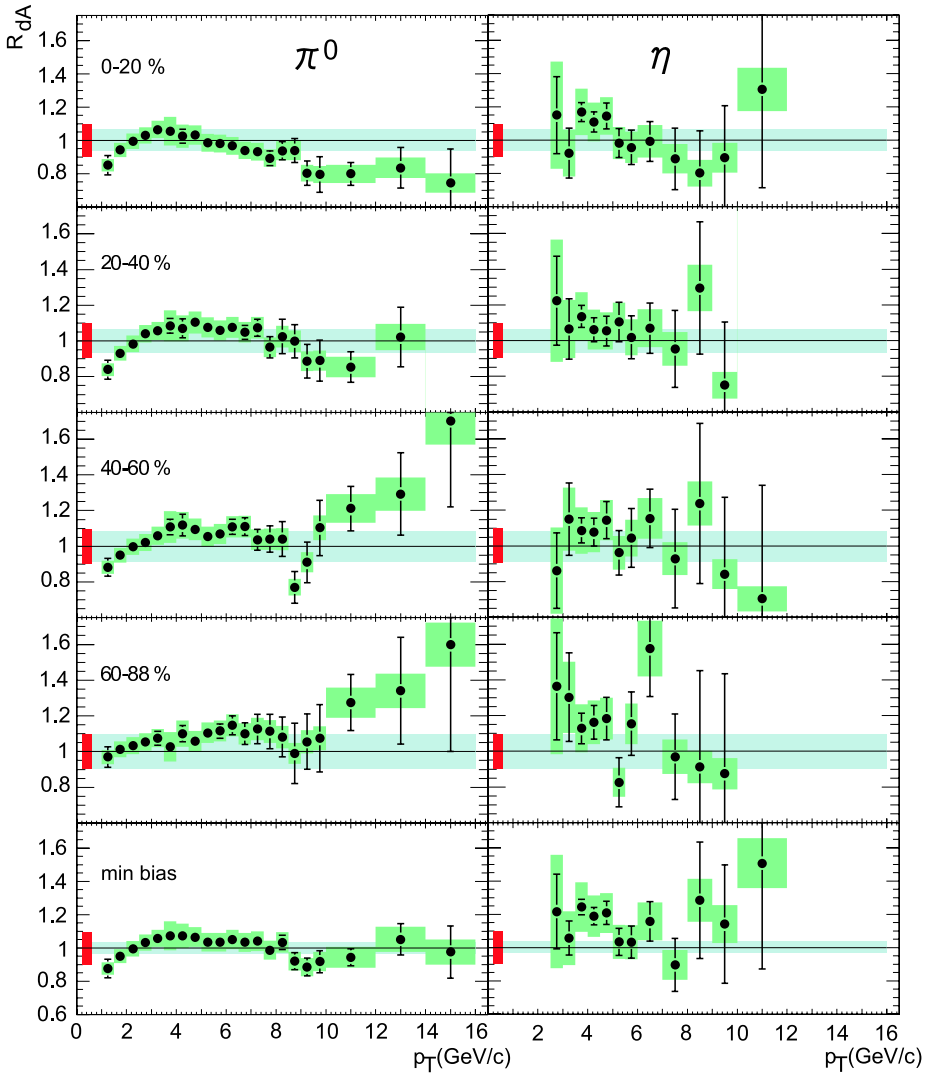

Figure 2.20: The R_{dA} for π^0 and η in different centrality selections and minimum bias data [51]. The boxes on the data points represent the p_T-correlated systematic errors and the shaded bands around $R_{dA} = 1.0$ indicate the p_T-uncorrelated systematic error including the uncertainties on the p+p absolute cross section and on the calculation of N_{coll}. The bands located at the left side of the data points indicate the normalization uncertainty due to the p+p reference.

p+p reference. The R_{dA} for both π^0, η look almost like unity for all centrality bins, and has a weak p_T dependence. The small shape variations with centrality in the R_{dA} for π^0 may be explainable due to nuclear shadowing.

As a result, the fact that the R_{dA} for all mesons is almost unity implies that the nuclear effects on the meson production is small and has no mass dependence, and the different behavior of the R_{dA} for protons compared to the ones for mesons indicates that baryons may have a different nuclear effect compared to mesons. Furthermore, it is interesting that the nuclear effects on the direct photon production is similar to those on the meson production or not.

2.4.2 Theoretical Expectation for Nuclear Effects on Direct Photon Production

The nuclear effects on the direct photon production are calculated by I. Vitev and B.W. Zhang [52, 53]. In their calculation, the initial state energy loss of a parton passing through a nucleus before the hard scattering is considered in addition to the nuclear effects described above.

Figure 2.21 shows the expectation of the nuclear effects on the direct photon production manifested in R_{dA} in d+Au and d+Cu collisions. The top and bottom panels show the results for $\sqrt{s_{NN}} = 200, 62.4$ GeV, respectively. The preliminary d+Au result measured by the EMCals in the PHENIX experiment is shown together in the top panel. The expectation of the nuclear effect for the direct photon is quite different from the observed nuclear effects for mesons. Surprisingly, the nuclear effects without the initial state energy loss increase more than 20% of the direct photon yield in $2.0 < p_T < 5.0$ GeV/c in this model calculation. Thus, the experimental d+Au result can play an important role to check the validity of the model calculation for the nuclear effects.

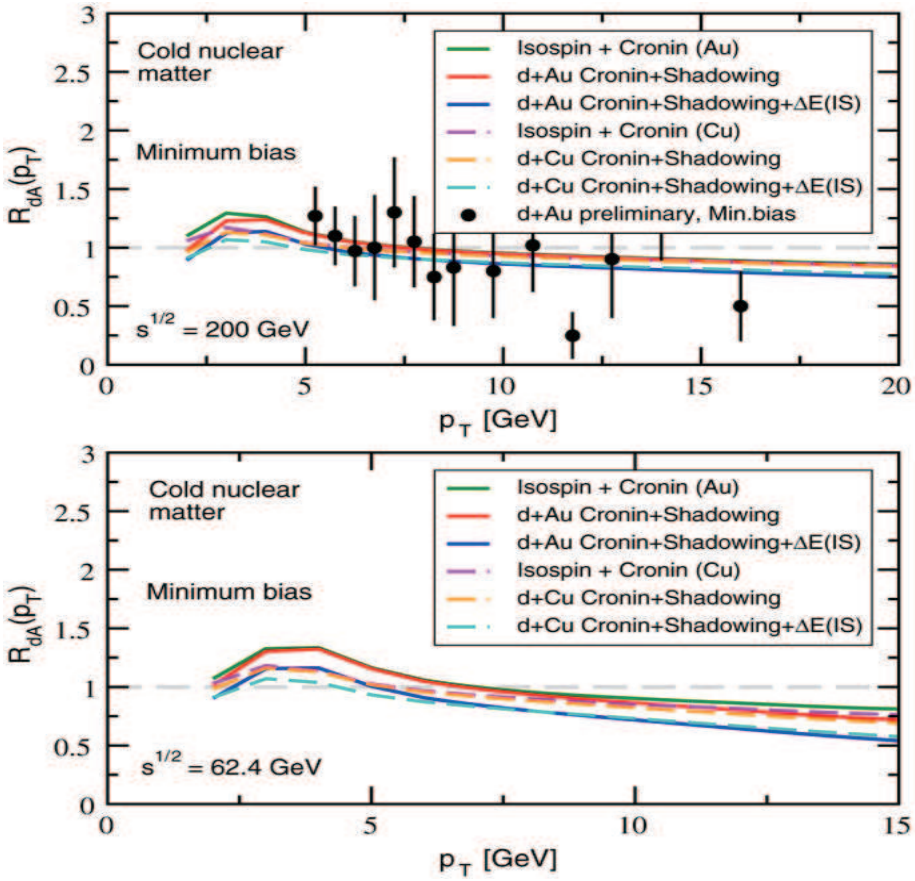

Figure 2.21: The expectation of the nuclear effects on the direct photon production in d+Au and d+Cu collisions with $\sqrt{s_{NN}} = 200$ (top), 62.4 GeV (bottom). The data points shown in the top panel are the preliminary d+Au result measured by the EMCals in the PHENIX experiment.

Chapter 3

Experimental Setup

The data analyzed in this thesis are the ones collected by the PHENIX detector for d+Au collisions with $\sqrt{s_{NN}} = 200$ GeV at RHIC. Especially, the two central arm spectrometers (East and West arms) of the PHENIX detector are used for this analysis. Each spectrometer covers $|\eta| < 0.35$ in pseudo-rapidity and $\Delta\phi < \pi/2$ in azimuth in a nearly back-to-back configuration. They have the capability of charged particle tracking and electron identification for measuring electron pairs. In this chapter, the accelerator complex including RHIC at BNL and the details for the PHENIX detector are described.

3.1 RHIC Accelerator Complex

The Relativistic Heavy Ion Collider (RHIC) is a colliding-type accelerator at BNL in the United States of America and started its operation in 2000 [54]. Figure 3.1 shows the layout of the accelerator complex, which consists of the Tandem Van de Graaff accelerator, the proton linac, the booster synchrotron, the Alternating Gradient Synchrotron (AGS) and RHIC. The RHIC circumference is 3834 m. RHIC can accelerate from protons to gold ions at the maximum center of mass energy of 500 GeV in p+p collisions and 200A GeV in Au+Au collisions.

A typical acceleration cycle of the Au ion beam starts from a pulsed sputter ion source. The negative ions extracted from the ion source are injected into the tandem with a peak intensity of 250 μA and are partially stripped of their electrons with a stripping foil at the high voltage terminal in the middle of the tandem. Then, they are accelerated to kinetic energy of 1 MeV per nucleon and are further stripped at the end of the tandem. After selecting a charge state of Au ions by bending magnets, Au^{32+} ion beams traverse the 840 m long Heavy Ion Transfer Line to the Booster synchrotron and are separated into six bunches after multi turn injections. They are accelerated to 431 MeV per nucleon and are further stripped to a Au^{77+} charge state at the exit of the Booster. Au^{77+} ions are accelerated to 9.75 GeV per nucleon in the AGS and then they are delivered to RHIC through the AGS-to-RHIC (AtR)

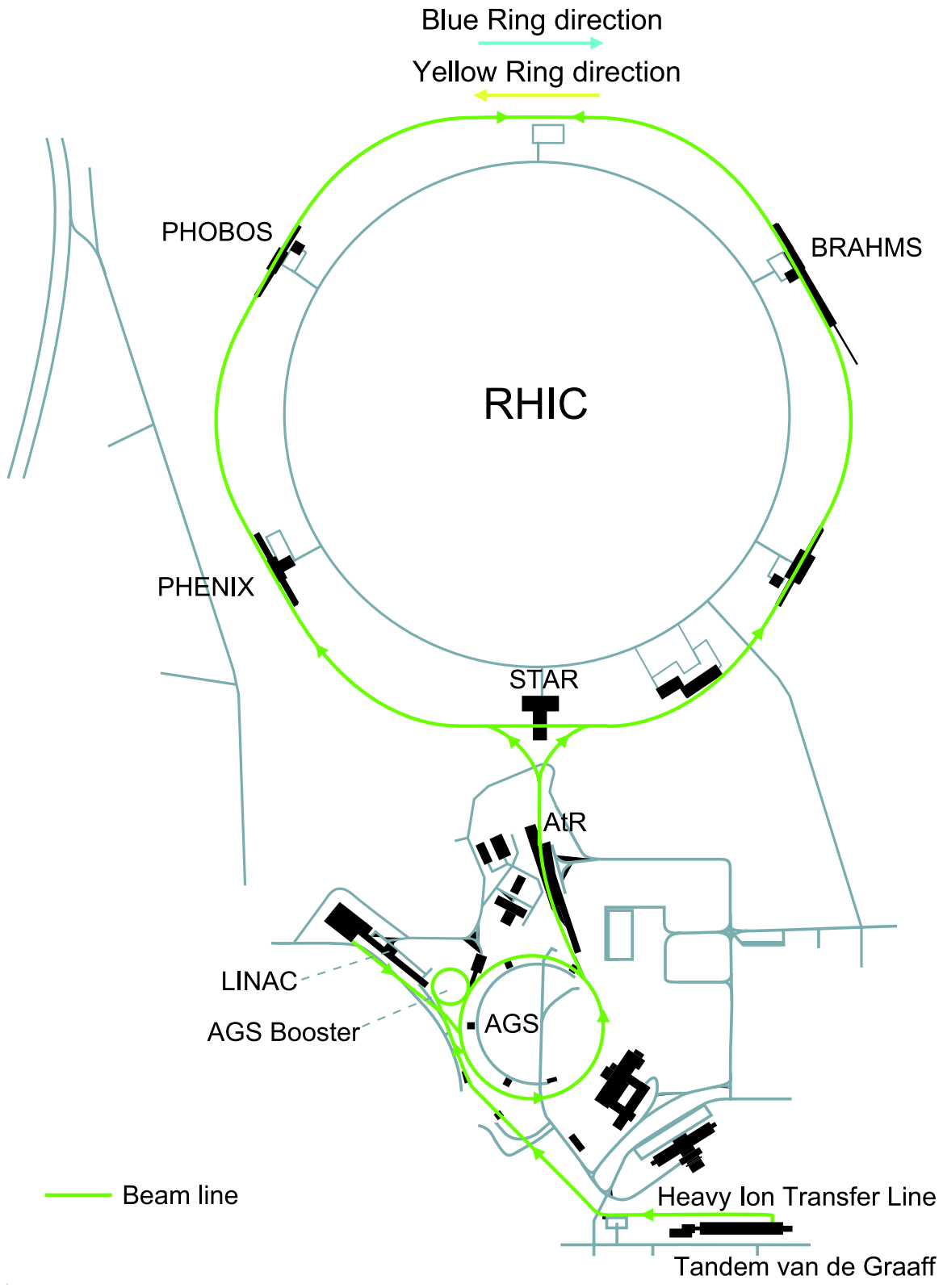

Figure 3.1: The accelerator complex including RHIC at BNL.

beam transfer line. During passage through the AtR, the last two electrons of Au^{77+} ions are removed to produce a fully stripped charge state Au^{79+}. RHIC has two rings: the Blue Ring (clockwise circulation, deuteron beam direction) and the Yellow Ring (counterclockwise circulation, gold beam direction). These rings cross at six interaction regions where four experiments (PHENIX [55], STAR [56], PHOBOS [57] and BRAHMS [58]) took place (PHOBOS and BRAHMS are shutdown as of 2010). Two different radio frequency (RF) systems are used for acceleration and storage of beam bunches at RHIC. The 28 MHz RF is to capture the AGS bunches and accelerate to the top energy, and the other is 197 MHz RF to limit the bunch length growth due to intra-beam scattering.

RHIC also serves as a polarized proton collider. Polarized protons are firstly accelerated to 200 MeV by the linac, and then they are further accelerated by the booster, the AGS and the RHIC up to 250 GeV.

The major design parameters of RHIC [54, 59] are summarized in Table 3.1.

Table 3.1: Summary of the major design parameters of RHIC.

	p+p	Au+Au
Maximum beam energy	250 GeV	100 GeV/A
Luminosity [cm^{-2}sec^{-1}]	1.4×10^{31}	2.0×10^{26}
Number of bunches	56	56
Number of particles/bunch	10^{11}	10^{9}
Bunch length [cm]	40	15
Crossing angle [mrad]	0 (<1.7)	0 (<1.7)
Luminosity life time [hour]	10	3

3.2 PHENIX Experiment

The PHENIX experiment is one of the largest experiments of four experiments at RHIC as well as STAR. The PHENIX detector was constructed with the aim to discover the signatures of the QGP and studying the QGP properties via measurements of a wide variety of physics observables. Especially, the PHENIX detector has a stronger capability to measure leptons compared to the other three experiments. A drift chamber (DC) and pad chambers (PC1,2,3) play the role of tracking, and a ring imaging Cherenkov detector (RICH) and an electromagnetic calorimeter (EMCal) are used for electron identification and electron trigger (ERTLL1). Beam-beam counters (BBCs), which are located at pseudo-rapidity $3.1 < |\eta| < 3.9$, measure the position of the collision vertex along the beam axis (z_{vertex}) for each collision and provide an event trigger (BBCLL1).

3.2.1 Global Coordinate System

Figure 3.2 illustrates the definition of the PHENIX global coordinate system. The

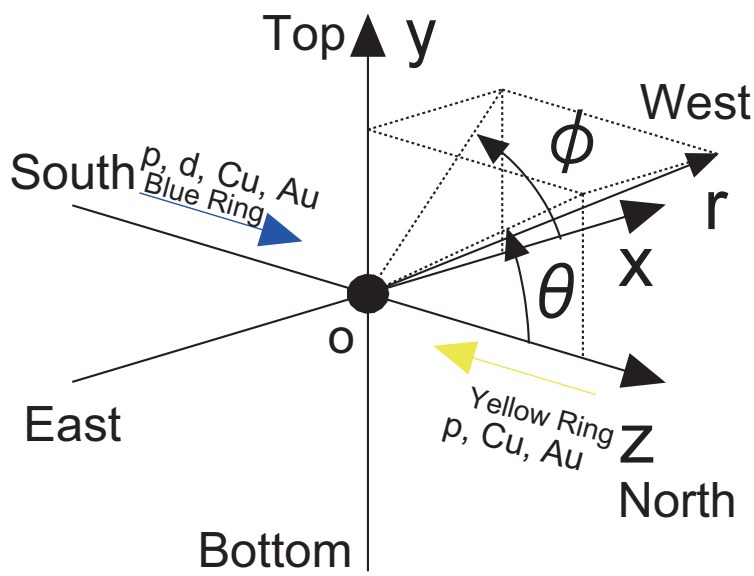

Figure 3.2: Definition of the global coordinate system used in the PHENIX experiment.

origin of the global coordinate system is set at the center of the interaction point along the center of the cylindrical beam pipe. The z-axis is defined as an axis along the center of the beam pipe with north defined as the positive direction. The y-axis is the altitude relative to the origin and the x-axis is defined to form a right handed coordinate system. The azimuthal angle ϕ is a counterclockwise angle with respect to the positive x direction and the polar angle θ is defined as an angle with respect to the positive z direction. The pseudo-rapidity η is written as:

$$\eta = -\ln \tan\left(\frac{\theta}{2}\right). \tag{3.1}$$

3.2.2 Detector Overview

Figure 3.3 shows the layout of the PHENIX detector configuration in the Year-2008 Run (Run8). Both beam (top panel) and side (bottom panel) views are shown. The PHENIX detector mainly consists of global detectors, central arms (East and West) and muon arms (North and South). Although the details on the detectors

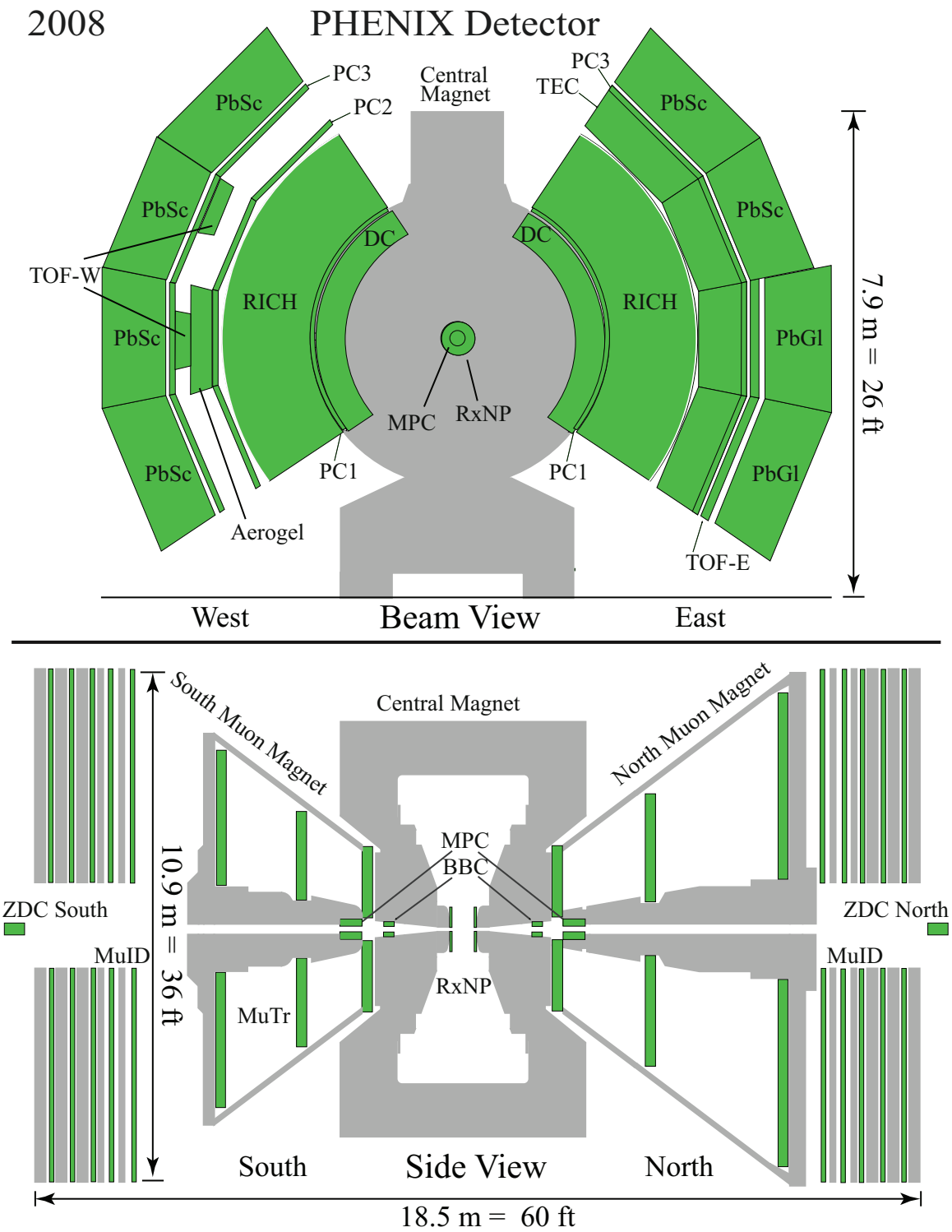

Figure 3.3: Layout of the PHENIX detector configuration in the Year-2008 Run. Beam view (top panel): Inner detectors, two Central Arms and Central Magnet are shown. Side view (bottom panel): Inner detectors, two Muon Arms, Central Magnet and Muon Magnets are shown.

are described in the following sections, the acceptance coverage and the feature of each detector is summarized briefly in Table 3.2. The acceptance coverages of the

Table 3.2: Summary of the information of the PHENIX subsystem detector.

Subsystems	$\Delta\eta$	$\Delta\phi$	Information
Central Magnet (CM)	± 0.5	360°	Up to 1.0 T·m
Muon Magnet (MM)	± 1.1-2.5	360°	0.72 T·m (for $\eta = \pm 2$),
			0.36 T·m (for $\eta = \pm 1.3$)
BBC	± 3.0-3.9	360°	Event trigger, Collision vertex
Drift Chamber (DC)	± 0.35	$90^\circ \times 2$	$\Delta p/p = 1.0\%$ at $p = 1$ GeV/c
Pad Chamber (PC)	± 0.35	$90^\circ \times 2$	Tracking for non-bend direction
RICH	± 0.35	$90^\circ \times 2$	Electron identification
EMCal (PbSc)	± 0.35	$90^\circ \times 1.5$	4 sectors in West and 2 sectors in East
EMCal (PbGl)	± 0.35	45°	2 sectors only in East
Muon Tracker	± 1.2-2.4	360°	Tracking for muons
Muon identifier	± 1.2-2.4	360°	Concrete absorbers plus chambers

central arms and the muon arms in pseudo-rapidity are $|\eta| < 0.35$ and $1.2 < |\eta| < 2.4$, respectively. Figure 3.4 shows the acceptance coverages of the central arms and muon arms with respect to η-ϕ plane. The beam pipe is made of Be, whose diameter and thickness are 76 mm and 1.0 mm (0.28% of radiation length), respectively.

3.3 PHENIX Global Detectors

The PHENIX global detectors consists of the Beam-Beam Counter (BBC) [60] and the Zero-Degree Calorimeter (ZDC) [61, 62, 63] to measure beam properties such as the luminosity, the collision vertex and the collision centrality.

3.3.1 Beam-Beam Counter

The Beam-Beam Counter (BBC) is designed to measure a charged particle multiplicity, a timing of the collision. Triggers for beam collision events and the collision vertex position along the beam axis are also derived from the observables measured by the BBC. The BBC consists of two arrays of Cherenkov counters which are located at 144 cm away from the interaction point in the north and south side separately, and its pseudo-rapidity coverage is $3.0 < |\eta| < 3.9$. Each array also consists of 64 modules of 1-inch diameter mesh-dynode phototubes (Hamamatsu R6178) equipped with 30 mm-quartz Cherenkov radiators on their heads. Pictures in Fig. 3.5 show (a) a single BBC module, (b) a BBC array comprising 64 single modules and (c) the BBC mounted on the PHENIX detector.

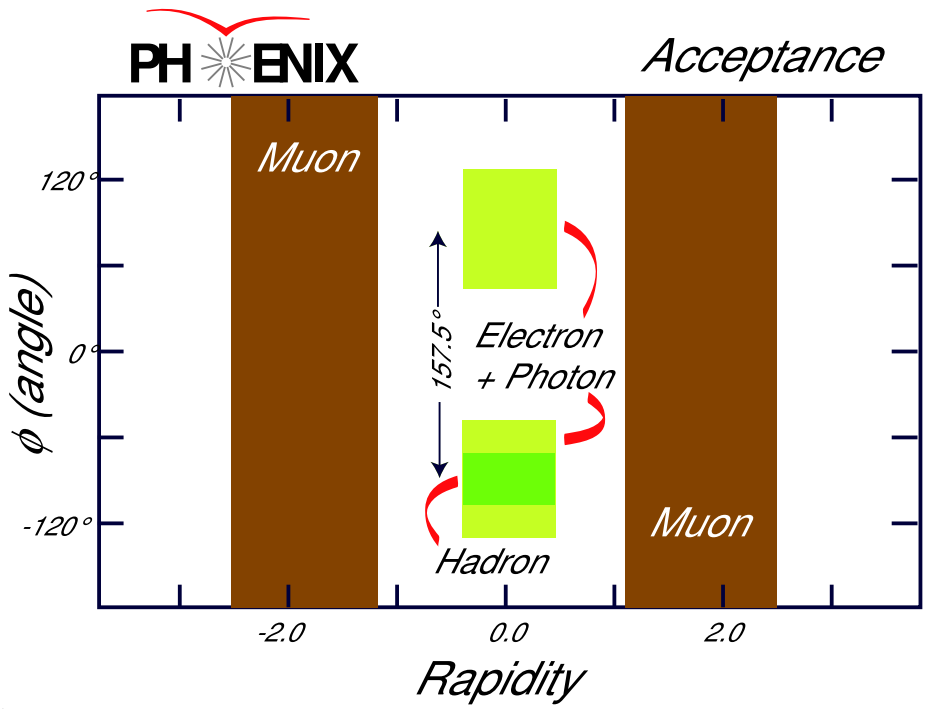

Figure 3.4: The acceptance coverages of the central and muon arms with respect to η-ϕ plane.

The start time (T_0) and the collision vertex position (z_{vertex}) are calculated using the average of the arrival times (T_1 for the south array and T_2 for the north array) of the fast leading charged particles from a beam collision into the BBC arrays as follows:

$$T_0 = \frac{T_1 + T_2}{2} - \frac{|z_{BBC}|}{c} + t_{\text{offset}}, \tag{3.2}$$

$$z_{vertex} = \frac{c \cdot (T_1 - T_2)}{2} + z_{\text{offset}}, \tag{3.3}$$

where z_{BBC} is the BBC located position at 144 cm from the interaction point and $t_{\text{offset}}, z_{\text{offset}}$ are the time and z-position offsets intrinsically introduced by devices. The time resolution of a single BBC module is 52 ± 4 ps (RMS) and the z-vertex resolution is ~ 0.5 cm under the experimental condition.

3.3.2 Zero-Degree Calorimeter

The Zero-Degree Calorimeter (ZDC) is a sampling-type hadron calorimeter designed to detect forward neutrons and measure the total energy of them. The ZDC is used among the four RHIC experiments as a common trigger device. Two ZDCs are located just behind the DX dipole magnets at $z = \pm 18.25$ m away from the interaction point

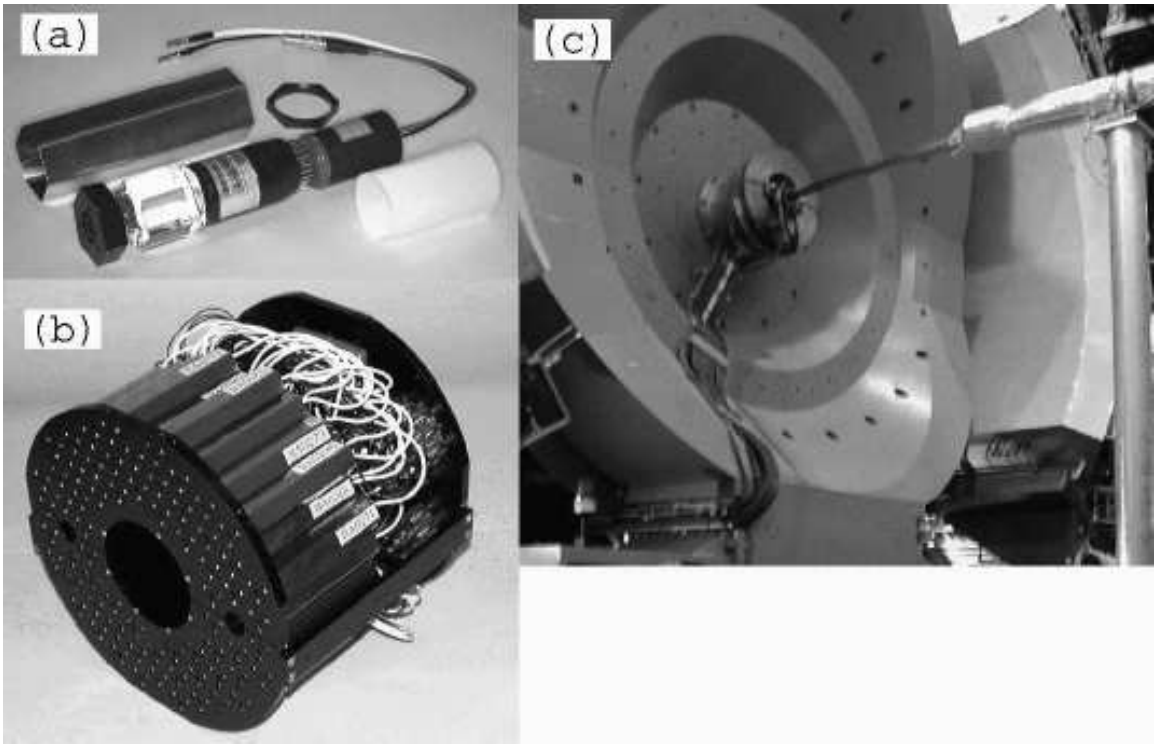

Figure 3.5: Pictures of the BBC. (a) A single BBC module consisting of a 1-inch diameter mesh-dynode phototube equipped with a 30 mm-quartz Cherenkov radiator. (b) A BBC array comprising 64 single modules. (c) The BBC mounted on the PHENIX detector.

as shown in Fig. 3.6. The ZDC angular acceptance is $|\theta| < 2$ mrad. The DX dipole magnets serve to bend the incoming beams to the colliding region and the outgoing beams to the beam line. Because of the bending by the DX dipole magnet, only neutrons can reach each ZDC.

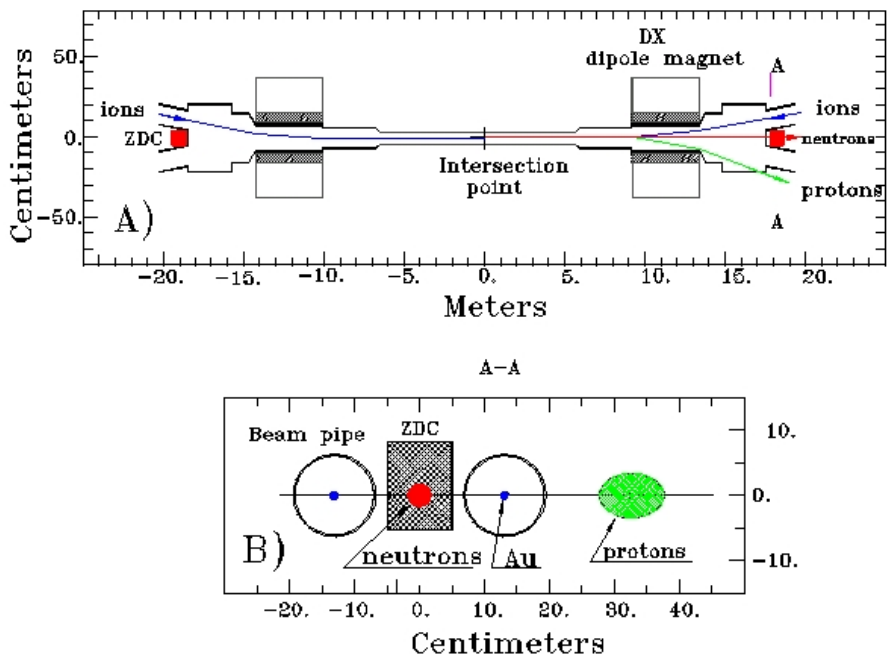

Figure 3.6: Layout of the ZDC location. A) Top view and B) beam view of the ZDC location. Protons and charged fragments are bent by DX dipole magnets to the outside of the ZDC acceptance coverage.

Each ZDC consists of 27 layers of tungsten absorbers and fibers connected to phototubes (Hamamatsu R329-2). The background due to single-beam interaction with the residual gas in the beam pipe can be rejected by taking the correlation between the south and north ZDCs. The energy resolution of the ZDC is $\delta E/E \simeq 218/\sqrt{E(\mathrm{GeV})}\%$ from the test beam results.

The ZDC plays an important role for centrality determination in Au+Au collisions by the correlation with the BBC charge, however the ZDC is not used for d+Au collisions because of a lack of neutrons from spectators.

3.4 PHENIX Magnet

The three magnets, Central Magnet (CM), North Muon Magnet (MMN) and South Muon Magnet (MMS) [64] form the PHENIX magnet system. Figure 3.7 shows the

layout of the magnets and, the magnetic field produced by the magnets is shown in Fig. 3.8.

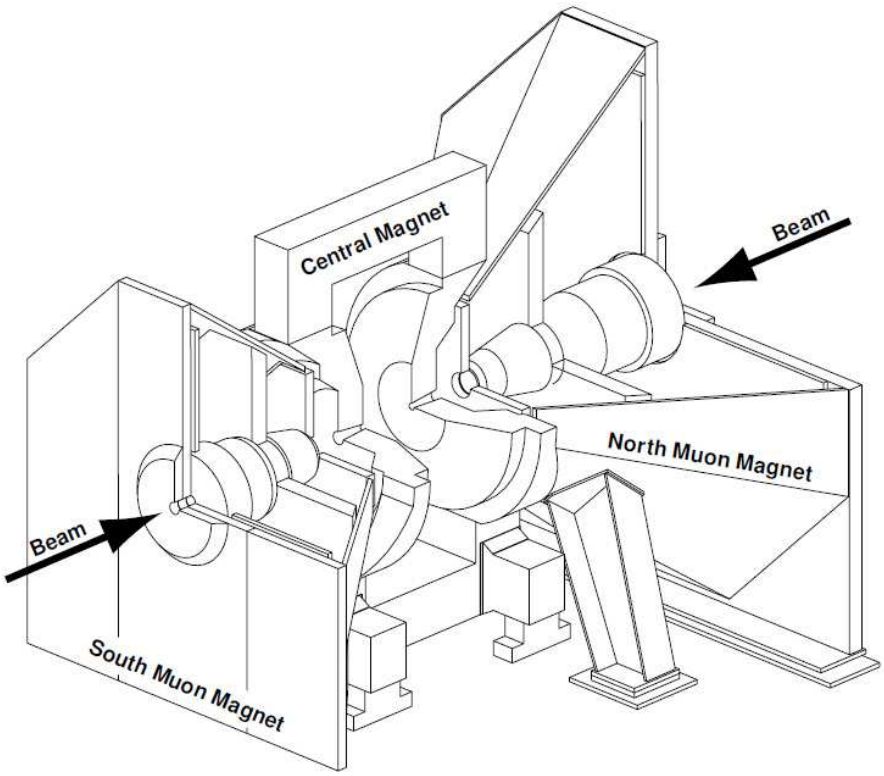

Figure 3.7: The layout of the PHENIX magnets with a cutaway to show the interior structures. Arrows indicate the beam lines in RHIC.

The PHENIX Central Magnet (CM) realizes an axial field and its integrated field is $\int B \cdot dl = 0.78$ T·m at $\theta = \pi/2$ rad. The momenta of charged particles are determined using the magnetic bending by the CM. The CM is energized by two, inner and outer, concentric coils, which can be operated separately, with the same polarities or opposite polarities. In Year-2008 Run (Run8), the same polarity operation was selected. The operation is denoted by CM++ or CM− − according to the polarity of the magnetic field. The pole faces of the magnet are positioned at $z = \pm 0.45$ m covering the pseudo-rapidity range of $|\eta| < 0.35$. The CM pole tips also serve as hadron absorbers for the muon spectrometers.

3.5 PHENIX Central Arms

The PHENIX central arms are designed to detect charged particles and photons. Tracking and momentum measurement of charged particles are performed by the drift chamber and the pad chamber [65]. The electromagnetic calorimeter measure

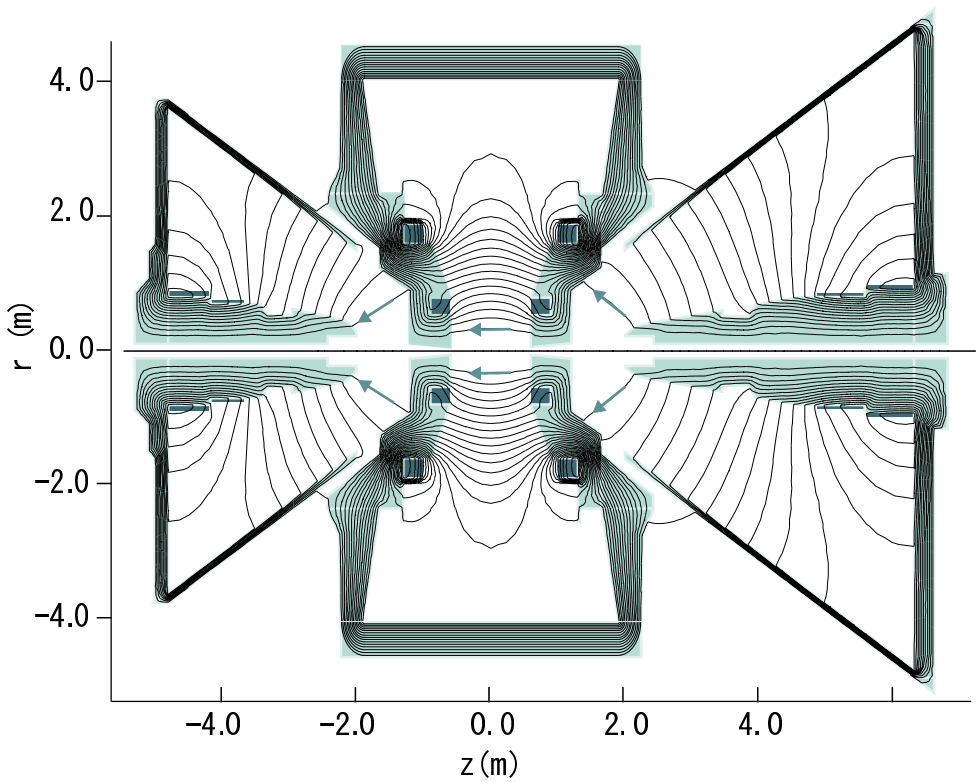

Figure 3.8: The field lines of the central magnet and muon magnets shown on a vertical cutaway drawing of the PHENIX magnets. The beams travel along the $r = 0$-axis in this figure and collide at $r = z = 0$. Arrows indicate the field direction.

energies of photons [66] and play a role for electron identification with the ring imaging Cherenkov detector [67]. The central arm contains other detectors such as the time of flight detector and the aerogel Cherenkov counter for hadron identification (π, K, p and d) and so on, which are not used in the direct photon measurement with the virtual photon method. In this section, the above detectors are briefly reviewed.

3.5.1 Drift Chamber

The drift chamber (DC) is used to measure charged particle trajectories in the r-ϕ plane and to determine their momenta with a good resolution. The required performances of the DC are as follows.

1. The resolution on a single wire is better than 150 μm in the r-ϕ plane.
2. The two track separation for a single wire is better than 1.5 mm.
3. The single track detection efficiency is better than 99%.
4. The spatial resolution in the z-direction is better than 2 mm.

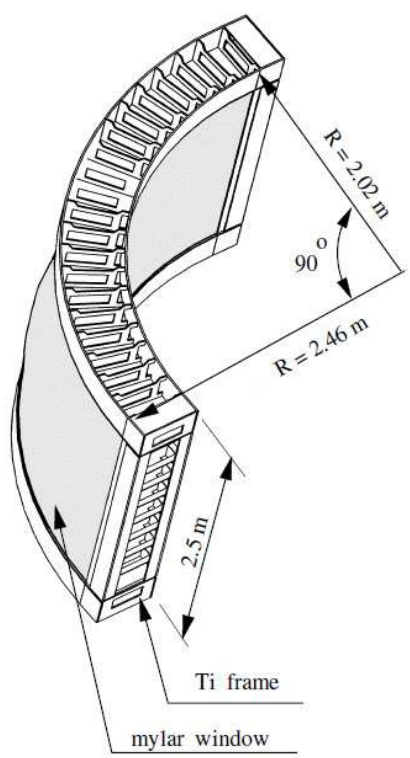

Figure 3.9: A frame of the drift chamber.

The DC system consists of two independent gas volumes located in the west and east arms. The gas volumes are filled with a gas mixture of 50% argon and 50% ethane. The DC occupies a radial budget from 2.02 to 2.46 m from the interaction point in each side and covers 1.8 m along the beam line direction as an active area. Each DC is located in the high residual magnetic field region up to 0.06 T at maximum. The DC is constructed with a cylindrical titanium frame as shown in Fig. 3.9. The frame is divided in 20 sectors covering 4.5° in ϕ. In each sector, six types of wire modules: X1, U1, V1, X2, U2, V2 are stacked radially as shown in Fig. 3.10. Each wire module contains twenty sensing (anode) planes (twelve X, four U and four V wire planes) and four cathode planes forming cells with a 20-25 mm drift space in the ϕ direction. The sensing (S) wires are separated by potential (P) wires, and surrounded by gate (G) and back (B) wires. The P wires form a strong electric field and separate sensitive

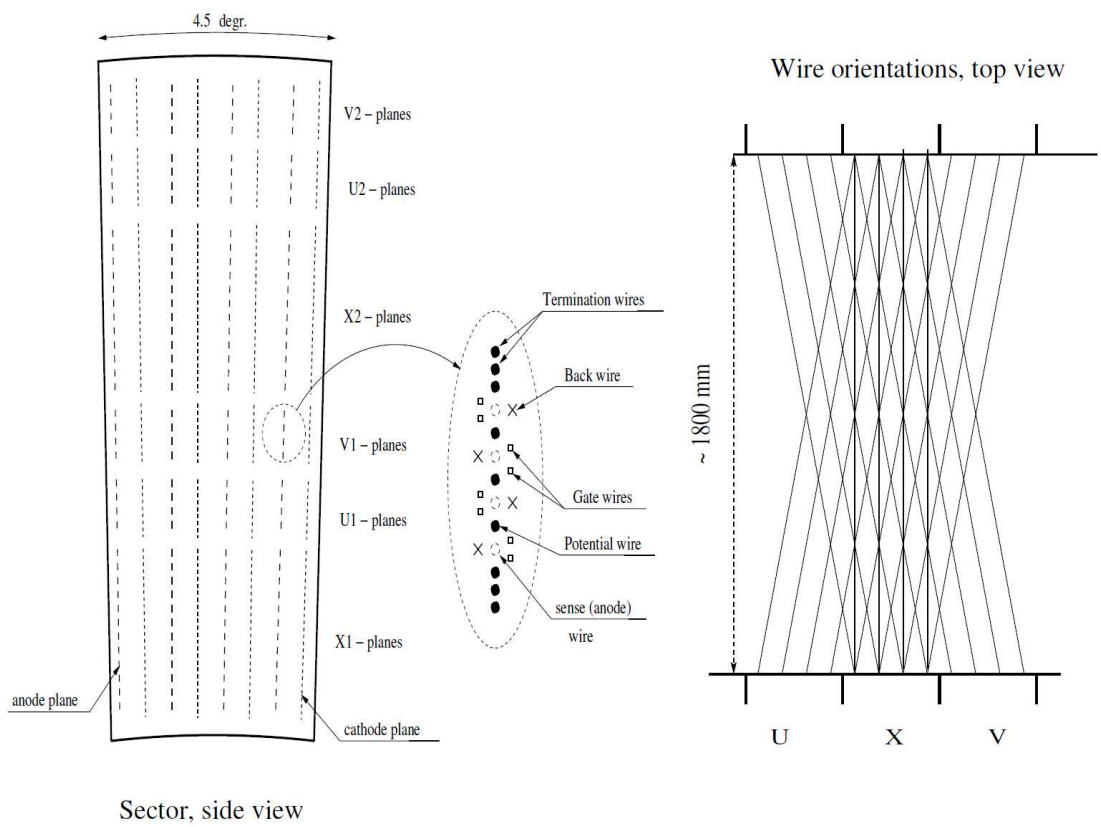

Figure 3.10: The layout of wire positions in one sector. (Left) Side view of the wire position layout together with an enlarged view inside the anode plane. (Right) Top view of the stereo wire orientation.

regions of individual S wires. The G wires limit the track sample length to roughly 3 mm and terminated unwanted drift lines. The B wires have a rather low potential and terminate most of the drift lines from their side, essentially eliminating left-right ambiguity and decreasing the signal rate per electronics channel by a factor of two.

The X1 and X2 wire cells run in parallel to the beam line to precisely measure tracks in the r-ϕ plane. U and V wire cells, which are used for pattern recognition, are located behind the X wire cell. The U and V wires have stereo angles of about 6° relative to the X wires and measure the z coordinate of the track. The stereo angle is set to minimize track ambiguities by matching the z coordinate of the pad chamber. Each sensing wire is separated into two halves at the center to satisfy the requirement of efficient track recognition for up to 500 tracks in the whole PHENIX fiducial volume, and signals are independently extracted.

With the 50%-Argon and 50%-Ethane gas mixture, the stable drift velocity plateau at 53 mm/μs is achieved for the field gradation from 800 V·cm to 1.4 kV·cm. The maximum drift time in a cell is approximately 470 ns.

3.5.2 Pad Chamber

The pad chamber (PC) is used to determine three dimensional spatial positions. The spatial position information from the PC is important for momentum determination in the z-direction (p_z). The PC is a multi-wire proportional chamber with a cathode

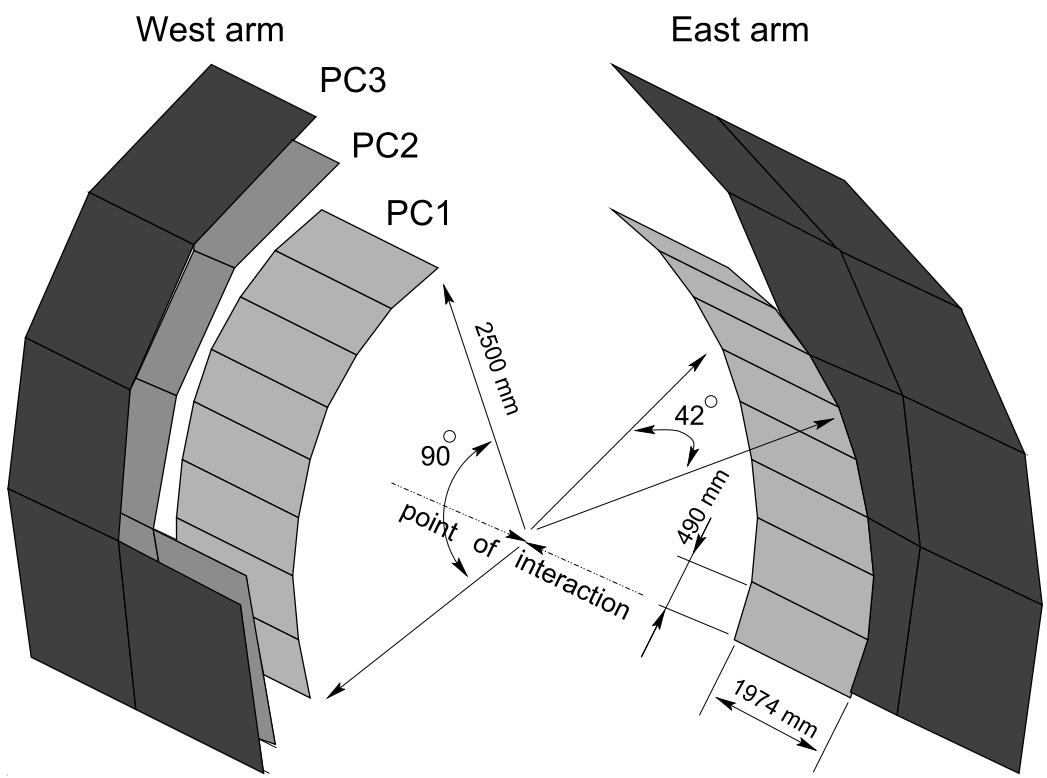

Figure 3.11: A schematic view of the PCs (PC1, PC2, PC3). Some sectors of PC2 and PC3 in the west arm are removed for clarity of the picture.

readout and forms three separate layers (PC1, PC2, PC3) as shown in Fig. 3.11.

The PC1 is the innermost chamber occupying 2.47∼2.52 m in radial distance from the interaction point, *i.e.* the region between DC and the ring imaging Cherenkov detector (RICH) in both east and west arms. The PC2 layer exists only in the west arm and is placed behind the RICH at $r = 4.15 \sim 4.21$ m. The PC3 is located in front of the electromagnetic calorimeter (EMCal) and occupies the region between $r = 4.91 \sim 4.98$ m.

The PC1 is essential for determination of the three dimensional momentum by providing the z coordinate at the exit of the DC. The information from the DC and PC gives the straight line particle trajectories outside the magnetic field. The PC2 and PC3 are needed to resolve ambiguities in outer detectors where about 30% of particles striking the EMCal are produced by either secondary interaction or decays outside the aperture of the DC and PC1.

Each detector consists of a cathode panel and a signal plane of anode and field wires. One cathode is finely segmented into an array of pixels as shown in Fig. 3.12. A gas mixture of 50% argon and 50% ethene is filled in the PC at atomospheric pressure. The performance of the PCs are summarized in Table 3.3.

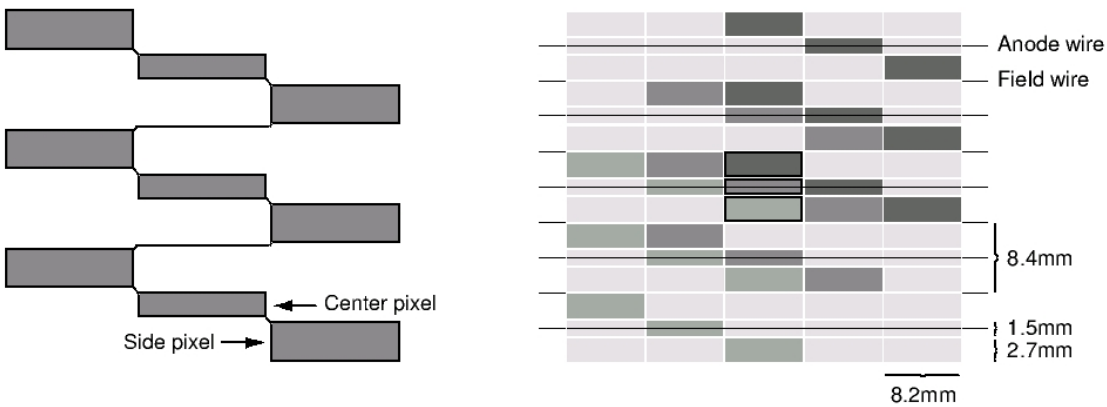

Figure 3.12: The pad and pixel geometry of the PC. A cell defined by three pixels is indicated at the center of the right figure.

Table 3.3: Performance of pad chambers in Year-2002 and a cosmic ray test.

	PC1	PC2	PC3
Pad size ($\phi \times z$ mm^2)	8.4×8.4	13.6×14.4	16.0×16.7
Single hit resolution in z (mm)	1.7	3.1	3.6
Efficiency	≥99%	≥99%	≥99%

3.5.3 Ring Imaging Cherenkov Detector

The ring imaging Cherenkov detector (RICH) [68] is the primary device to identify electrons among a large number of charged hadrons. RICH is placed in both central arms between 2.5 $\sim$ 4.1 m in radial distance from the interaction point, covering $70° \leq \theta \leq 110°$ and 90° per arm in the azimuth. Figure 3.13 shows a cutaway view of RICH. In each arm, RICH has a 40 m^3-volume aluminium vessel with an entrance

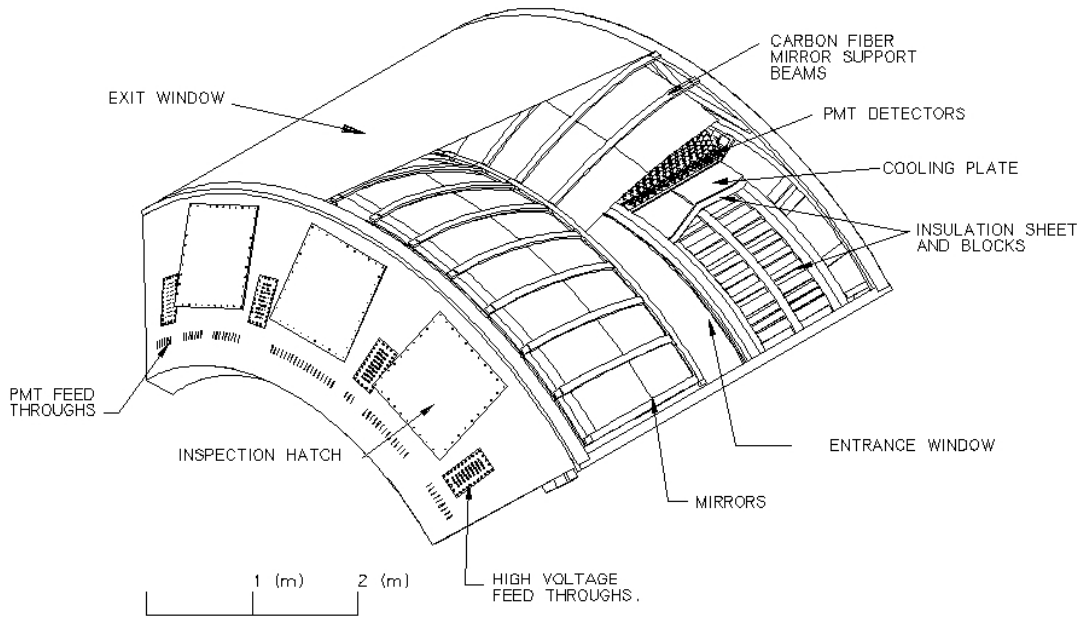

Figure 3.13: A cutaway view of RICH.

window of 8.9 m^2 and an exit window of 21.6 m^2, which are made of 125 μm-thick aluminized Kapton foils. In the gas vessel, two arrays of 24 aluminium-evaporated mirror panels are mounted on the graphite-epoxy mirror support, and they are located symmetrically with respect to $z = 0$. The mirror panel substrates have a $\sim$ 4.01 m-radius curvature. The Cherenkov light emitted from a charged particle is reflected by the spherical mirrors, and the reflected light is focused on two arrays of 1280 Hamamatsu H3171S UV phototubes with a cathode diameter of 25 mm. Each phototube array is located on either side of the RICH entrance window. The phototubes are fitted with 2 inch diameter Winston cones and have magnetic shields which allow to operate at up to the magnetic field of 0.01 T. Their UV glass windows absorb photons with a wavelength of below 200 nm. The phototube has a bi-alkaline photocathode and a linear focus 10 stage dynode. The maximum quantum efficiency is 27% ($>$ 19% at $\lambda = 300$ nm and $>$ 5% at $\lambda = 200$ nm). The typical dark current is 10 nA and the typical operation is 1.5 kV with a gain of 10^7.

Figure 3.14 shows a schematic view of RICH cut along the beam axis. In the

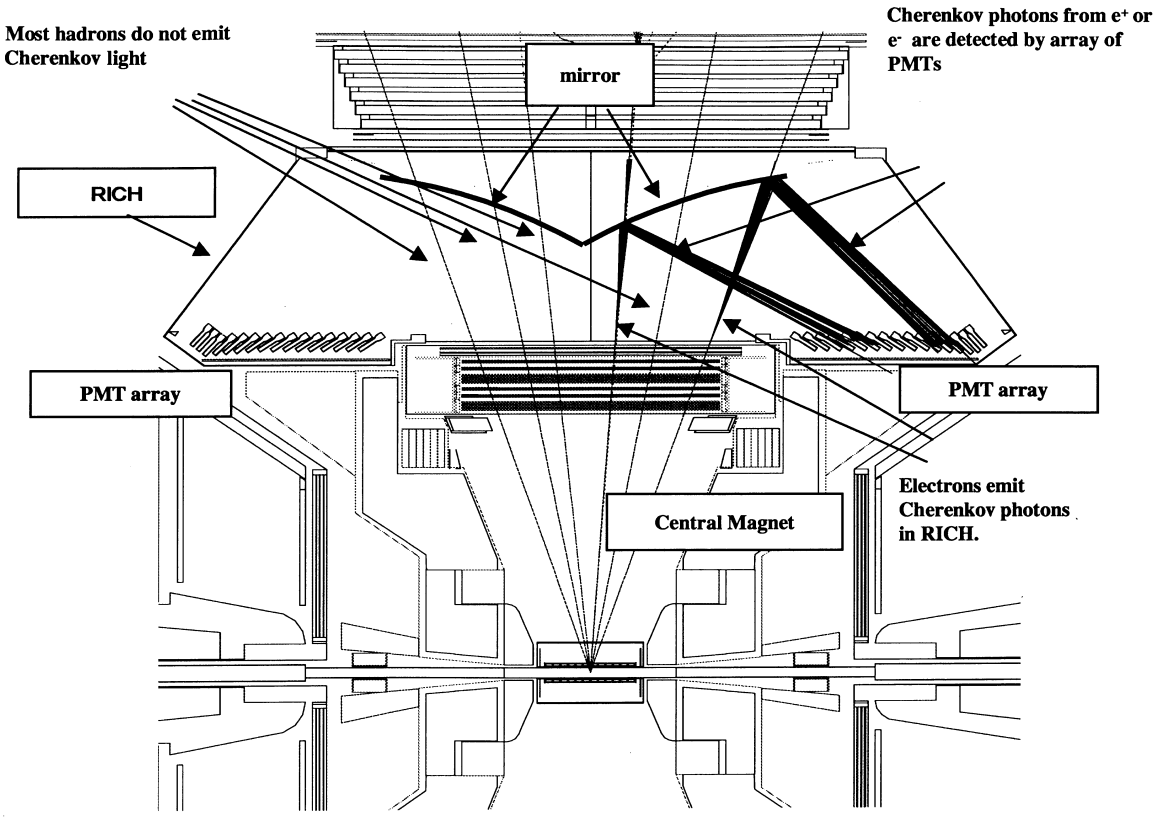

Figure 3.14: A schematic view of RICH cut along the beam axis.

RICH gas vessel, charged particles moving faster than the speed of light in the gas emit Cherenkov photons. The emitted photons are reflected and focused by the spherical mirror on the phototube array plane. The radiator gas filled in the RICH vessel is CO_2 whose index is 1.000410 at 20 °C and 1 atm [69]. A charged particle with $\beta\gamma > 35$ emits Cherenkov photons. The corresponding momentum thresholds for electron and pion are 18 MeV/c and 4.9 GeV/c, respectively.

The RICH Front-End Electronics (FEE) processes the phototube signals at each bunch crossing (9.4 MHz) and transmits digitized data to the PHENIX data acquisition system on the trigger signal supplied by the PHENIX global trigger system ($\sim$ 25 kHz) [70]. The acceptable charge range is from 0 to 10 photoelectrons, which corresponds to the input charge from 0 to 160 pC preceded by the preamplifier. The charge resolution is $\sim$ 1/10 photoelectron and the timing resolution is $\sim$ 240 ps. Both of the charge and timing outputs are stored in Analog Memory Unit (AMU) clocked at the RHIC bunch crossing frequency. The analog data stored in the AMU are digitized only after the receipt of an acceptance from the PHENIX global trigger system.

3.5.4 Electromagnetic Calorimeter

The electromagnetic calorimeter (EMCal) is used to measure the energy and spatial position of electrons and photons produced in beam collisions. It covers the full central spectrometer acceptance of $70° \leq \theta \leq 110°$, 90° in the azimuth. The EMCal in the west arm comprises four sectors of a lead scintillator sampling calorimeter (PbSc) and the one in the east arm has two sectors of a PbSc and another two sectors of a lead glass Cherenkov calorimeter (PbGl). The pseudo-rapidity coverage is $|\eta| < 0.35$ for both PbSc and PbGl. The azimuthal coverage is $6 \times \pi/4$ for PbSc and $2 \times \pi/4$ for PbGl.

Lead Scintillator Calorimeter

The lead scintillator calorimeter (PbSc) is a shashlik type sampling calorimeter consisting of 15552 individual towers and covering area of $\sim$ 50 m^2. Each PbSc tower contains 66 sampling cells consisting of alternating tiles of Pb and scintillator. These cells are optically connected by 36 longitudinally penetrating wavelength shifting fibers for light connection. 30 mm FEU115M phototubes are equipped at the back of the towers. Optically isolated four towers are mechanically grouped together into a single structural entity called a module as shown in Fig. 3.15. 36 modules are attached to a backbone and held together by welded stainless steel skins on the outside to form a rigid structure called a supermodule. 18 supermodules make one sector, a 2×4 m^2 plane with its own rigid steel frame. The energy resolution of PbSc from

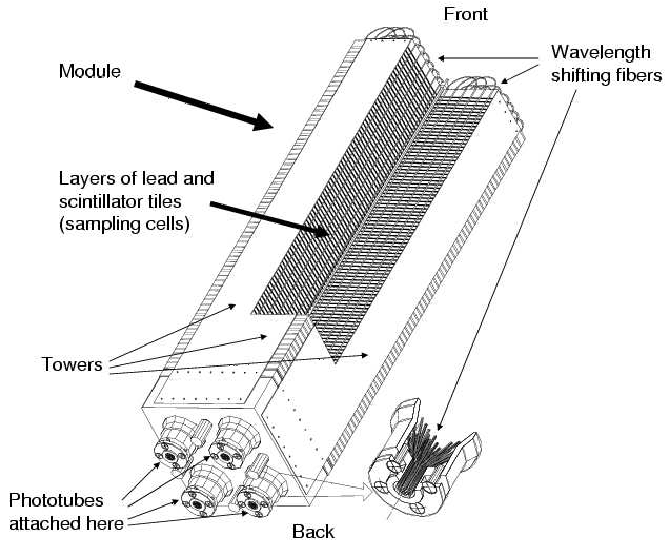

Figure 3.15: Interior view of a lead scintillator calorimeter module showing a stack of scintillator and lead plates, wavelength shifting fiber readout and leaky fiber inserted in the central hole. Its active depth is 375 mm (18 radiation length) and lateral segmentation size is 55.35×55.35 mm^2.

tests with electron beams is given by:

$$\frac{\sigma_E}{E} = \frac{8.1\%}{E\ (\mathrm{GeV})} \oplus 2.1\%. \tag{3.4}$$

Lead Glass Calorimeter

The lead glass calorimeter (PbGl) array comprises 9216 modules. Each module has a lead glass crystal of 40 mm×40 mm×400 mm. The active depth of 400 mm corresponds to 16 radiation length. The Cherenkov photons emitted by electrons in the electromagnetic shower process are read out by FEU84 phototube in the back end. The modules are individually wrapped with aluminized myler and shrink tube and 24 modules are glued together with a carbon fiber and an epoxy resin to form a selfsupporting supermodule as shown in Fig. 3.16. Each PbGl sector comprises 192 supermodules (16 supermodule wide by 12 supermodule high). The energy resolution of PbGl from the tests with electron beams is given by:

$$\frac{\sigma_E}{E} = \frac{5.9\%}{E\ (\mathrm{GeV})} \oplus 0.8\%. \tag{3.5}$$

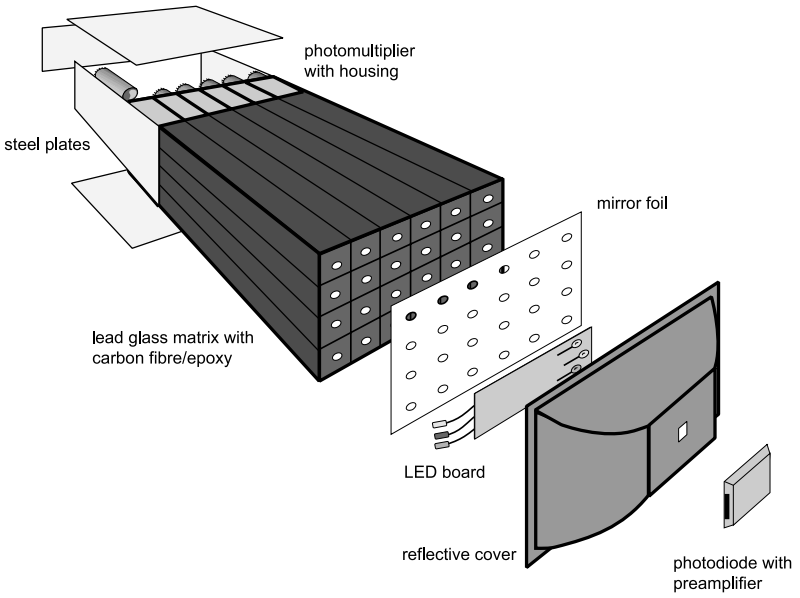

Figure 3.16: Exploded view of a lead glass calorimeter supermodule.

3.6 Trigger

The Level-1 trigger (LVL1) is designed to select interesting events with a sufficient rejection of uninterested events to reduce the data rate to an acceptable level which can be handled by the PHENIX data acquisition system [71]. The LVL1 trigger is a parallel, pipelined and deadtimeless system.

The trigger system consists of two separate subsystems. One is the Local Level-1 (LL1) system and the other is the Global Level-1 (GL1) system. The LL1 system communicates directly with participating detectors such as the BBC, EMCal and RICH. The input data from these detectors are processed by the following LL1 algorithms to produce a set of reduced-bit input data for each RHIC beam crossing. The GL1 receives and combines the LL1 data to make a trigger decision, and also manages busy signals.

3.6.1 BBC Local Level-1 Trigger

The BBC Local Level-1 trigger (BBCLL1) is an event trigger to record collision events with a requirement of the coincident hit information on the south and north BBC modules with at least one hit. The timing information of the BBC is used to select events which occur in beam crossings and within the nominal interaction region ($|z| < 38$ cm). The minimum bias (MB) trigger condition requires the BBCLL1 trigger bit, and the MB events in this thesis is defined as events recorded by the BBCLL1 trigger.

3.6.2 EMCal-RICH Local Level-1 Trigger

The EMCal-RICH Local Level-1 trigger (ERTLL1) plays as electron and photon triggers. Acceptance coverage of each of the EMCal and the RICH is divided into 16 trigger segments. Each segment consists of 9 (for PbSc)/16 (for PbGl, RICH) trigger tiles. Each trigger tile consists of 144 EMCal towers (20 RICH phototubes). The EMCal has two different methods to sum deposited energies in towers, 2×2 tower sum and 4×4 tower sum. The energy threshold value of the EMCal for the hit definition can be changed. If there is a hit tile defined by a 4×4 sum (2×2 sum), ERTLL1_4x4 (ERTLL1_2x2) is issued. There are 3 ERTLL1_4x4 triggers with different energy thresholds, namely 4×4a, 4×4b and 4×4c. They serve as photon triggers.

If the energy sum in a 2×2 tower tile exceeds threshold value (600 or 800 MeV in Run8) and a RICH hit tile is found along the same trajectory with the 2×2 tower tile as shown in Fig. 3.17, ERTLL1_E is issued as an electron trigger. Association

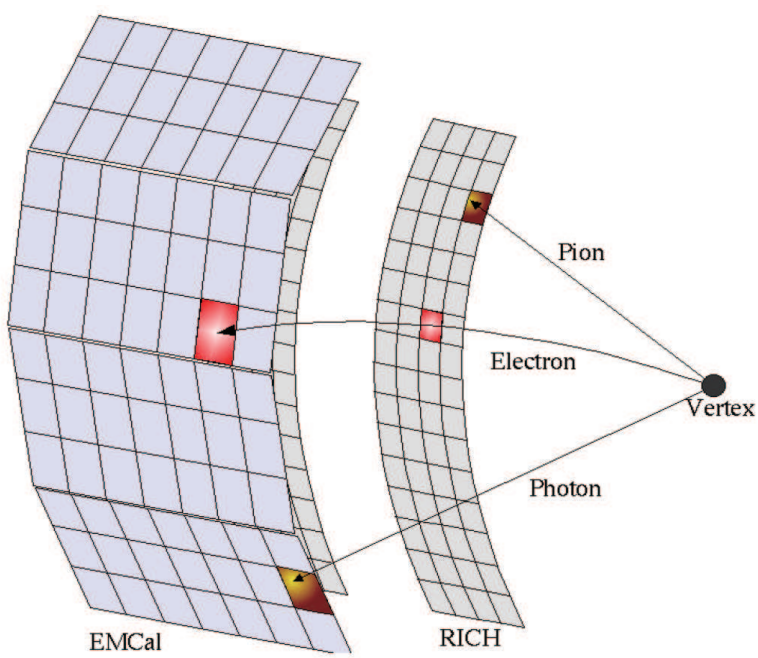

Figure 3.17: The principal scheme of the ERTLL1_E trigger.

of the EMCal and RICH tiles is performed using the look-up table in the ERTLL1 module.

3.7 Data Acquisition System

The PHENIX data acquisition (DAQ) system processes the signals from detector subsystems, produces the trigger decision, and stores the triggered data [71]. The typical data logging rate of d+Au collisions in Run8 was 7 kHz. The schematic flow diagram of the data acquisition system is shown in Fig. 3.18.

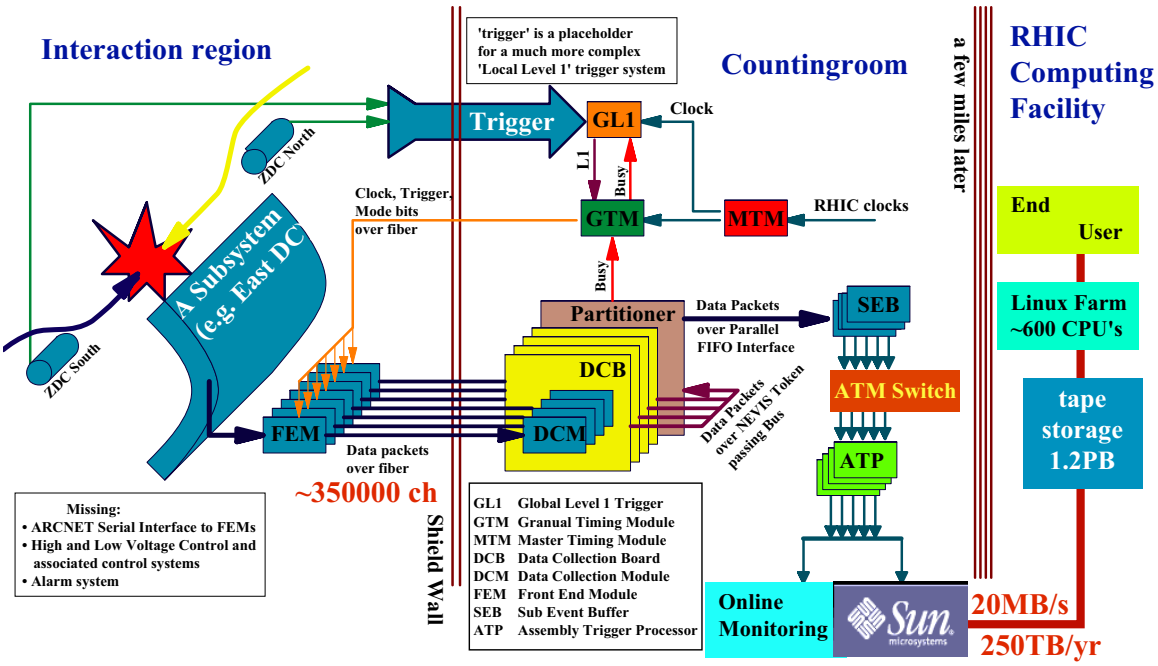

Figure 3.18: The schematic flow diagram of the data acquisition system.

Overall control of the DAQ is provided by the Master Timing Module (MTM), the Granule Timing Module (GTM) and the GL1. The MTM receives 9.4 MHz RHIC clock and delivers it to the GTM and GL1. The GTM delivers the clock, the control commands (Mode bits), an event accept signal to the Front End Module (FEM) of each detector. The GTM equips a fine delay tuning of the clock with ~ 50 ps step in order to compensate the timing difference among the FEMs. The GL1 produces the first LVL1 trigger decision combining LVL1 signals from detector components.

The FEM of each detector is designed to convert the analog response of the detector into the digitized signal. The LVL1 trigger signals are simultaneously generated. The generation of the global decision, whether an event should be taken or not, takes ~ 30 bunch crossings. While the GL1 system is making a decision, the event data are stored in the FEM. After receiving the accept signal, each FEM starts to digitize the data.

The data collection from each FEM is performed by a Data Collection Module

(DCM) via an optical fiber cable. The DCMs provide data buffering, zero suppression, error checking and data formatting. The DCMs send the compressed data to the Event Builder (EvB).

The EvB is the system which consists of 39 Sub Event Buffers (SEBs), an Asynchronous Transfer Mode (ATM) switch and 52 Assembly Trigger Processors (ATPs). The SEBs are the front end of the EvB and communicate with each granule and transfer the data from granules to the ATP via the ATM, where event assembly is performed. The combined data is stored to the disk with the maximum logging rate of 400 Mbytes/s and is used for online monitoring.

Chapter 4

Experiment

This analysis is based on the data collected in d+Au collisions at $\sqrt{s_{NN}} = 200$ GeV with the PHENIX experiment during Year-2008 RHIC Run (Run8). The run condition in Run8 is reviewed in this chapter.

4.1 RHIC Run Overview

The RHIC has accelerated and provided collisions with different species at various collision energies before Run8 as summarized in Table 4.1. The PHENIX experiment

Table 4.1: The recorded data summary at the PHENIX experiment before Run8.

	Year	Species	$\sqrt{s_{NN}}$ (GeV)	$\int Ldt$
Run1	2000	Au+Au	130	1 μb^{-1}
Run2	2001-2	Au+Au	200	24 μb^{-1}
		p+p	200	0.15 pb^{-1}
Run3	2002-3	d+Au	200	2.74 nb^{-1}
		p+p	200	0.35 pb^{-1}
Run4	2003-4	Au+Au	200	241 μb^{-1}
		Au+Au	62.4	9 μb^{-1}
Run5	2004-5	Cu+Cu	200	3 nb^{-1}
		Cu+Cu	62.4	0.19 pb^{-1}
		Cu+Cu	22.5	2.7 μb^{-1}
		p+p	200	3.8 pb^{-1}
Run6	2006	p+p	200	10.7 pb^{-1}
		p+p	62.4	0.1 pb^{-1}
Run7	2007	Au+Au	200	813 μb^{-1}
Run8	2008	d+Au	200	80 nb^{-1}
		p+p	200	5.2 pb^{-1}

has achieved to accumulate 30 times more d+Au data in Run8 than in Run3.

4.2 d+Au Collisions at $\sqrt{s_{NN}} = 200$ GeV in 2008

During the d+Au run period in the RHIC Run8, the data in d+Au collisions at $\sqrt{s_{NN}} = 200$ GeV were collected by the PHENIX detector. The peak luminosity per one day was 3.2 nb^{-1}, which is more than the integrated luminosity recorded during Run3. The integrated luminosity in Run8 as a function of date is shown in Fig. 4.1 and the recorded integrated luminosity is 80 nb^{-1}.

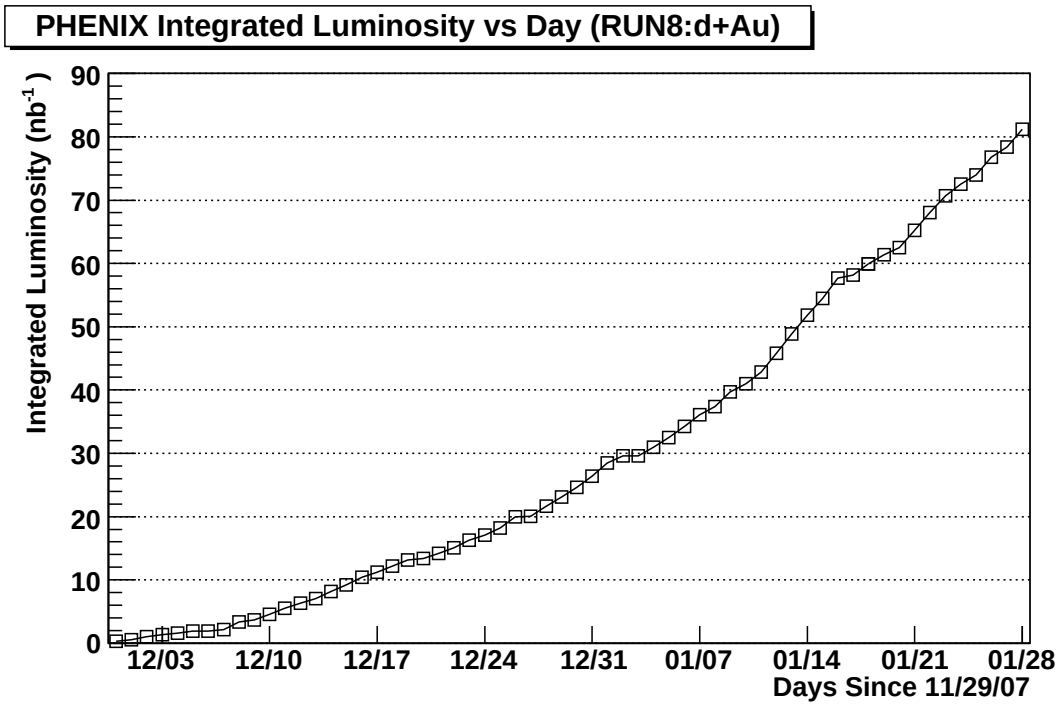

Figure 4.1: The integrated luminosity of d+Au collisions in Run8 recorded at the PHENIX experiment as a function of date.

The data were taken with the Minimum Bias (MB) and ERT electron (ERT_E) triggers and the trigger logics for these triggers are defined as:

$$\text{Minimum Bias} \equiv \text{BBCLL1}(> 0\text{tubes}), \tag{4.1}$$

$$\text{ERT electron} \equiv \text{ERTLL1_E} \cap \text{BBCLL1}(> 0\text{tubes}), \tag{4.2}$$

where BBCLL1($>$ 0tubes) means that at least one hit is required in both BBCs and the vertex position obtained by BBCLL1 online in z direction, z_{BBCLL1}, required to be less than 38 cm. ERTLL1_E denotes the coincidence of a hit of the EMCal

with an energy deposit above the ERTLL1_2x2 threshold and a RICH hit of ≥ 3 photoelectrons.

In Table 4.2, the run numbers, magnet polarity and the ERTLL1_2x2 energy threshold for each run group in Run8 are summarized.

Table 4.2: The configurations in the Run8 d+Au 200 GeV period.

Run Group	Run Number	Magnet Polarity	ERTLL1_2x2 energy threshold
G1	246444-250484	CM++	600MeV
G2	250515-253701	CM– –	800MeV

Chapter 5

Data Analysis

The invariant yield of direct photon in d+Au collisions at $\sqrt{s_{NN}} = 200$ GeV has been measured from the direct virtual photon fractions obtained from invariant e^+e^- mass spectra. In this chapter, the analysis procedure to determine the invariant yield of direct photon is described.

5.1 Invariant Yield

The e^+e^- pair yield in the PHENIX central arm ($|y| < 0.35$) is calculated as:

$$\frac{dN}{dm_{ee}} = \frac{1}{N_{evt}^{MB}} \cdot \frac{N_{ee}}{\Delta m_{ee}} \cdot \frac{C_{bias}^{BBC}}{\varepsilon_{MB}} \cdot \frac{1}{\varepsilon_{all}(p_T)}, \tag{5.1}$$

where,

- N_{evt}^{MB} : The number of minimum bias (MB) triggered events. For the ERT triggered data, the equivalent number of sampled MB triggered events in the ERT triggered data, N_{evt}^{equiv} is used instead of N_{evt}^{MB}.
  - N_{evt}^{equiv} is calculated as:
  $N_{evt}^{equiv} = scale_down_factor \times N_{evt}^{MB}$,
  where $scale_down_factor$ is the fraction of recorded MB events in the ERT triggered events for each run.

- Δm_{ee} : The m_{ee} bin width.

- $\varepsilon_{MB}, C_{bias}^{BBC}$: The MB trigger efficiency and trigger bias factor. A detailed explanation for $\varepsilon_{MB}, C_{bias}^{BBC}$ is given in Sections 5.2.1, 5.2.3.

- $\varepsilon_{all}(p_T)$: The overall efficiency including acceptance, pair cuts, reconstruction and electron identification efficiencies for e^+e^- pairs. The ERT trigger efficiency is also included for the ERT triggered data.

The enhanced yield over the expected hadron decay contribution in the invariant e^+e^- mass spectrum is interpreted as the direct virtual photon decay contribution. The direct virtual photon fraction in the inclusive photon yield is determined from invariant e^+e^- mass spectrum, and a detailed explanation is given in Section 5.11. Finally, the invariant yield of the direct photon is determined from the direct virtual photon fraction as:

$$E\frac{d^3N}{dp^3} = r_{\gamma^*} \times \frac{1}{2\pi p_T}\frac{d^2N_\gamma^{incl}}{dp_T dy}, \tag{5.2}$$

where r_{γ^*} is the direct virtual photon fraction and $\frac{1}{2\pi p_T}\frac{d^2N_\gamma^{incl}}{dp_T dy}$ is the inclusive photon yield in d+Au collisions.

5.2 Event Classification

In this section, the event classification method in the PHENIX experiment is described. The Glauber model is used to calculate parameters characterize each collision such as the impact parameter of the two colliding nuclei and the number of binary nucleon-nucleon collisions. Determination of the MB trigger efficiency for d+Au collisions is also described in this section.

5.2.1 Determination of Minimum Bias Trigger Efficiency

The efficiency of inelastic d+Au collisions by the MB trigger, ε_{MB}, is evaluated with a Glauber simulation of the number of binary collisions (N_{coll}) and a negative binomial distribution (NBD) modeling of the real BBC charge distribution in the South arm, *i.e.* the gold going direction. The MB efficiency determination is done under the assumption that the BBC charge distribution in the South arm is proportional to the number of binary collisions in each d+Au reaction. The MB trigger efficiency for d+Au collisions is evaluated to be $\varepsilon_{MB} = 88 \pm 2$ (syst) %.

5.2.2 Centrality Determination

The collision centrality of each event in d+Au collisions is also determined by the measured BBC charge distribution in the South arm. The centrality is classified into 4 different classes: 0-20%, 20-40%, 40-60%, and 60-88%. The BBC South charge distribution in the Glauber simulation for each centrality class is compared to the real one, and then the BBC South charge region corresponding to each centrality class is determined as shown in Fig. 5.1. The open symbols show the real data and the color filled histograms show the results from the Glauber simulation.

The number of binary collisions is also determined from the Glauber simulation together with the centrality classification. The Glauber simulation is based on a purely geometric picture of a heavy ion reaction with the following assumptions:

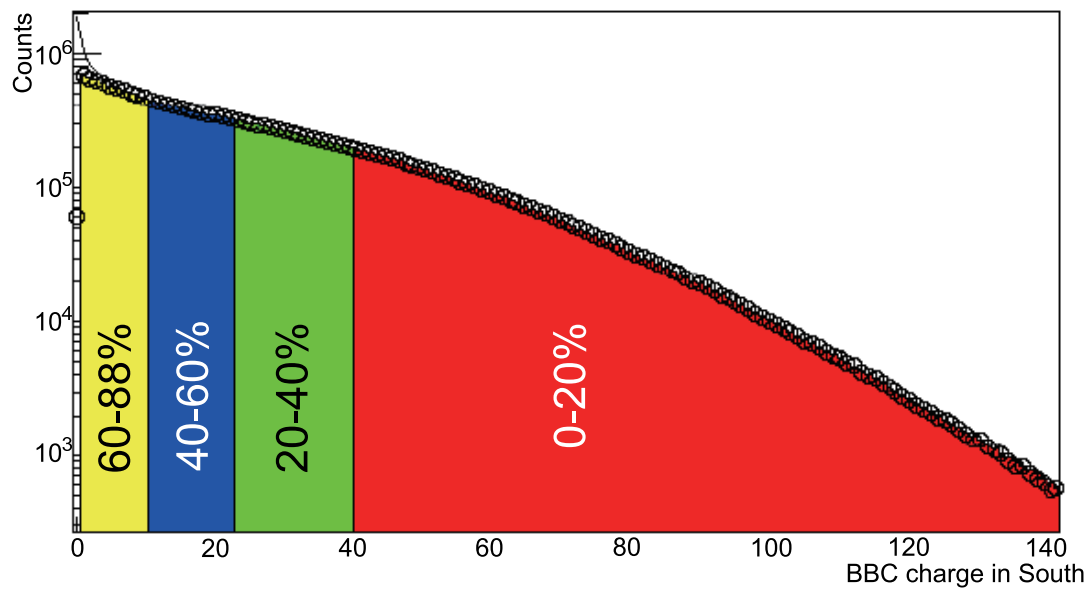

Figure 5.1: The BBC South charge distribution in the real data showing the charge region corresponding to each centrality class. The open symbols show the real data and the color filled histograms show the results from the Glauber simulation.

- A d+Au reaction is regarded as a superposition of $p+p$ collisions.
- A collision between two nucleons takes place if a distance in the transverse plane between them is smaller than $\sqrt{\sigma_{NN}/\pi}$, where $\sigma_{NN} = 42$ mb is the inelastic nucleon-nucleon collision cross section at $\sqrt{s_{NN}} = 200$ GeV.

The number of binary collisions for each centrality class in d+Au collisions are summarized in Table 5.1 together with the trigger bias factors (C_{bias}^{BBC}), which are explained below.

Table 5.1: The mean number of binary collisions in d+Au collisions and the trigger bias factor for each centrality class.

centrality	$\langle N_{coll} \rangle$	Trigger bias factor (C_{bias}^{BBC})
0-20%	15.1 ± 1.0	0.941 ± 0.010
20-40%	10.2 ± 0.7	1.000 ± 0.006
40-60%	6.58 ± 0.4	1.034 ± 0.017
60-88%	3.20 ± 0.2	1.031 ± 0.055
0-88%	8.42 ± 0.4	0.889 ± 0.001

5.2.3 BBC Trigger Bias

Some events have a large multiplicity due to high p_T hadrons from a hard parton scattering and consequently a large signal appears in the BBC South. Such events would be considered as more central events than ones without a hard scattering, even if the actual number of collisions is exactly the same between these events. The correction factor for the bias due to the measured BBC South charge is evaluated using the consistent framework for the centrality determination and it is denoted as the 'trigger bias factor' (C_{bias}^{BBC}).

5.3 Track Reconstruction and Momentum Determination

The track reconstruction technique in the PHENIX central arm is described in Ref.[72], and a brief description on it is given in this section.

The left and right panels in Fig. 5.2 show schematic views of a trajectory of a charged particle pass through the axial magnetic field in the x-y and z-r planes at the track reconstruction in the DC. The measured variables to determine the trajectory

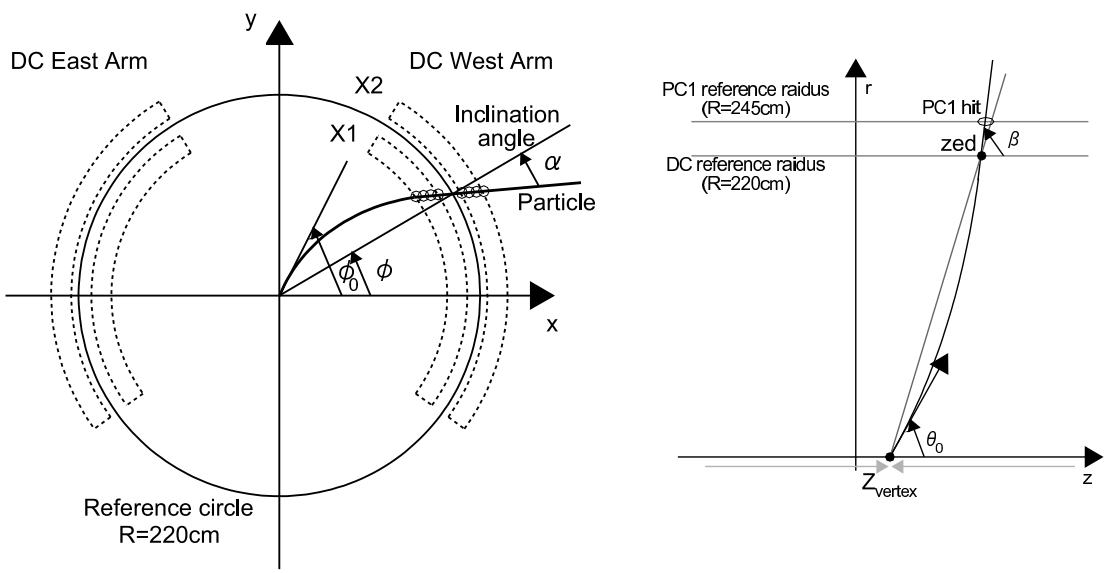

Figure 5.2: Schematic views of a trajectory of a charged particle in the x-y (left) and z-r (right) planes at the track reconstruction in the DC. The Hough transform parameters, ϕ_0, ϕ, α are illustrated.

and momentum are as follows:

- α : The angle between the projection of the trajectory in the x-y plane and the radial direction at the DC reference radius of 220 cm.
- ϕ : The azimuthal angle of the intersection point at the DC reference radius of 220 cm.
- β : The polar angle of the intersection point at the DC reference radius of 220 cm.
- zed : The z coordinate of the intersection point at the DC reference radius of 220 cm.
- p_T : The reconstructed transverse momentum.
- θ_0 : The reconstructed polar angle of the initial direction.
- ϕ_0 : The reconstructed azimuthal angle of the initial direction.

5.3.1 Track Reconstruction Technique

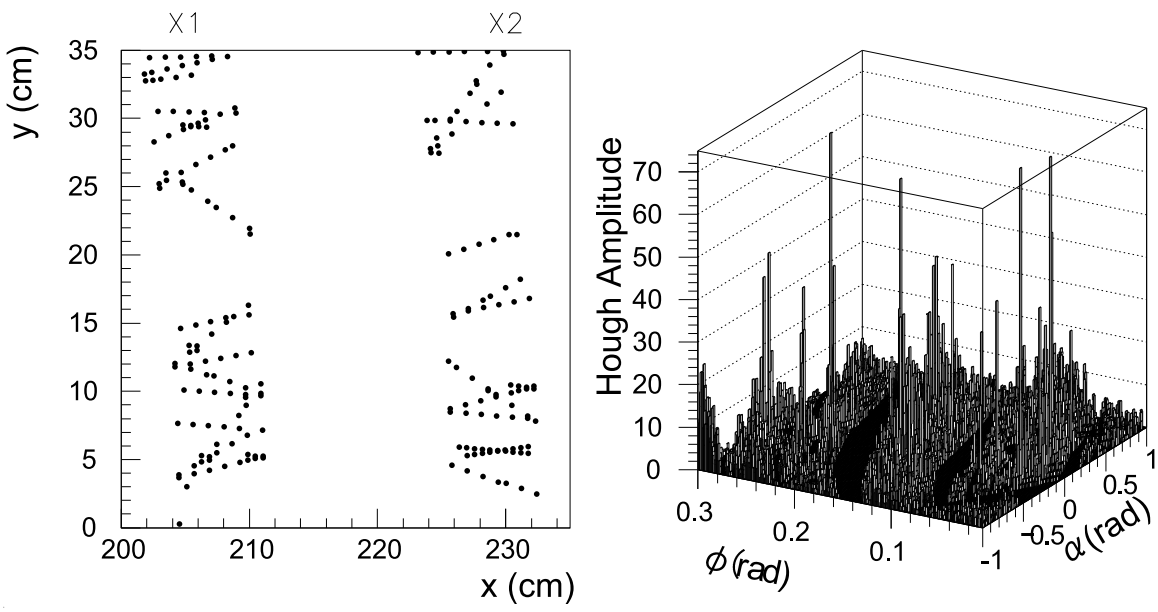

Figure 5.3: The Hough transformation of the DC hits in the x-y plane to the feature space of α and ϕ. The left panel shows simulated hits for a small physical region of the DC, and the right panel shows the Hough transform feature space for this region. Tracks appear as peaks in this plot.

The trajectory of a particle is uniquely determined by the four variables, p_T, θ_0, ϕ_0 and z_{vertex}. They are reconstructed from the measured variables, α, ϕ, zed and z_{vertex}.

The track reconstruction starts from finding hits in X1 and X2 wires of the DC in the x-y plane. The angles of α and ϕ are determined from the X1 and/or X2 hit positions by the Hough transformation with an assumption that tracks are straight in the DC. The Hough transformation is a general algorithm for finding straight lines. Figure 5.3 shows an example of the Hough transformation in a part of the DC hits and the amplitude in the feature space. The following procedures are performed for the track reconstruction.

1. Find hits in the X1 and X2 wires and project them onto the x-y plane.
2. Determine α and ϕ for possible combinations with X1 and X2 hits by the Hough transformation.
3. Reconstruct the tracks in the z-r plane by associating with the information of PC1 hits, UV-wire hits and collision vertex (z_{vertex}) measured by the BBC.
4. If there is an unambiguous associated PC1 hit within 2 cm in the x-y plane, the track vector in the z-r plane is fixed using the z position of the PC1 hit and z_{vertex}.
5. If UV hits are within 5 cm from the track in the z-r plane, these UV hits are associated with the track.

Then, each reconstructed track is associated with the hit information of outer detectors (PC2, PC3, EMCal and RICH). At the association with the outer detectors, the residual magnetic field is not taken into account and the track is assumed to be a straight line.

Track Quality

A quality of a reconstructed charged track is defined using the hit information of X and UV wires in the DC and the associated PC1 hit. The track quality is implemented in the data as the 6-bit variable, quality, for each track. Table 5.2 is the bit definition of quality. The best case is quality = 63 and the second best case is quality = 31, wherein the PC1 hit is ambiguous, but the UV hit is unique.

5.3.2 Momentum Determination

An accurate analytical expression for a momentum of a charged particle is difficult due to a small non-uniformity of the focusing magnetic field along a flight path of the charged particle. Thus, the non-linear grid interpolation technique [73] is used to determine the initial kinematic parameters of charged particles traveling the magnetic field,

A four-dimensional field integral grid is constructed within the entire radial extent of the central arm for the momentum determination based on the DC hits. The

Table 5.2: The bit definition of quality.

	bit	decimal	description
LSB	0	1	X1 hit is used
	1	2	X2 hit is used
	2	4	UV hit is found
	3	8	UV hit is unique (No hit sharing)
	4	16	PC1 hit is found
MSB	5	32	PC1 hit is unique (No hit sharing)

variables in the field integral grid are z_{vertex}, θ_0, the total momentum p and the radius r at which the field integral $f(p, r, \theta_0, z_{vertex})$ is calculated. The field integral grid is generated by explicitly swimming particles through the measured magnetic field map and numerically integrating to obtain $f(p, r, \theta_0, z_{vertex})$ for each grid point.

The transverse momentum p_T (GeV/c) and the angle α (rad) have the following relation:

$$p_T \simeq \frac{K}{\alpha}, \tag{5.3}$$

where $K \simeq 0.10$ GeV/c is the effective field integral in the central arm expressed as:

$$K = \frac{e}{R} \int lBdl, \tag{5.4}$$

where e is the elementary charge in the hybrid unit ($e = 0.2998$ GeV/c T^{-1} m^{-1}) and R is the DC reference radius (=220 cm). An iterative procedure is used to determine the initial kinematic parameters of the reconstructed tracks with the initial assumption of Eq. 5.3. The momentum resolution depends on (1) the intrinsic angular resolution of the DC and (2) the multiple scattering of a charged particle as it travels to the DC due to the intervening material. As a result, the momentum resolution is about 1% for tracks with $p_T = 1$ GeV/c and the reconstruction efficiency is above 99% for a single track.

5.3.3 Analysis Variable

The information of the reconstructed track and the associated hits of the detectors are recorded in the nano Data Summary Tape (nDST). Parameters which characterize events such as the collision vertex and centrality, are also recorded in the nDST. In this thesis, the variables in the nDST are written in sans serif font. The 3-momentum of a track is calculated from the total momentum mom, the initial polar angle the0

and the initial azimuthal angle phi0:

$$p_z = \mathsf{mom} \cdot \cos(\mathsf{the0}), \tag{5.5}$$
$$p_T = \mathsf{mom} \cdot \sin(\mathsf{the0}), \tag{5.6}$$
$$p_x = p_T \cdot \cos(\mathsf{phi0}), \tag{5.7}$$
$$p_y = p_T \cdot \sin(\mathsf{phi0}). \tag{5.8}$$

The global and track variables used in this thesis are summarized in Table 5.3.

Table 5.3: Summary of the global and track variables used in this thesis.

Variables	Descriptions
bbcz	z position of the collision vertex measured by the BBC.
mom	Total momentum of a track.
the0	Initial ϕ angle of a track at the vertex.
phi0	Initial θ angle of a track at the vertex.
dcphi	ϕ coordinate at which the track crosses the DC reference radius.
zed	z coordinate at which the track crosses the DC reference radius.
quality	Quality of the DC tracks.
ppc1phi	ϕ coordinate of a reconstructed track projection point in the PC1.
ppc1z	z coordinate of a reconstructed track projection point in the PC1.
pemcphi	ϕ coordinate of a reconstructed track projection point on the EMCal surface.
pemcz	z coordinate of a reconstructed track projection point on the EMCal surface.

5.4 RICH Calibration

RICH plays the main role for electron identification. Gain calibration for RICH phototubes and alignment calibration for RICH mirrors are very important for the electron related analyses. The ways for these calibrations are described in this section.

5.4.1 Charge Calibration

Gain calibration was performed for each phototube by fitting the raw ADC spectrum. A Gaussian function was fitted to the pedestal and one photo-electron peaks separately and, the ADC values of those peak positions ($ADC_{pedestal}$ and $ADC_{1p.e.}$) were obtained. Then, the number of photo-electrons ($N_{p.e.}$) of a phototube was calculated from its ADC value (ADC) as follows:

$$N_{p.e.} = \frac{ADC - ADC_{pedestal}}{ADC_{1p.e.} - ADC_{pedestal}}. \tag{5.9}$$

Figure 5.4 shows the number of photo-electron distribution after the gain calibration.

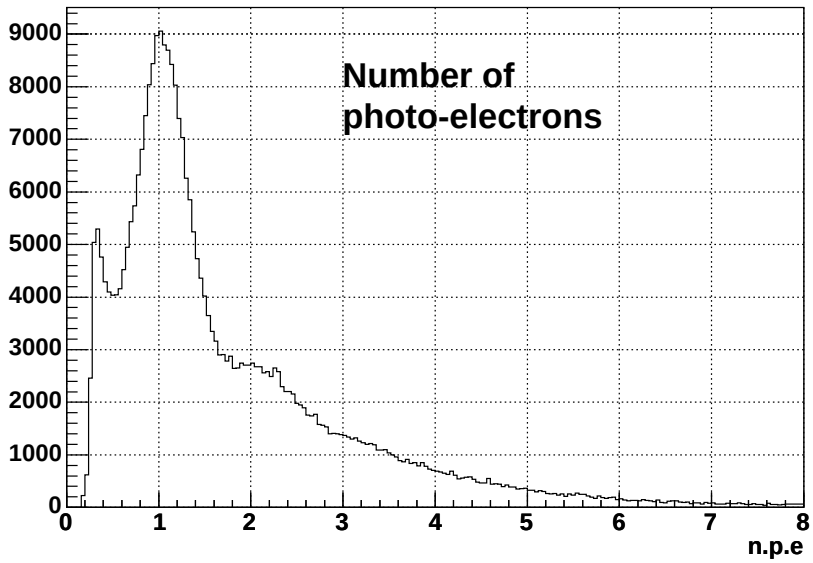

Figure 5.4: The number of photo-electron distribution after the gain calibration.

5.4.2 Mirror Alignment Calibration

The spherical mirrors reflect Cherenkov photons to the phototube planes as shown in Fig. 3.14. 24 mirrors are located in each arm and side, and in total $24 \times 2 \times 2 = 96$ mirrors are used. Alignment calibration was done offline by adjusting the position of each mirror in z and ϕ directions. Electron candidates are selected with the following requirements:

- $0.5 < \mathsf{mom} < 5.0$ GeV/c,
- $0.7 < \mathsf{ecore}/\mathsf{mom} < 1.3$,
- $\mathsf{ecore} > 0.75$ GeV,
- $\mathsf{quality} > 10$,

where descriptions for the above variables are found in Tables 5.3, 5.4.

The straight line between the associated cluster positions of PC1 and PC2(PC3) is used as a charged particle trajectory for the west (east) arm. The trajectory is reflected to the RICH mirror surface and then projected to the RICH phototube plane. Figure 5.5 shows an example of the track association to the RICH phototube

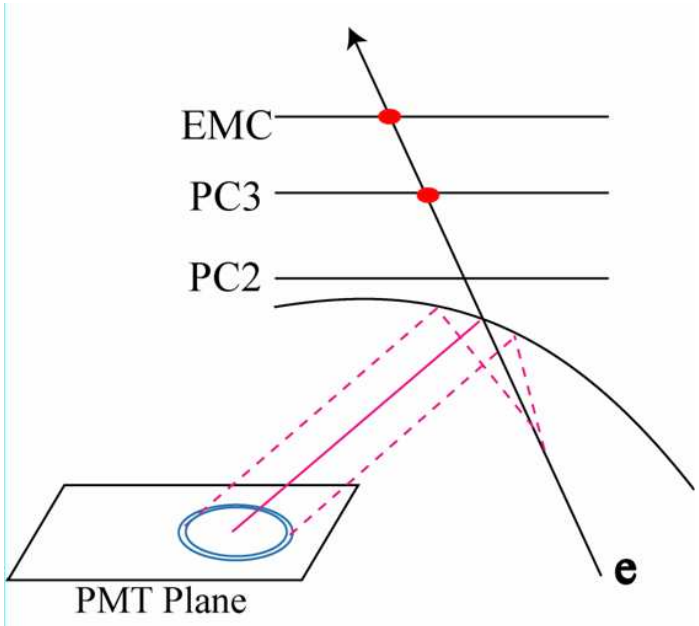

Figure 5.5: Example of the track association to the RICH phototube plane.

plane. The projection point at the RICH phototube plane should be located at the ring center. Since the displacement of a mirror position leads to the displacement of the projection point of a particle passing through the mirror, the mirror position in z and ϕ directions were adjusted so that the projection point matches the ring center obtained from the positions of fired phototubes. Figure 5.6 shows the accumulated RICH ring image after the alignment calibration. Figure 5.7 shows the obtained ring radius distribution after the alignment calibration. The black line shows the raw ring radius distribution and the shade portion represents the ring radius distribution for the net electron candidates obtained by subtracting accidental associations from raw distribution (details of the accidental associations is described presently). The obtained ring radius distribution has a peak at the ideal ring radius (= 5.9 cm) indicated as the red dotted line.

Accidental Association with RICH

The z-swapped point $R_0^{z-swap} = (x_0, y_0, -z_0)$ is defined by flipping the track projection point $R_0 = (x_0, y_0, z_0)$ in the z direction in order to estimate the background due to the accidental association of charged hadron tracks to the fired phototubes. Then, an inquiry to the associated fired phototubes around the z-swapped point R_0^{z-swap} is made. The net electron candidates without accidental associations are obtained by subtracting electron candidates with the z-swapped variables from those with the normal (non-swapped) variables.

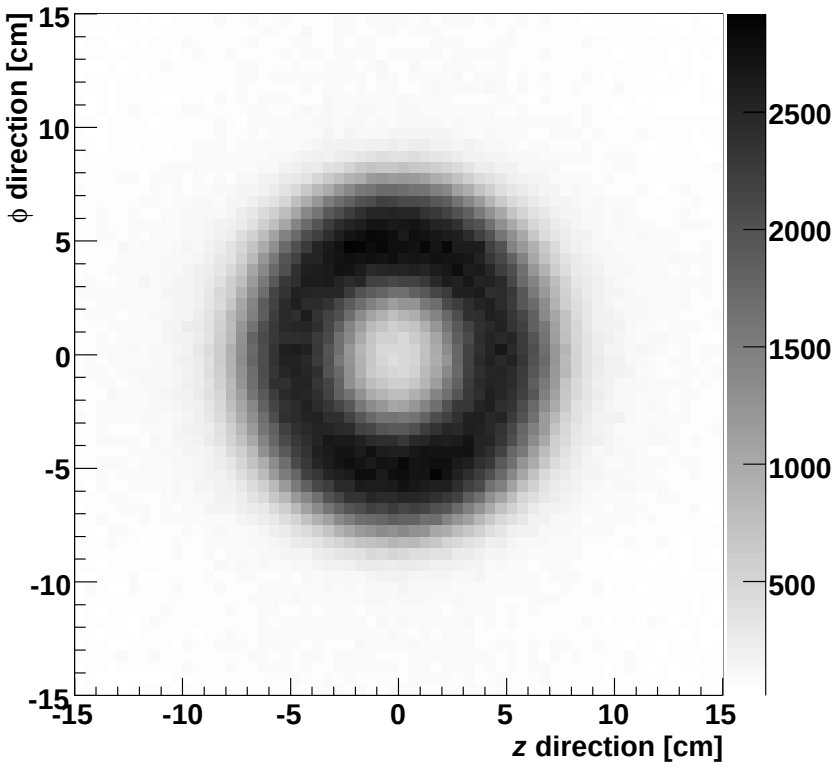

Figure 5.6: The accumulated RICH ring image after the alignment calibration.

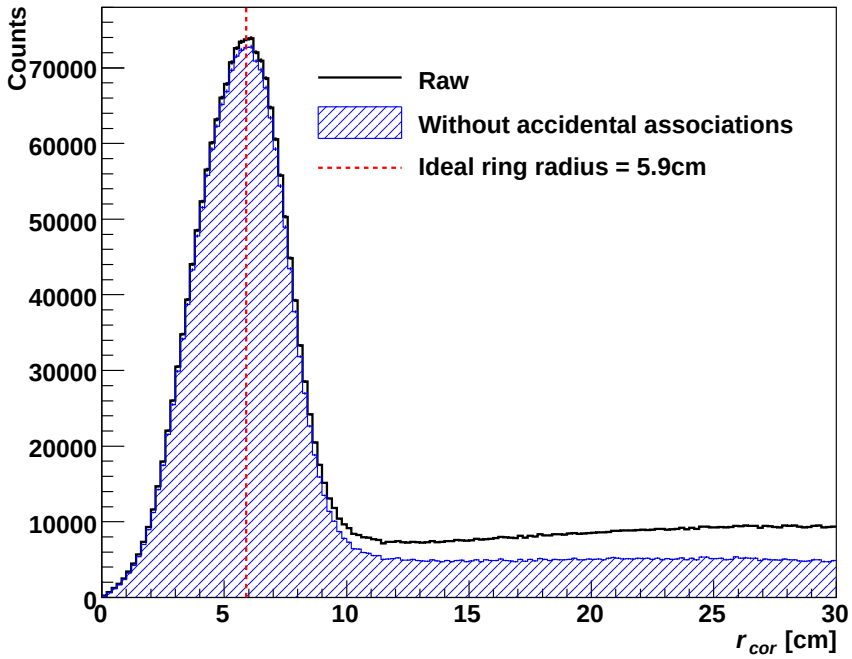

Figure 5.7: The obtained ring radius distribution after the alignment calibration and the shade portion represents the ring radius distribution for the net electron candidates. The ideal ring radius (= 5.9 cm) is indicated as the red dotted line.

5.5 Electron Identification

Identification of electron tracks is performed by RICH and EMCal, and the method of electron identification is described in this section. The variables used for electron identification are listed in Table. 5.4 with descriptions of their specifications.

Table 5.4: Summary of the variables for electron identification.

Variables	Descriptions
RICH	
n0	The number of fired phototubes in the nominal ring area ($3.4 \leq r \leq 8.4$ cm)
n1	The number of fired phototubes in the larger disk ($r \leq 11.0$ cm)
npe0	The number of photo-electrons detected in the nominal ring area
npe1	The number of photo-electrons detected in the larger disk
disp	Displacement between the track projection point on the RICH phototube plane and the point reconstructed from the associated fired phototubes
chi2	Ring shape parameter
EMCal	
ecore	The EMCal shower core energy (GeV)
emcsdphi_e	The difference between the track projection and the EMCal cluster position in the ϕ direction at the EMCal surface normalized to σ
emcsdz_e	The difference between the track projection and the EMCal cluster position in the z direction at the EMCal surface normalized to σ

5.5.1 Electron Identification with RICH

After track reconstruction by the DC and PC1 (DC-PC1 track), tracks are associated with the PC2, PC3 and EMCal. Track association with RICH is performed using the hit information of PC1 and PC2 (PC1-PC2 track) in the west arm and PC1 and PC3 (PC1-PC3 track) in the east arm. If there is not any associated hit in PC2 and PC3, the hit position of the outer detectors (PC3/EMCal for the west arm and EMCal for the east arm), or projection points of the DC-PC1 track are used for track association with RICH. The tracks are reflected with respect to the RICH mirrors and the reflected tracks are projected onto onto the RICH phototube plane. Then, fired phototubes around the projection points of the reflected tracks are associated with the tracks. Figure 5.8 shows a schematic view of the definition of variables used for determination of the RICH variables. The variable r^i_{cor} is the distance between the center of the phototube i and the track projection vector.

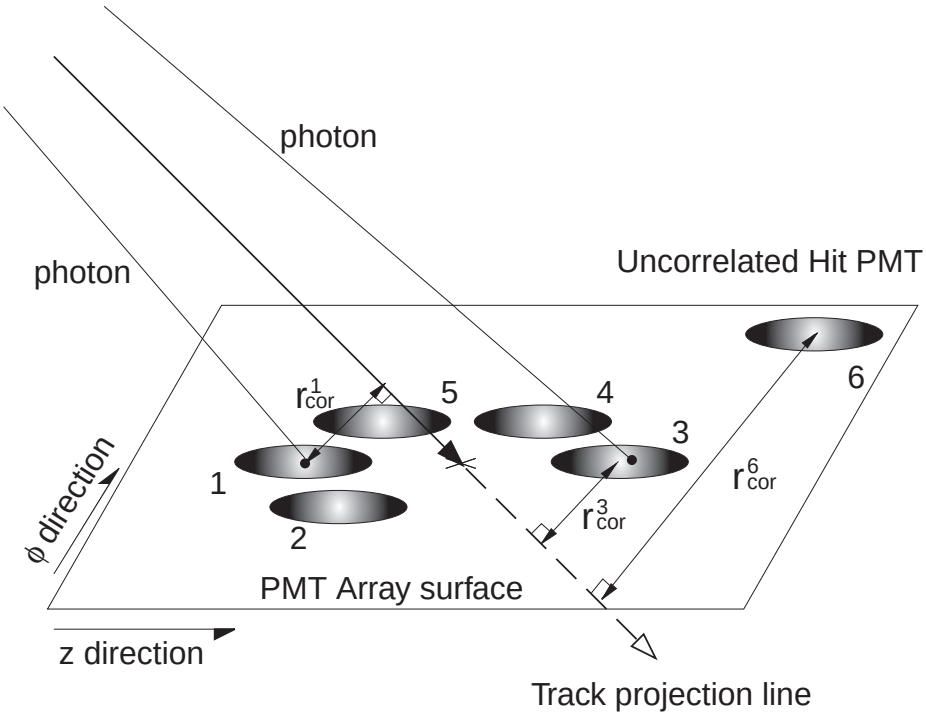

Figure 5.8: A schematic view of the definition of variables used for determination of the RICH variables. A track projection, five associated fired phototubes and one uncorrelated fired phototube are shown as an example. The distance between the center of the fired phototubes 1, 3, 6 and the track projection vector are represented as r^1_{cor}, r^3_{cor} and r^6_{cor}, respectively.

Ring Association: n0, n1, npe0, npe1, disp

The RICH variables n0 and n1 are defined as:

$$\mathsf{n0} \equiv \text{the number of fired phototubes in } 3.4 \leq r^i_{cor} \leq 8.4 \text{ cm}, \tag{5.10}$$

$$\mathsf{n1} \equiv \text{the number of fired phototubes in } r^i_{cor} \leq 11.0 \text{ cm}, \tag{5.11}$$

where the fired phototube is defined to have greater than 0.2 photo-electrons. The variables npe0 and npe1 are the summation of the number of photo-electrons, $N_{p.e.}(i)$, of the fired phototubes in $3.4 \leq r^i_{cor} \leq 8.4$ cm and $r^i_{cor} \leq 11.0$ cm, respectively.

$$\mathsf{npe0} \equiv \sum_{3.4 \leq r^i_{cor} \leq 8.4 \text{ cm}} N_{p.e.}(i), \tag{5.12}$$

$$\mathsf{npe1} \equiv \sum_{r^i_{cor} \leq 11.0 \text{ cm}} N_{p.e.}(i), \tag{5.13}$$

The position of the ring center, R_{center}, is calculated from the weighted average of the positions of fired phototubes, R_i, by $N_{p.e.}(i)$,

$$R_{center} \equiv \frac{\sum_{3.4 < r^i_{cor} < 8.4 \text{ cm}} N_{p.e.}(i) \cdot R_i}{\mathsf{npe0}}. \tag{5.14}$$

The distance between R_{center} and the track projection line is defined as disp.

Ring Shape: chi2/npe0

The variable chi2/npe0, which means the observed ring shape, is the weighted average of the deviation of the fired phototube from the ideal ring radius, $r_0 = 5.9$ cm. The weight is the number of photo-electrons in each phototube,

$$\mathsf{chi2/npe0} \equiv \frac{\sum_{r^i_{cor} < 11.0 \text{ cm}} N_{p.e.}(i) \cdot (r^i_{cor} - r_0)^2}{\mathsf{npe0}}. \tag{5.15}$$

5.5.2 Electron Identification with EMCal

The EMCal measures the energy and hit positions of charged particles and photons. The EMCal has eight sectors, W0-W3 (from bottom to top in the west arm) and E0-E3 (from bottom to top in the east arm). The sector E0 and E1 are PbGl and the others are PbSc. The energy calibration of each EMCal tower was performed using the π^0 peak mass reconstructed from two photons.

Hit Position Association: emcsdz_e, emcsdphi_e

Distances between the projection point of a reconstructed track on the EMCal surface (pemcz, pemcphi) and the hit position (the center of the electromagnetic shower:

emcz, emcphi) are expressed by emcdz and emcdphi in the z and ϕ directions, respectively.

$$\mathsf{emcdz} = \mathsf{emcz} - \mathsf{pemcz} \tag{5.16}$$

$$\mathsf{emcdphi} = \mathsf{emcphi} - \mathsf{pemcphi} \tag{5.17}$$

The variables emcdz, emcdphi depend on the total momentum, the momentum direction, the electric charge of electrons/positrons and the sector and position of the EMCal by the residual field. Since they have typical momentum dependent widths ($\sigma_{\mathsf{emcdz}}(p), \sigma_{\mathsf{emcdphi}}(p)$), they are normalized to the standard normal distribution with a mean of 0 and a σ of 1 for convenience of the analysis. The normalized variables emcsdz_e, emcsdphi_e are written as:

$$\mathsf{emcsdz_e} = \frac{\mathsf{emcdz} - \langle \mathsf{emcdz} \rangle}{\sigma_{\mathsf{emcdz(p)}}} \tag{5.18}$$

$$\mathsf{emcsdphi_e} = \frac{\mathsf{emcdphi} - \langle \mathsf{emcdphi} \rangle}{\sigma_{\mathsf{emcdphi(p)}}} \tag{5.19}$$

Energy-Momentum Matching: ecore/mom

In the case of electron tracks, the ratio of the energy measured by the EMCal (ecore) to the total momentum measured by the DC (mom) is about 1 since the electron mass is negligible compared to the total momentum in high energy heavy ion collisions and, the electron deposits all of its energy in the EMCal. Thus, ecore/mom can improve the electron identification capability in the analysis.

5.5.3 Cuts for Electron Identification

Tracks which pass through the following cuts are identified as electron track candidates:

- |bbcz| <20 cm
- n0 $\geq$1
- disp $\leq$10 cm
- chi2/npe0 $\leq$15 cm^2
- 0.5$\leq$ ecore/mom $\leq$2.0
- $\sqrt{\mathsf{emcsdz_e}^2 + \mathsf{emcsdphi_e}^2} \leq 4$
- quality $\geq$15
- $p_T \geq 0.3$ GeV/c

The above cuts are called 'standard eID cuts' in this thesis.

5.5.4 Check of Detector Response

A precise simulation which can well-reproduce the responses of the detectors used for the electron identification is needed for correction factor determination. Thus, it is very important to evaluate how well simulated distributions of the variables used in the standard eID cuts can reproduce those in real case.

PISA Simulation

The GEANT3 based simulation for the PHENIX detector [74] is called the 'PISA' simulation. Detector responses for single electrons and positrons are studied using the PISA simulation. In real events, more than 90% of e^+e^- pairs in $m_{ee} \leq 30$ MeV/c^2 come from π^0, η Dalitz decays. Thus, the electrons and positrons which make a pair in $m_{ee} \leq 30$ MeV/c^2 are suitable for checking the detector responses. Electrons and positrons from π^0, η Dalitz decays are generated using a fast Monte Carlo simulation, and they are put through the PISA simulation. The input kinematic conditions for π^0, η are as follows:

- z-vertex : $|z\text{-vertex}| < 30$ cm
- Rapidity : $|y| < 0.5$ (flat)
- Azimuthal angle : $0 \leq \phi < 2\pi$ (flat)
- Transverse momentum : $0 < p_T < 10$ GeV/c (flat)

The simulated distributions of the variables which characterize detector responses are weighted according to the input p_T of π^0 and η so that the input p_T distributions for π^0 and η are in agreement with the real p_T distributions which already measured at the PHENIX experiment. The p_T distributions for measured hadron at the PHENIX are described in Section 5.10.

Comparison between Real and Simulation

Electrons and positrons in $0.3 \leq p_T < 4.0$ GeV/c which pass through the standard eID cuts and make a pair in $m_{ee} \leq 30$ MeV/c^2 are selected as samples. The normalization of the simulated results to the real ones is done by the e^+e^- pair yield in $m_{ee} \leq$ 30 MeV/c^2. The real and simulated results are shown by black circle and red square symbols in the following figures (Figs. 5.9, 5.10).

Figure 5.9 shows the real and simulated p_T distributions for single electrons from π^0 and η Dalitz decays. The simulated p_T distribution is in good agreement with the real one. Figure 5.10 shows the real and simulated distributions for the eID variables of n0, disp, chi2/npe0, ecore/mom, emcsdz_e, emcsdphi_e from top-left to bottom-right panels. The eID variables in simulation are well-tuned to match those in real case.

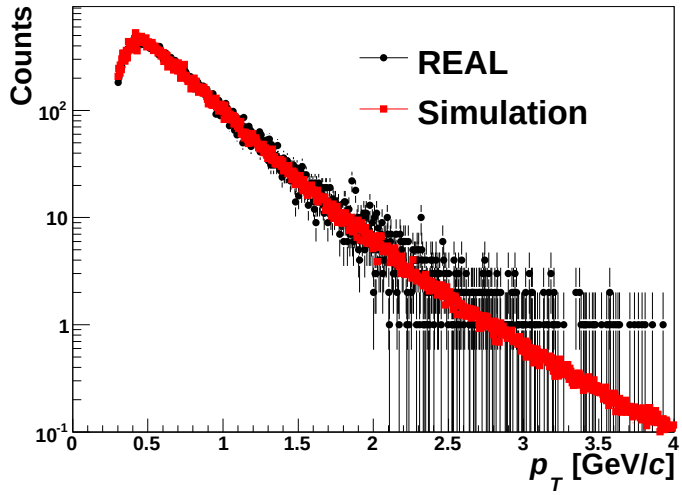

Figure 5.9: The single electron p_T distributions from the experiment (black circle) and from the simulation (red square) for check of the detector response. These electrons are ones which pass through the standard eID cuts and make a pair in $m_{ee} \leq 30$ MeV/c^2. Thus, most of them are identified as ones from π^0 and η Dalitz decays.

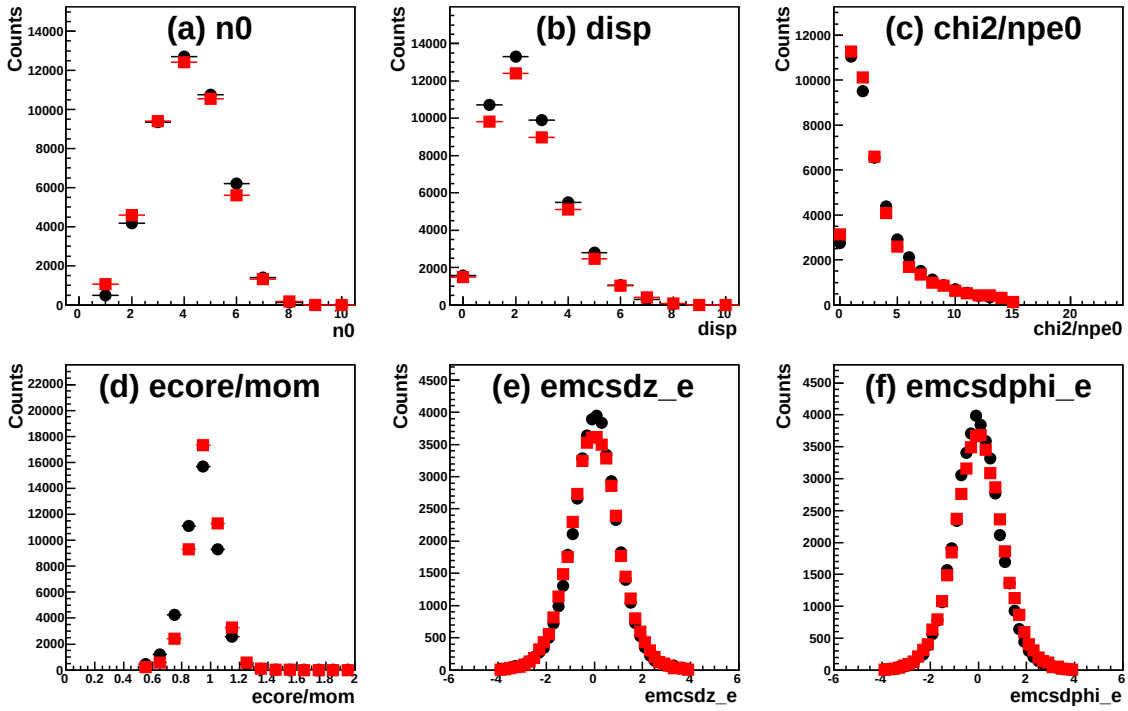

Figure 5.10: The real (black circle) and simulated (red square) distributions for the eID variables. (a) n0, (b) disp, (c) chi2/npe0, (d) ecore/mom, (e) emcsdz_e, (f) emcsdphi_e.

5.6 Acceptance Evaluation

The following hit maps were made to find dead and low efficiency areas in the DC, PC1 and EMCal; dead and low efficiency detector areas are removed from the analysis in order to treat active detector areas as fiducial volumes.

- Map of DC hits in the z-ϕ plane: zed-dcphi
- Map of track hit points projected to the PC1 plane in the z and ϕ directions: ppc1z-ppc1phi
- Map of track hit points projected to the EMCal surface in the z and ϕ directions: pemcz-pemcphi

The same fiducial cuts are applied to the real data and simulated data, and the simulated acceptance for each detector (DC, PC1 and EMCal) is checked if it well-reproduces the real one. A single electron simulation using the PISA simulation is carried out to check an acceptance reproducibility in the simulation. The input kinematic condition for single electrons is as follows:

- z-vertex : $|z\text{-vertex}| < 30$ cm
- Rapidity : $|y| < 0.5$ (flat)
- Azimuthal angle : $0 \leq \phi < 2\pi$ (flat)
- Transverse momentum : $0 < p_T < 10$ GeV/c (flat)

The simulated distributions of the variables related to the acceptance are weighted according to the input p_T of e^+, e^- so that the simulated p_T distribution matches to the real one. Electrons in $0.6 < p_T < 5.0$ GeV/c are selected as samples for the acceptance check.

Figures 5.11, 5.12, 5.13, 5.14 show the simulated distributions for dcphi, zed, pemcphi, pemcz compared to the real ones. The black circle and red square symbols show the results in the real and simulation. Differences on counts between the real and simulation for each DC side and EMCal sector are summarized in Tables 5.5, 5.6. The simulated acceptance is in good agreement with the real one within 4% for single electrons.

Table 5.5: Difference on counts between the real and simulation (simulation/real) for each DC side.

DC side	East South	East North	West South	West North
simulation/real	0.99	1.03	0.96	1.02

Table 5.6: Difference on counts between the real and simulation (simulation/real) for each EMCal sector.

EMCal sector	E0	E1	E2	E3	W0	W1	W2	W3
simulation/real	1.03	1.04	0.97	1.04	0.98	1.03	0.97	0.97

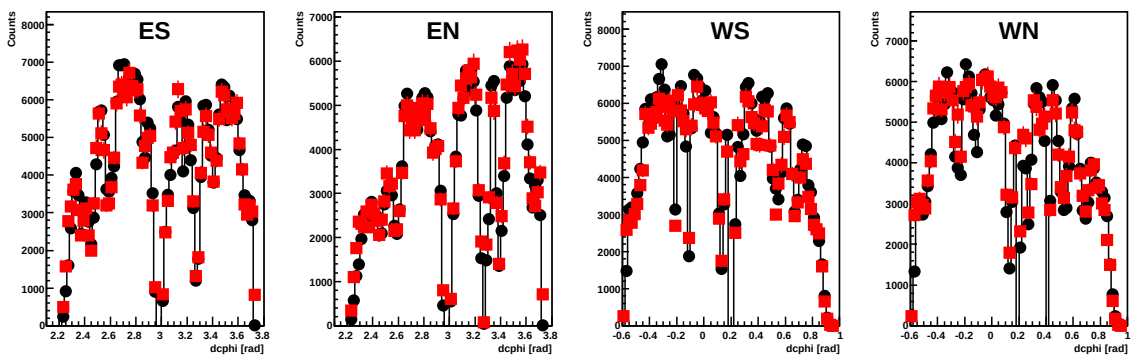

Figure 5.11: The simulated dcphi distribution (red square) compared to the real one (black circle) with electrons in $0.6 < p_T < 5.0$ GeV/c.

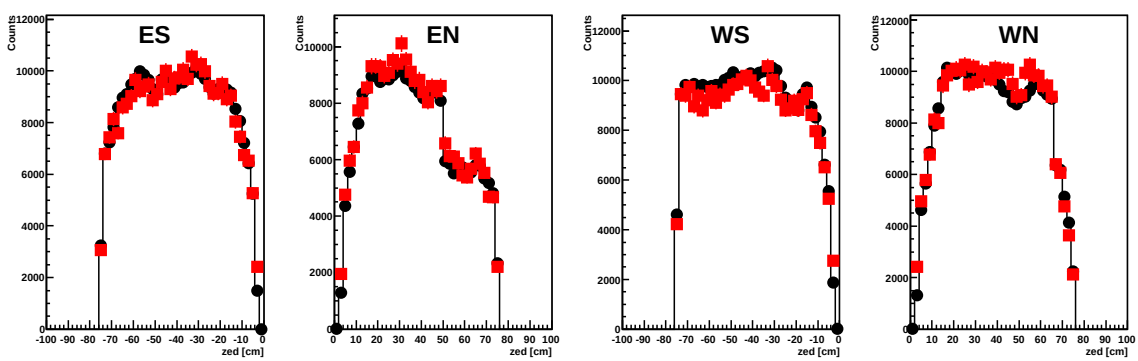

Figure 5.12: The simulated zed distribution (red square) compared to the real one (black circle) with electrons in $0.6 < p_T < 5.0$ GeV/c.

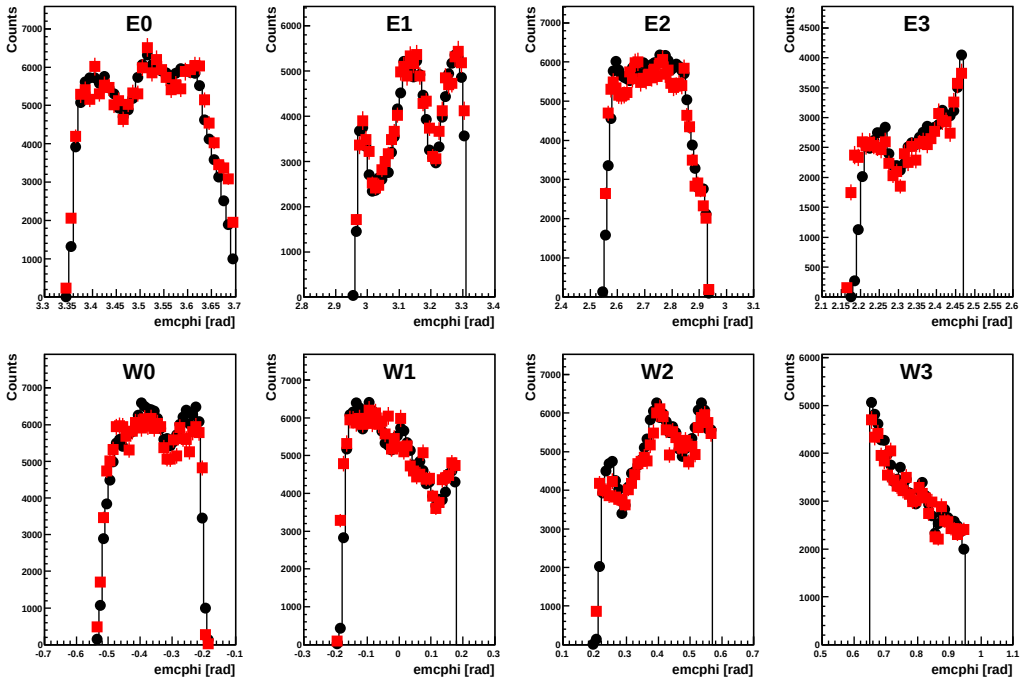

Figure 5.13: The simulated pemcphi distribution (red square) compared to the real one (black circle) with electrons in $0.6 < p_T < 5.0$ GeV/c.

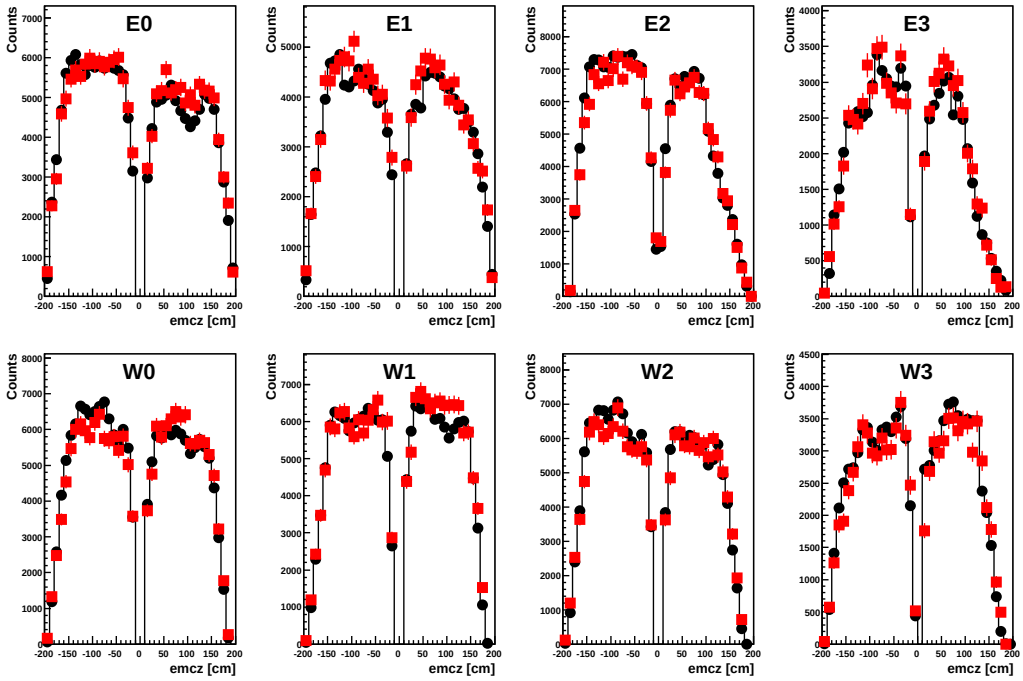

Figure 5.14: The simulated pemcz distribution (red square) compared to the real one (black circle) with electrons in $0.6 < p_T < 5.0$ GeV/c.

5.7 Run Selection

First of all, all runs are categorized into two run groups (G1, G2) depending on the the detector and trigger configurations as summarized presently in Table 4.2. After Run249716, an additional significant dead area in PC1 appeared. Therefore the run group G1 is separated into two run groups (G1A, G1B) depending on the acceptance and run groups in this analysis are summarized in Table 5.7. The runs with a converter were made during the run group G2 and they are removed before run quality assurance (QA). Good runs for each run group are selected by the following

Table 5.7: Summary of run groups.

Run Group	Run Numbers	Magnet Polarity	ERTLL1_2x2 energy threshold	significant dead area in PC1
G1A	246444-249716	CM++	600MeV	no
G1B	249720-250484	CM++	600MeV	yes
G2	250515-253701	CM– –	800MeV	yes

procedure based on the number of electrons per event with the standard eID cuts using MB data.

1. Calculate the number of electrons per event with p_T of $0.5 - 5.0$ GeV/c for each run.

2. Calculate mean and RMS values of the number of electrons per event ($\langle N_{elec} \rangle$, σ_{elec}).

3. Remove runs which do not match the following criterion:

$$|N_{elec} - \langle N_{elec} \rangle| < 3\sigma_{elec}. \tag{5.20}$$

4. The above process 1-3 is iterated until any run is not removed by the criterion 5.20.

The runs which survive through the above procedure are assigned as good runs for this analysis. Figure 5.15 shows the number of electrons per event with the $0.5 < p_T < 5.0$ GeV/c cut in MB data. The black and red symbols show the good and bad runs, respectively.

The trigger QA is also performed based on the number of triggered electrons per MB equivalent event in the ERT data for good runs selected by the above run QA using the MB data. Trigger supermodules with dead and low efficiency are masked. The triggered electrons in $0.8 < p_T < 4.0$ GeV/c and $1.1 < p_T < 4.0$ GeV/c are used for G1 and G2, respectively. Figure 5.16 shows the number of triggered electrons per

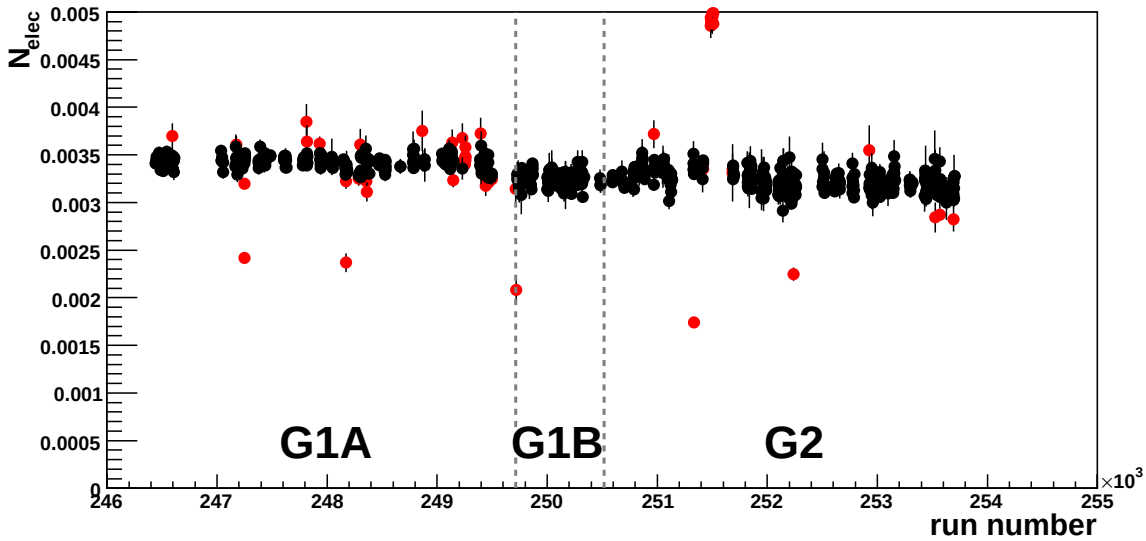

Figure 5.15: The number of electrons per event with p_T of $0.5 - 5.0$ GeV/c in MB data. The black and red symbols show the good and bad runs, respectively.

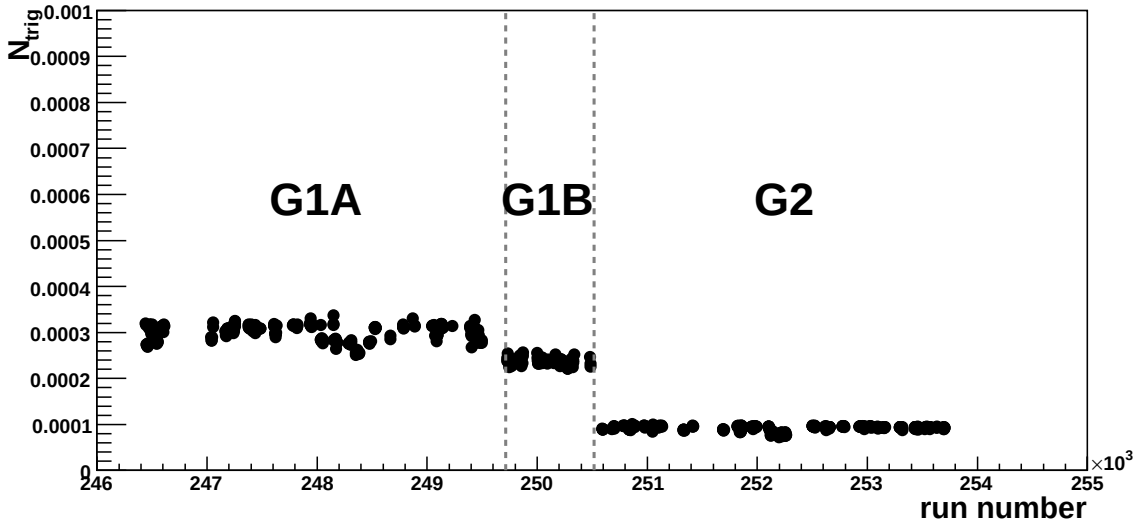

Figure 5.16: The number of triggered electrons per MB equivalent event in the ERT data for all good runs. The triggered electrons in $0.8 < p_T < 4.0$ GeV/c and $1.1 < p_T < 4.0$ GeV/c are used for G1 and G2, respectively.

MB equivalent event in the ERT data. The trigger conditions for all good runs look fine.

As a result of the above run QA, 787 runs out of 846 runs are selected as good runs.

5.8 Invariant Mass Spectrum

All combinations between electrons and positrons in an event are taken since the source of them is unknown. In the case of the ERT data, there are 2 special instructions at making pairs. The first one is that the ERT trigger threshold is re-defined at $p_T = 0.9$ for G1 and 1.1 GeV/c for G2 in offline, *i.e.* the trigger electrons with p_T of above re-defined trigger threshold are regarded as 'real' trigger electrons in order to reject electrons which accidentally fired the trigger with an electrical noise even if the deposited energy is lower than EMC 2x2 trigger threshold. The second one is that at least one electron in each pair is the triggered electron.

The invariant mass (m_{ee}) and transverse momentum (p_T^{ee}) of the e^+e^- pair are calculated as:

$$m_{ee} = \sqrt{(E_{e^+} + E_{e^-})^2 - (\vec{p_{e^+}} + \vec{p_{e^-}})^2}, \tag{5.21}$$

$$p_T^{ee} = \sqrt{(\vec{p_{x,e^+}} + \vec{p_{x,e^-}})^2 + (\vec{p_{y,e^+}} + \vec{p_{y,e^-}})^2}, \tag{5.22}$$

where E_{e^+,e^-} and $\vec{p_{e^+,e^-}}$ are the total energies and momenta of electron and positron. The total energy of the electron and positron, E_e is calculated from the total momentum measured by the DC and PC1 (mom) as:

$$E_e = \sqrt{m_e^2 + \mathsf{mom}^2}, \tag{5.23}$$

where m_e is the electron mass, i.e. $m_e = 0.000511$ GeV/c^2.

In principle, the foreground e^+e^- pairs are separated into physical and unphysical pairs. The physical pairs are basically defined as pairs which originates from the same parent particle, which can be either a hadron or a photon. The virtual photon converts internally, for instance, a virtual photon appears in the π^0 Dalitz decay: $\pi^0 \rightarrow \gamma\gamma^* \rightarrow \gamma e^+e^-$. The real photon also can convert in a material known as a photon conversion. The virtual and real photon conversions to e^+e^- are referred to as internal and external conversions in this thesis. The external conversion pairs are not reconstructed with their real mass $m_{ee} = 0$ due to a magnetic field in the PHENIX detector and contaminate the invariant e^+e^- pair mass spectrum. They need to be removed from the sample of physical pairs in order to extract the physical signal of hadron decays and internal photon conversions. A detailed explanation for how to remove the external conversion pairs will be given in Section 5.8.2. The e^+e^- pairs from semi-leptonic open charm and bottom decays do not share the same parent, but can be regarded as one of the physical pairs because the cross sections of charm

and bottom quarks in $\sqrt{s} = 200$ GeV p+p collisions have been measured via e^+e^- pairs at the PHENIX experiment [75]. Heavy quark pairs ($c\bar{c}, b\bar{b}$) are produced by inelastic hard scattering processes between constituent quarks (or gluons) of the two incoming nucleons. The generated heavy quarks (anti-quarks) lose their energy and then form open charmed and bottom mesons with light anti-quarks (quarks). The formed charmed and bottom meson pairs can preserve most of the initial correlations of the heavy quark pairs because of the heavy quark mass. Finally an electron pair is created as a result of the semi-leptonic decays of the charmed (or bottom) mesons.

The unphysical pairs, whose contribution to the foreground pairs is much larger than that of the physical pairs, are defined as pairs which are not from the same parent particles, but just pairs as a result of combining all electrons in an event. Unlike the physical pairs, the unphysical pairs can be either of unlike- or like-sign charge combinations. Most of the unphysical pairs are uncorrelated combinations of electrons which can be described by a combinatorial background generated with an event mixing technique. However, some of the unphysical pairs have correlations in their decay history and such correlated unphysical pairs are denoted as 'semi-correlated' pairs. There are two types of semi-correlated pairs. The first one is cross pairs from decays with 2 e^+e^- pairs in the final state such as π^0 double Dalitz decays ($\pi^0 \to \gamma^*\gamma^* \to e^+e^-e^+e^-$) and π^0 Dalitz decays with the external conversion ($\pi^0 \to \gamma e^+e^- \to e^+e^-e^+e^-$). The cross pair does not originate from the same parent, but from the same grandparent particle. The second one is pairs produced within the same jet, which are denoted as jet pairs. Some π^0 in the same jet have strong correlations and electrons from these π^0 can inherit the correlations between their parents. Ghost pairs as one of the unphysical pairs also appear when tracks share the same detector hit information.

All described sources of the physical and unphysical pairs are summarized below.

Physical pairs

1. internal photon conversions
2. hadron decays
3. external photon conversions
4. semi-leptonic decays of open charmed and bottom mesons

Unphysical pairs

1. uncorrelated combinations (combinatorial pair)
2. semi-correlated combinations
   i. cross pairs from decays with 2 e^+e^- pairs in the final state (cross pair)
   ii. combinations within the same jet (jet pair)
3. detector ghost tracks

5.8.1 Pair Cuts

The ghost pairs should be removed from the pairs in real events. The ghost tracks are generated when the same detector information is accidentally associated to different track candidates. Such situation can occur in the DC and RICH.

DC Ghost tracks

If there are some DC hits at almost the same position, these DC hits are associated multiple times, and some tracks are reconstructed along almost the same trajectory. The DC area in $|\Delta\mathsf{zed}|$ <0.5 cm and $|\Delta\mathsf{dcphi}|$ <0.02 rad corresponds to a one cell size in the PC1. Figure 5.17 shows the $\Delta\mathsf{zed}$ distribution for like-sign pairs. The closed black symbols show the all pairs and the open blue symbols show the pairs when a difference between track trajectories is within a cell size of the PC1. Such pairs have

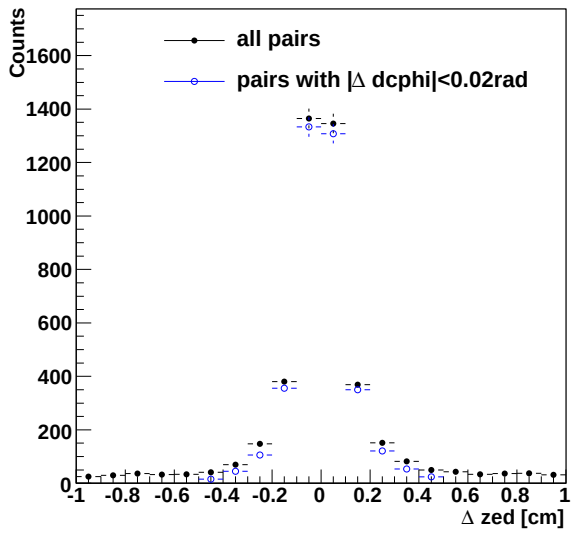

Figure 5.17: The $\Delta\mathsf{zed}$ distribution for like-sign pairs. The closed black and open blue symbols show the all pairs and the pairs when a difference between track trajectories is within a cell size of the PC1.

a strong correlation and they are removed by the following cuts:

$$\text{DC ghost cuts} \quad = \quad \overline{(|\Delta\mathsf{dcphi}| < 0.02 \cap |\Delta\mathsf{zed}| < 0.5)}. \tag{5.24}$$

RICH Ring Sharing

If two tracks traverse along parallel trajectories, their track projection points are very close to each other in the RICH phototube plane. As a result, the same firing phototubes are shared even if one of the tracks is a charged hadron which itself does not emit Cherenkov photons. The distance between the ring centers of the tracks in

a pair is a useful condition to remove the charged hadrons which share RICH rings with electrons accidentally; the distances in the ϕ and z directions are defined as:

$$\Delta\phi_{cross} = \phi^{i}_{cross} - \phi^{j}_{cross}, \tag{5.25}$$

$$\Delta z_{cross} = z^{i}_{cross} - z^{j}_{cross}, \tag{5.26}$$

where $\phi^{i,j}_{cross}$ and $z^{i,j}_{cross}$ are the ϕ and z positions of the ring center defined by the i, j-th tracks, respectively. If the distance between the ring centers is within $|\Delta\phi_{cross}| < 0.06$ rad and $|\Delta z_{cross}| < 25$ cm, such pairs are removed by the following cut:

$$\text{RICH ghost cuts} = \overline{(|\Delta\phi_{cross}| < 0.06 \cap |\Delta z_{cross}| < 25)}. \tag{5.27}$$

Figure 5.18 show the $\Delta\phi_{cross}$ and Δz_{cross} distributions for like-sign pairs. The closed black and open blue symbols show the all pairs and ghost pairs. The red shaded portion shows the combinatorial contribution calculated by an event mixing technique, which is described later.

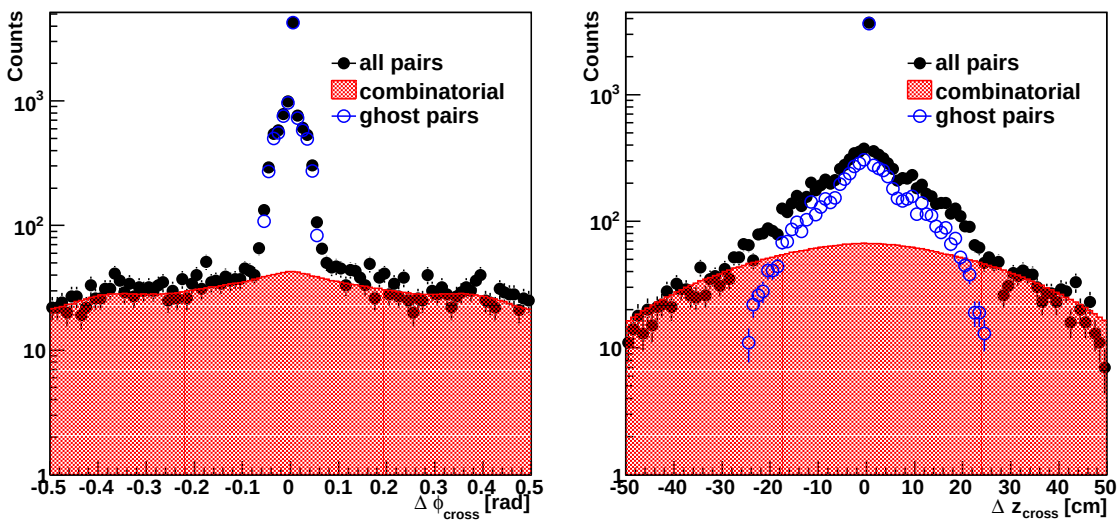

Figure 5.18: The $\Delta\phi_{cross}$ (left) and Δz_{cross} (right) distributions for like-sign pairs. The closed black and open blue symbols show the all pairs and ghost pairs. The red shaded portion shows the combinatorial contribution.

5.8.2 External Photon Conversion

The reconstructed invariant mass spectrum of e^+e^- pairs has peaks in the low mass region. These peaks are produced by electron pairs from external photon conversions. The electrons which are produced off-vertex by the external conversion have incorrect opening angle and momenta since the PHENIX tracking algorithm assumes that all primary and secondary tracks come from the collision vertex, and conversion electrons

pass through less integrated magnetic field than the PHENIX tracking algorithm assumes, as illustrated in Fig. 5.19. As a result, the conversion pair has an apparent

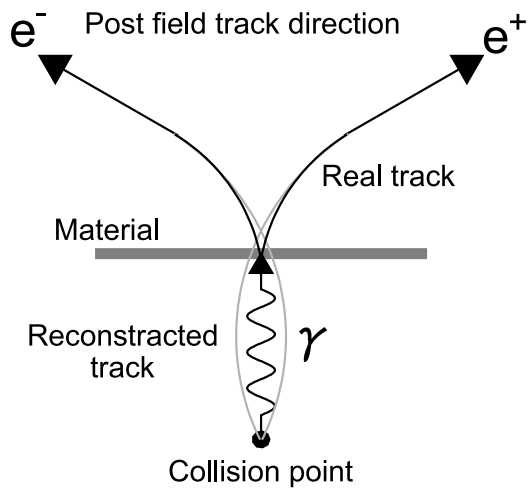

Figure 5.19: Production of a conversion electron pair.

mass proportional to the distance between the conversion point and the collision vertex.

Figure 5.20 shows the invariant e^+e^- mass spectra before/after external conversion pairs are removed. The closed black symbols show all the pairs and the open red symbols indicate the pairs passing through ϕ_V cuts described in this section; these may be regarded as non-conversion pairs. The sharp peak at 0.020 GeV/c^2 and the broad peak around 0.300 GeV/c^2 result from conversions in the beam pipe made of Beryllium (0.3% X_0) and air between the beam pipe and the DC (0.6% X_0), respectively. The conversion component is removed using the angle between the decay plane and the z-axis, denoted by ϕ_V, since the decay plane of the conversion pair is perpendicular to the magnetic field along the z-axis. The angle ϕ_V is calculated as follows:

$$\vec{u} = \frac{\vec{p_{e^+}} + \vec{p_{e^-}}}{|\vec{p_{e^+}} + \vec{p_{e^-}}|}, \tag{5.28}$$

$$\vec{v} = \frac{\vec{p_{e^+}} \times \vec{p_{e^-}}}{|\vec{p_{e^+}} \times \vec{p_{e^-}}|}, \tag{5.29}$$

$$\vec{w} = \vec{u} \times \vec{v}, \tag{5.30}$$

$$\vec{e_z} = (0,0,1)\ (\mathrm{CM}{+}{+}), (0,0,-1)\ (\mathrm{CM}{-}{-}), \tag{5.31}$$

$$\vec{a} = \frac{\vec{u} \times \vec{e_z}}{|\vec{u} \times \vec{e_z}|}, \tag{5.32}$$

$$\phi_V = \cos^{-1}(\vec{w} \cdot \vec{a}). \tag{5.33}$$

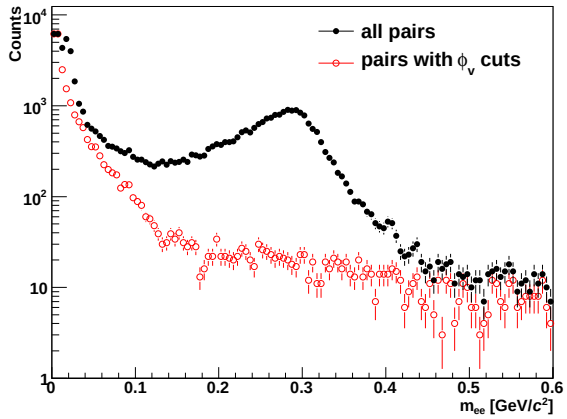

Figure 5.20: The invariant e^+e^- mass spectra before/after external conversion pairs are removed. The closed black symbols show the all pairs and the open red symbols indicate the pairs passing through ϕ_V cuts which can be regarded as non-conversion pairs. The sharp peak at 0.020 GeV/c^2 and the broad peak around 0.300 GeV/c^2 result from conversions at the beam pipe and air between the beam pipe and the DC, respectively.

Figure 5.21 shows the ϕ_V distributions in different mass regions for $1.0 < p_T^{ee} < 2.0$ GeV/c compared to non-conversion pair contribution. The closed black symbols show all the pairs in the real events and the red shaded portion shows the non-conversion pair contribution. The non-conversion pair contribution consists of hadron decay and background components. The way to evaluate the contribution of background components (combinatorial, cross and jet pairs) are described in Section 5.8.3, and the hadron decay contribution is calculated by a well-tuned simulation. A detailed description for the hadron decay simulation can be found in Section 5.10. The peaks around $\phi_V = 0$ which can not be reproduced by non-conversion pair contribution are clearly seen in the mass regions except for in $0.00 \leq m_{ee} < 0.01$ GeV/c^2. Since these peaks result from external conversion pairs, the following cuts are applied to remove conversion pairs:

$$\phi_V \text{ cuts in } 0.01 \leq m_{ee} < 0.03 \quad = \quad \phi_V \geq 0.45, \tag{5.34}$$
$$\phi_V \text{ cuts in } 0.03 \leq m_{ee} < 0.09 \quad = \quad \phi_V \geq 0.30, \tag{5.35}$$
$$\phi_V \text{ cuts in } 0.09 \leq m_{ee} < 0.14 \quad = \quad \phi_V \geq 0.25, \tag{5.36}$$
$$\phi_V \text{ cuts in } 0.14 \leq m_{ee} \quad = \quad \phi_V \geq 0.20. \tag{5.37}$$

The threshold value for each mass region is indicated as a blue dotted line in Fig. 5.21. How well conversion pairs are eliminated by the ϕ_V cuts has been evaluated by an additional converter in the PHENIX experiment [31], and we estimated that more than 99.5% of conversion pairs are removed by the ϕ_V cuts.

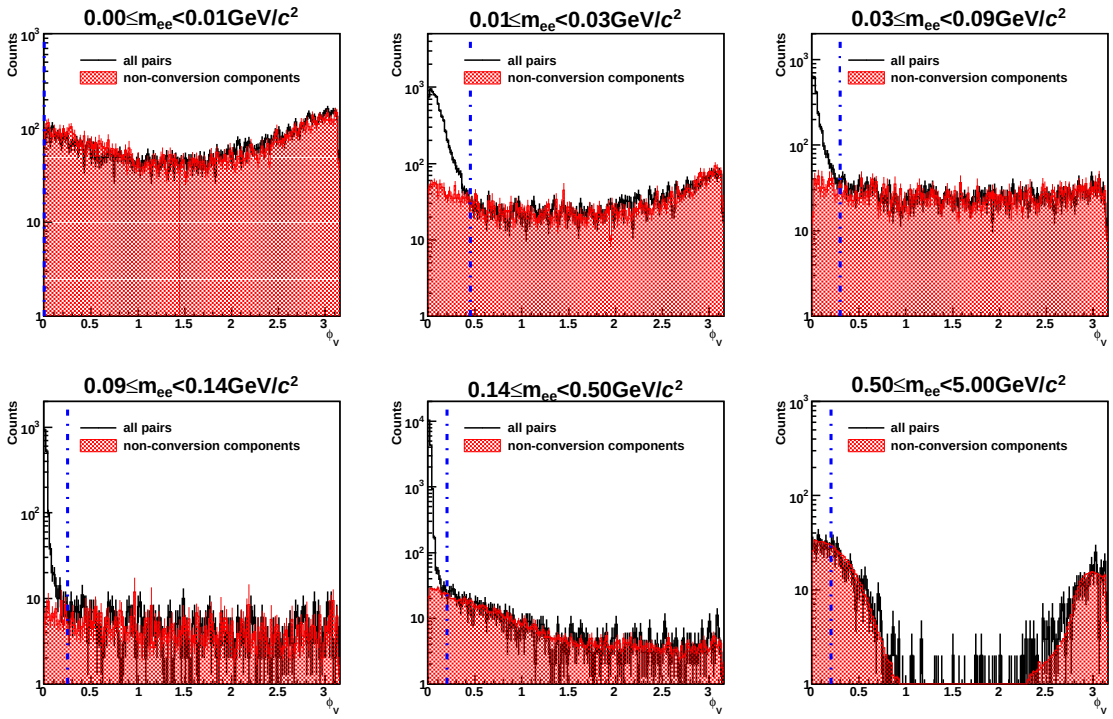

Figure 5.21: The ϕ_V distributions in different mass regions for $1.0 < p_T^{ee} < 2.0$ GeV/c compared to non-conversion pair contribution. The closed black symbols show the all pair in the real events, and the red shaded portion shows the non-conversion pair contribution. The blue dotted line indicates the threshold value for each mass region. The peaks around $\phi_V = 0$ are clearly seen in the mass regions except for in $0.00 \leq m_{ee} < 0.01$ GeV/c^2 due to external conversions.

5.8.3 Background Pairs

After the above-mentioned selections to eliminate detector ghost and conversion pairs are imposed, the unphysical pairs which are mentioned in the introduction of this section still remain as a background for the signal of the physical pairs in the e^+e^- pair sample. The contribution of the background pairs is evaluated for subtraction. The like-sign pair distributions (e^-e^-, e^+e^+) are useful to evaluate the contributions of background components such as the combinatorial pair, the cross pair and the jet pair, since e^-e^- and e^+e^+ distributions consist of only these background pairs.

Combinatorial Pairs

An event mixing technique is employed to evaluate unlike-sign and like-sign mass shapes of combinatorial background pairs. All MB events in which one electron at least is found are categorized according to their centrality (10 classes) and z-vertex (8 classes) and are stored in the event buffer with depth, $N_{buff} = 5$. The mixed unlike-sign and like-sign pairs are combined using electrons from different events in the same event buffer.

For the ERT data, the mixed events are generated using the MB data and at least one of the electrons in every pair must be the triggered electron as in the real events. Thus, the correct mass shape of combinatorial background pairs for the ERT data can be generated.

Cross Pairs

The cross pairs result from mainly π^0, η decays with 2 e^+e^- pairs in the final state. Possible decays with 2 e^+e^- pairs in the final sate are as follows:

1. $\pi^0(\eta) \to \gamma_1^*\gamma_2^* \to e_1^+e_1^-e_2^+e_2^-$ (double Dalitz decay)

2. $\pi^0(\eta) \to \gamma_1\gamma_2^* \to \gamma_1 e_2^+e_2^- \to e_1^+e_1^-e_2^+e_2^-$ (Dalitz decay + external conversion)

3. $\pi^0(\eta) \to \gamma_1\gamma_2 \to e_1^+e_1^-e_2^+e_2^-$ (double external conversion)

In principle, the above decays are decays including two photons, but with two, one or zero virtual photons. The $e_1^+e_1^-$ and $e_2^+e_2^-$ pairs are considered to be the physical pairs, because they are from the same parent photons; if they are external conversion pairs, they can be removed by the ϕ_V cuts already described in Section 5.8.2. The two cross unlike-sign pairs ($e_1^+e_2^-, e_2^+e_1^-$) as well as two cross like-sign pairs ($e_1^+e_2^+, e_1^-e_2^-$) have a strong correlation below the parent hadron mass $m_{ee} < m_{\pi^0,\eta}$.

The mass shapes of the cross pairs are calculated using the PISA simulation for π^0, η double Dalitz decays as the same way in the hadronic cocktail calculation described later. The branching ratios of $\pi^0(\eta)$ double Dalitz decays can be computable

from branching ratios of $\pi^0(\eta) \to 2\gamma$ and their Dalitz probabilities, since the Dalitz process is a pure Quantum Electrodynamics (QED) process. Therefore,

$$\begin{aligned} BR(\pi^0 \to 2e^+e^-) &= BR(\pi^0 \to 2\gamma) \times (P^{\pi^0}_{Dalitz})^2 \\ &= 0.988 \times (0.006)^2 = 3.56 \times 10^{-5}, \qquad (5.38) \\ BR(\eta \to 2e^+e^-) &= BR(\eta \to 2\gamma) \times (P^{\eta}_{Dalitz})^2 \\ &= 0.393 \times (0.008)^2 = 2.52 \times 10^{-5}, \qquad (5.39) \end{aligned}$$

where $P^{\pi^0,\eta}_{Dalitz}$ are the Dalitz probabilities for π^0 and η.

Jet Pairs

The mass shapes of the jet pairs are calculated by a Monte Carlo simulation based on PYTHIA simulation (version 8.108) [76]. The particle interactions are calculated using leading order matrix elements and the Lund string fragmentation model [77]. CTEQ5L function [78] is used as a parton distribution function in PYTHIA. In this simulation, all $2 \to 2$ hard QCD processes (*e.g.* $gg \to gg$, $gg \to q\bar{q}$ and so on, where $g, q, \bar{q}$ denote a gluon, quark and anti-quark, respectively) are activated, and the Dalitz probability is set to a 50 times higher value than the nominal one to increase the sample of e^+e^- pairs. Since only one parton-parton interaction is simulated in an event by PYTHIA, and we never know which e^+e^- pairs from different parents are strongly correlated, all combinations of electrons in the final state, but not from the same parent, are taken as the jet pairs. All existing effects in the real events such as the acceptance, angular and momentum smearing, trigger efficiency and so on are parameterized and then are implemented in the PYTHIA based simulation.

5.8.4 Background Evaluation

It is difficult to estimate fractions of cross pairs and jet pairs in the real distribution only from simulations due to the following reasons:

- The effective yield of the cross pairs from both double Dalitz decays and double Dalitz decay-like processes can not be calculated since the external conversion probability for single photons is not measured yet with the detector configuration in Run8.
- Which jet pair has a strong correlation is unknown so far.

Thus, the background normalization is performed by a fit to the real like-sign pair distributions using a combination of mass shapes of the combinatorial pairs, cross pairs and jet pairs. The fit using the combination of the above three background components are denoted as the 3-component fit in this thesis. An advantage on the 3-component fit is that the normalization factor for each background component can be determined from the real data.

3-component Fit

The 3-component fit function is a mass-dimensional function expressed as

$$f_{BG}^{fit}(m_{ee}) = r_{comb} \cdot f_{comb}(m_{ee}) + r_{jet} \cdot f_{jet}(m_{ee}) + r_{cross} \cdot f_{cross}(m_{ee}), \tag{5.40}$$

where $f_{comb,jet,cross}(m_{ee})$ and $r_{comb,jet,cross}$ are mass distributions and normalization factors for the combinatorial pairs, jet pairs and cross pairs, respectively. The normalization factors, $r_{comb}, r_{jet}, r_{cross}$ are free parameters during fitting. The 3-component fit is performed simultaneously to e^-e^- and e^+e^+ pair distributions in the real events for $0.0 < m_{ee} < 3.0$ GeV/c^2. Figure 5.22 shows the like-sign pair distributions (e^-e^-, e^+e^+) in the real data and the background components with the normalization factors determined by the 3-component fit are also shown together. The open

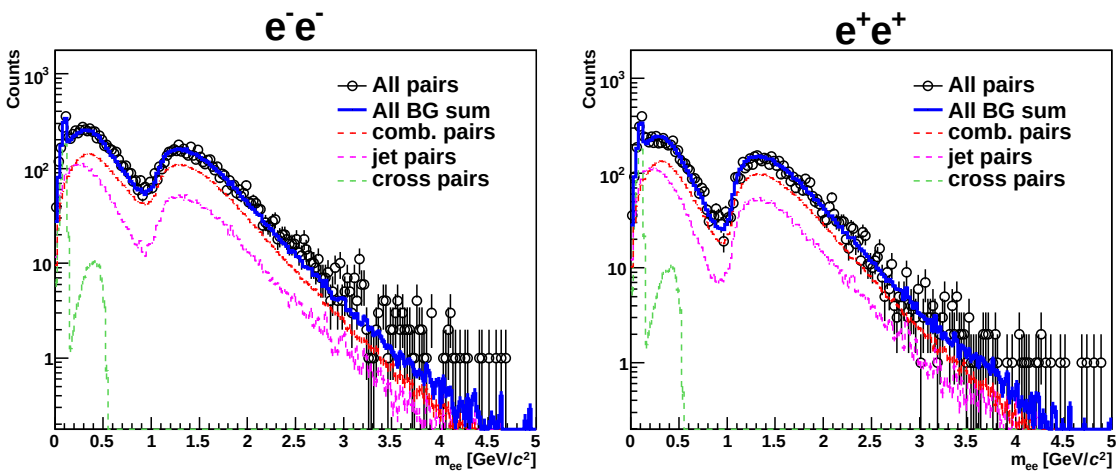

Figure 5.22: The like-sign pair distributions (left: e^-e^-, right: e^+e^+) in the real data and the background components with the normalization factors determined by the 3-component fit are also shown,

symbols show the all pairs in the real events, and the dotted lines show the distributions of the background components (red: combinatorial pairs, magenta: jet pairs, green: cross pairs), and the solid blue line shows the sum of the background components. The like-sign pair mass distributions have a two-humped structure. The two humps around $m_{ee} = 0.4, 1.5$ GeV/c^2 correspond to pairs traversing into the same arm and different arms, respectively. The sum of the background components with normalization factors determined by the 3-component fit looks agreement with the real data. If the 3-component fit is made separately to the e^+e^+, e^-e^- pair distributions, the normalization factors for each background component in e^+e^+ and e^-e^- are consistent with the normalization factor determined by the fit simultaneously to e^+e^+, e^-e^- within fitting errors.

The opening angle $\Delta\phi_{ee}$ distributions of like-sign pairs also reflect their origins. Thus, the $\Delta\phi_{ee}$ distributions of like-sign pairs in the real data should be reproduced by

the sum of the background components as well as in the case of the mass distributions if the normalization factors determined by the 3-component fit are correct. Figure 5.23 shows the $\Delta\phi_{ee}$ distributions of like-sign pairs in the real data together with the sum of the background components with normalization factors. The same symbol and

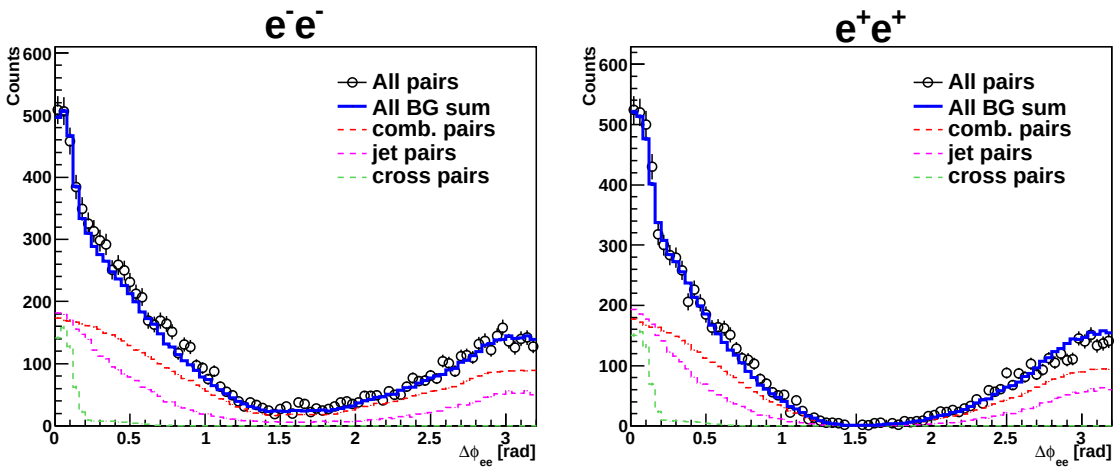

Figure 5.23: The $\Delta\phi$ distributions of like-sign pairs (left: e^-e^-, right: e^+e^+) in the real data together with the sum of the background components with normalization factors,

lines in Fig 5.22 are used to show the results. The $\Delta\phi_{ee}$ distributions of like-sign pairs in the real data can be reproduced by the sum of the background components as well as the mass distributions. Therefore, the compositions of the background pairs in the real data are well understood.

Background Subtraction

Since the unlike- and like-sign pair mass distributions for all background components are calculated with consideration for the acceptance and efficiencies, the normalization factors determined using the like-sign pair sample are applicable to unlike-sign pair mass distribution. Thus, the background pairs for a e^+e^- pair sample are normalized by the determined normalization factors, and then subtracted from the e^+e^- pair sample. Figure 5.24 shows the e^+e^- pair distribution in the real data together with the all background pair contributions and the correlated e^+e^- pairs after the background subtraction. All e^+e^- pairs before the background subtraction are shown as open black symbols and colored dotted lines show the background component contributions and the blue solid line shows the sum of these background pairs. The e^+e^- pairs, which remain after all background pairs are subtracted, can be identified as the correlated physical pairs shown as the closed red symbols. The peaks for ω (0.782 GeV/c^2), ϕ (1.020 GeV/c^2) and J/ψ (3.096 GeV/c^2) mesons are clearly seen in the correlated e^+e^- pair distribution.

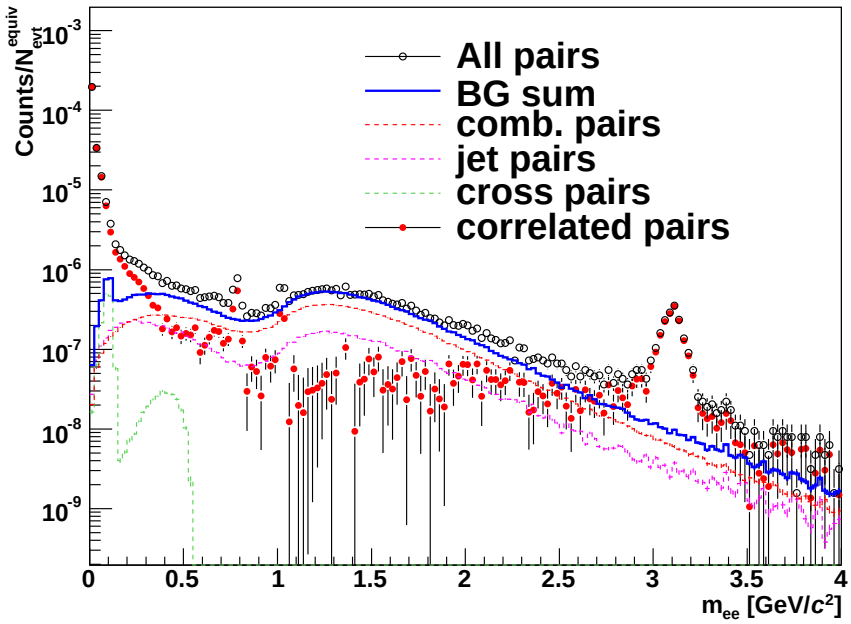

Figure 5.24: The e^+e^- pair distribution in the real data together with the all background pair contributions and the correlated e^+e^- pairs remaining after all background pairs are subtracted.

5.9 Efficiency Correction

As described in Eq. 5.1, the overall efficiency (ε_{all}) should be corrected to determine dN/dm_{ee}. The overall efficiency can be decomposed into three parts:

$$\varepsilon_{all}(p_T^{ee}, m_{ee}) = \varepsilon_{elec}^{pair}(p_T^{ee}, m_{ee}) \times \varepsilon_{acc+cut}^{pair}(p_T^{ee}, m_{ee}) \times \varepsilon_{ERT}^{pair}(p_T^{ee}, m_{ee}), \tag{5.41}$$

where $\varepsilon_{elec}^{pair}$ is the electron efficiency for e^+e^- pairs and $\varepsilon_{acc+cut}^{pair}$ is a combination of efficiencies of the geometrical acceptance and additional pair cuts (DC ghost, RICH ghost and ϕ_V cuts), and ε_{ERT}^{pair} is the ERT trigger efficiency for e^+e^- pairs. The efficiencies for e^+e^- pairs are calculated as a function of m_{ee} for every 0.1 GeV/c-p_T^{ee}.

5.9.1 Electron Efficiency

In this section, the ways to calculate the above efficiencies are described. First, the electron efficiencies for single electrons and positrons are defined as a combination of the reconstruction and eID efficiencies as shown in Eq. 5.42, and they are calculated using the PISA simulation for single electrons and positrons used for the acceptance evaluation (Section 5.6).

$$\varepsilon_{elec}^{e^+,e^-}(p_T) = \varepsilon_{reco}^{e^+,e^-}(p_T) \times \varepsilon_{eID}^{e^+,e^-}(p_T) = \frac{dN_{eID}/dp_T^{reco}}{dN_0/dp_T^{mc}}, \tag{5.42}$$

where $\varepsilon_{reco}^{e^+,e^-}, \varepsilon_{eID}^{e^+,e^-}$ are the reconstruction and eID efficiencies for single electrons, where positrons and N_{eID} means the number of electrons which pass through the standard eID cuts, and N_0 means the number of electrons in the PHENIX acceptance and $p_T^{reco,mc}$ are p_T of electrons at reconstruction and generation.

Figure 5.25 shows the electron efficiencies for single electrons and positrons calculated using the PISA simulation. The symbols show the calculated results and lines

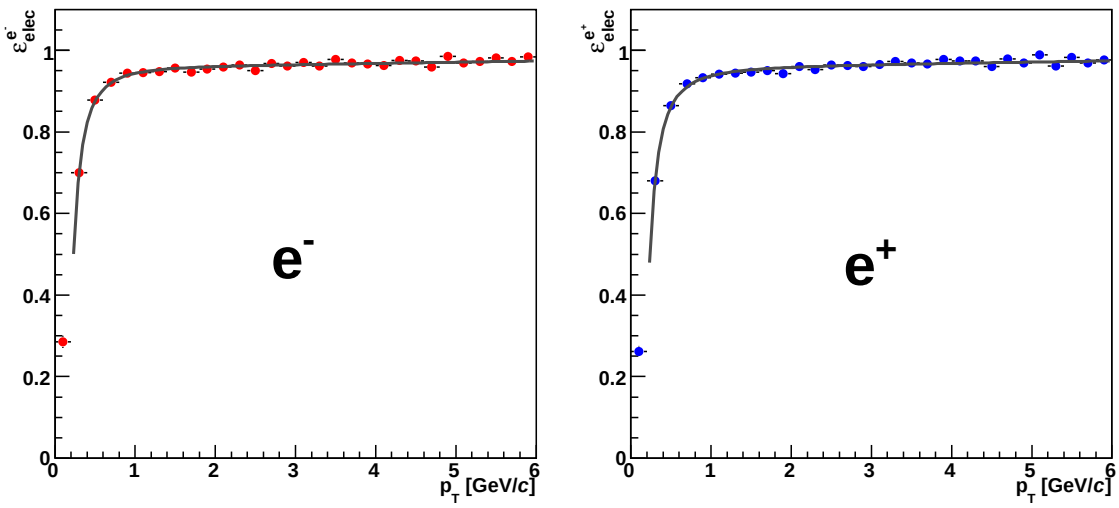

Figure 5.25: The electron efficiencies for single electrons (left) and positrons (right) calculated using the PISA simulation.

are results of fit with a polynomial function to parameterize the electron efficiencies. The obtained parameterized electron efficiencies for single electrons and positrons are as follows:

$$\varepsilon_{elec}^{e^-}(p_T) = 9.5 \times 10^{-1} + \frac{1.3 \times 10^{-2}}{p_T} - \frac{2.7 \times 10^{-2}}{p_T^2} + 3.1 \times 10^{-3} \cdot p_T + e^{(-1.4 \times 10^{-6} \cdot p_T - 5.6)}, \tag{5.43}$$

$$\varepsilon_{elec}^{e^+}(p_T) = 9.5 \times 10^{-1} + \frac{2.2 \times 10^{-2}}{p_T} - \frac{2.6 \times 10^{-2}}{p_T^2} + 2.8 \times 10^{-3} \cdot p_T + e^{(-5.3 \times 10^{-9} \cdot p_T - 5.0)}. \tag{5.44}$$

These parameterized efficiencies are implemented in a fast Monte Carlo simulation for hadrons, then the electron efficiency for e^+e^- pairs are expressed as:

$$\varepsilon_{elec}^{pair}(p_T^{ee}, m_{ee}) = \frac{d^2 N_{elec}^{pair} / dp_T^{ee} dm_{ee}}{d^2 N_0^{pair} / dp_T^{ee} dm_{ee}}, \tag{5.45}$$

where $N_{elec}^{pair}, N_0^{pair}$ are the number of e^+e^- pairs with and without electron efficiencies for single electrons and positrons. Figure 5.26 shows the electron efficiency as a function of m_{ee} for e^+e^- pairs in $1.0 \leq p_T^{ee} < 1.1$ GeV/c as an example of the electron

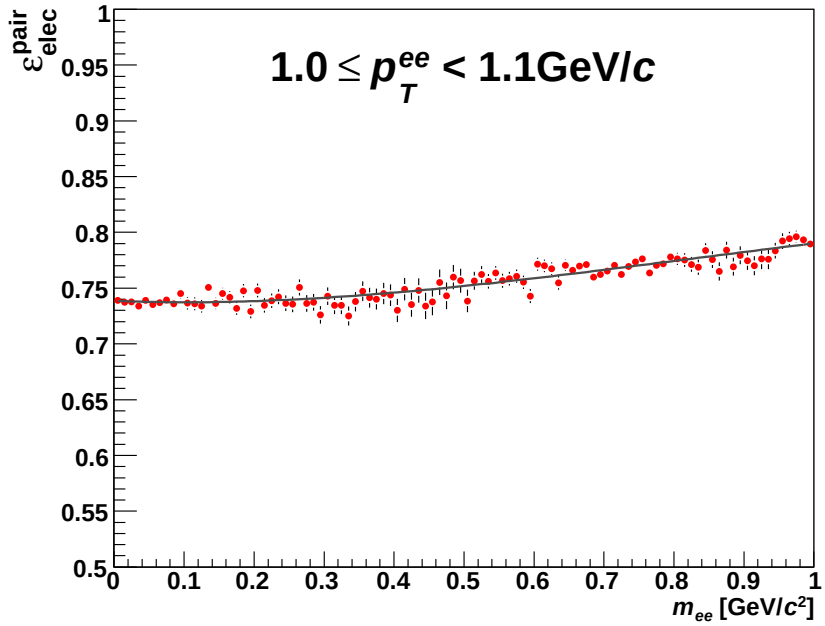

Figure 5.26: The electron efficiency as a function of m_{ee} for e^+e^- pairs in $1.0 \leq p_T^{ee} < 1.1$ GeV/c as an example of the electron efficiency for every 0.1 GeV/c-p_T^{ee}.

efficiency for every 0.1 GeV/c-p_T^{ee}. The solid line shows the fit result with a polynomial function in $0 < m_{ee} < 1.1$ GeV/c^2. Figure 5.27 shows the mean values of the electron efficiency for e^+e^- pairs in $0.00 < m_{ee} < 0.05$ GeV/c^2 and $0.10 < m_{ee} < 0.30$ GeV/c^2 as a function of p_T^{ee}. These mean values are calculated using the obtained fit function for every 0.1 GeV/c-p_T^{ee} as shown in Fig. 5.26. The closed and open symbols show the mean values in $0.00 < m_{ee} < 0.05$ GeV/c^2 and $0.10 < m_{ee} < 0.30$ GeV/c^2, respectively. The electron efficiency for e^+e^- pairs is almost flat in the low mass region of $0.00 < m_{ee} < 0.30$ GeV/c^2.

5.9.2 Acceptance and Pair Cuts Efficiency

There are e^+e^- pairs which are lost due to dead areas in the PHENIX detector, and which accidentally fulfill the criteria on the detector ghost pairs or the external conversion pairs and then are removed even though they are real physical pairs. The loss efficiency due to dead areas and pair cuts for e^+e^- pairs, $\varepsilon^{pair}_{acc+cut}$ is evaluated using the PISA simulation for known hadrons, which is described in Section 5.10. The loss efficiency, $\varepsilon^{pair}_{acc+cut}$ is calculated as:

$$\varepsilon^{pair}_{acc+cut}(p_T^{ee}, m_{ee}) = \frac{d^2 N^{pair}_{acc+cut}/dp_T^{ee}dm_{ee}}{d^2 N^{pair}_0/dp_T^{ee}dm_{ee}}, \tag{5.46}$$

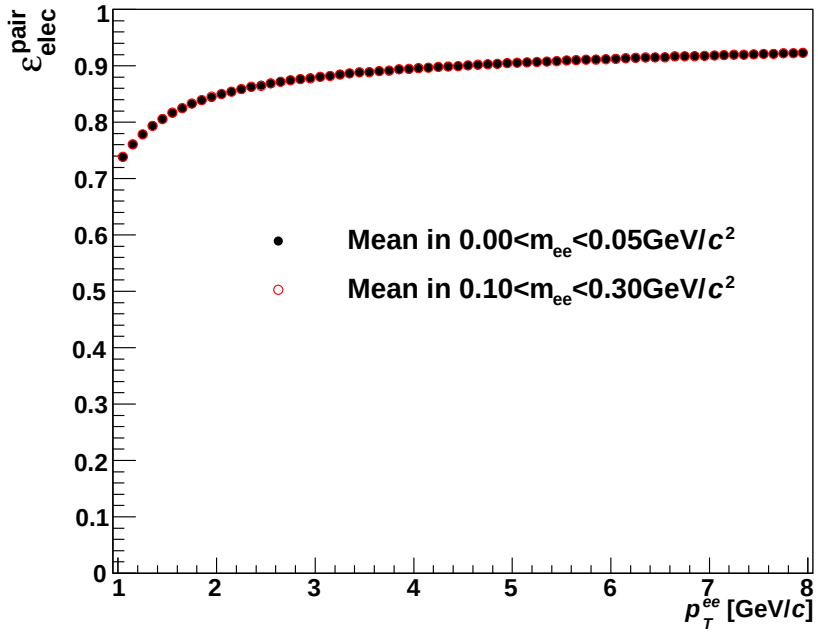

Figure 5.27: Mean values of the electron efficiency for e^+e^- pairs in $0.00 < m_{ee} < 0.05$ GeV/c^2 and $0.10 < m_{ee} < 0.30$ GeV/c^2 as a function of p_T^{ee}. The closed and open symbols show the mean values in $0.00 < m_{ee} < 0.05$ GeV/c^2 and $0.10 < m_{ee} < 0.30$ GeV/c^2, respectively.

where $N^{pair}_{acc+cut}$ is the number of e^+e^- pairs with dead areas and additional pair cuts, and N^{pair}_0 is the number of e^+e^- pairs in the perfect PHENIX acceptance from known hadron decays. Figure 5.28 shows the loss efficiency due to dead areas and pair cuts as a function of m_{ee} for e^+e^- pairs in $2.0 \leq p_T^{ee} < 2.1$ GeV/c. The result is not smooth

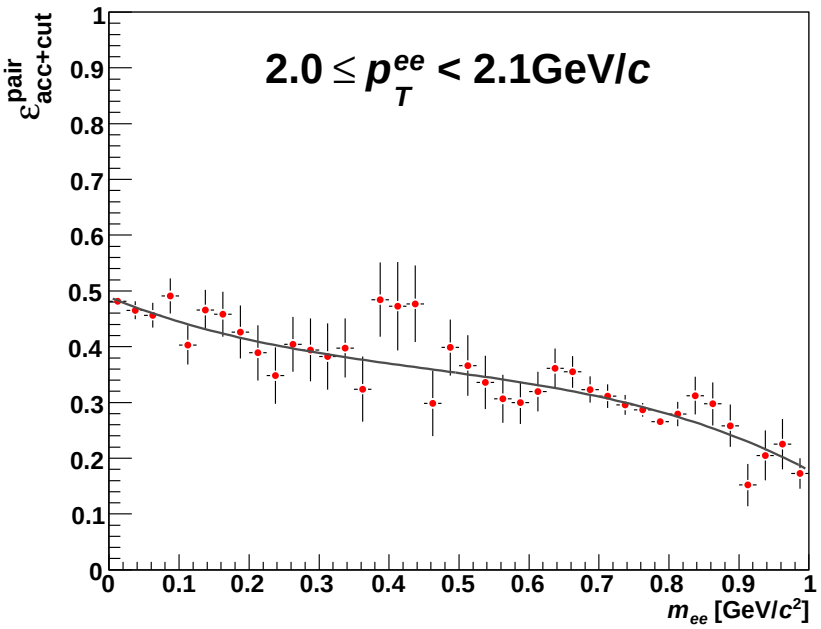

Figure 5.28: The loss efficiency due to dead areas and pair cuts as a function of m_{ee} for e^+e^- pairs in $2.0 \leq p_T^{ee} < 2.1$ GeV/c.

due to a statistical limit for the PISA simulation of the known hadron decays. Thus, the fit result with a third-order polynomial function in $0 < m_{ee} < 1.1$ GeV/c^2 shown as a solid line is used for the correction.

Figure 5.29 shows the mean values of the loss efficiency due to dead areas and pair cuts for e^+e^- pairs in $0.00 < m_{ee} < 0.05$ GeV/c^2 and $0.10 < m_{ee} < 0.30$ GeV/c^2 as a function of p_T^{ee}. These mean values are calculated using the obtained fit function for every 0.1 GeV/c-p_T^{ee} as shown in Fig. 5.28. The closed and open symbols show the mean values in $0.00 < m_{ee} < 0.05$ GeV/c^2 and $0.10 < m_{ee} < 0.30$ GeV/c^2, respectively. The loss efficiency due to dead areas and pair cuts for e^+e^- pairs declines as m_{ee} increases in $p_T^{ee} < 4.0$ GeV/c.

5.9.3 ERT Trigger Efficiency

In the ERT data analysis, one electron at least has fired the ERT trigger at making pairs as already described in Section 5.8. The e^+e^- pair mass spectrum in the ERT data needs to be corrected for the pair ERT trigger efficiency, which is derived from the ERT trigger efficiencies for single electrons as same as the pair electron efficiency.

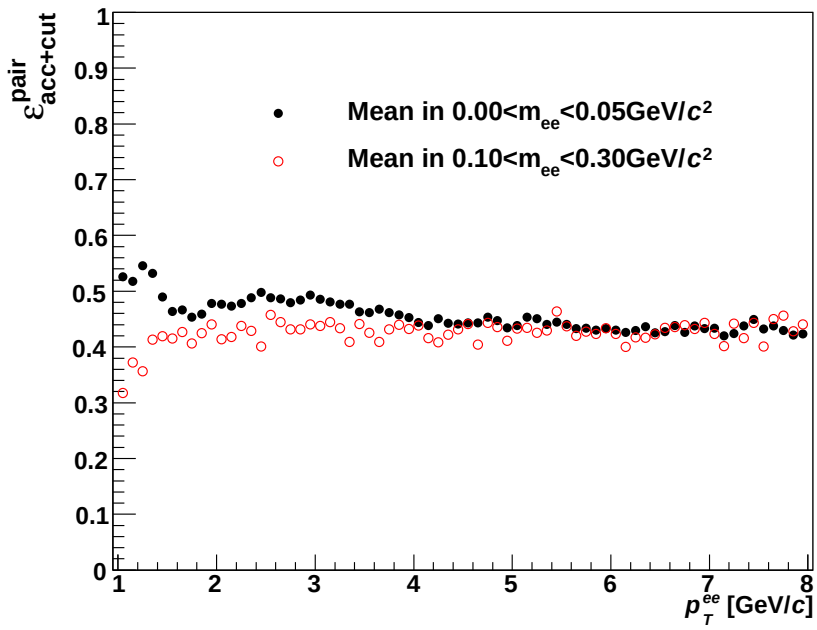

Figure 5.29: Mean values of the loss efficiency due to dead areas and pair cuts for e^+e^- pairs in $0.00 < m_{ee} < 0.05$ GeV/c^2 and $0.10 < m_{ee} < 0.30$ GeV/c^2 as a function of p_T^{ee}. The closed and open symbols show the mean values in $0.00 < m_{ee} < 0.05$ GeV/c^2 and $0.10 < m_{ee} < 0.30$ GeV/c^2, respectively.

Since the ERT trigger requires that both EMC2x2 and RICH triggers fire, the EMC2x2 and RICH trigger efficiencies are separately evaluated. The ERT Level-1 trigger decision is also recorded in the MB events. Thus, electrons in the MB data are used for determination of both trigger efficiencies and efficiencies for each EMC2x2 and RICH supermodules are determined to be implemented in the PISA simulation. RICH has 8 sectors with 32 supermodules in each, resulting in a total of 256 supermodules, and the EMCal has 2 PbGl sectors with 32 supermodules in each and 6 PbSc sectors with 18 supermodules in each, resulting in a total of 172 supermodules. In addition, efficiencies for each EMCal sector are also determined for the PYTHIA-based simulation because it is very difficult to introduce the concept of the trigger supermodule into the PYTHIA-based simulation.

First, the p_T distribution for all single electrons, that is, tracks which pass through the standard eID cuts in the MB data sample is built, then it is compared to the p_T distribution for electrons which are obtained with the additional requirement of having an associated fired trigger tile. Therefore, the EMC2x2 and RICH trigger efficiencies for single electrons are given by the ratio of the above two p_T distributions:

$$\varepsilon^{e^\pm}_{EMC2x2}(p_T) = \frac{dN^{e^\pm}_{MB\cap EMC2x2}/dp_T}{dN^{e^\pm}_{MB}/dp_T}, \tag{5.47}$$

$$\varepsilon^{e^\pm}_{RICH}(p_T) = \frac{dN^{e^\pm}_{MB\cap RICH}/dp_T}{dN^{e^\pm}_{MB}/dp_T}, \tag{5.48}$$

where $N^{e^\pm}_{MB\cap EMC2x2(RICH)}, N^{e^\pm}_{MB}$ are the number of electrons with and without an associated fired EMC2x2 (RICH) trigger tile in the MB events.

The left and right panels in Fig. 5.30 show the p_T distributions and the EMC2x2 trigger efficiency for the EMC2x2 supermodule in the run group G1 (the energy threshold is 600 MeV, see Section 5.7). The closed and open symbols show the results for all electrons and triggered electrons falling into this supermodule in the left panel. The EMC2x2 efficiency for each supermodule is parameterized by fitting to the data with the following function:

$$f^{fit}_{EMC2x2}(p_T) = \frac{p0}{e^{-(p_T-p1)/p2}+1}\cdot\frac{p6}{e^{-(p_T-p7)/p8}+1}+\left(1-\frac{p6}{e^{-(p_T-p7)/p8}+1}\right)\cdot\frac{p3}{e^{-(p_T-p4)/p5}+1}, \tag{5.49}$$

where, $p0-p8$ are the free parameters for fitting and functions with $p0-p2$ and $p3-p5$ describe the low and high p_T regions. The fit result to the data points with Eq. 5.49 is shown as a line in the right panel of Fig. 5.30. The fit result for each EMC2x2 supermodule is implemented into the PISA simulation to evaluate the ERT trigger efficiency for e^+e^- pairs.

Figure 5.31 shows the p_T distributions and the RICH trigger efficiency for the RICH supermodule in the run group G1. The closed and open symbols show the results for all and triggered electrons. The RICH trigger efficiency for each super-

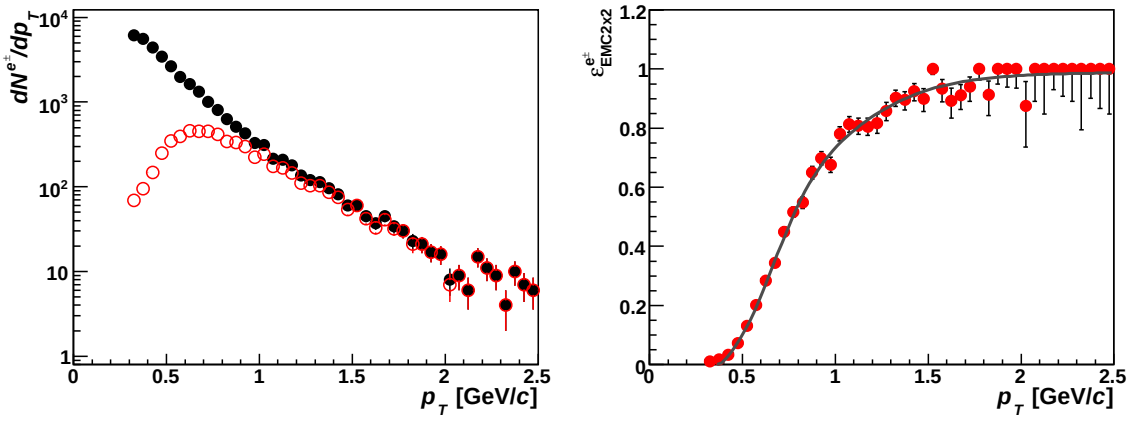

Figure 5.30: Left: The p_T distributions for all electrons and triggered electrons falling into this supermodule as shown by the closed and open symbols. Right: The EMC2x2 trigger efficiency for this supermodule. The fit result with Eq. 5.49 is shown as a line.

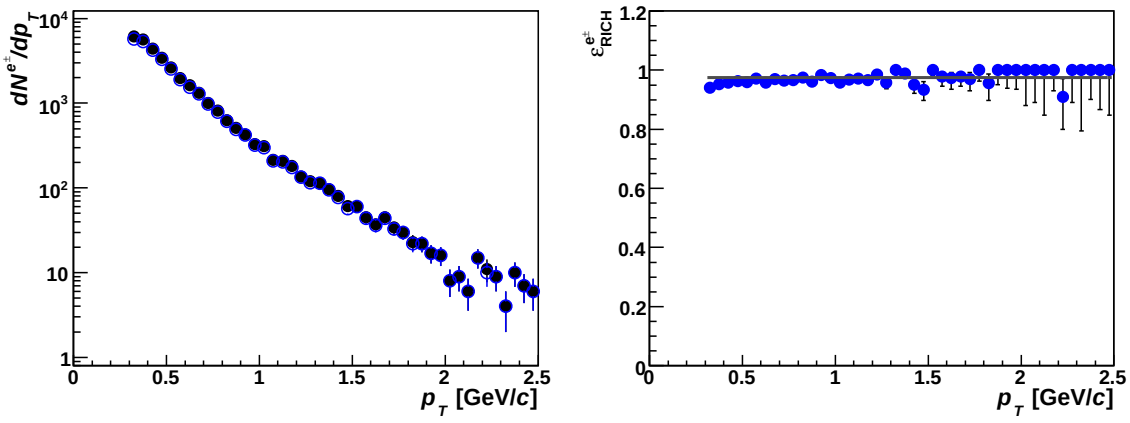

Figure 5.31: Left: The p_T distributions for all electrons and triggered electrons falling into this supermodule as shown by the closed and open symbols. Right: The RICH trigger efficiency for this supermodule. The data points are fitted with a constant shown as a line.

module is parameterized by fitting with a constant value as same as the EMC2x2 trigger efficiency.

The ERT trigger efficiency for e^+e^- pairs, ε_{ERT}^{pair} is evaluated using the PISA simulation including the parameterized EMC2x2 and RICH trigger efficiencies for each supermodule, and this simulation is the same one used for calculation of the acceptance and pair cuts efficiency. ε_{ERT}^{pair} is calculated as:

$$\varepsilon_{ERT}^{pair}(p_T^{ee}, m_{ee}) = \frac{d^2N_{ERT}^{pair}/dp_T^{ee}dm_{ee}}{d^2N_0^{pair}/dp_T^{ee}dm_{ee}}, \tag{5.50}$$

where N_{ERT}^{pair} is the number of e^+e^- pairs in which at least one electron fires both EMC2x2 and RICH triggers, and N_0^{pair} is the number of e^+e^- pairs in the PHENIX acceptance. Figure 5.32 shows the ERT trigger efficiency for e^+e^- pairs as a function of m_{ee} in $2.5 \leq p_T^{ee} < 2.6$ GeV/c. The fit result with a third-order polynomial function

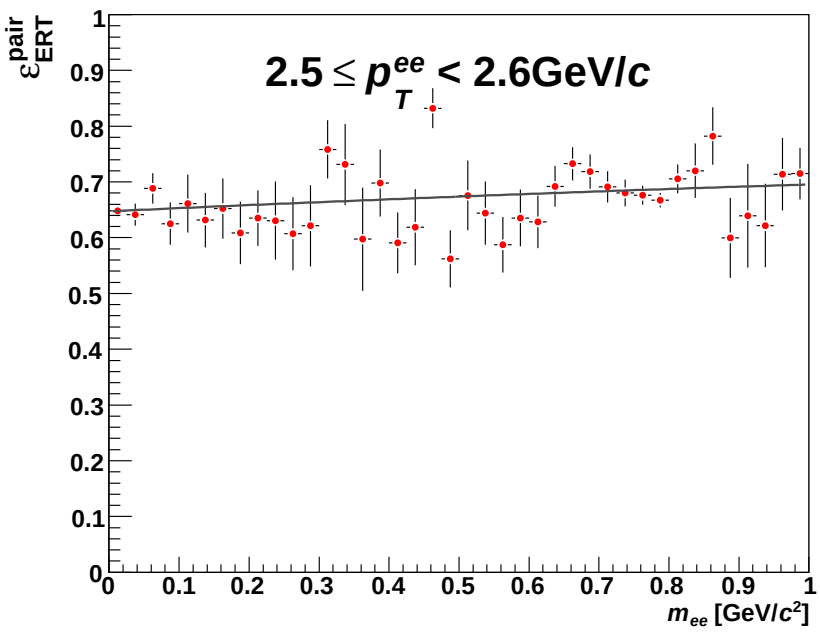

Figure 5.32: The ERT trigger efficiency for e^+e^- pairs as a function of m_{ee} in $2.5 \leq p_T^{ee} < 2.6$ GeV/c.

in $0 < m_{ee} < 1.1$ GeV/c^2 shown as a solid line is used for the correction as same as the acceptance and pair cuts efficiency.

Figure 5.33 shows the mean values of the ERT trigger efficiency for e^+e^- pairs in $0.00 < m_{ee} < 0.05$ GeV/c^2 and $0.10 < m_{ee} < 0.30$ GeV/c^2 as a function of p_T^{ee}. These mean values are calculated using the obtained fit function for every 0.1 GeV/c-p_T^{ee} as shown in Fig. 5.32. The closed and open symbols show the mean values in $0.00 < m_{ee} < 0.05$ GeV/c^2 and $0.10 < m_{ee} < 0.30$ GeV/c^2, respectively. The ERT trigger efficiency for e^+e^- pairs is almost flat in $p_T^{ee} > 2.0$ GeV/c.

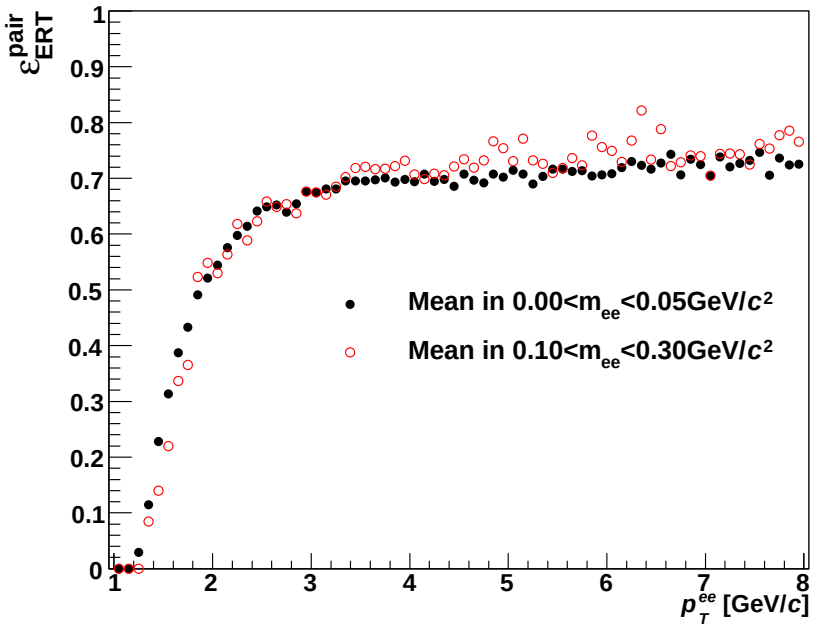

Figure 5.33: Mean values of the ERT trigger efficiency for e^+e^- pairs in $0.00 < m_{ee} < 0.05$ GeV/c^2 and $0.10 < m_{ee} < 0.30$ GeV/c^2 as a function of p_T^{ee}. The closed and open symbols show the mean values in $0.00 < m_{ee} < 0.05$ GeV/c^2 and $0.10 < m_{ee} < 0.30$ GeV/c^2, respectively.

5.10 Hadronic Cocktail Calculation

A fast Monte Carlo simulation for known hadron decays has been developed in the PHENIX experiment and it is called 'EXODUS'. EXODUS can also play a role as an event generator for hadron decays to generate input events to the PISA simulation for calculations of efficiencies and the acceptance. The key input for EXODUS is the invariant cross sections of neutral and charged pions in d+Au collisions measured by the PHENIX experiment [50, 51]. The neutral and charged pion data are parameterized by a fit with a modified Hagedorn function:

$$E\frac{d^3N}{dp^3} = A\left(e^{-\left(a\cdot p_T + b\cdot p_T^2\right)} + p_T/p_0\right)^{-n} \tag{5.51}$$

with $A = 35.37\pm0.46\ \mathrm{GeV}^{-2}, a = 0.335\pm0.003\ (\mathrm{GeV}/c)^{-1}, b = 0.094\pm0.001\ (\mathrm{GeV}/c)^{-2}, p_0 = 0.776 \pm 0.002\ \mathrm{GeV}/c$, and $n = 8.301 \pm 0.003$.

The measured invariant cross sections of $\pi^0, \pi^\pm, \eta, K^\pm, \omega, \phi$, and J/ψ in d+Au collisions are shown in Fig. 5.34. The fit of the neutral and charged pion data with Eq. 5.51 is shown as a solid line.

The modified Hagedorn parameterization of the pion data with an assumption of the m_T scaling is applied to the other mesons, that is, the functions expressed by Eq. 5.51 with a replacement of p_T by $m_T = \sqrt{(p_T/c)^2 - m_{\pi^0}^2 + m_h^2}$ are fitted to the measured cross sections of the other mesons with a free normalization factor. Here, m_{π^0}, m_h are the masses of π^0 and the other mesons. The m_T scaling fit results for the other mesons are also shown as dotted lines. The good description of the data by the fits indicates that meson production in d+Au collisions follows the m_T scaling of the pion spectrum just as good as p+p collisions [75]. In particular, the m_T scaling description for mesons is strongly supported by the fact that the kaons follow the same m_T scaling prediction of the η due to their similar masses ($m_\eta = 547.8\ \mathrm{MeV}/c^2, m_K = 493.7\ \mathrm{MeV}/c^2$). In accordance with this, the m_T scaling is extended to other mesons which are not measured yet in the PHENIX experiment for d+Au collisions such as η', ρ, ψ'. The particle ratios of the meson yields to the pion yield are listed together with reference data for mesons in Table 5.8. The particle ratios for η', ρ, ψ' for which data in d+Au collisions are not available is assumed as the same values in p+p collisions [75]. A precision of the η/π^0 ratio is crucial, since the direct virtual photon contribution is extracted from the e^+e^- mass spectrum using the η dominant mass region. A systematic uncertainty on the η/π^0 ratio of 6.25% arises from the measured value of 0.48 ± 0.03 at the PHENIX experiment [51]. Figure 5.35 shows the measured yield over the m_T scaling function for η. A constant fit to the data gives 1.0 ± 0.044. The solid and dotted lines indicate the mean value and $\pm1\sigma$ of the constant fit. The m_T scaling function for η as an input for EXODUS is determined with a smaller uncertainty than the uncertainty on the measured value of 6.25%.

Once the yields and p_T spectra for mesons are implemented in EXODUS, the e^+e^- pair distributions are given by decay kinematics and branching ratios. The

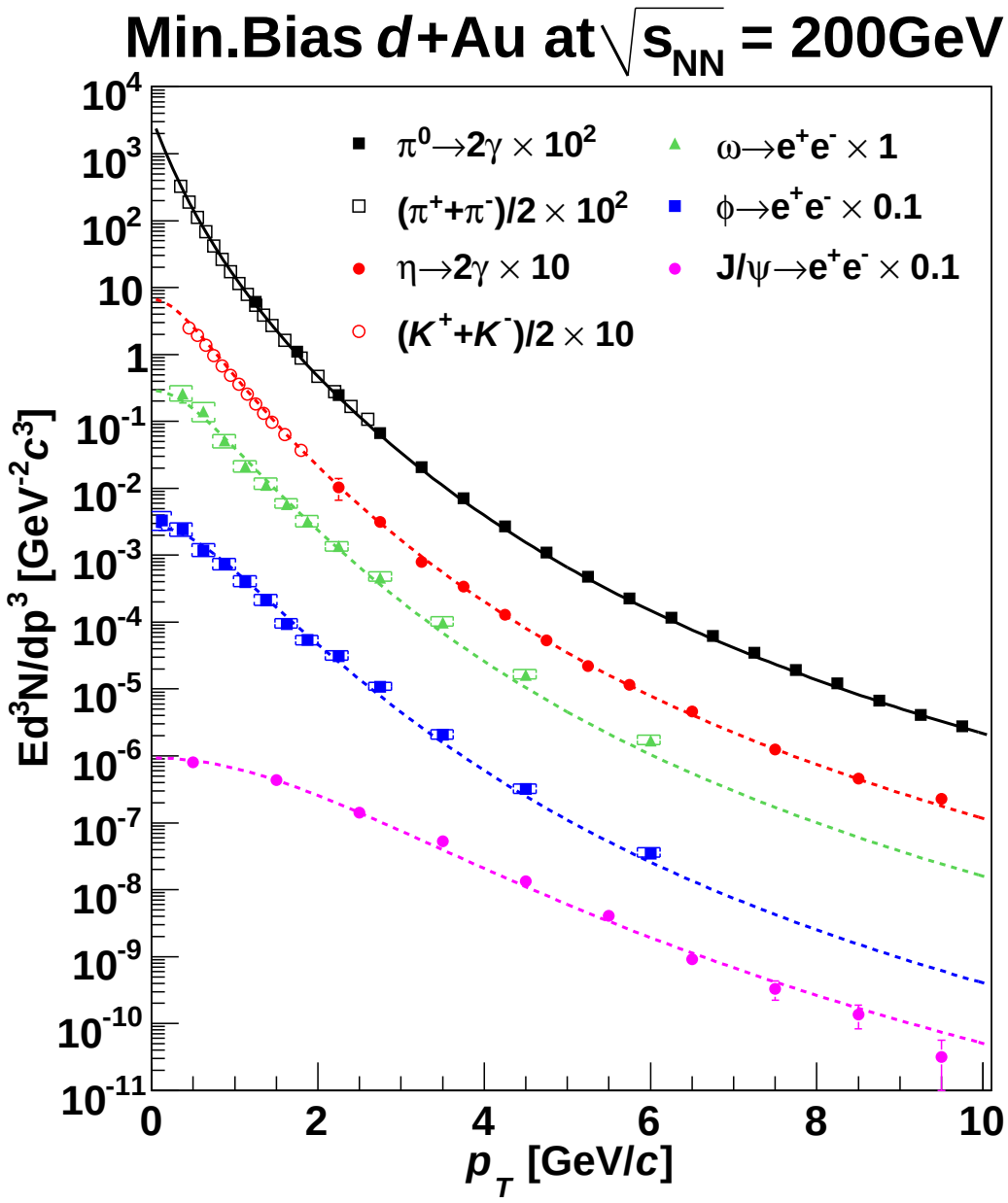

Figure 5.34: The compilation of meson production cross sections in d+Au collisions at $\sqrt{s_{NN}} = 200$ GeV together with m_T scaled modified Hagedorn functions determined by a fit to the pion data. Shown are data for π^0 [51], $\pi^{\pm}$ [50], η [51], $K^{\pm}$ [50], ω [79], ϕ [79], and J/ψ [80].

Table 5.8: The normalization factors of the meson yields to the pion yield with uncertainties.

	meson/π^0	uncertainty	reference	available d+Au data
π^0	1.0	–	Ref [51]	yes
η	0.1265	6.25%	Ref [51, 81]	yes
ω	0.10515	6.67%	Ref [79, 82]	yes
η'	0.0127	30.0%	Ref [75, 83]	no
ϕ	0.012448	30.0%	Ref [79, 82]	yes
ρ	0.0834	30.0%	Ref [75, 83]	no
J/ψ	0.0000196	–	Ref [80]	yes
ψ'	0.0000023	–	Ref [75]	no

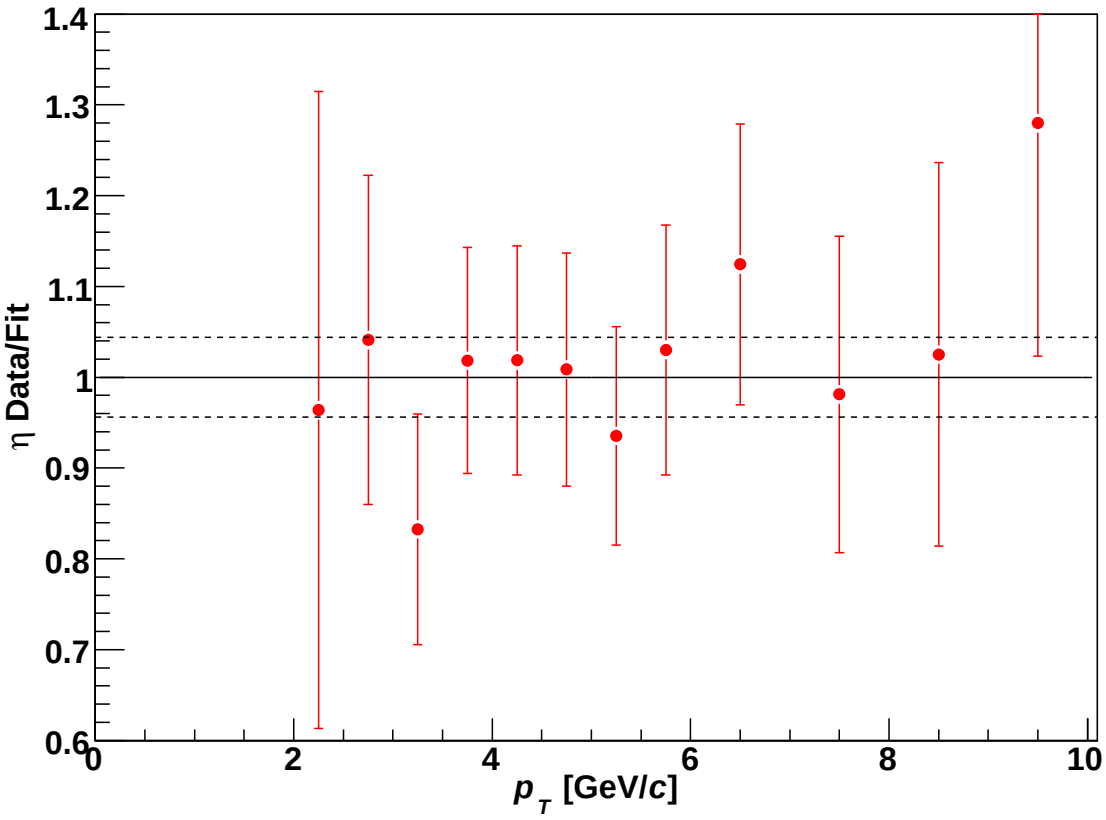

Figure 5.35: The measured yield over the m_T scaling function for η. A constant fit to the data gives 1.0 ± 0.044, which is smaller than the uncertainty on the measured value of 6.25%.

branching ratios are taken from the compilation of particle properties in ref. [69]. For the Dalitz decays of $\pi^0, \eta, \eta' \to \gamma e^+e^-$ and the decay of $\omega \to \pi^0 e^+e^-$, the Kroll-Wada expression [33] is used with electromagnetic transition form factors measured by the Lepton-G collaboration [34, 84]. All vector mesons are assumed to be unpolarized and the expression derived by Gounaris and Sakurai [85] is used for the decays of $\rho, \omega, \phi \to e^+e^-$. The same expression including radiative corrections, which is discussed in ref. [86], is used for $J/\psi, \psi' \to e^+e^-$.

Simulated Hadron Decays

The following hadron decays are generated by EXODUS as an input to the PISA simulation for calculations of efficiencies and the acceptance.

- $\pi^0 : \pi^0 \to \gamma e^+e^-, \pi^0 \to 2e^+e^-$
- $\eta : \eta \to \gamma e^+e^-, \eta \to 2e^+e^-$
- $\omega : \omega \to e^+e^-, \omega \to \pi^0 e^+e^-$
- $\eta' : \eta' \to \gamma e^+e^-$
- $\phi : \phi \to e^+e^-, \phi \to \eta e^+e^-$
- $\rho : \rho \to e^+e^-$
- $J/\psi : J/\psi \to e^+e^-$
- $\psi' : \psi' \to e^+e^-$

Hadrons with the above decays are generated in $|z\text{-vertex}| < 30$ cm, $|y| < 0.5$ and $0 \leq \phi < 2\pi$ with a flat distribution each.

5.11 Determination of Direct Virtual Photon Fraction

As discussed in Section 2.3, the direct virtual photon fraction in the e^+e^- mass spectrum is determined by utilizing the e^+e^- mass shape difference due to the process dependent factor S in Eq. 2.14. Figure 5.36 shows the number of e^+e^- pairs in the p_T^{ee}-m_{ee} space from the MB data and the ERT data. The p_T^{ee} cutoff around $p_T^{ee} = 0.6$ GeV/c in the MB data is due to the p_T threshold of 0.3 GeV/c for single electrons, and the cutoff around $p_T^{ee} = 1.2$ GeV/c in the ERT data is caused by the p_T threshold of 0.9 GeV/c for triggered electrons. Thus, the e^+e^- pair mass spectrum from the MB data is used for only the lowest p_T bin ($1.0 < p_T < 1.5$ GeV/c) and e^+e^- spectra from the ERT triggered data are used for $p_T > 1.5$ GeV/c since the

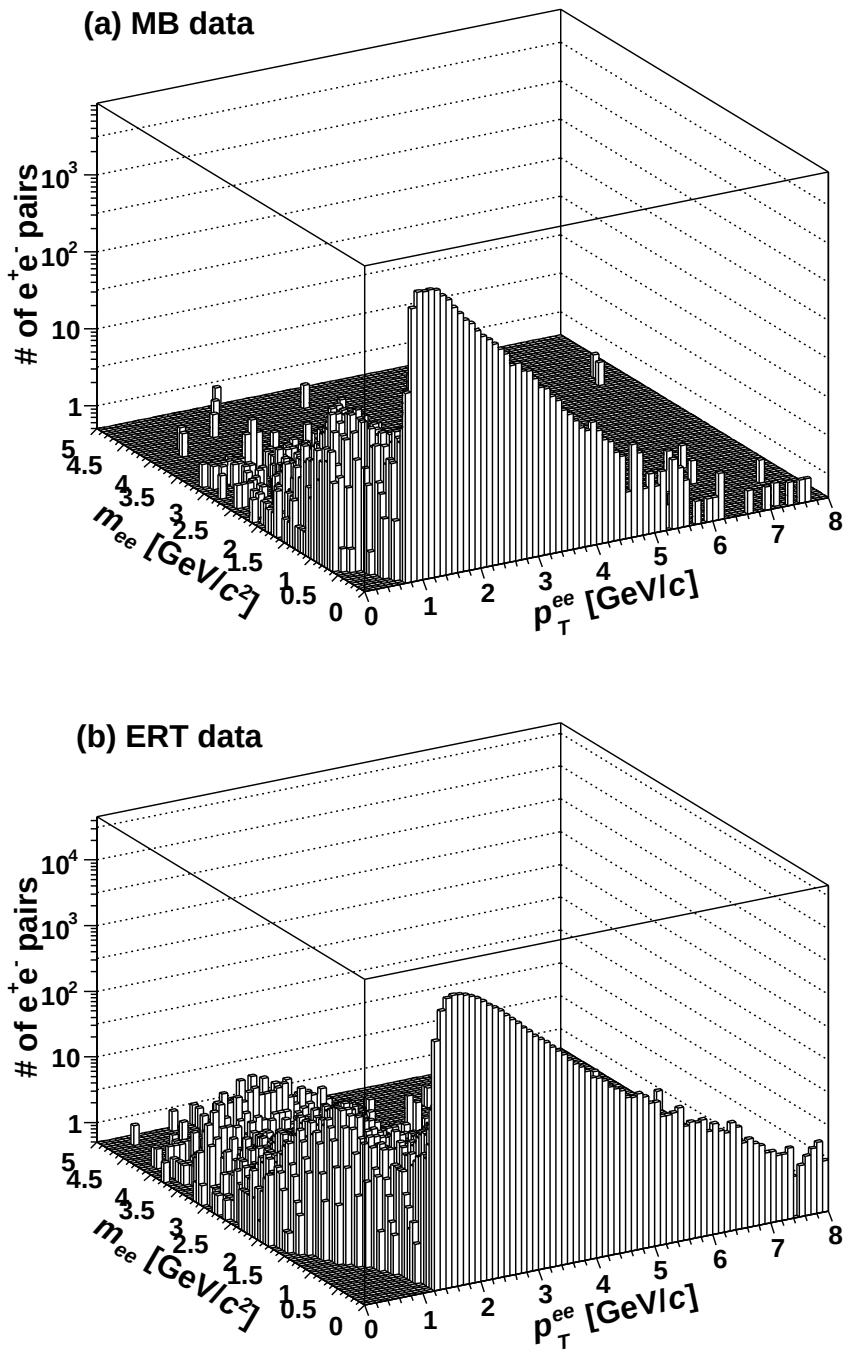

Figure 5.36: The number of e^+e^- pairs in the p_T^{ee}-m_{ee} space from (a) the MB data and (b) the ERT data. The p_T^{ee} cutoffs occur due to the p_T threshold of 0.3 GeV/c for single electrons in the MB data and due to the p_T threshold of 0.9 GeV/c for triggered electrons in the ERT data, respectively.

ERT triggered data have much more statistics in $p_T > 1.5$ GeV/c. After this section, all real e^+e^- pair mass spectra are already corrected as Eq. 5.1.

The kinematic region in $0.1 < m_{ee} < 0.3$ GeV/c^2 and $p_T > 1.0$ GeV/c is selected to extract the direct virtual photon contribution from the e^+e^- mass spectrum. This region satisfies the following conditions:

1. It is ensured that the important assumption that the S factor for the direct virtual photon decay is almost unity at $m_{ee} \ll p_T$ even in the lowest p_T bin ($1.0 < p_T < 1.5$ GeV/c).

2. The signal to background ratio for the direct virtual photon signal is improved dramatically since the π^0 contribution is suppressed due to the π^0 mass (=135 MeV/c^2).

3. Little contribution from other sources of e^+e^- pairs is expected since $\pi^+\pi^- \rightarrow e^+e^-$ can only contribute for $m_{ee} \geq 2m_\pi$.

4. The contribution of $c\bar{c} \rightarrow e^+e^-$ with semi-leptonic decays is minimized.

The enhanced yield over the known hadron decay contribution is assumed to be entirely due to virtual direct photon decays and the following 2-component function, f_{fit} is fitted to the data to quantify the enhanced e^+e^- pair yield.

$$f_{fit}(m_{ee} : r_{\gamma^*}) = (1 - r_{\gamma^*}) \cdot f_c(m_{ee}) + r_{\gamma^*} \cdot f_{dir}(m_{ee}), \tag{5.52}$$

where $f_c(m_{ee})$ is the shape of the hadronic cocktail mass spectrum, $f_{dir}(m_{ee})$ is the expected shape of the direct virtual photon internal conversion mass spectrum and r_{γ^*} is the only fit parameter. The both functional forms of $f_c(m_{ee})$ and $f_{dir}(m_{ee})$ is calculated using the fast Monte Carlo simulation, EXODUS which takes into account the PHENIX acceptance and detector effects such as finite mass resolution.

Both $f_c(m_{ee})$ and $f_{dir}(m_{ee})$ are separately normalized to the data for $m_{ee} < 0.05$ GeV/c^2. In this low mass region, the form factor $F(m)$ of the Dalitz decay is very close to unity by definition and then the relation between photon and e^+e^- pair productions for the Dalitz decay, Eq. 2.23 can be simplified as:

$$\frac{d^2 n_{ee}^{Dalitz}}{dm_{ee}} = \frac{2\alpha}{3\pi}\frac{1}{m_{ee}}\sqrt{1 - \frac{4m_e^2}{m_{ee}^2}}\left(1 + \frac{2m_e^2}{m_{ee}^2}\right)\left(1 - \frac{m_{ee}^2}{m_h^2}\right)^3 dn_\gamma^{Dalitz}. \tag{5.53}$$

The difference on the e^+e^- pair emission rates for direct virtual photon decays and Dalitz decays is generated only by $(1 - m_{ee}^2/m_h^2)^3$. From the integration of $(1 - m_{ee}^2/m_h^2)^3$ in $m_{ee} < 0.05$ GeV/c^2 for π^0, the difference between direct virtual photon and π^0 Dalitz decays is only about 4%. The differences between direct virtual photon and Dalitz decays of other mesons $(\eta, \eta', \omega, \phi)$ are much smaller than 4% as the difference for π^0 Dalitz decays. Therefore the factor $S(m_{ee})$ of the Dalitz decays

is very close to unity. The functional shapes of f_c and f_{dir} are essentially identical to $\sqrt{1-4m_e^2/m_{ee}^2}\,(1+2m_e^2/m_{ee}^2)\,/m_{ee}$. This means that the fit function $f_{fit}(m_{ee} : r_{\gamma^*})$ is independent of the fit parameter r_{γ^*} in this low mass region. Thus it is ensured that the yield of the fit function $f_{fit}(m_{ee} : r_{\gamma^*})$ is always normalized to the data for $m_{ee} < 0.05$ GeV/c^2. The parameter r_{γ^*} can be interpreted as the direct photon fraction of the inclusive photon yield.

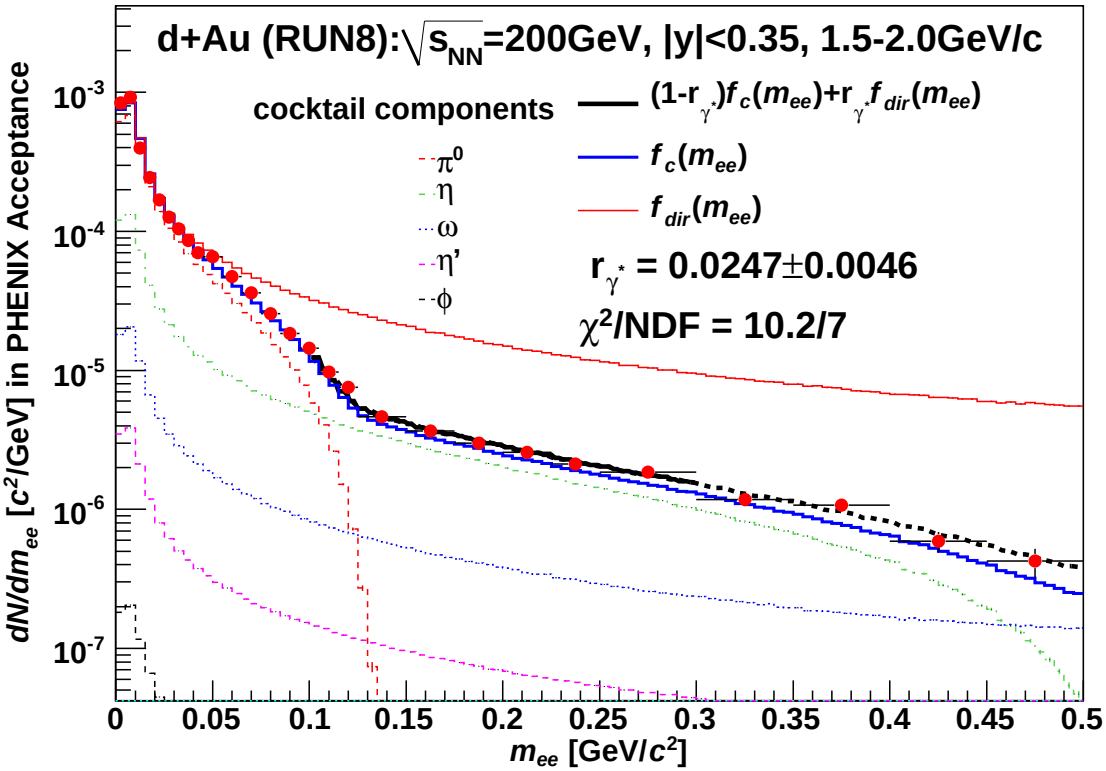

Figure 5.37: The e^+e^- pair mass spectrum in $1.5 < p_T^{ee} < 2.0$ GeV/c together with the fit result as the solid line and the cocktail components. The dashed line shows $f_{fit}(m_{ee})$ extended over out of the fit range and it can also well describe the data in above the fit range.

Figure 5.37 shows the e^+e^- pair mass spectrum in $1.5 < p_T^{ee} < 2.0$ GeV/c together with the fit result and the cocktail components. The symbols show the data and the blue solid line shows the hadronic cocktail contribution with each hadron decay component as a colored dotted line, and the red solid line indicates the shape of $f_{dir}(m_{ee})$ normalized to the data for $m_{ee} < 0.05$ GeV/c^2. The fit result is shown as the black solid line and its extended result in above the fit range is also shown as the black dotted line together with the data points. The fit function seems to well describe the data even in $m_{ee} > 0.3$ GeV/c^2. The e^+e^- mass spectra together with fit results for other p_T^{ee} bins are shown in Appendix A.1. The direct virtual photon fractions for

all p_T bins are summarized together with χ^2/NDF for fitting in Table 5.9.

Table 5.9: Summary of the fit results with Eq. 5.52 in the range $0.10 < m_{ee} < 0.30$ GeV/c^2.

p_T^{ee} [GeV/c]	r_{γ^*}	χ^2/NDF
1.0-1.5	0.0341±0.0160	6.3/5
1.5-2.0	0.0247±0.0046	10.2/7
2.0-2.5	0.0519±0.0048	13.9/7
2.5-3.0	0.0386±0.0064	5.3/7
3.0-3.5	0.0648±0.0102	9.6/7
3.5-4.0	0.0766±0.0156	6.5/5
4.0-4.5	0.0697±0.0222	5.2/5
4.5-5.0	0.1158±0.0334	3.9/5
5.0-5.5	0.0829±0.0435	6.1/5
5.5-6.0	0.0261±0.0518	6.4/5

The validity of the assumption that the excess is entirely due to direct virtual photon internal conversions with $S(m_{ee}) = 1$, *i.e.* direct virtual photons from purely point-like processes is examined from the data. Here $f_{dir}(m_{ee})$ is normalized to the data for $m_{ee} < 0.05$ GeV/c^2 and it can be also expressed in a simple form as Eq. 2.15:

$$f_{dir}(m_{ee}, p_T^{ee}) \simeq \varepsilon_{PHENIX} \frac{1}{m_{ee}} \frac{dN_\gamma^{incl}(p_T^{ee})}{dp_T^{ee}}, \tag{5.54}$$

where ε_{PHENIX} means the efficiency including detector effects and acceptance of the PHENIX detector. A ratio of $R(m_{ee}) = (\text{data} - \text{cocktail})/f_{dir}(m_{ee})$ for each p_T bin is calculated as:

$$\begin{aligned} R(m_{ee}, p_T^{ee}) &\simeq \frac{dN_{ee}^{excess}(m_{ee}, p_T^{ee})}{dp_T^{ee}} \Big/ \left(\varepsilon_{PHENIX} \frac{1}{m_{ee}} \frac{dN_\gamma^{incl}(p_T^{ee})}{dp_T^{ee}} \right), && (5.55) \\ &= \left(\varepsilon_{PHENIX} \frac{dN_{\gamma^*}^{direct}(m_{ee}, p_T^{ee})}{dp_T^{ee}} \right) \Big/ \left(\varepsilon_{PHENIX} \frac{dN_\gamma^{incl}(p_T^{ee})}{dp_T^{ee}} \right), && (5.56) \\ &= S(m_{ee}, p_T^{ee}) dN_\gamma^{direct}(p_T^{ee}) / dN_\gamma^{incl}(p_T^{ee}). && (5.57) \end{aligned}$$

Thus $R(m_{ee}, p_T^{ee})$ is a good indicative valuable to test that the excess yield has the expected shape for the internal conversion of direct photons. In addition, it can reveal the m_{ee} dependence of the factor S for direct virtual photons.

Figure 5.38 shows the R as a function of m_{ee} for $1.5 < p_T^{ee} < 2.0$ GeV/c. The yellow band indicates the measured r_{γ^*} value within $\pm 1\sigma$ of statistical errors. The ratio can not be measured for $m_{ee} < 0.1$ GeV/c^2 because the direct virtual photon signal is masked by the π^0 Dalitz decay contribution in this mass region. The R seems to be consistent with the measured r_{γ^*} value as well as other p_T bins shown

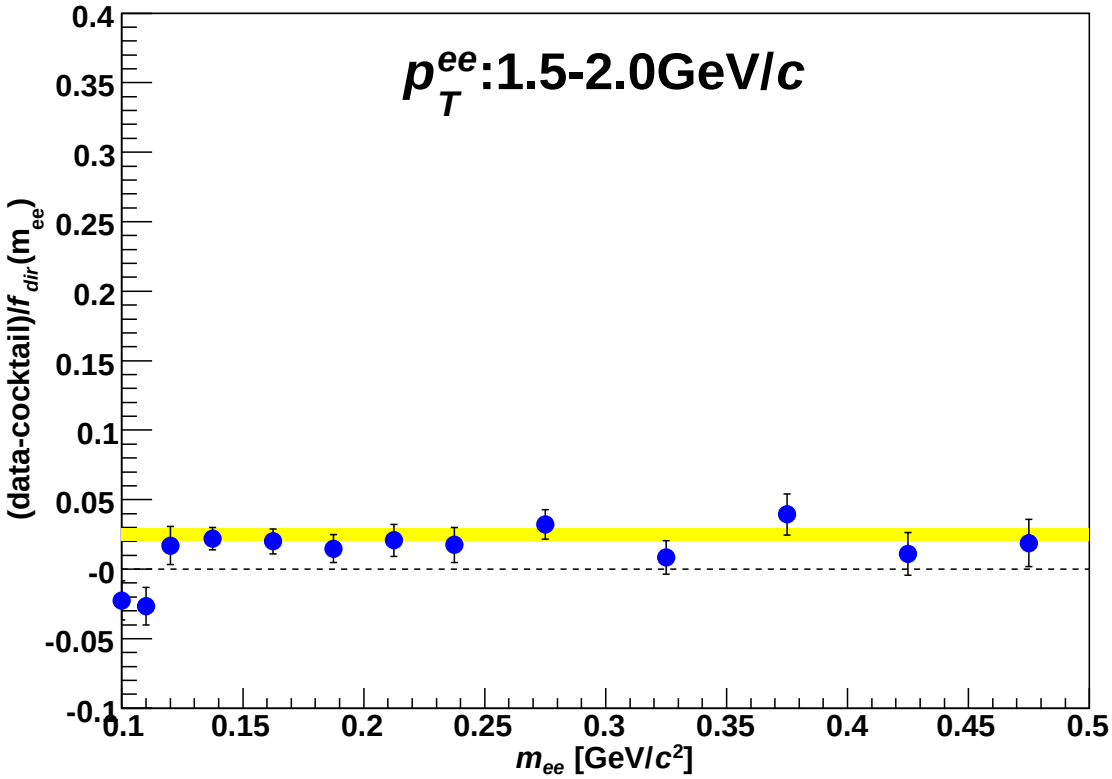

Figure 5.38: The R as a function of m_{ee} for $1.5 < p_T^{ee} < 2.0$ GeV/c. The yellow band indicates the measured r_{γ^*} value within $\pm 1\sigma$ of statistical errors.

in Appendix A.2. This observed behavior of $R(m_{ee})$ demonstrates that the factor S for direct virtual photons is almost unity in the kinematic region for determination of r_{γ^*}.

5.12 Inclusive Photon Spectrum

The direct virtual photon fractions are obtained from the shape analysis of the e^+e^- pair mass spectra. The inclusive photon spectrum is needed in order to convert the obtained direct virtual photon fraction to the real direct photon yield as Eq. 5.2. The inclusive photon spectrum can be also determined from the e^+e^- pair yield in the very low mass region ($m_{ee} < 0.05$ GeV/c^2). The way to determine the inclusive photon yield and its result are described in this section.

The measured e^+e^- pair mass spectrum is already corrected for the ideal PHENIX acceptance. Thus, the measured yield of e^+e^- pairs, $N_{ee}^{data}(p_T^{ee})$ in $m_{ee} < m_{max} = 0.05$ GeV/c^2 for a given p_T bin can be written as:

$$N_{ee}^{data}(p_T^{ee}) = \varepsilon_{PHENIX} \times (1 + \delta\varepsilon) \times C^{incl}(m_{max}) \times \frac{dN_\gamma^{incl}}{dp_T}, \tag{5.58}$$

where ε_{PHENIX} and $\delta\varepsilon$ are the ideal PHENIX acceptance and its error at the correction of the data, and dN_γ^{incl}/dp_T means the inclusive photon yield in a given p_T bin. The factor $C(m_{max})$ is the conversion probability of a photon to an e^+e^- pair for $m_{ee} < m_{max}$ and it can be expressed as Eq. 5.59 since the process dependent factor $S(m_{ee})$ is very close to unity in the low mass region ($m_{max} = 0.05$ GeV/c^2) regardless a production process as already discussed in the previous section.

$$C(m_{max}) = \frac{2\alpha}{3\pi} \int_0^{m_{max}} \frac{1}{m_{ee}} \sqrt{1 - \frac{4m_e^2}{m_{ee}^2}} \left(1 + \frac{2m_e^2}{m_{ee}^2}\right) dm_{ee}. \tag{5.59}$$

The similar equation to Eq. 5.58 for the hadronic cocktail calculation can be also written as:

$$N_{ee}^{cock}(p_T^{ee}) = \varepsilon_{PHENIX} \times C^{cock}(m_{max}) \times \frac{dN_\gamma^{cock}}{dp_T}, \tag{5.60}$$

where, dN_γ^{cock}/dp_T is the photon spectrum from known hadron decays calculated by EXODUS.

According to the measured direct virtual photon fraction r_{γ^*} summarized in Table 5.9, the maximum value of direct photon contribution in the inclusive photon yield is about 10%. Since the π^0 and η contributions in the hadron decay photon yield are about 80% and 20%, the difference betweem $C^{incl}(m_{max})$ and $C^{cock}(m_{max})$ is less than 0.4% (it is negligibly small). Therefore, comparing Eq. 5.58 with Eq. 5.60, we get

$$\frac{dN_\gamma^{incl}}{dp_T} = \frac{N_{ee}^{data}}{N_{ee}^{cock}} \times \frac{dN_\gamma^{cock}}{dp_T} \times \frac{1}{1 + \delta\varepsilon}. \tag{5.61}$$

From Eq. 5.61, the real inclusive photon yield in the data can be determined by the comparison of the e^+e^- pair yield in the low mass peak for the data and the hadronic cocktail calculation. The systematic error on this method shown as $\frac{1}{1+\delta\varepsilon}$ is the absolute systematic error on the acceptance and efficiency correction for the data and it will be discussed in Section 5.13.2.

Figure 5.39 shows the inclusive real photon spectrum in d+Au collisions determined from the e^+e^- pair yields in the data and the photon cocktail calculation for known hadron decays as shown in Eq. 5.61. The data points are plotted at the average point in each 0.5 GeV/c-bin, $\langle p_T \rangle$. The ratio $\frac{N_{ee}^{data}}{N_{ee}^{cock}}$ is consistent with 1 within about 15% for all p_T bins.

5.13 Systematic Error Evaluation

The ways to evaluate systematic errors due to various sources are described in this section.

5.13.1 Systematic Errors on r_{γ^*}

At determination of direct virtual photon fractions, the cocktail calculation is normalized to the data for $m_{ee} < 0.05$ GeV/c^2 for each p_T bin. Thus, it is important for evaluating systematic errors on direct virtual photon fraction correctly to understand how affects the modification of the e^+e^- pair mass shape due to possible systematic sources to the resulting direct virtual photon fraction. The possible sources of the systematic errors on the direct virtual photon fraction are separated into those can modify the e^+e^- mass shapes in the real data and in the cocktail calculation, and they are listed below together with the related sections:

Sources related to the real data

1. background normalization (Section 5.8.4)
2. efficiency correction function (Section 5.9)

Sources related to the cocktail calculation

1. particle composition (Section 5.10)
2. parameterization of the measured pion cross section (Section 5.10)
3. normalization of the cocktail calculation (Section 5.11)
4. variation of the fit range (Section 5.11)

The systematic error due to each systematic source is evaluated as the difference on the direct virtual photon fractions with nominal and modified mass shapes. The overall systematic errors are calculated in quadrature.

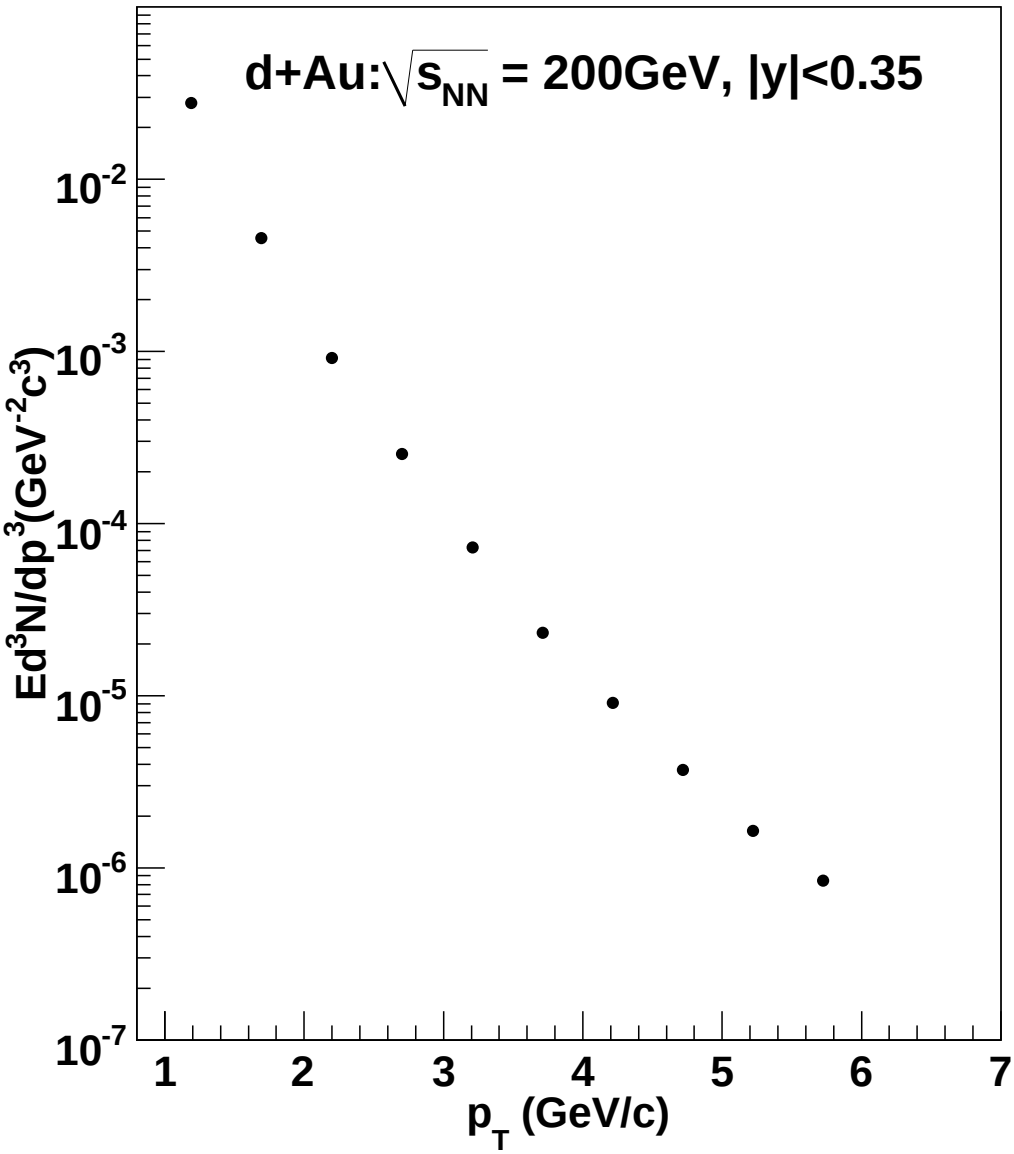

Figure 5.39: The inclusive real photon spectrum in d+Au collisions determined from the e^+e^- pair yields in the data and the photon cocktail calculation for known hadron decays as shown in Eq. 5.61.

Background Normalization

The background pairs are separated into pairs from the three different sources, *i.e.* combinatorial pairs, cross pairs and jet pairs. The contribution of each background component is determined by the 3-component fit with Eq. 5.40 as already described in Section 5.8.4. The e^+e^- mass shapes of these background pairs are different as shown in Fig. 5.24 and the effects from the mass shape modification due to uncertainties of normalization factors for these background pair contributions should be evaluated.

The normalization factor for one of the three background components is set to $\pm 1\sigma$ values from the nominal one, and then the normalization factors for the other two components are determined by fitting to the data with Eq. 5.40. The differences of the resulting direct virtual photon fractions with $\pm 1\sigma$ variation of the normalization factors from the nominal value for each p_T bin are summarized in Table 5.10. The quadratic sum of these values are assigned as the systematic error due to the uncertainty of background normalization.

Table 5.10: The differences of the resulting direct virtual photon fractions with $\pm 1\sigma$ variation of the normalization factors (for combinatorial, jet and cross pairs) from the nominal value.

p_T [GeV/c]	comb.:$+1\sigma$	comb.:-1σ	jet:$+1\sigma$	jet:-1σ	cross:$+1\sigma$	cross:-1σ
1.0-1.5	–0.0011	+0.0013	+0.0014	–0.0014	+0.0001	+0.0011
1.5-2.0	–0.0019	+0.0001	+0.0004	–0.0022	–0.0010	–0.0008
2.0-2.5	–0.0016	+0.0003	+0.0004	–0.0018	–0.0007	–0.0006
2.5-3.0	–0.0014	+0.0003	+0.0004	–0.0015	–0.0006	–0.0005
3.0-3.5	–0.0016	+0.0005	+0.0006	–0.0017	–0.0006	–0.0005
3.5-4.0	–0.0015	+0.0003	+0.0004	–0.0015	–0.0005	–0.0006
4.0-4.5	–0.0023	+0.0005	+0.0006	–0.0024	–0.0011	–0.0006
4.5-5.0	–0.0027	+0.0007	+0.0007	–0.0028	–0.0014	–0.0007
5.0-5.5	–0.0026	+0.0009	+0.0010	–0.0027	–0.0013	–0.0004
5.5-6.0	–0.0038	+0.0008	+0.0009	–0.0039	–0.0023	–0.0008

Efficiency Correction Function

Uncertainties in the efficiency correction functions is one of the systematic error sources on the direct virtual photon fraction. The nominal fit mass range for determination of the efficiency correction function is $0 < m_{ee} < 1.1$ GeV/c^2. The variations of the efficiency correction function with different fit ranges ($0 < m_{ee} < 1.0, 1.1, 1.2$ GeV/c^2) are assigned as uncertainties in the efficiency correction function. Then the differences on the direct photon fraction due to the variations of the efficiency correction function are evaluated as systematic errors as summarized in Table 5.11.

Table 5.11: The difference on the direct virtual photon fraction due to the variations of the efficiency correction function with different fit range.

p_T [GeV/c]	upper limit	lower limit
1.0-1.5	+0.0044	–0.0001
1.5-2.0	+0.0023	–0.0001
2.0-2.5	+0.0040	–0.0001
2.5-3.0	+0.0050	–0.0001
3.0-3.5	+0.0033	–0.0001
3.5-4.0	+0.0075	–0.0003
4.0-4.5	+0.0069	–0.0001
4.5-5.0	+0.0043	–0.0001
5.0-5.5	+0.0074	–0.0014
5.5-6.0	+0.0052	–0.0006

Particle Composition

Uncertainties on yield ratios of mesons to the pion yield (particle ratios) are one of the largest sources of the systematic errors on the direct virtual photon fraction. The uncertainties on particle ratios for $\eta, \omega, \eta', \phi, \rho$ are listed in Table 5.8. The effects from particle ratios for $J/\psi, \psi'$ are negligible in the fit range for determination of the direct virtual photon fraction. The hadronic cocktail calculations are carried out with $\pm 1\sigma$ variation of the particle ratio for each meson independently. Then, the differences of the direct virtual photon fraction with the nominal and $\pm 1\sigma$ varied particle compositions are evaluated for each p_T bin as summarized in Table 5.12. It is noted that the uncertainty of particle ratio for η provides a particularly large systematic error since the η contribution is dominant in the mass region for determination of the direct virtual photon fraction ($0.1 < m_{ee} < 0.3$ GeV/c^2. The quadratic sum of them are assigned as the systematic error due to the uncertainty of particle composition of the hadron decay contribution in the e^+e^- pair mass spectrum.

Parameterization of Measured Pion Cross Section

The input p_T distribution for mesons in the cocktail calculation is based on the modified Hagedorn parameterization of the measured pion data as shown in Fig. 5.34. Uncertainties of the coefficients in Eq. 5.51 can modify the e^+e^- pair mass shape from hadron decays. The upper and lower limit of the input p_T function are parameterized according to the $\pm 1\sigma$ uncertainties of the coefficients in Eq. 5.51. The hadronic e^+e^- pair mass spectra are calculated with upper and lower limits of the modified Hagedorn parameterization of the pion data. The difference on the direct virtual photon fraction for each p_T bin is summarized in Table 5.13.

Table 5.12: The differences of the direct virtual photon fraction with the nominal and $\pm 1\sigma$ varied particle compositions.

p_T [GeV/c]	η	ω	η'	ϕ	ρ	total
			$+1\sigma$			
1.0-1.5	–0.0080	–0.0026	–0.0001	–0.0003	–0.0001	–0.0084
1.5-2.0	–0.0094	–0.0032	–0.0021	–0.0009	–0.0010	–0.0102
2.0-2.5	–0.0080	–0.0019	–0.0009	–0.0001	–0.0001	–0.0082
2.5-3.0	–0.0086	–0.0022	–0.0013	–0.0001	–0.0003	–0.0090
3.0-3.5	–0.0087	–0.0031	–0.0019	–0.0003	–0.0004	–0.0095
3.5-4.0	–0.0085	–0.0028	–0.0020	–0.0001	–0.0008	–0.0092
4.0-4.5	–0.0084	–0.0025	–0.0020	–0.0001	–0.0005	–0.0090
4.5-5.0	–0.0080	–0.0024	–0.0013	–0.0005	–0.0004	–0.0085
5.0-5.5	–0.0086	–0.0033	–0.0022	–0.0009	–0.0001	–0.0095
5.5-6.0	–0.0092	–0.0030	–0.0022	–0.0005	–0.0001	–0.0099
			-1σ			
1.0-1.5	+0.0074	+0.0020	+0.0010	+0.0002	+0.0006	+0.0078
1.5-2.0	+0.0070	+0.0023	+0.0008	+0.0001	+0.0001	+0.0074
2.0-2.5	+0.0089	+0.0029	+0.0014	+0.0004	+0.0009	+0.0095
2.5-3.0	+0.0086	+0.0024	+0.0018	+0.0001	+0.0002	+0.0091
3.0-3.5	+0.0078	+0.0026	+0.0013	+0.0001	+0.0001	+0.0083
3.5-4.0	+0.0081	+0.0024	+0.0012	+0.0001	+0.0001	+0.0085
4.0-4.5	+0.0085	+0.0023	+0.0014	+0.0001	+0.0001	+0.0089
4.5-5.0	+0.0078	+0.0023	+0.0016	+0.0001	+0.0001	+0.0083
5.0-5.5	+0.0080	+0.0025	+0.0013	+0.0001	+0.0002	+0.0085
5.5-6.0	+0.0089	+0.0028	+0.0014	+0.0004	+0.0002	+0.0094

Table 5.13: The difference on the direct virtual photon fraction with the nominal and upper/lower limit of the modified Hagedorn parameterization of the pion data as an input p_T distribution for mesons in the cocktail calculation.

p_T [GeV/c]	upper limit	lower limit
1.0-1.5	+0.0014	–0.0027
1.5-2.0	+0.0008	–0.0025
2.0-2.5	+0.0017	–0.0016
2.5-3.0	+0.0014	–0.0019
3.0-3.5	+0.0013	–0.0022
3.5-4.0	+0.0011	–0.0022
4.0-4.5	+0.0009	–0.0022
4.5-5.0	+0.0013	–0.0022
5.0-5.5	+0.0015	–0.0019
5.5-6.0	+0.0014	–0.0026

Normalization of Cocktail Calculation

The difference on the finite mass resolution in the real data and the cocktail calculation results in modification of the e^+e^- pair mass shape, especially in the very low mass region used for the normalization of the cocktail calculation to the data. However it does not significantly affect the mass region for determination of the direct virtual photon fraction because this region is almost flat. Thus, the effect from the difference on the mass resolution in the real data and the cocktail calculation should be evaluated. The mass region for the cocktail normalization is varied from $m_{ee} < 0.03$ GeV/c^2 to $m_{ee} < 0.07$ GeV/c^2, then the resulting differences on the direct virtual photon fraction are calculated as summarized in Table 5.14.

Variation of Fit Range

A selection of the mass range for determination of the direct virtual photon fraction is one of the systematic error sources. The direct virtual photon signal is not significant in $m_{ee} < 0.1$ GeV/c^2 due to the π^0 Dalitz decay contribution. Thus, the three different mass ranges such as $0.10 < m_{ee} < 0.40$GeV/c^2, $0.12 < m_{ee} < 0.40$GeV/c^2, and $0.14 < m_{ee} < 0.50$GeV/c^2 are used for evaluation of the systematic errors due to the selection of the mass range for fitting. The differences on the resulting direct virtual photon fractions within the different mass ranges for fitting are summarized in Table 5.15. The maximum difference for each p_T bin is assigned as the systematic error.

Table 5.14: The differences on the direct virtual photon fraction due to different mass regions for the cocktail normalization.

p_T [GeV/c]	$m_{ee} < 0.03$ GeV/c^2	$m_{ee} < 0.07$ GeV/c^2
1.0-1.5	–0.0021	+0.0021
1.5-2.0	–0.0019	+0.0017
2.0-2.5	–0.0031	+0.0018
2.5-3.0	–0.0027	+0.0017
3.0-3.5	–0.0039	+0.0032
3.5-4.0	–0.0045	+0.0017
4.0-4.5	–0.0087	+0.0023
4.5-5.0	–0.0130	+0.0031
5.0-5.5	–0.0114	+0.0031
5.5-6.0	–0.0160	–0.0034

Table 5.15: The differences on the resulting direct virtual photon fractions with the different mass ranges for fitting.

p_T [GeV/c]	$0.10 - 0.40$ GeV/c^2	$0.12 - 0.40$ GeV/c^2	$0.14 - 0.50$ GeV/c^2
1.0-1.5	+0.0036	+0.0054	+0.0020
1.5-2.0	–0.0007	–0.0045	–0.0053
2.0-2.5	–0.0012	–0.0010	+0.0016
2.5-3.0	–0.0058	–0.0060	–0.0010
3.0-3.5	–0.0069	–0.0075	–0.0055
3.5-4.0	–0.0018	+0.0079	–0.0014
4.0-4.5	+0.0029	+0.0086	+0.0094
4.5-5.0	–0.0035	+0.0090	–0.0368
5.0-5.5	+0.0147	+0.0138	–0.0141
5.5-6.0	+0.0198	+0.0142	–0.0339

Summary of Systematic Errors on r_{γ^*}

The described systematic errors on r_{γ^*} are summarized in Table 5.16.

Table 5.16: Summary of the systematic errors on the direct γ^* fraction.

1.0-1.5	1.5-2.0	2.0-2.5	2.5-3.0	3.0-3.5	3.5-4.0	4.0-4.5	4.5-5.0	5.0-5.5	5.5-6.0
background normalization									
+7%	+2%	+1%	+1%	+1%	+1%	+1%	+1%	+2%	+5%
–5%	–12%	–5%	–6%	–4%	–3%	–5%	–4%	–5%	–23%
efficiency correction function									
+13%	+10%	+8%	+13%	+5%	+10%	+10%	+4%	+9%	+20%
–	–	–	–	–	–4%	–	–	–2%	–2%
particle composition									
+23%	+30%	+18%	+24%	+13%	+11%	+13%	+7%	+10%	+36%
–25%	–41%	–16%	–23%	–15%	–12%	–13%	–7%	–11%	–38%
parameterization of measured π cross section									
+4%	+3%	+3%	+4%	+2%	+1%	+1%	+1%	+2%	+5%
–8%	–10%	–3%	–5%	–3%	–3%	–3%	–2%	–2%	–10%
normalization of cocktail calculation									
+6%	+7%	+3%	+4%	+5%	+2%	+3%	+3%	+4%	–
–6%	–8%	–6%	–7%	–6%	–6%	–13%	–11%	–14%	–61%
variation of fit range									
+16%	–	+3%	–	–	+10%	+14%	+8%	+18%	+130%
–	–21%	–2%	–15%	–12%	–24%	–	–32%	–17%	–
total systematic error									
+32%	+32%	+21%	+27%	+15%	+18%	+21%	+12%	+23%	+137%
–27%	–48%	–17%	–29%	–20%	–14%	–18%	–35%	–25%	–73%

5.13.2 Systematic Errors on Inclusive Photon Yield

The systematic error sources on the inclusive photon yield derived from Eq. 5.61 are as follows;

1. acceptance (Section 5.6)
2. electron efficiency (Section 5.9.1)
3. MB trigger efficiency (Section 5.2.1)
4. ERT trigger efficiency (Section 5.9.3)

Since they are independent of each other, the quadratic sum of them is assigned as the systematic error on the inclusive photon yield.

Acceptance

As described in Section 5.6, the acceptance in the real data is reproduced within 4% even for each EMCal sector by the simulation. Thus, the maximum value of the uncertainty on the acceptance for e^+e^- pairs is $2\times4\% = 8\%$.

Electron Efficiency

The uncertainty on the electron efficiency is evaluated based on the fitting errors on the coefficients in Eq. 5.43 for electrons and in Eq. 5.44 for positrons. The calculated systematic error due to the electron efficiency for e^+e^- pairs are less than 0.1% and negligible.

MB Trigger Efficiency

The MB trigger efficiency is $\varepsilon_{MB} = 0.88 \pm 0.02$ as described in Section 5.2.1. Thus, the systematic error is about 2.3%.

ERT Trigger Efficiency

Since the e^+e^- pair mass spectra in $p_T^{ee} > 1.5$ GeV/c are derived from the ERT triggered data, the systematic error due to the uncertainty on the ERT trigger efficiency should be considered for the inclusive photon yield in $p_T > 1.5$ GeV/c. The uncertainty on the ERT trigger efficiency originates mainly from the fitting error of the EMC2x2 trigger efficiency. Considering the fitting error of the efficiency curve for each supermodule, the systematic error is evaluated to be 2.5%, which is consistent with the value from an analysis for measurements of ω and ϕ via $\omega, \phi \to e^+e^-$ [79].

Chapter 6

Results

In this chapter, the results of the direct virtual photon fraction in d+Au collisions are shown, and then the direct photon invariant yield in d+Au collisions for $p_T <$ 6.0 GeV/c is also determined from the measured direct virtual photon fraction.

6.1 Direct Virtual Photon Fraction

The direct virtual photon fractions as a function of p_T is obtained from the e^+e^- pair mass spectrum, as already described in Section 5.11. Figure 6.1 shows the obtained direct virtual photon fractions in d+Au collisions side by side with the results in p+p and Au+Au collisions [14]. The yellow boxes on the data points indicate systematic errors on the direct virtual photon fractions. The mean value, the statistical error, the systematic error and mean p_T of each data point in d+Au collisions are summarized in Table 6.1. The colored curves are expectations from

Table 6.1: Summary of the mean value, the statistical error, the systematic error and mean p_T of each data point in d+Au collisions.

p_T bin [GeV/c]	mean p_T [GeV/c]	mean	stat. error	syst. error
1.0-1.5	1.1882	0.0341	± 0.0160	$^{+0.0108}_{-0.0091}$
1.5-2.0	1.6937	0.0247	± 0.0046	$^{+0.0080}_{-0.0120}$
2.0-2.5	2.1991	0.0519	± 0.0048	$^{+0.0108}_{-0.0090}$
2.5-3.0	2.7040	0.0386	± 0.0064	$^{+0.0106}_{-0.0113}$
3.0-3.5	3.2083	0.0648	± 0.0102	$^{+0.0095}_{-0.0129}$
3.5-4.0	3.7122	0.0766	± 0.0156	$^{+0.0140}_{-0.0107}$
4.0-4.5	4.2157	0.0697	± 0.0222	$^{+0.0149}_{-0.0127}$
4.5-5.0	4.7188	0.1158	± 0.0334	$^{+0.0134}_{-0.0401}$
5.0-5.5	5.2215	0.0829	± 0.0435	$^{+0.0189}_{-0.0206}$
5.5-6.0	5.7238	0.0261	± 0.0518	$^{+0.0356}_{-0.0190}$

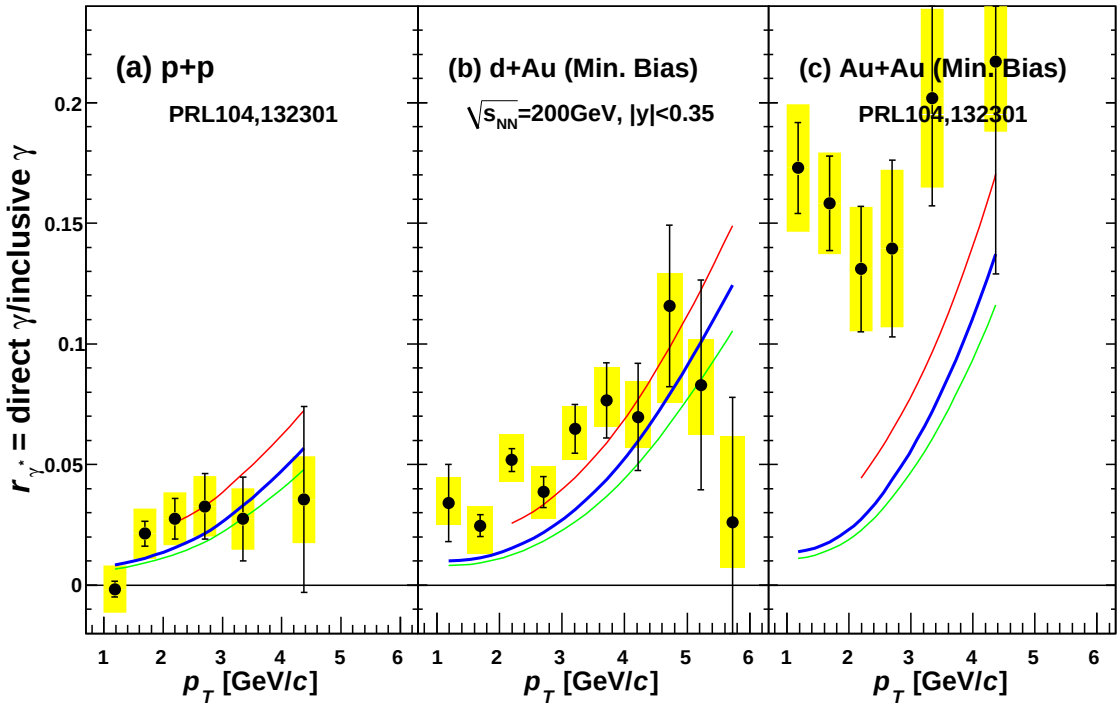

Figure 6.1: The obtained direct virtual photon fractions in d+Au collisions (middle) side by side with the results in p+p (left) and Au+Au (right) collisions [14]. The yellow boxes on the data points indicate systematic errors on the direct virtual photon fractions. The colored curves are expectations from NLO pQCD calculation with different theoretical scales: $\mu = 0.5p_T$(red), p_T(blue), $2p_T$(green) [11], for each collision system.

NLO pQCD calculation with different theoretical scales: $\mu = 0.5p_T$(red), p_T(blue), $2p_T$(green) [11], for each collision system. It is obviously found that the Au+Au result has a different trend compared to the d+Au result in $p_T < 2.0$ GeV/c while the trends of the p+p and d+Au results are almost consistent with the NLO pQCD expectations.

6.2 Direct Photon Yield

Finally, the direct photon yield in d+Au collisions as a function of p_T is obtained from the measured direct virtual photon fraction and the inclusive real photon yield, which is described in Section 5.12.

Figure 6.2 shows the direct photon spectrum in d+Au collisions compared to the NLO pQCD calculations with different theoretical scales: $\mu = 0.5p_T$(red), p_T(blue), $2p_T$(green) [11]. The closed symbols represent the result with the virtual photon method from the Run8 data. The boxes surrounding the symbols indicate the systematic errors on the results. The mean values, the statistical errors and the systematic errors on the direct photon yield determined by the virtual photon method are summarized in Table 6.2.

Table 6.2: Summary of the mean values, the statistical errors, the systematic errors on the direct photon yield determined by the virtual photon method in d+Au collisions.

p_T bin [GeV/c]	mean	stat. error	syst. error
1.0-1.5	9.45×10^{-4}	$\pm4.43\times10^{-4}$	$^{+3.09}_{-2.64}\times10^{-4}$
1.5-2.0	1.12×10^{-4}	$\pm2.09\times10^{-5}$	$^{+3.75}_{-5.52}\times10^{-5}$
2.0-2.5	4.75×10^{-5}	$\pm4.37\times10^{-6}$	$^{+1.07}_{-0.92}\times10^{-5}$
2.5-3.0	9.79×10^{-6}	$\pm1.63\times10^{-6}$	$^{+2.82}_{-2.98}\times10^{-6}$
3.0-3.5	4.70×10^{-6}	$\pm7.38\times10^{-7}$	$^{+0.80}_{-1.02}\times10^{-6}$
3.5-4.0	1.78×10^{-6}	$\pm3.64\times10^{-7}$	$^{+3.60}_{-2.92}\times10^{-7}$
4.0-4.5	6.35×10^{-7}	$\pm2.02\times10^{-7}$	$^{+1.47}_{-1.28}\times10^{-7}$
4.5-5.0	4.28×10^{-7}	$\pm1.24\times10^{-7}$	$^{+0.62}_{-1.53}\times10^{-7}$
5.0-5.5	1.36×10^{-7}	$\pm7.14\times10^{-8}$	$^{+3.32}_{-3.58}\times10^{-8}$
5.5-6.0	2.20×10^{-8}	$\pm4.38\times10^{-8}$	$^{+3.02}_{-1.62}\times10^{-8}$

The open symbols also represent the result with the subtraction method by the EMCal from the Run3 data [87]. The both results have an overlapping region in $5.0 < p_T < 6.0$ GeV/c. While they are consistent within errors in $5.0 < p_T < 5.5$ GeV/c, there is a difference in $5.5 < p_T < 6.0$ GeV/c. The result with the subtraction method is reliable at this p_T point since the virtual photon method suffers from poor statistics in the high p_T region. Thus, the results with different analyses can be combined smoothly at $5.0 < p_T < 5.5$ GeV/c and look almost consistent with the NLO pQCD calculation.

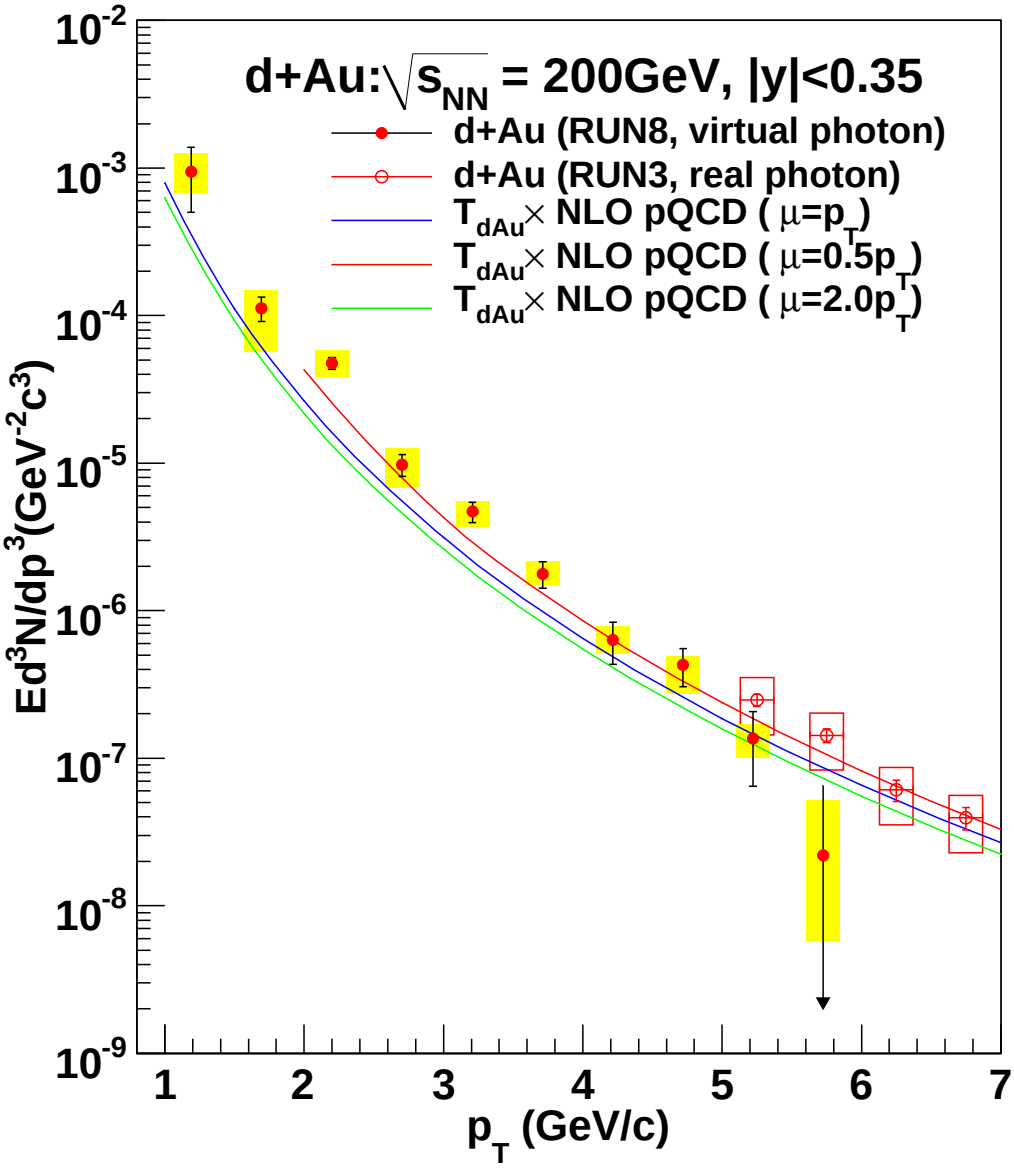

Figure 6.2: The direct photon spectrum in d+Au collisions compared to the NLO pQCD calculations with different theoretical scales: $\mu = 0.5p_T$(red), p_T(blue), $2p_T$(green) [11].

Chapter 7

Discussion

Discussions are presented to understand an implication on the obtained direct photon spectrum in d+Au collisions in this chapter. In Section 7.1, the nuclear effects on the direct photon production is discussed comparing with the p+p result and the nuclear modification factor for the d+Au result, R_{dA} is introduced to visualize a magnitude of the modification of the direct photon spectrum due to the nuclear effects. In Section 7.2, an attempt to extract the contribution of the photons from non-initial state effects, *i.e.* thermal photons from the QGP in the observed excess yield in Au+Au collisions is done with a comparison between the d+Au and Au+Au results.

7.1 Nuclear Effects

As described in Section 2.4, the nuclear effects can modify the shape of the direct photon spectrum compared to the one in p+p collisions. The theoretical model for the nuclear effects on the direct photon production is not established well yet due to large uncertainties on the origin of the nuclear effects, *e.g.* PDFs for sea quarks and gluons in a heavy nucleus is quite different in various parameterizations. Thus, it is very important to quantitatively understand the nuclear effects on the direct photon production from the experimental result in p+A collisions.

7.1.1 Comparison with p+p Result

Figure 7.1 shows the invariant yield of the direct photons in d+Au collisions compared to the binary-scaled p+p result. The p+p and d+Au results are shown as the box and circle symbols, and the results from analyses with the virtual photon and the subtraction methods are indicated as closed and open symbols, respectively. The boxes and brackets mean the systematic errors of the data. The binary-scaled p+p fit result, which is obtained from the modified power-law function fit to the data as described in Section 2.3.1, is also drawn together with the data as a dotted line.

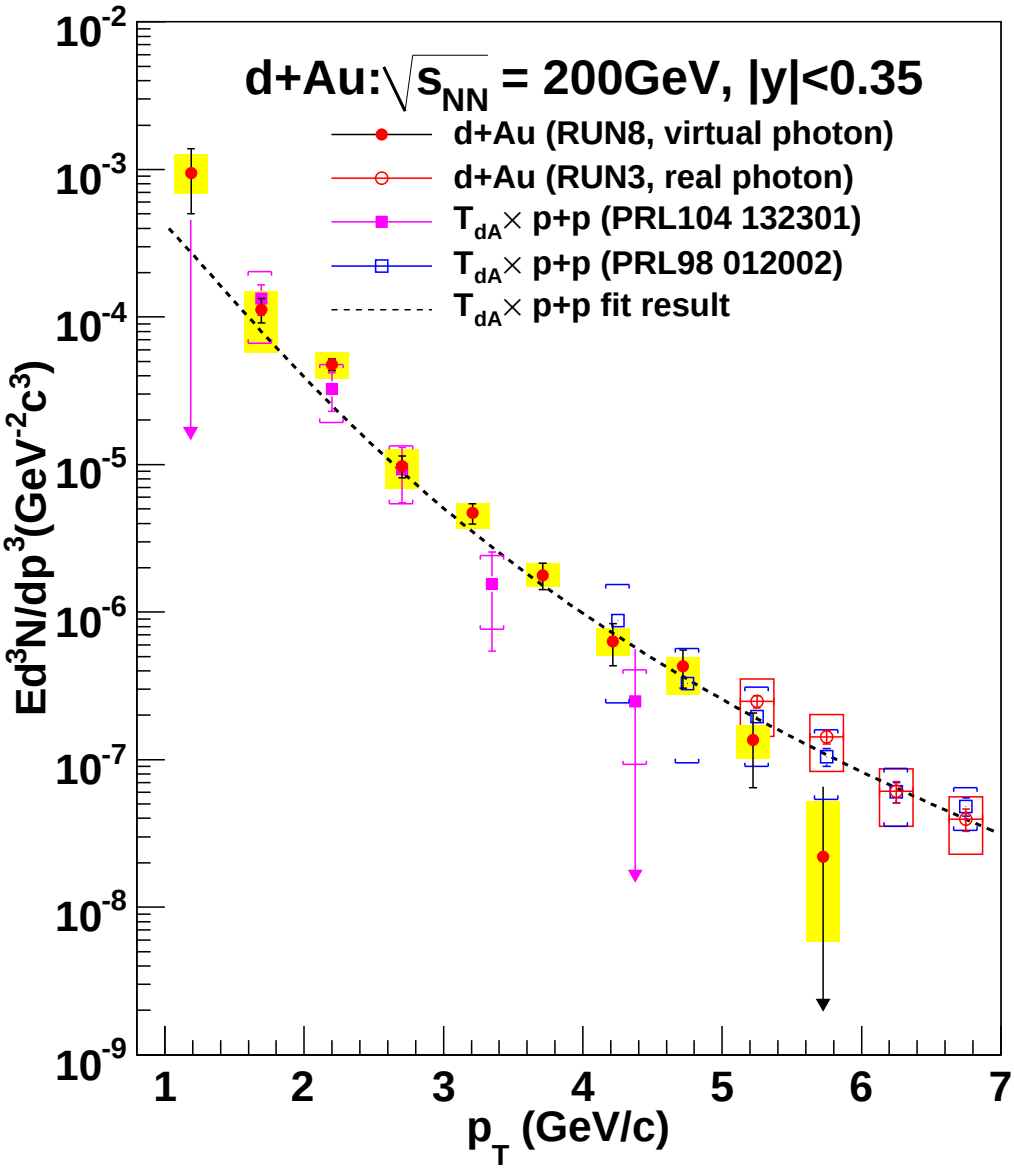

Figure 7.1: The invariant yield of the direct photons in d+Au collisions compared to the binary-scaled p+p result [14]. The p+p and d+Au results include the both results with the virtual photon and the subtraction methods shown as closed and open symbols, respectively. The binary-scaled modified power-law fit result to the p+p data is also drawn together with the data as a dotted line.

While the d+Au result is consistent with the p+p result within errors, the mean values of the d+Au data points look slightly higher compared to the p+p fit result in $p_T < 4$ GeV/c.

7.1.2 Nuclear Modification Factor R_{dA}

The nuclear modification factor R_{dA} is calculated in order to visualize the magnitude of the modification of the direct photon spectrum in d+Au collisions. Figure 7.2 shows the R_{dA} for the direct photons compared to the R_{dA} for π^0. The closed and

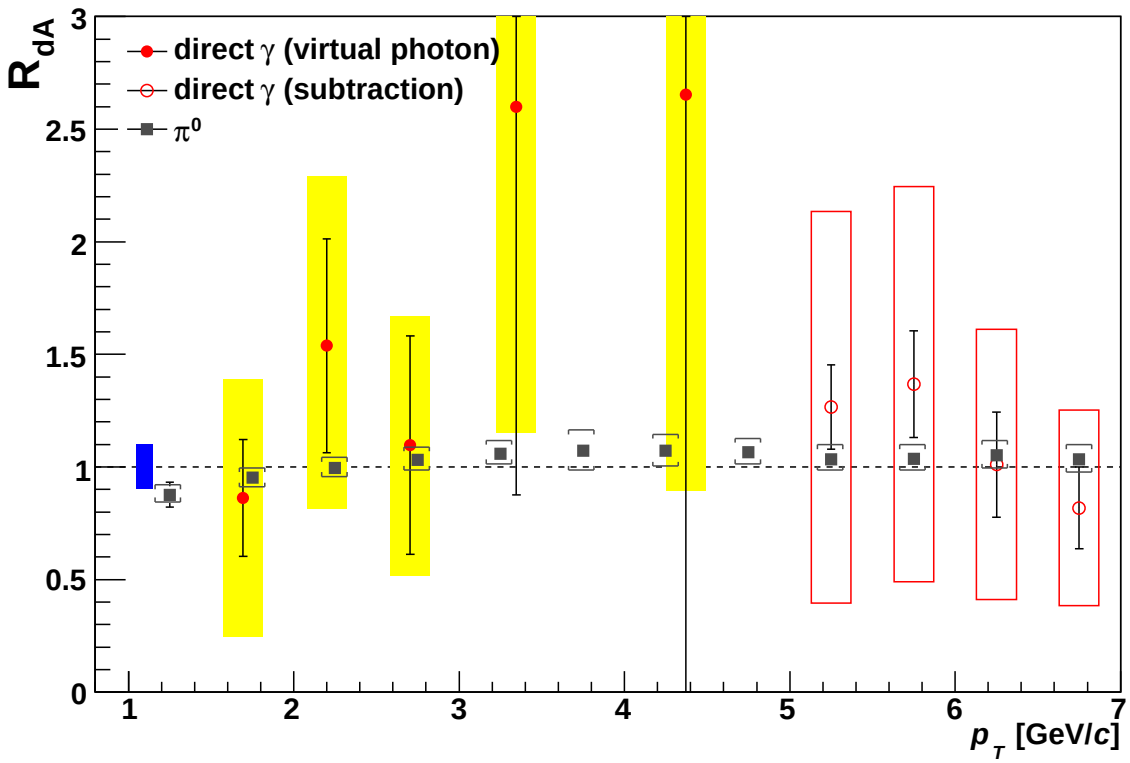

Figure 7.2: The R_{dA} for the direct photons compared to the R_{dA} for π^0. The box around 1.0 indicates the p_T-uncorrelated systematic error. The boxes and brackets on the data points represent the p_T-correlated systematic errors.

open circle symbols show the result for direct photons with the virtual photon and the subtraction methods, and the square symbols show the result for π^0 [51]. The box around 1.0 indicates the p_T-uncorrelated systematic error. The boxes and brackets on the data points represent the p_T-correlated systematic errors. Although the errors on the direct photon result with the virtual photon method are very large due to the p+p data, the direct photon results are consistent with the π^0 result within errors, *i.e.* $R_{dA} \simeq 1$. Thus, the nuclear effects on the direct photon production seem to be small similar to the observed nuclear effects on the meson production.

7.1.3 Parameterization of d+Au Data

The d+Au data are parameterized by fitting with the modified power-law function, $A_{dAu}(1 + p_T^2/b)^{-n}$ with an assumption of small nuclear effects on the direct photon production. The d+Au fit result can replace the p+p fit result as a baseline for the Au+Au data.

For the d+Au data parameterization, only the statistical errors are considered in the nominal fit. Then, the systematic uncertainty of the nominal fit is evaluated by moving the data points to $\pm 1\sigma$ of systematic errors because the main systematic errors on the data points are p_T correlated errors.

Figure 7.3 shows the direct photon spectrum in d+Au collisions fitted with the modified power-law function for parameterization of the d+Au data. The nominal fit result is shown as a black solid line and the systematic upper and lower limits of the fit result are shown as blue and red solid lines, and they can well describe the data. The binary-scaled p+p fit result is also drawn together as a dotted line. The d+Au fit result is slightly higher than the scaled p+p result in $p_T > 3.0$ GeV/c and the discrepancy between them is significantly large in $p_T \leq 3.0$ GeV/c. The coefficients of the d+Au fit result and χ^2/NDF at fitting are summarized in Table 7.1.

Table 7.1: Summary of the coefficients of the d+Au fit results and χ^2/NDF at fitting.

	A_{dAu}	b	n	χ^2/NDF
nominal	6.65×10^{-3}	1.32	3.35	12.96/9
upper limit	6.88×10^{-3}	1.65	3.61	11.71/9
lower limit	2.61×10^{-3}	1.68	3.37	14.16/9

7.2 Thermal Photons

An attempt to extract the mean contribution of the photons from the non-initial state effects in the observed enhanced yield of the direct photons in Au+Au collisions is made with a comparison between the N_{coll}-scaled d+Au and Au+Au results.

7.2.1 Comparison with Au+Au Result

Figure 7.4 shows the direct photon spectrum in minimum bias Au+Au collisions compared to the scaled d+Au result. The square and circle symbols show the results in MB Au+Au and d+Au collisions and the brackets and boxes on the data points are the systematic errors. The d+Au result is scaled by T_{AA}/T_{dA} to the number of binary collisions in MB Au+Au collisions. Here the number of binary collisions in MB Au+Au collisions is 257.8±25.4 from the Glauber calculation [31]. The Au+Au result can not be described by the scaled d+Au result, especially the significant enhanced

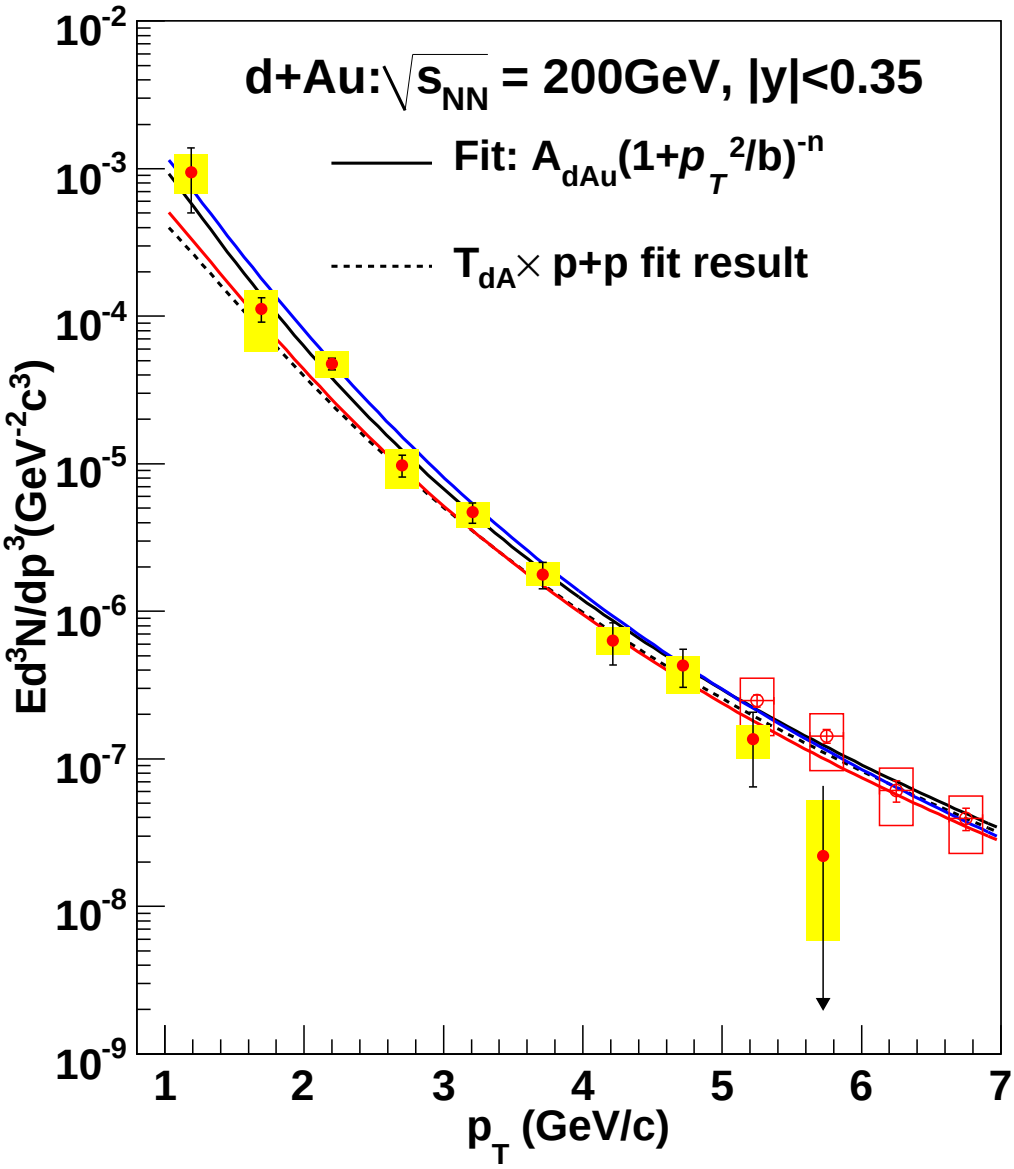

Figure 7.3: The direct photon spectrum in d+Au collisions fitted with the modified power-law function for parameterization of the d+Au data.

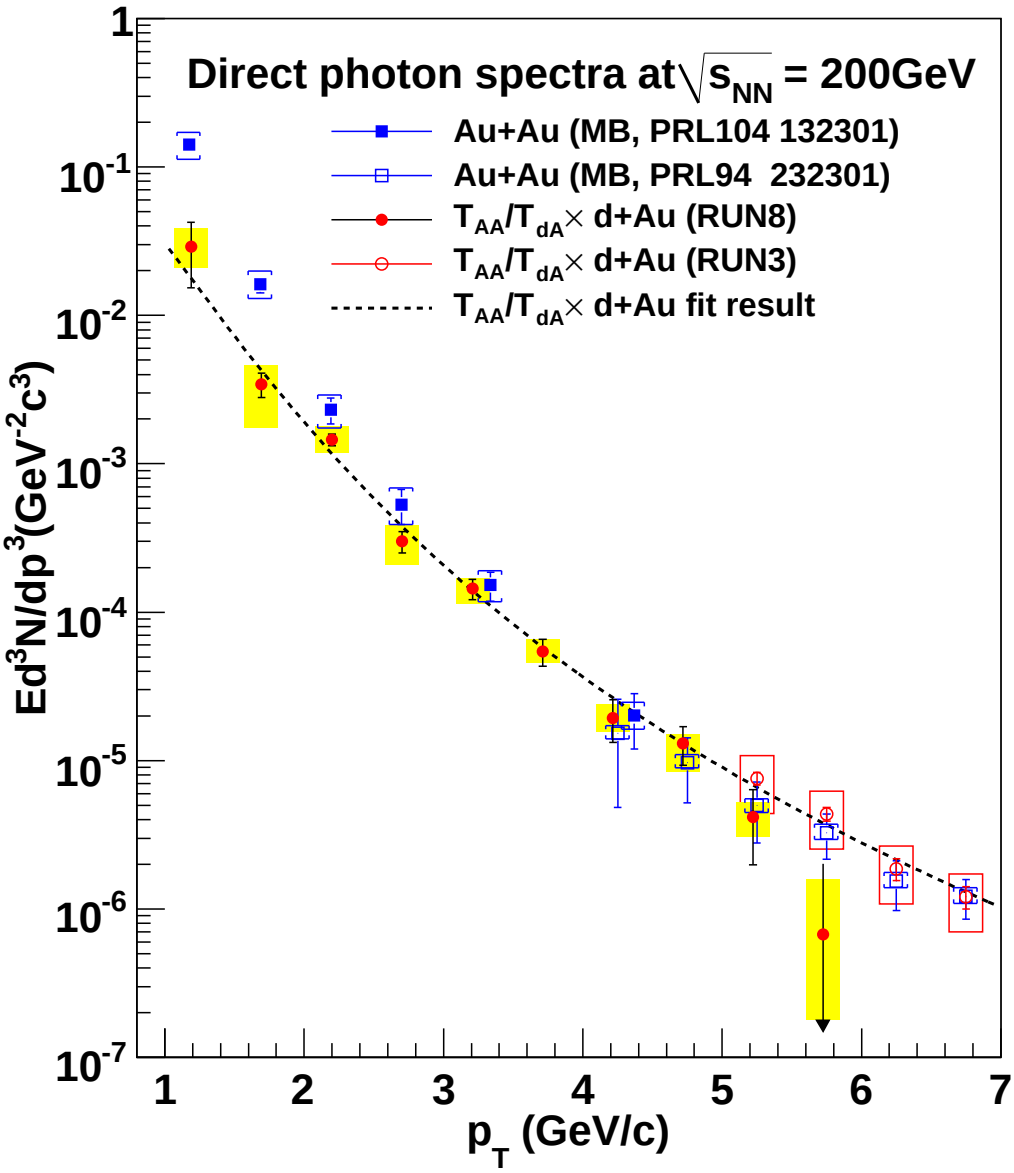

Figure 7.4: The direct photon spectrum in minimum bias Au+Au collisions compared to the d+Au result scaled by T_{AA}/T_{dA}. The number of binary collisions in MB Au+Au collisions is 257.8±25.4 from the Glauber calculation [31].

yield over the scaled d+Au result is seen in $p_T < 2.0$ GeV/c. Figure 7.5 shows the ratio of the MB Au+Au data to the scaled d+Au data. In $p_T \leq 2.0$ GeV/c, the direct

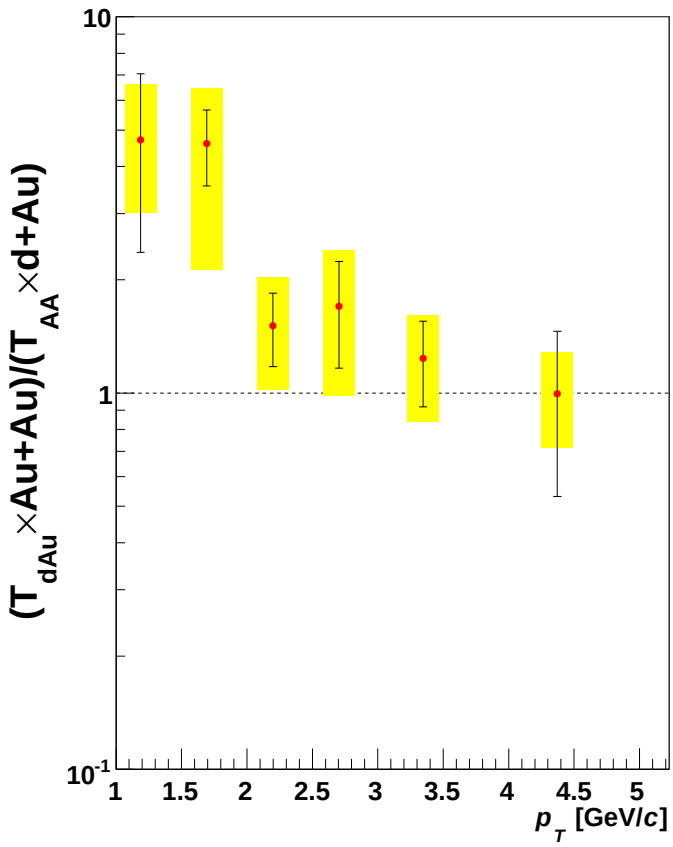

Figure 7.5: The ratio of the MB Au+Au data to the scaled d+Au data.

photon yield for MB Au+Au collisions is more than twice the expected yield from the d+Au data, implying that an additional source of the direct photon production other than nuclear effects exists in Au+Au collisions.

We fit to the Au+Au data with an exponential plus scaled d+Au fit function as Eq. 7.1.

$$f_{fit}^{Au+Au}(p_T) = Ae^{-p_T/T} + \frac{T_{AA}}{T_{dA}} \times A_{dA} \left(1 + \frac{p_T^2}{b}\right)^{-n}. \tag{7.1}$$

At fitting, A and the inverse slope T are only free parameters. Figure 7.6 shows the nominal fit result to the MB Au+Au data with Eq. 7.1. In the nominal fit, only the statistical errors are considered as well as the nominal fit for d+Au data.

The sources of systematic uncertainty on the fit to the Au+Au data are as follows:

1. systematic uncertainty of the d+Au fit function,

2. uncertainty on the number of collisions,

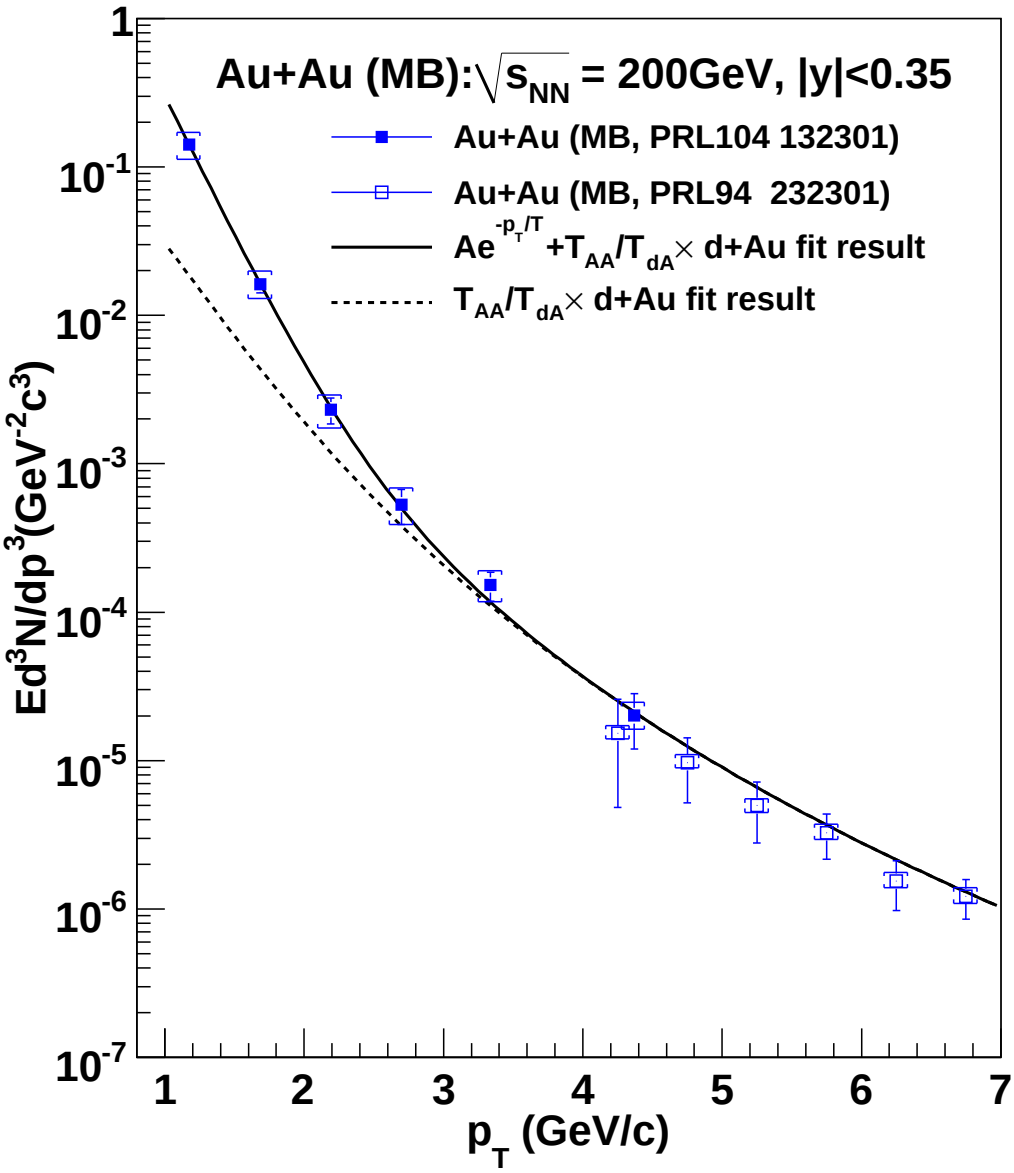

Figure 7.6: The fit result to the MB Au+Au data with Eq. 7.1. The scaled d+Au fit result is also shown as a dotted line to clarify the observed excess direct photon yield in $p_T < 2.0$ GeV/c.

3. systematic errors on the Au+Au data points.

The systematic uncertainty due to the systematic uncertainty of the d+Au fit function is evaluated by fitting with the upper and lower limits of the d+Au fit function shown in Fig. 7.3 as a baseline for the Au+Au data. The uncertainty in the number of collisions (N_{coll}) is about 11%. For evaluation of the systematic uncertainty due to N_{coll}, the fits are made with the nominal d+Au fit function scaled by $\pm 11\%$ N_{coll} values. The uncertainty due to the systematic errors on the Au+Au data points are evaluated in the same way for evaluation of the uncertainty on the d+Au fit function.

The resulted dN/dy of the observed excess yield in the Au+Au data for $p_T >$ 1 GeV/c and the inverse slope T are listed in Table 7.2. Finally, the systematic errors

Table 7.2: Summary of the fits to the Au+Au data with the d+Au fit result as a baseline.

	dN/dy ($p_T > 1$ GeV/c)	T	χ^2/NDF
nominal	0.457	220	1.23/4
d+Au fit syst.uncertainty			
upper limit	0.437	208	0.56/4
lower limit	0.485	232	3.33/4
uncertainty on N_{coll}			
upper limit	0.449	215	0.76/4
lower limit	0.464	225	2.12/4
syst.uncertainty on Au+Au data			
upper limit	0.563	230	4.85/4
lower limit	0.347	206	0.77/4

on dN/dy ($p_T > 1$ GeV/c) and T are calculated by the quadratic sum of the described uncertainties, and their values with the statistical and systematic errors are shown compared to those with p+p fit result as a baseline [14] in Table 7.3.

Table 7.3: dN/dy ($p_T > 1$ GeV/c) and the inverse slope T obtained by fitting to the Au+Au data (MB) with p+p and d+Au fit results as a baseline. The first and second errors are statistical and systematic ones, respectively.

baseline	dN/dy ($p_T > 1$ GeV/c)	T
p+p	$0.49 \pm 0.05 \pm 0.11$	$233 \pm 14 \pm 19$
d+Au	$0.46 \pm 0.07 \pm 0.11$	$220 \pm 15 \pm 18$

Assuming that the excess direct photon yield is due to thermal origin, the inverse slope T is related to the initial temperature of the dense partonic matter created by Au+Au collisions. The initial temperature T_{init} is $1.5 \sim 3$ times higher than T due to the space-time evolution [37] according to several hydrodynamical models.

Therefore, the initial temperature of the created matter is higher than the transition temperature predicted by lattice QCD calculations ($T_c \sim 170$ MeV [88]).

7.2.2 Upper Limit of Nuclear Effects

While the discussion in the previous section is made with the assumption that nuclear effects are very small, the upper limit of nuclear effects in Au+Au collisions is estimated by interpreting a difference between the d+Au data and the N_{coll}-scaled p+p fit result as an excess yield due to the nuclear effects.

The d+Au data are fitted with the following function:

$$f_{fit}^{d+Au}(p_T) = T_{dA} \cdot \left(1 + \alpha^{\beta p_T^2}\right) \times A_{pp} \left(1 + \frac{p_T^2}{b}\right)^{-n}, \tag{7.2}$$

where α, β are only free parameters at fitting, and $A_{pp}(1 + p_T^2/b)^{-n}$ is the p+p fit result. The term, $\alpha^{\beta p_T^2}$, means effective nuclear effects in a binary-collision interval during a deuteron passes through a Au nucleus. Figure 7.7 shows the fit result to the d+Au data with Eq. 7.2 for determination of an effective nuclear effects. The black solid line shows the nominal fit result with only statistical errors. The upper and lower limits of the fit result, which are shown as blue and red solid lines, are determined by moving $\pm 1\sigma$ of systematic errors of the d+Au data. The difference between the upper limit and the N_{coll}-scaled p+p fit result are highlighted by a light blue band. Summary of the fit parameters, α, β, and χ^2/NDF at fitting are as follows:

Table 7.4: Summary of α, β and χ^2/NDF at fitting.

	α	β	χ^2/NDF
nominal	0.898	1.07	14.1/10
upper limit	0.949	1.05	15.9/10
lower limit	0.694	4.80	15.0/10

In the case of Au+Au collisions, the expected hard photon contribution with nuclear effects can be expressed as Eq. 7.3 because of a simple logic that nucleons in both Au nuclei have the same amount of effective nuclear effects.

$$f_{hardphoton}^{Au+Au}(p_T) = T_{AA} \cdot \left(1 + \alpha^{\beta p_T^2}\right)^2 \times A_{pp} \left(1 + \frac{p_T^2}{b}\right)^{-n}. \tag{7.3}$$

Figure 7.8 shows the Au+Au result compared to the N_{coll}-scaled p+p fit result plus the nuclear effects extrapolated from the d+Au fit result with consideration for systematic uncertainties shown in Fig. 7.7. The N_{coll}-scaled p+p fit result is shown as a dotted line, and the nuclear effects for Au+Au collisions is indicated by a yellow band. In $p_T < 2.0$ GeV/c, a significant excess over the upper limit of the nuclear effects is seen.

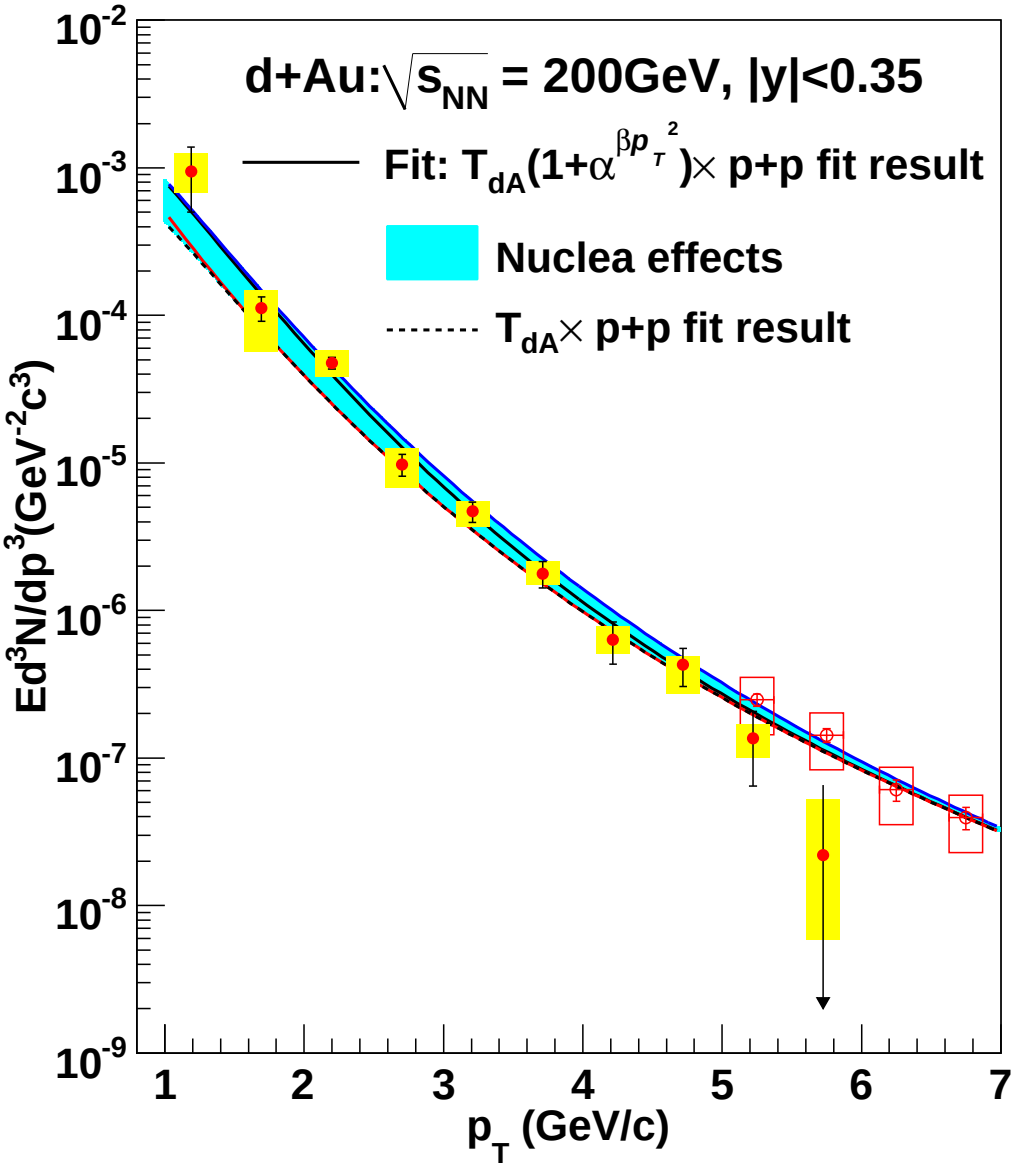

Figure 7.7: The fit result to the d+Au data with Eq. 7.2 for determination of effective nuclear effects. The black solid line shows the nominal fit result with only statistical errors, and the upper and lower limits of the fit result are shown as blue and red solid lines. The dotted line indicates the N_{coll}-scaled p+p fit result.

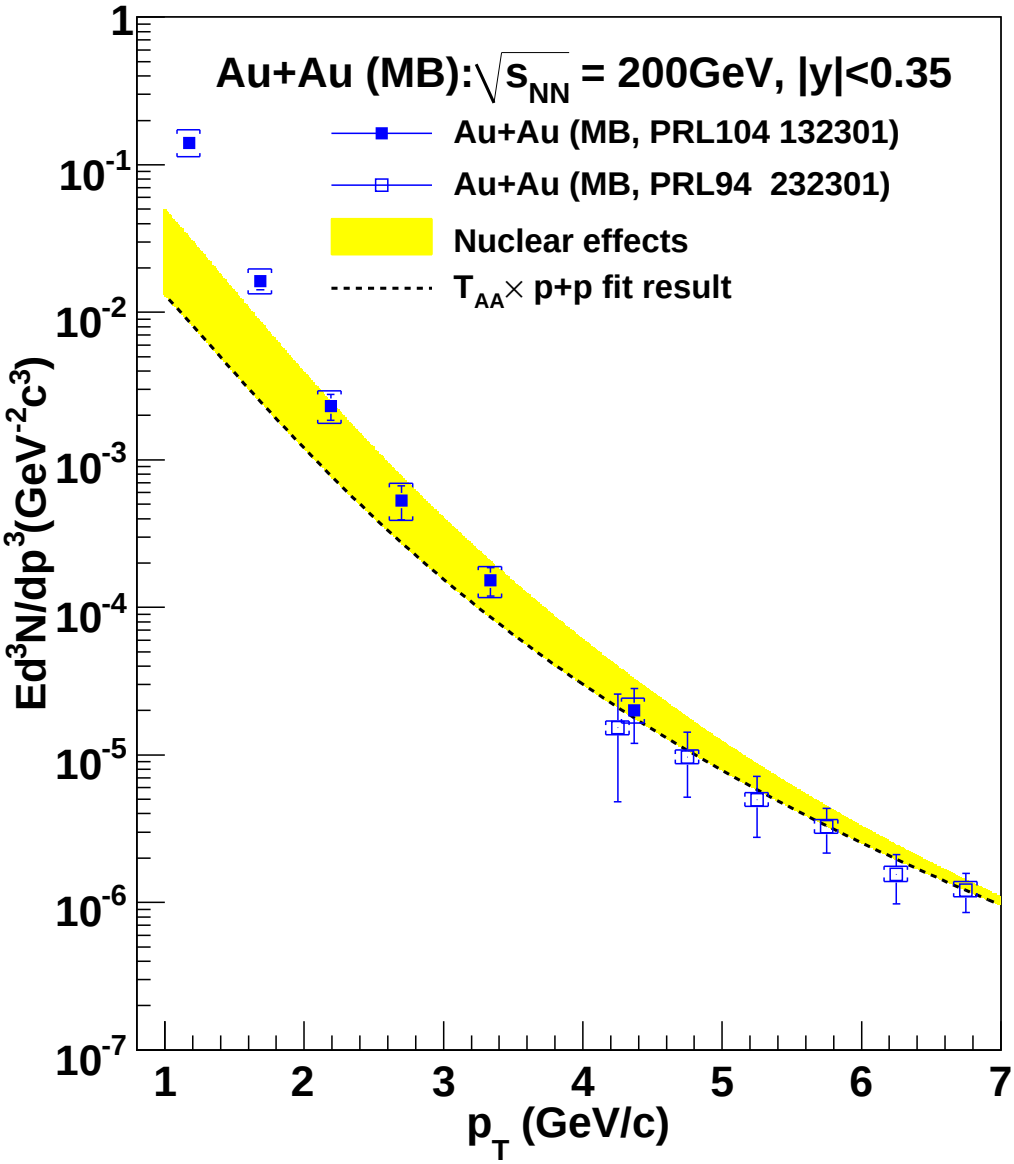

Figure 7.8: The Au+Au result compared to the N_{coll}-scaled p+p fit result (dotted line) plus the nuclear effects (yellow band) extrapolated from the d+Au fit result with consideration for systematic uncertainties.

Chapter 8

Conclusion

The measurement of direct photons with the virtual photon method in d+Au collisions at $\sqrt{s_{NN}} = 200$ GeV has been performed in the PHENIX experiment in RHIC Year-2008 Run (Run8). The virtual photon method has been successfully established in the PHENIX experiment to break through the difficulty on the measurement of the low p_T direct photons with the subtraction method using the EMCal. The d+Au result provides understanding for nuclear effects on the direct photon production, and then allows one to evaluate the net contribution of non-initial state effects in the excess yield of the direct photon over the binary collision-scaled p+p result observed in Au+Au collision for $p_T < 3.0$ GeV/c.

The e^+e^- pairs are measured at mid-rapidity $|y| < 0.35$. The contribution of e^+e^- pairs from hadron decays in the measured e^+e^- pair spectrum is evaluated with the hadronic cocktail calculation, which is tuned to match hadron yields individually measured in the PHENIX experiment. The fraction of the component of the direct photon internal conversions ($\gamma^* \to e^+e^-$) is extracted by utilizing the mass shape difference with the hadron decay component for $1.0 < p_T < 6.0$ GeV/c. The obtained direct photon fractions are converted to the direct photon yields by multiplying the inclusive photon yields, which are also evaluated from the e^+e^- yield in $m_{ee} < 0.50$ GeV/c^2.

The direct photon spectra in d+Au collisions determined by both virtual photon and subtraction methods have an overlapping region between $5.0 < p_T < 6.0$ GeV/c, and they are consistent within errors. The d+Au result is in agreement with the binary collision-scaled p+p result within errors for wide p_T range. The nuclear modification factor R_{dA} for the direct photon shows the same trend with one for π^0 indicating that nuclear effects on the direct photon production is very small. The d+Au result is parameterized by fitting with the modified power-law function, $A_{dAu}(1+p_T^2/b)^{-n}$, and the fit gives $6.65 \times 10^{-3}(1 + p_T^2/1.32)^{-3.35}$, which serves as a new baseline including the nuclear effects for the Au+Au data.

The minimum bias Au+Au direct photon spectrum cannot be described by the binary collision-scaled d+Au result for $p_T < 2.0$ GeV/c, implying that an additional

source of the direct photon production other than nuclear effects exists in Au+Au collisions. The observed excess yield in Au+Au collisions are fitted with an exponential plus scaled d+Au fit result. The obtained inverse slope of the exponential function is $220 \pm 15^{stat} \pm 18^{syst}$ MeV. Assuming that the excess yield is due to thermal origin, the inverse slope is related to the initial temperature of the created matter and it is higher than the transition temperature of the QGP predicted by lattice QCD calculations ($T_c \sim 170$ MeV).

Acknowledgments

First of all, I would like to express my gratitude to my supervisor, Prof. H. Hamagaki, for his appropriate advice and profound comments on my analysis and physics. His rich knowledge and entire support guided me to the completion of this thesis.

I am grateful to Dr. T. Gunji for his wealth of knowledge about physics and analysis techniques, especially the electron analysis in the PHENIX experiment. Whenever I suffered from a trouble on my analysis, I could find a solution on the trouble through a discussion with him. I wish to thank Prof. K. Ozawa for his insightful comments on my analysis, and I enjoyed staying at BNL with his kind support although I caused a lot of trouble to him. I am obliged to Prof. Y. Akiba for his many valuable advices and comments on my analysis. He established the virtual photon method in the PHENIX experiment and introduced me to the virtual photon analysis. He always encouraged me to complete this analysis.

I would like to express my appreciations to Prof. T. Sakaguchi, Dr. S. Kametani, Dr. F. Kajihara, Dr. T. Isobe, Dr. S.X. Oda, Dr. Y. Morino, Dr. Y. Aramaki and Mr. N. Kurihara for their thoughtful advices on my scientific activity and usual kindness. I have spent a lot of fun times with them chatting and discussing many things such as scientific subjects and topical news. I wish to thank the preset-past members of our group, Dr. M. Inuzuka, Dr. K. Kino, Dr. T. Horaguchi, Mr. Y. Tsuchimoto, Mr. S. Saito, Mr. S. Sano, Mr. A. Takahara, Mr. R. Akimoto, Mr. Y. Hori, Mr. T. Tsuji, Mr. A. Nukariya, and Mr. S. Hayashi for their tender helps and friendships.

I express my acknowledgments to all the collaborators of the PHENIX experiment. I would like to give many thanks to the previous and present spokespersons, Prof. W.A. Zajc and Prof. B.V. Jacak, for their excellent leaderships and continuous supports. I appreciate the Year-2008 Run coordinator, Dr. M.J. Leitch, for his great leadership. I wish to thank Dr. J.S. Haggerty for his rich knowledge about the PHENIX detector. I am also obliged to Dr. C. Pinkenburg, Dr. D.P. Morison and Dr. J.T. Mitchel for their marvelous assistance on the analysis environment at BNL. I wish to thank the present-past conveners of the Heavy/Light and Hard/Photon Physics Working Groups, Dr. R.G. de Cassagnac, Prof. T.K. Hemmick, Prof. A. Lebedev, Dr. A. Toia, Dr. V. Riabov, Dr. L.A. Linden Levy, Dr. C.L. da Silva, Prof. K. Shigaki, Prof. J. Frantz, Prof. J. Velkovska, Dr. W.G. Holzmann, Dr. G. David, Dr. J. jia, Prof. C. Ogilvie for many constructive comments and suggestions on my analysis. I

would like to acknowledge Ms. R. Inguanta, Ms. M. Faulkner, Ms. Y. Suenaga for their secretarial support at BNL. I appreciate all the staff of the RHIC project, Collider-Accelerator and Physics Departments at BNL.

I would like to express my gratitude to Prof. H. En'yo for his kind support. I thank Dr. S. Yokkaichi, Dr. T. Ichihara, Dr. Y. Watanabe, Dr. T. Nakamura for their steady operation of CC-J at RIKEN. I am grateful to Ms. N. Kiyama, Ms. K. Suzuki, Ms. E. Adachi for their usual kindness and tender supports. I wish to express my appreciation to all the members of the En'yo Radiation Laboratory and the RIKEN BNL Research Center for their helps. I thank all the members of the PHENIX-J group for their gentle supports.

I appreciate all the members of the Center for Nuclear Study, University of Tokyo for their generous support and kindness, especially the CNS secretaries, Ms. M. Hirano, Ms. T. Endo, Ms. I. Yamamoto, Ms. Y. Kishi, Ms. T. Itagaki, Ms. Y. Soma, Ms. K. Takeuchi, Ms. M. Yamaguchi, Ms. Y. Fujiwara. I wish to express my appreciation to Mr. D. Kahl. He kindly agreed to my request for the English correction in this thesis.

I am obliged to Prof. S. Asai, Prof. T. Matsui, Prof. H. Sakamoto, and Prof. S. Shimoura for their valuable comments and important advice. I would like to appreciate Prof. K. Tokushuku for his truly relevant advice.

Final of all, I dedicate this thesis to my father, my mother, my brother, and my grandparents in heaven. I wish to express my gratitude from bottom of my heart for their generous affection and continuous support through my life.

Appendix A

e^+e^- Mass Spectra

A.1 Determination of r_{γ^*}

Figures A.1-A.9 show the e^+e^- pair mass spectra for every 0.5 GeV/c-p_T^{ee} bin in $1.0 < p_T^{ee} < 6.0$ GeV/c at determination of direct r_{γ^*}.

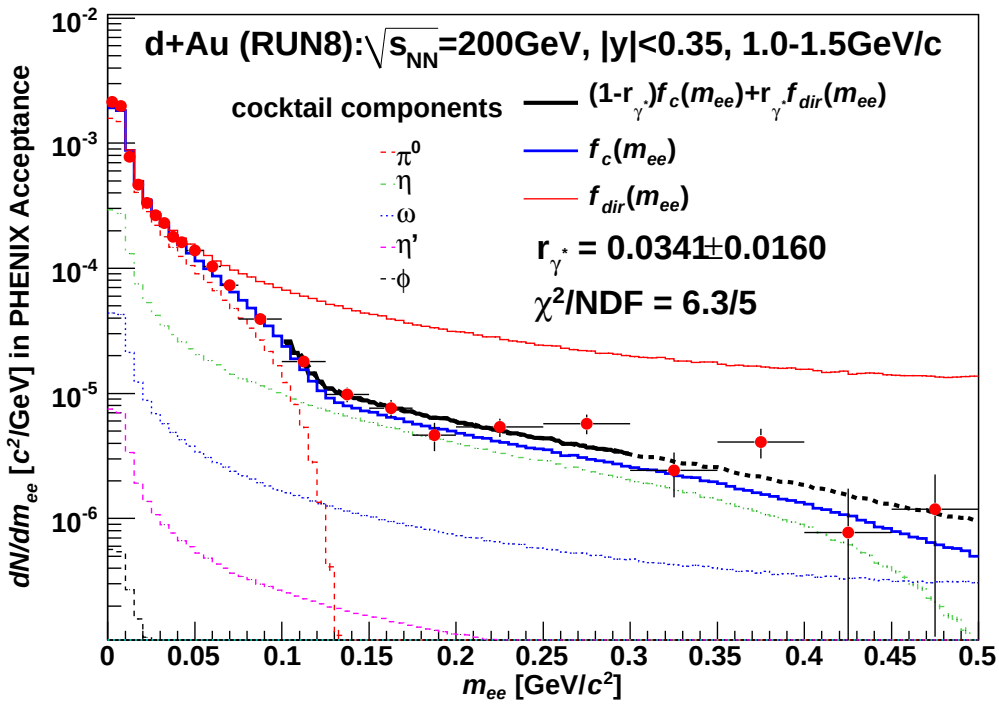

Figure A.1: The e^+e^- pair mass spectrum in $1.0 < p_T^{ee} < 1.5$ GeV/c together with the fit result at determination of direct r_{γ^*}.

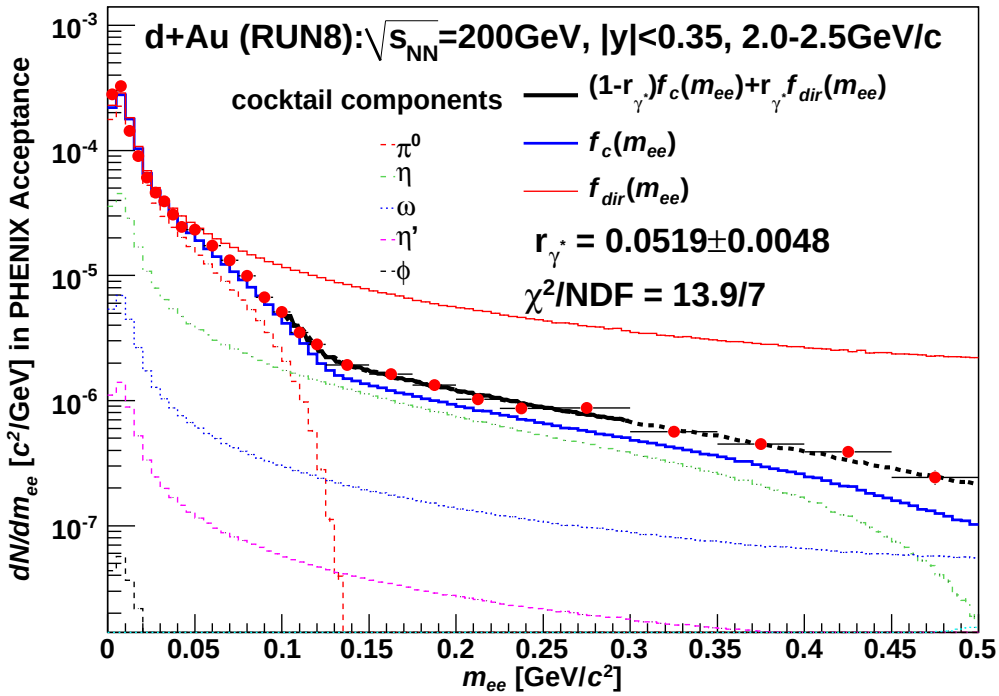

Figure A.2: The e^+e^- pair mass spectrum in $2.0 < p_T^{ee} < 2.5$ GeV/c together with the fit result at determination of direct r_{γ^*}.

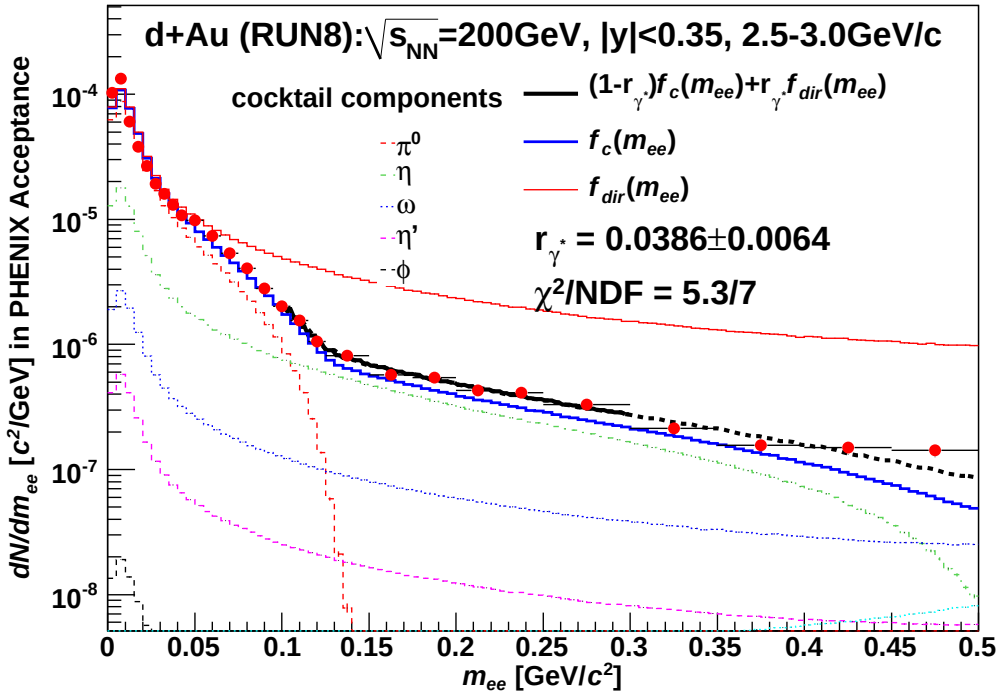

Figure A.3: The e^+e^- pair mass spectrum in $2.5 < p_T^{ee} < 3.0$ GeV/c together with the fit result at determination of direct r_{γ^*}.

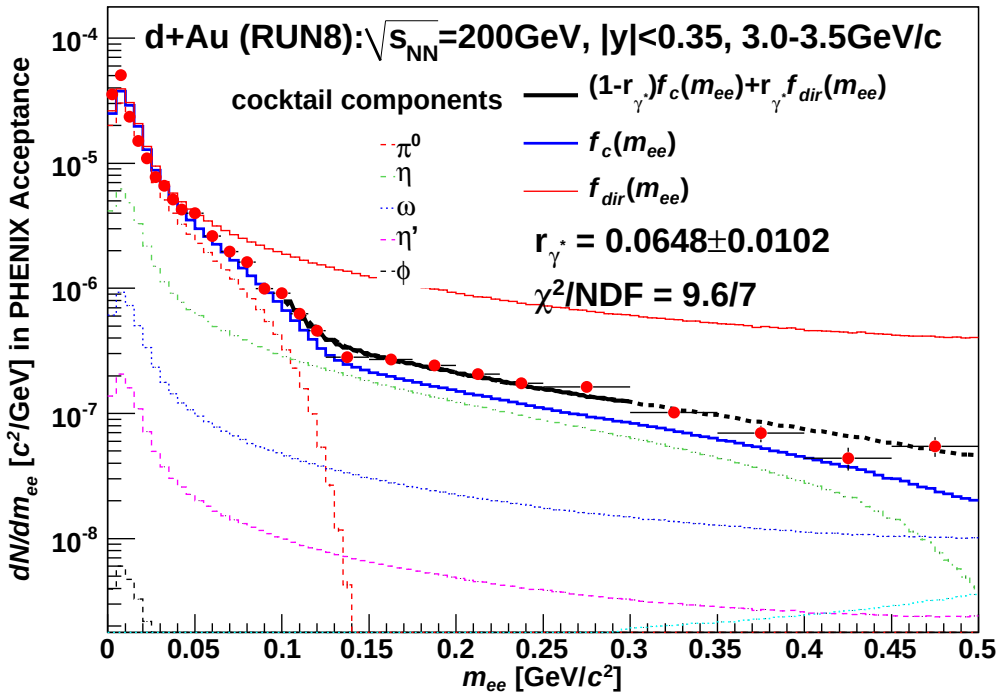

Figure A.4: The e^+e^- pair mass spectrum in $3.0 < p_T^{ee} < 3.5$ GeV/c together with the fit result at determination of direct r_{γ^*}.

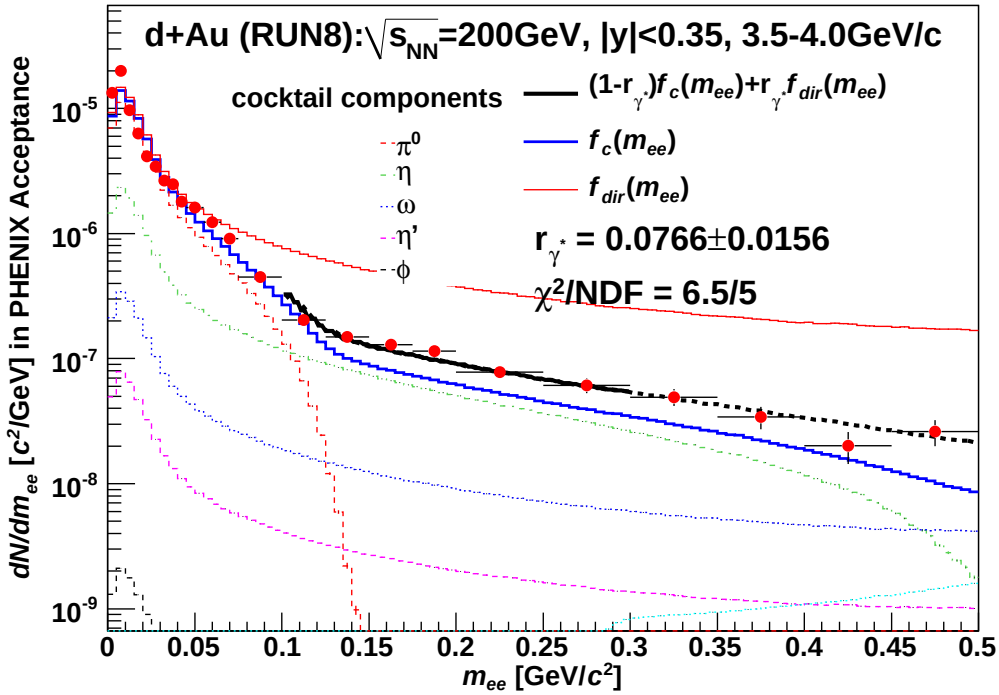

Figure A.5: The e^+e^- pair mass spectrum in $3.5 < p_T^{ee} < 4.0$ GeV/c together with the fit result at determination of direct r_{γ^*}.

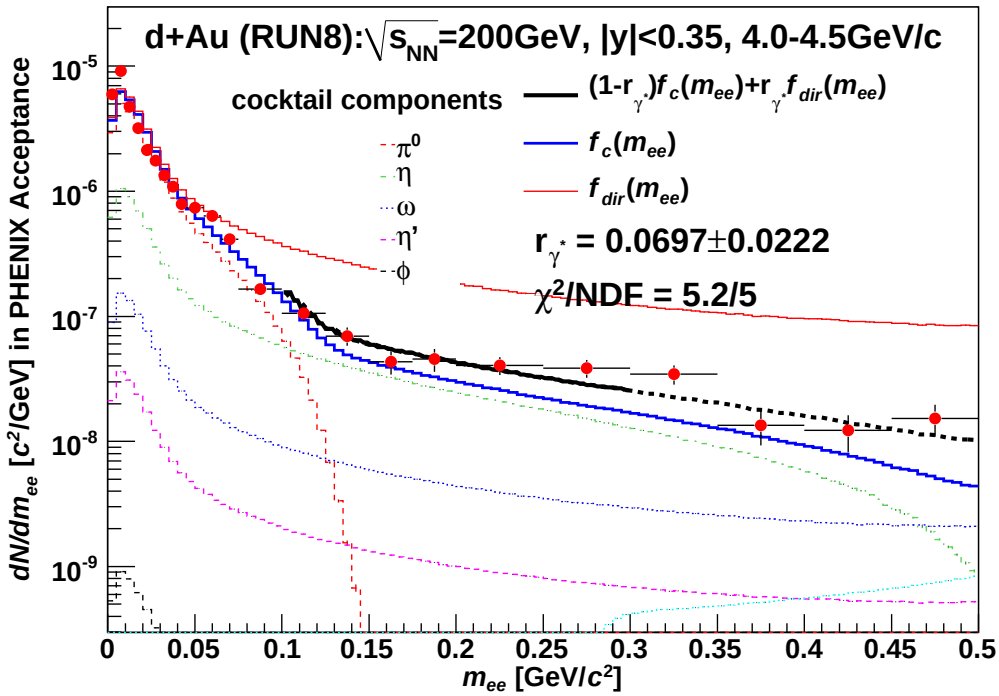

Figure A.6: The e^+e^- pair mass spectrum in $4.0 < p_T^{ee} < 4.5$ GeV/c together with the fit result at determination of direct r_{γ^*}.

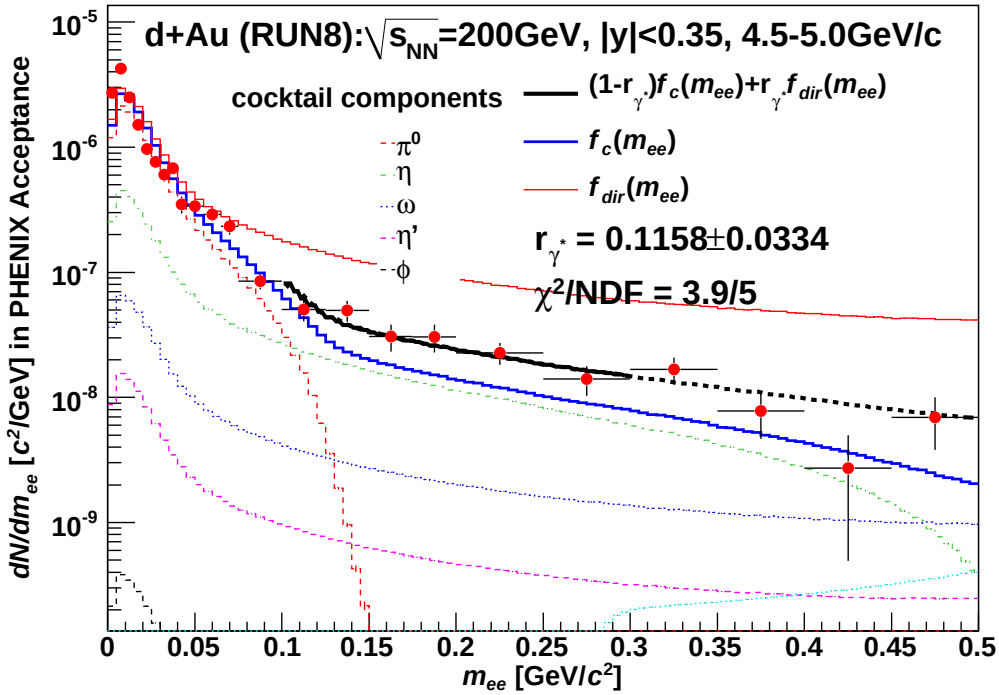

Figure A.7: The e^+e^- pair mass spectrum in $4.5 < p_T^{ee} < 5.0$ GeV/c together with the fit result at determination of direct r_{γ^*}.

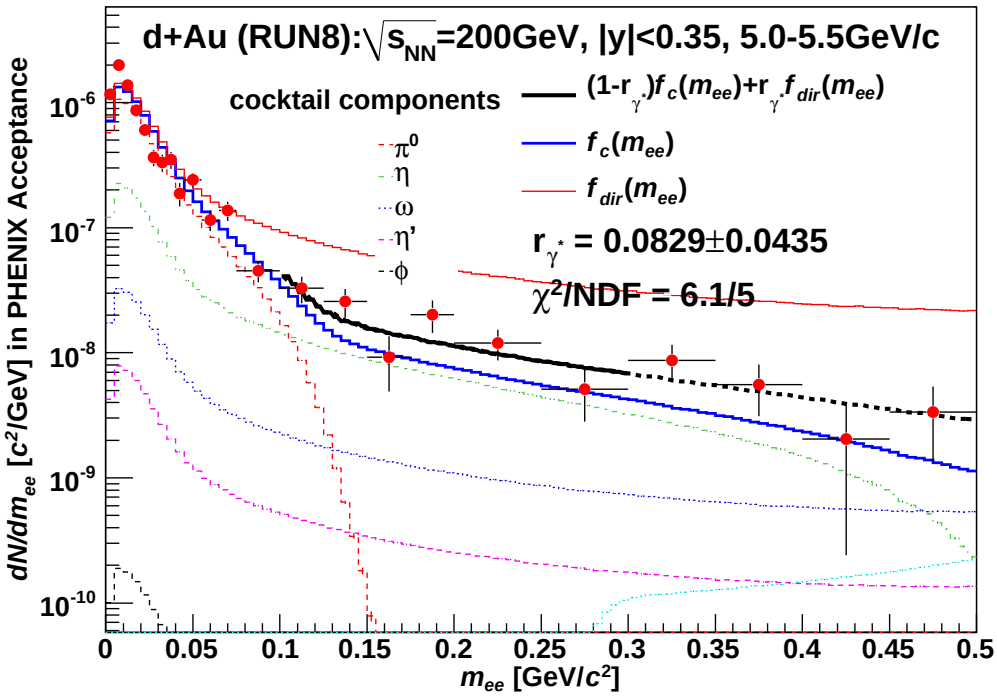

Figure A.8: The e^+e^- pair mass spectrum in $5.0 < p_T^{ee} < 5.5$ GeV/c together with the fit result at determination of direct r_{γ^*}.

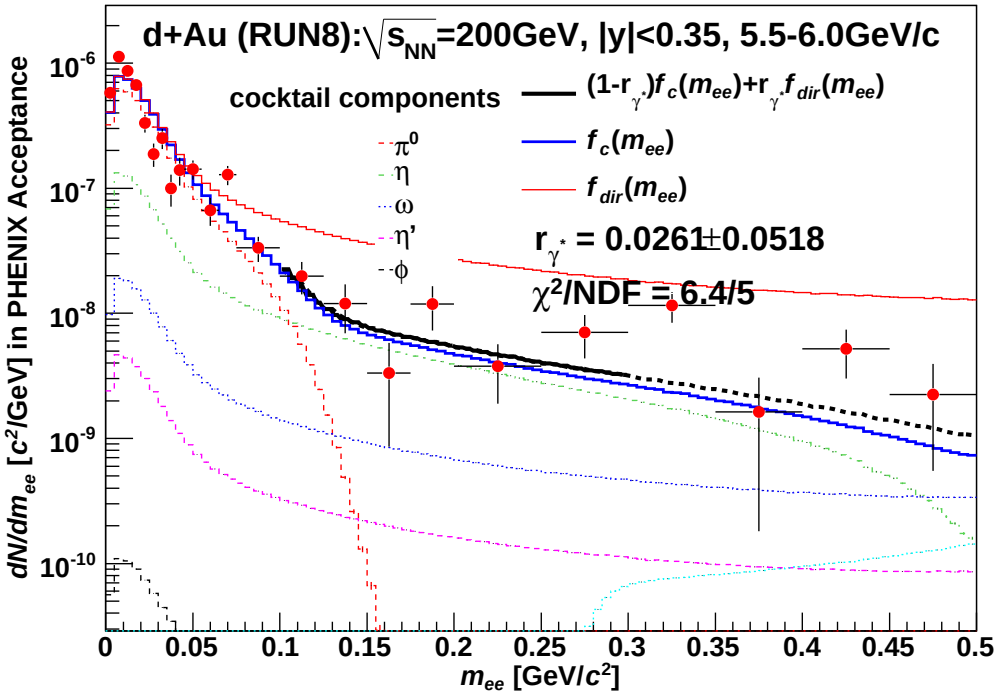

Figure A.9: The e^+e^- pair mass spectrum in $5.5 < p_T^{ee} < 6.0$ GeV/c together with the fit result at determination of direct r_{γ^*}.

A.2 $R(m_{ee}) = (\mathbf{data} - \mathbf{cocktail})/f_{dir}(m_{ee})$

Figures A.10-A.18 show the R as a function of m_{ee} for every 0.5 GeV/c-p_T^{ee} bin in $1.0 < p_T^{ee} < 6.0$ GeV/c with the $r_{\gamma^*} \pm 1\sigma$ band (statistical errors).

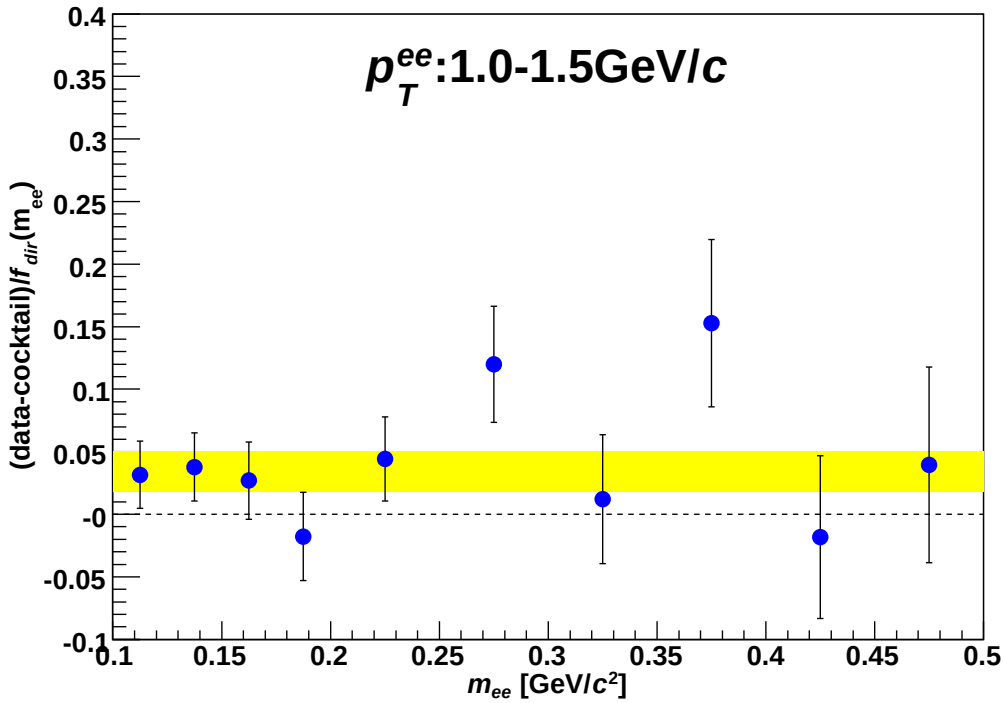

Figure A.10: The R as a function of m_{ee} for $1.0 < p_T^{ee} < 1.5$ GeV/c with the $r_{\gamma^*} \pm 1\sigma$ band (statistical errors).

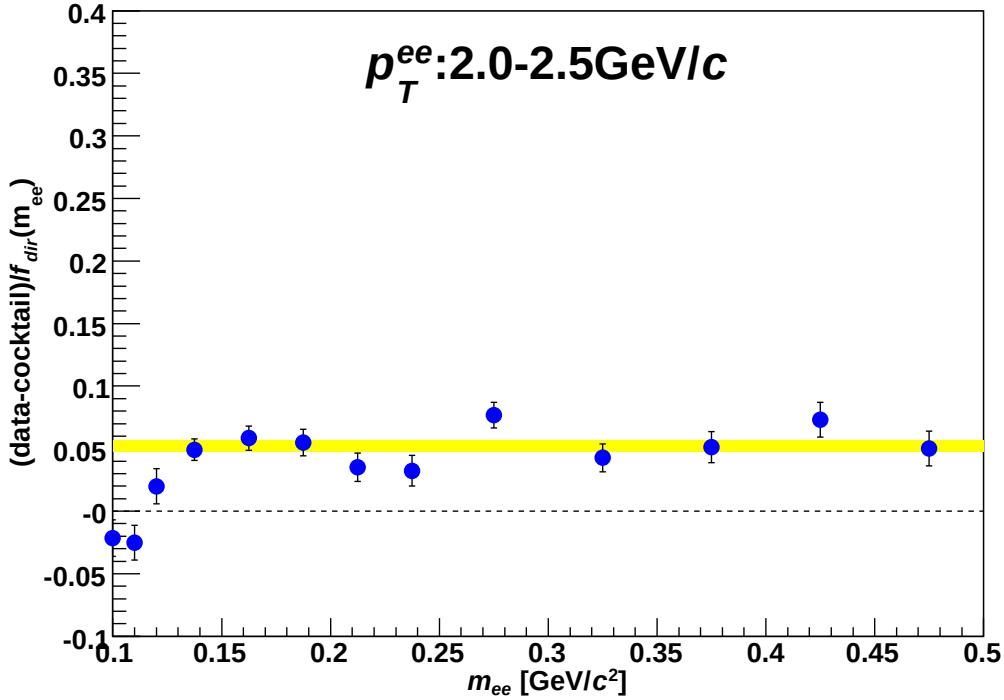

Figure A.11: The R as a function of m_{ee} for $2.0 < p_T^{ee} < 2.5$ GeV/c with the $r_{\gamma^*} \pm 1\sigma$ band (statistical errors).

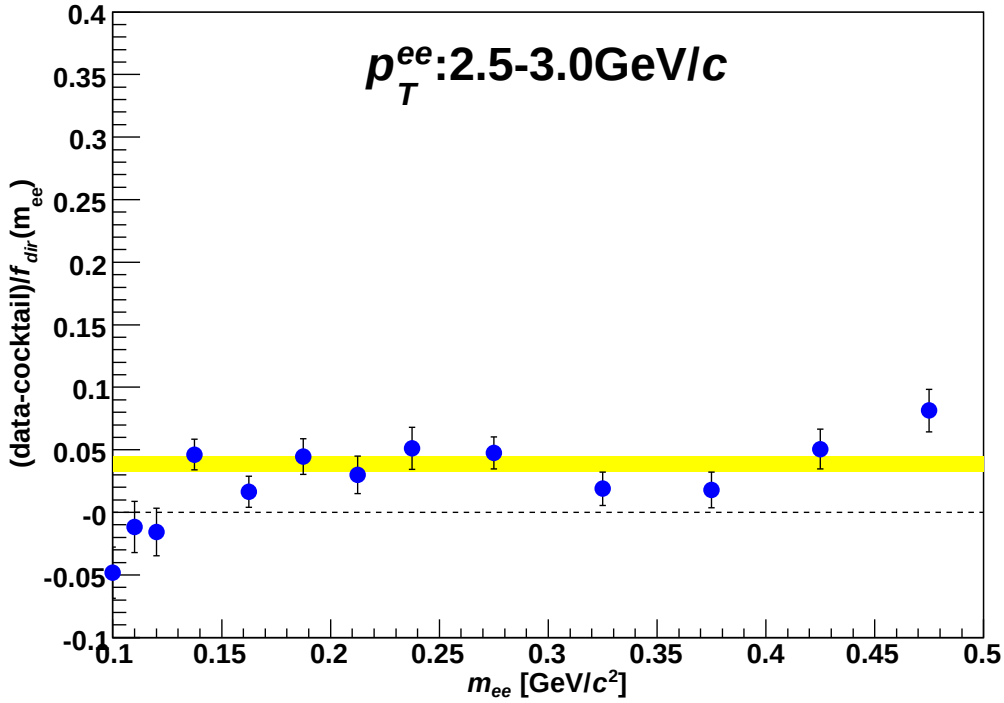

Figure A.12: The R as a function of m_{ee} for $2.5 < p_T^{ee} < 3.0$ GeV/c with the $r_{\gamma^*} \pm 1\sigma$ band (statistical errors).

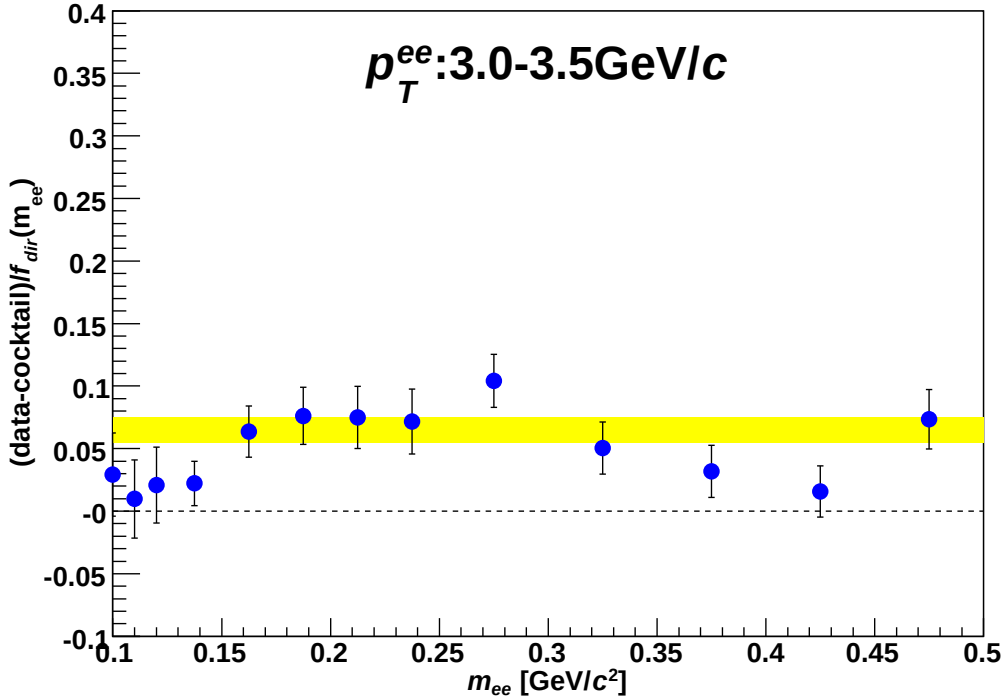

Figure A.13: The R as a function of m_{ee} for $3.0 < p_T^{ee} < 3.5$ GeV/c with the $r_{\gamma^*} \pm 1\sigma$ band (statistical errors).

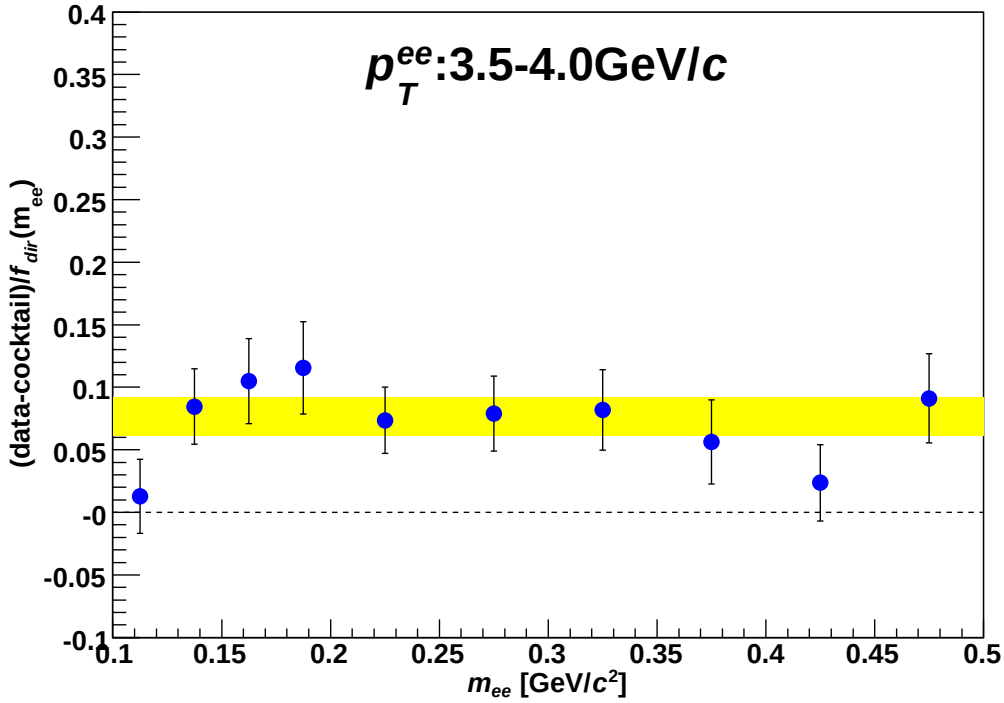

Figure A.14: The R as a function of m_{ee} for $3.5 < p_T^{ee} < 4.0$ GeV/c with the $r_{\gamma^*} \pm 1\sigma$ band (statistical errors).

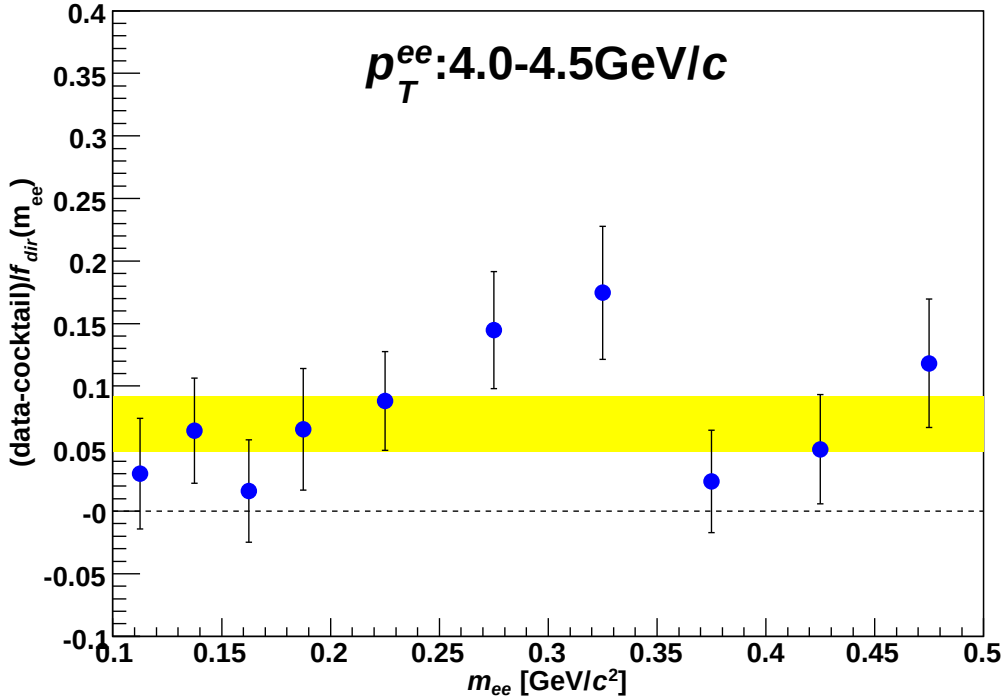

Figure A.15: The R as a function of m_{ee} for $4.0 < p_T^{ee} < 4.5$ GeV/c with the $r_{\gamma^*} \pm 1\sigma$ band (statistical errors).

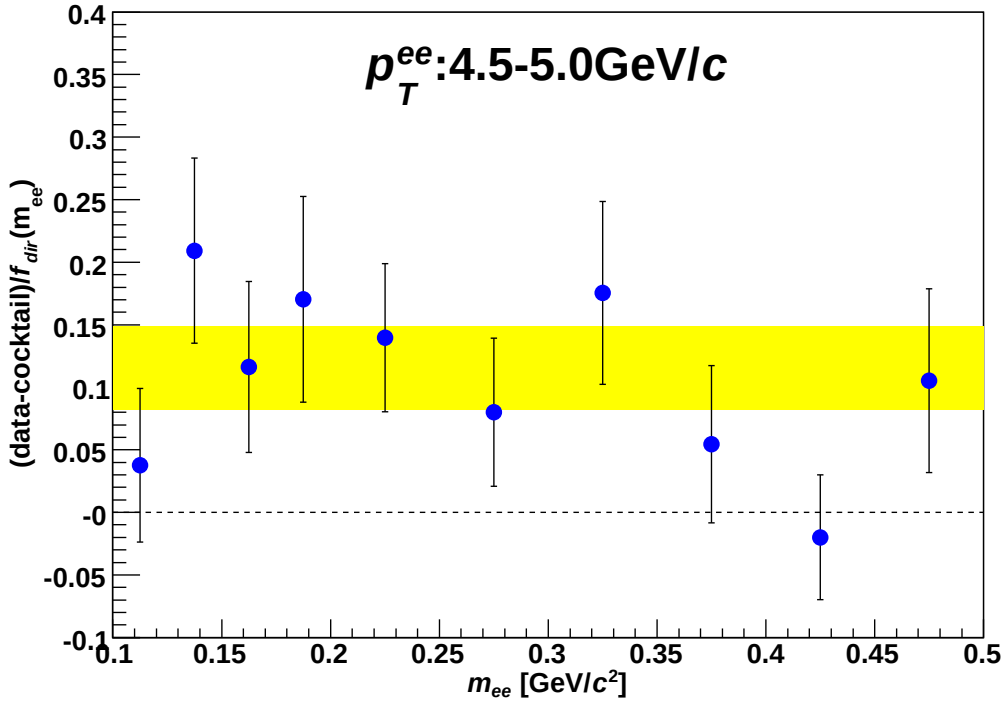

Figure A.16: The R as a function of m_{ee} for $4.5 < p_T^{ee} < 5.0$ GeV/c with the $r_{\gamma^*} \pm 1\sigma$ band (statistical errors).

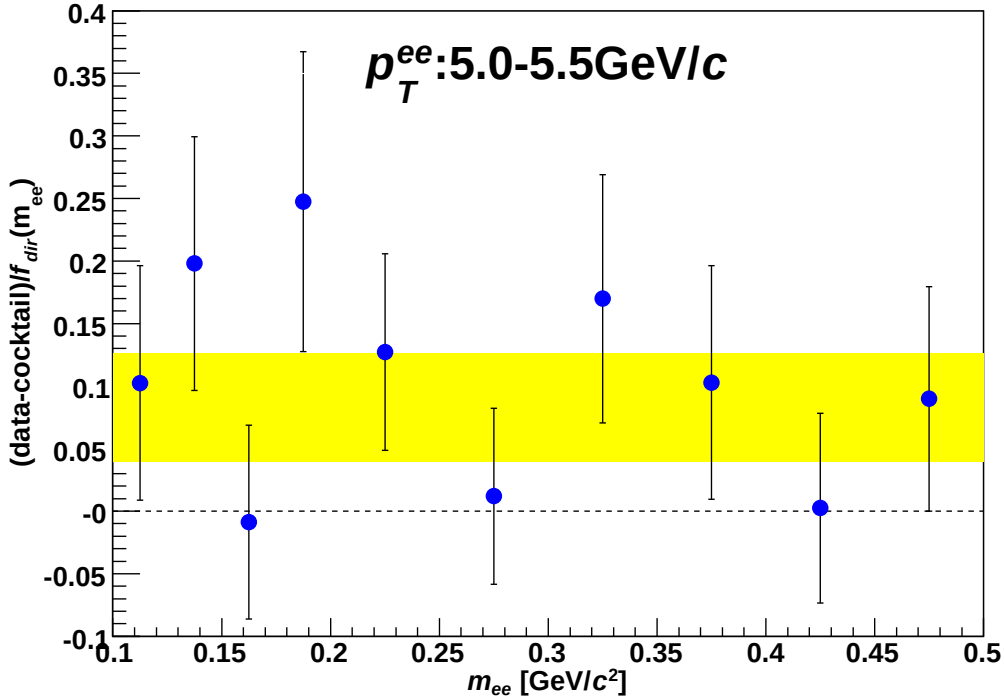

Figure A.17: The R as a function of m_{ee} for $5.0 < p_T^{ee} < 5.5$ GeV/c with the $r_{\gamma^*} \pm 1\sigma$ band (statistical errors).

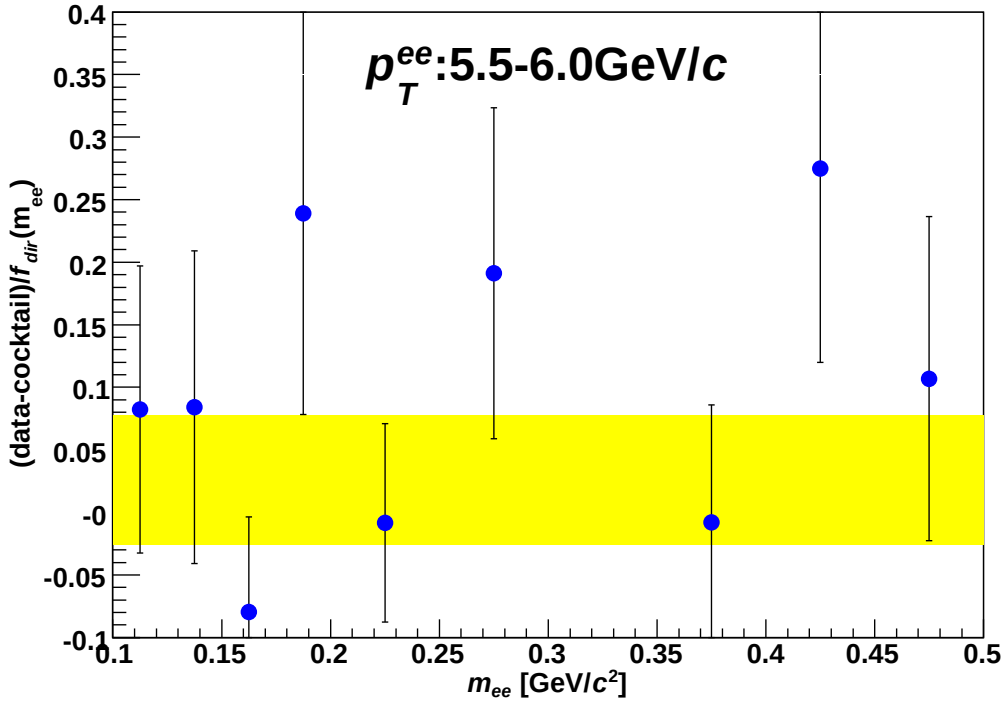

Figure A.18: The R as a function of m_{ee} for $5.5 < p_T^{ee} < 6.0$ GeV/c with the $r_{\gamma^*} \pm 1\sigma$ band (statistical errors).

Bibliography

[1] D.J. Gross and F. Wilczek, Phys. Rev. Lett. **30**, 1343 (1973).

[2] H.D. Politzer, Phys. Rev. Lett. **30**, 1346 (1973).

[3] J.C. Collins and M.J. Perry, Phys. Rev. Lett. **34**, 1353 (1975).

[4] K.G. Wilson, Phys. Rev. D**10**, 2445 (1974).

[5] J.B. Kogut, Rev. of Mod. Phys. **55**, 775 (1983).

[6] H. Satz, Nucl. Phys. **A418**, 447 (1984).

[7] F. Karsch, E. Laermann and A. Peikert, Phys. Lett. B**478**, 447 (2000).

[8] F. Karsch, Nucl. Phys. **A698**, 199 (2002).

[9] F. Karsh, PoSCPOD **07**, 026 (2007).

[10] S. Turbide, *et al.*, Phys. Rev. C**69**, 014903 (2004).

[11] Gordon L.E and W. Vogelsang, Phys. Rev. D**48**, 3136 (1993).

[12] Gordon L.E and W. Vogelsang, Phys. Rev. D**50**, 1901 (1994).

[13] W. Vogelsang. private communication.

[14] A. Adare, *et al.*, Phys. Rev. Lett. **104**, 132301 (2010).

[15] R.J. Glauber and G. Matthiae, Nucl. Phys. **B21**, 135 (1970).

[16] R.J. Glauber. Lectures in theoretical physics, 1959.

[17] J.D. Bjorken, Phys. Rev. D**27**, 140 (1983).

[18] P.F. Kolb, Heavy Ion Phys. **21**, 243 (2004).

[19] R. Albrecht, *et al.*, Phys. Rev. Lett. **76**, 3506 (1996).

[20] D.K. Srivastava and B. Sinha, Phys. Rev. Lett. **73**, 2421 (1994).

[21] A. Dumitru, *et al.*, Phys. Rev. C**51**, 2166 (1995).

[22] M.M. Aggarwal, *et al.*, Phys. Rev. Lett. **85**, 3595 (2000).

[23] M.M. Aggarwal, *et al.*, Phys. Rev. Lett. **93**, 022301 (2004).

[24] R. Hanbury Brown and R.Q. Twiss, Phil. Mag. **45**, 663 (1954).

[25] R. Hanbury Brown and R.Q. Twiss, Nature **178**, 1046 (1956).

[26] S.S. Adler, *et al.*, Phys. Rev. Lett. **98**, 012002 (2007).

[27] S.S. Adler, *et al.*, Phys. Rev. Lett. **94**, 232301 (2005).

[28] A. Adare, *et al.*, Phys. Rev. Lett. **101**, 232301 (2008).

[29] A. Adare, *et al.*, Phys. Rev. C**82**, 011902 (2010).

[30] P. Lichard, Phys. Rev. D**51**, 6017 (1995).

[31] A. Adare, *et al.*, Phys. Rev. C**81**, 034911 (2010).

[32] Y. Akiba, T. Dahms, A. Toia and Y.Yamaguchi, PHENIX Analysis Note **695**, 1 (2008).

[33] N.M. Kroll and W.Wada, Phys. Rev. **98**, 1355 (1955).

[34] L.G. Landsberg, Phys. Rep. **128**, 301 (1985).

[35] R.I. Djhelyadin, *et al.*, Phys. Lett. B**94**, 548 (1980).

[36] H.J. Behrend, *et al.*, Z. Phys. C **49**, 401 (1991).

[37] D. d'Enterria and D. Peressounko, Eur. Phys. J. **46**, 451 (2006).

[38] P.Huovinen, P.V. Ruuskanen and S.S. Rasanen, Phys. Lett. B**535**, 109 (2002).

[39] D.K. Srivastava and B. Sinha, Phys. Rev. C**64**, 034902 (2001).

[40] F.M. Liu, *et al.*, Phys. Rev. C**79**, 014905 (2009).

[41] Jan e Alam, *et al.*, Phys. Rev. C**63**, 021901 (2001).

[42] I. Vitev and B.W. Zhang, Phys. Lett. B**669**, 337 (2008).

[43] I. Vitev and B.W. Zhang, Mod. Phys. Lett. A **24**, 2649 (2009).

[44] J.J. Aubert, *et al.*, Phys. Lett. B**123**, 275 (1983).

[45] D. de Florian and R. Sassot, Phys. Rev. D**69**, 074028 (2004).

[46] K.J. Eskola, V.J. Kolhinen and C.A. Salgado, Eur. Phys. J. C **9**, 61 (1999).

[47] M. Hirai, S. Kumano and M. Miyama, Phys. Rev. D**64**, 034003 (2001).

[48] J.W Cronin, *et al.*, Phys. Rev. D**11**, 3105 (1975).

[49] X.N. Wang, Phys. Rev. C**61**, 064910 (2000).

[50] S.S. Adler, *et al.*, Phys. Rev. C**74**, 024904 (2006).

[51] S.S. Adler, *et al.*, Phys. Rev. Lett. **98**, 172302 (2007).

[52] I. Vitev and B.W. Zhang, Phys. Lett. B**669**, 337 (2008).

[53] B.W. Zhang and I. Vitev, Mod. Phys. Lett. A **24**, 2649 (2009).

[54] H. Hahn, *et al.*, Nucl. Instrum. Meth. **A499**, 245 (2003).

[55] K. Adcox, *et al.*, Nucl. Instrum. Meth. **A499**, 469 (2003).

[56] K.H. Ackermann, *et al.*, Nucl. Instrum. Meth. **A499**, 624 (2003).

[57] B.B. Back, *et al.*, Nucl. Instrum. Meth. **A499**, 603 (2003).

[58] M. Adamczyk, *et al.*, Nucl. Instrum. Meth. **A499**, 437 (2003).

[59] K. Hagiwara, *et al.*, Phys. Rev. D**66**, 010001 (2002).

[60] M. Allen, *et al.*, Nucl. Instrum. Meth. **A499**, 549 (2003).

[61] T. Ludlam, Nucl. Instrum. Meth. **A499**, 428 (2003).

[62] C. Adler, *et al.*, Nucl. Instrum. Meth. **A470**, 488 (2001).

[63] C. Adler, *et al.*, Nucl. Instrum. Meth. **A499**, 433 (2003).

[64] S.H. Aronson, *et al.*, Nucl. Instrum. Meth. **A499**, 480 (2003).

[65] K. Adcox, *et al.*, Nucl. Instrum. Meth. **A499**, 489 (2003).

[66] L. Aphecetche, *et al.*, Nucl. Instrum. Meth. **A499**, 521 (2003).

[67] M. Aizawa, *et al.*, Nucl. Instrum. Meth. **A499**, 508 (2003).

[68] Y. Akiba, *et al.*, Nucl. Instrum. Meth. **A433**, 143 (1999).

[69] C. Amsler, *et al.*, Phys. Lett. B**667**, 1 (2008).

[70] T. Sakaguchi, *et al.*, Nucl. Instrum. Meth. **A453**, 382 (2000).

[71] S.S. Adler, *et al.*, Nucl. Instrum. Meth. **A499**, 560 (2003).

[72] J.T. Mitchell, *et al.*, Nucl. Instrum. Meth. **A482**, 491 (2002).

[73] J. Myrhiem and L. Bugge, Nucl. Instrum. Meth.**160**, 43 (1979).

[74] GEANT Detector description and simulation tool. CERN Program Library Long Write-up W5013, CERN, Geneve.

[75] A. Adare, *et al.*, Phys. Lett. B**670**, 313 (2009).

[76] T. Sjöstrand, S. Mrenna and P. Skands, Comput. Phys. Comm. **178**, 852 (2008).

[77] B. Andersson, G. Gustafson, G. Ingelman and T. Sjöstrand, Phy. Rept. **97**, 31 (1983).

[78] H.L. Lai, *et al.*, Eur. Phys. J **12**, 375 (2000).

[79] D. Sharma, *et al.*, PHENIX Analysis Note **840**, 1 (2010).

[80] D.C. McGlinchey, *et al.*, PHENIX Analysis Note **933**, 1 (2010).

[81] S.S Adler, *et al.*, Phys. Rev. Lett. **96**, 202301 (2006).

[82] S.S Adler, *et al.*, Phys. Rev. C**75**, 051902 (2007).

[83] R. Averbeck, *et al.*, PHENIX Analysis Note **89**, 1 (2001).

[84] R.I. Djhelyadin, *et al.*, Phys. Lett. B**102**, 296 (1981).

[85] G.J. Gounaris and J.J. Sakurai, Phys. Rev. Lett. **21**, 244 (1968).

[86] A. Adare, *et al.*, Phys. Rev. Lett. **98**, 232002 (2007).

[87] H. Torii, *et al.*, PHENIX Analysis Note **451**, 1 (2005).

[88] F. Karsh, Lect. Notes Phys. **583**, 209 (2002).